FLAVOURED NEUTRINO MASS MODELS

A taste of leptons at low and high energies

Tanja Geib

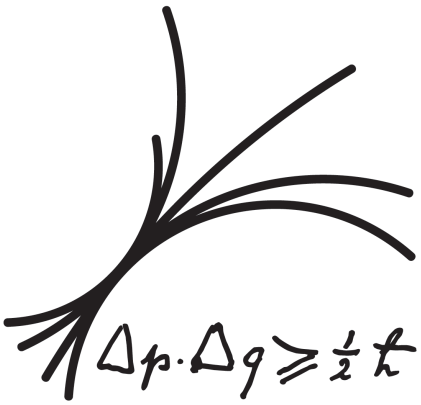

München 2017

Flavoured Neutrino Mass Models

A taste of leptons at low and high energies

Dissertation
an der Fakultät für Physik
der Ludwig–Maximilians–Universität
München

vorgelegt von
Tanja Geib
aus Stuttgart

München, den 18. Dezember 2017

Dissertation

an der Fakultät für Physik
der Ludwig-Maximilians-Universität München
vorgelegt von Tanja Geib
am 18. Dezember 2017.

Erstgutachter: PD Dr. Georg Raffelt
Zweitgutachter: Prof. Dr. Gerhard Buchalla

Tag der mündlichen Prüfung: 09. Februar 2018
Vorsitzende der Prüfungskommission: Prof. Dr. Dorothee Schaile
Weitere Prüfer: Prof. Dr. Jochen Weller, Dr. Alexander Merle

Max-Planck-Institut für Physik,
München, den 14. Februar 2018.

Zusammenfassung

Der einzige direkte experimentelle Beweis für Physik jenseits des Standardmodells sind die Oszillationen der Neutrinoarten. Die Suche nach einer Erklärung für diese überraschende Entdeckung hat zu einer Vielzahl möglicher Modelle für Neue Physik geführt. Da Neutrinooszillationen gezeigt haben, dass die Leptonflavourzahl in der Natur nicht erhalten ist, tendieren Modelle Neuer Physik dazu eine darüber hinaus gehende Verletzung der Leptonflavourzahl und mitunter sogar der Gesamtleptonenzahl einzuführen. Die Gültigkeit dieser Konfigurationen Neuer Physik wird anhand der Vereinbarkeit ihrer Vorhersagen mit den experimentellen Daten bewertet. In naher Zukunft wird erwartet, dass die Umwandlungen gebundener Myonen, welche die Leptonflavour- und/oder Gesamtleptonenzahl verletzen, die deutlichsten experimentellen Fortschritte erfahren werden. Durch die Verbesserung der aktuellen experimentellen Grenzen um mehrere Größenordnungen, werden diese Umwandlungen zu den empfindlichsten Tests für geladene Leptonflavour-/Gesamtleptonenzahlverletzung. Die Untersuchung derartiger neuer Möglichkeiten ist deshalb essentiell für die Entschlüsselung neuartiger Physik jenseits des Standardmodells. Das Ziel dieser Arbeit ist es, einen Beitrag zur Verbesserung der Testbarkeit von Modellen Neuer Physik in Bezug auf zwei verschiedene Aspekte zu leisten, wobei der Fokus auf Neutrinomodellen mit zusätzlicher Leptonflavour- und/oder Gesamtleptonenzahlverletzung liegt. Um ihr Potential zur Untersuchung viel versprechender Modelle Neuer Physik voll auszuschöpfen, erfordern sowohl die die Leptonflavourzahl verletzende $\mu^- - e^-$ Umwandlung als auch die die Leptonflavour- und Gesamtleptonenzahl verletzende $\mu^- - e^+$ Umwandlung solide theoretische Vorhersagen. Da die theoretischen Verfahren zur Beschreibung beider Arten der Umwandlung gebundener Myonen derzeit unvollständig sind, arbeiten wir daran, diese Lücken zu schließen. Zu diesem Zweck präsentieren wir unsere detaillierten und umfassenden Berechnungen mit dem Ziel, beide Prozesse für Teilchenphysiker zugänglich zu machen. Darüber hinaus vergleichen wir die Vorhersagen einer Auswahl an Modellen Neuer Physik mit aktuellen experimentellen Daten sowie mit zukünftig erwarteten Genauigkeiten. Wir zeigen zudem, wie Experimente bei niedrigen Energien, die indirekt nach neuer Physik anhand von Prozessen mit geladener Leptonflavour- und Gesamtleptonenzahlverletzung suchen, und solche bei hohen Energien, die direkt nach neuen Teilchen suchen, komplementäre Bedingungen liefern können. Folglich untermauern unsere Ergebnisse die Notwendigkeit der Suche nach niederenergetischer Leptonflavour- und Gesamtleptonenzahlverletzung im Zusammenhang mit der Erforschung der Physik jenseits des Standardmodells. Des Weiteren muss bei der Herleitung der Modellvorhersagen beachtet werden, dass

viele Modelle Neuer Physik bei hohen Energieskalen definiert sind, wohingegen experimentelle Oszillationsdaten bei niedrigen Energien gemessen werden. Da sich die Parameter einer Theorie mit der betrachteten Energieskala verändern, müssen Renormierungsgruppeneffekte berücksichtigt werden. In diesem Zusammenhang präsentieren wir die erste umfassende Renormierungsgruppenanalyse des Littlest-Seesaw-Modells. Unsere Analyse zeigt, dass es entscheidend ist, die Auswirkungen sich verändernder Parameter einzubeziehen, wenn Modelle Neuer Physik und Oszillationsdaten einander gegenübergestellt werden.

Abstract

The only direct experimental evidence for physics beyond the Standard Model are the oscillations of neutrino species. Explaining this surprising discovery has led to a variety of potential New Physics models. Since neutrino oscillations demonstrate that lepton flavour is not conserved in Nature, New Physics models tend to introduce additional lepton flavour and sometimes even lepton number violating physics. The validity of any New Physics setting is assessed based on the consistency of its predictions with experimental data. In the near future, lepton flavour and/or number violating conversions of bound muons are expected to undergo the most dramatic experimental advances. By improving currents limits by several orders of magnitude, these reactions will become the most sensitive probe for charged lepton flavour/number violation. Therefore, exploring new opportunities such as these is essential to unravel novel physics beyond the Standard Model. The goal of this thesis is to contribute to improving the testability of New Physics models with respect to two different aspects, focusing on neutrino models with additional lepton flavour and/or lepton number violation. First, both the lepton flavour violating $\mu^- - e^-$ conversion and the lepton flavour and lepton number violating $\mu^- - e^+$ conversion require solid theoretical predictions to fully exploit their potential for investigating promising New Physics models. Since both types of bound muon conversions currently lack certain elements in their theoretical treatment, we work towards closing these gaps. To that end, we present our detailed and comprehensive computations which aim at making both processes accessible to the particle physics community. Furthermore, we compare predictions from a selection of New Physics models to current experimental data and future expected sensitivities. We also show how experiments at low energies, indirectly looking for New Physics via charged lepton flavour and lepton number violating processes, and experiments at high energies, directly looking for new particles, can provide complementary constraints. Thus, our results considerably strengthen the case for low-energy lepton flavour and lepton number violation searches being vital contributions to the search for physics beyond the Standard Model. Second, when deriving model predictions, one must take into account that many New Physics models are defined at high energy scales, whereas experimental oscillation data are measured at low energies. Since the parameters of a theory change with the energy scale under consideration, it is crucial to incorporate renormalisation group effects. In this context, we present the first comprehensive renormalisation group analysis of the Littlest Seesaw model. Our analysis demonstrates that the inclusion of running effects is crucial when confronting New Physics models with oscillation data.

Publications

This thesis is based on a number of publications to which I contributed during my research conducted at the Max-Planck-Institut für Physik from February 2015 to December 2017. Parts of this thesis were, therefore, originally published in the corresponding papers written in collaboration with Prof. Dr. Stephen F. King, Dr. Alexander Merle, Dr. Jose Miguel No, Dr. Luca Panizzi and Prof. Dr. Kai Zuber [1–5]:

1. T. Geib, S. F. King, A. Merle, J. M. No and L. Panizzi, *Probing the Origin of Neutrino Masses and Mixings via Doubly Charged Scalars: Complementarity of the Intensity and the Energy Frontiers*, Phys. Rev. D **93** (2016) no.7, 073007, [arXiv:1512.04391].

2. T. Geib and A. Merle, *Conversions of bound muons: Lepton flavor violation from doubly charged scalars*, Phys. Rev. D **93**, no. 5, 055039 (2016), [arXiv:1512.04225].

3. T. Geib, A. Merle and K. Zuber, $\mu^- - e^+$ *conversion in upcoming LFV experiments*, Phys. Lett. B **764**, 157 (2017), [arXiv:1609.09088].

4. T. Geib and A. Merle, $\mu^- - e^+$ *Conversion from Short-Range Operators*, Phys. Rev. D **95**, no. 5, 055009 (2017), [arXiv:1612.00452].

5. T. Geib and S. F. King, *A Comprehensive Renormalisation Group Analysis of the Littlest Seesaw Model*, [arXiv:1709.07425].

Plots, tables, and figures throughout this thesis can be taken from these publications. Furthermore, the structure of arguments and sections can also be inspired by the respective sections in these papers.

Contents

Chapter 1

Introduction

The Standard Model (SM) of particle physics is a exceptionally successful description of the smallest building blocks of the Universe, and its predictive power is unparalleled. Despite its many achievements, though, the SM fails to explain the observation of neutrino oscillations. These were experimentally verified by Super-Kamiokande in 1998 [7] and by the Sudbury Neutrino Observatory (SNO) in 2002 [8], leading to the Nobel prize for Takaaki Kajita and Arthur B. McDonald in 2015. The existence of neutrino flavour oscillations has since been confirmed by a number of other experiments [9–28].
For neutrino oscillations to occur, both distinct neutrino masses and non-vanishing leptonic mixing angles are required. Since neither can be accommodated within the SM of particle physics, due to the absence of right-handed neutrinos, it proves necessary to extend the SM. The question which extension is actually realised in Nature remains unresolved: the theoretical origin of neutrino masses and leptonic mixing is still unclear. Moreover, several features, such as the absolute neutrino mass scale, the mass ordering, or the Dirac/Majorana nature of neutrinos, also remain unknown. This has triggered intense research activities, both on the theoretical and on the experimental side. In other words, the fundamental questions raised by the discovery of neutrino oscillations are among the leading motivations to search for New Physics beyond the SM.

How do physicists explore and test the fundamental questions posed by and beyond neutrino physics? On the theoretical side, research efforts focus on the origin of neutrino mass and mixing. These open questions may imply that the SM is merely an effective low-energy theory of some yet unknown complete high-energy theory. This suggests that neutrinos and their mixing behaviour may provide key information on the nature of the New Physics beyond the SM. The major goals for model building in the neutrino sector are to explain both the smallness of neutrino masses relative to the charged-lepton masses and the large leptonic mixing compared to the mixing in the quark sector. Numerous models, mechanisms, and ideas on how to generate neutrino masses and leptonic mixing have been proposed to date. Some of them focus

on naturally implementing the smallness of the neutrino masses and are referred to as neutrino mass models, while others concentrate on predicting the leptonic mixing pattern and are referred to as neutrino flavour models. The New Physics model predictions need to be consistent with current data and, ideally, are testable further by near-future experiments. Hence, on the experimental side, the central question is which phenomenological consequences to study.
The most obvious course of action is to test a given model by comparing its predictions for the leptonic mixing and neutrino mass squared differences with the experimental oscillation data. This procedure requires an accurate determination of the model predictions. Neutrino, in particular flavour, models are often defined at the scale of some grand unified theory, $\mathcal{O}(10^{16}$ GeV), while the scales accessible to experiment are lower by many orders of magnitude, $\mathcal{O}(10^{2-3}$ GeV). Since the parameters of a theory change with the energy scale under consideration, it is crucial to incorporate renormalisation group corrections to properly derive the low-energy model predictions for the neutrino parameters. For example, the Littlest Seesaw model [29–31], which combines the Seesaw mechanism [32–36] with constrained sequential dominance [37–43] and, as a result, provides highly accurate predictions both for neutrino masses and leptonic mixing parameters, is strongly influenced by running effects. This important aspect with regard to systematically testing the phenomenological viability of this model motivates parts of my research presented in this thesis.

There are other complementary ways to test potential New Physics settings. Due to the existence of neutrino oscillations, it is clear that Nature does realise lepton flavour violation (LFV). In addition to the LFV in the neutrino sector, massive neutrinos also give rise to LFV reactions in the charged-lepton sector. Nevertheless, the contributions to charged LFV processes stemming from solely augmenting the SM by massive neutrinos are suppressed to virtually undetectable levels by the famous Glashow-Iliopoulos-Maiani (GIM) mechanism [44]. As lepton flavour is not a fundamental symmetry of Nature, New Physics models tend to introduce additional LFV physics, which might be sizeable enough to be detected. Therefore, charged LFV searches can open a window to study New Physics with additional LFV. Most importantly, any experimental observation of LFV in the charged sector would be an unambiguous signal for New Physics – even beyond massive neutrinos. In addition to LFV, several New Physics models also introduce lepton number violation (LNV) at the perturbative level, which has not been observed for the SM. Its detection might be considered an even more fundamental discovery regarding the properties of Nature. As a consequence, the hunt for both LFV and LNV processes is considered to be a matter of high priority in experimental advances towards unravelling New Physics. To maximise the benefit from ongoing and future experiments, the information from complementary searches at low and high energies needs to be combined. By doing so, one might be able to not

only study specific phenomenological consequences of potential New Physics models but to probe the physics beyond the SM more profoundly.
Among the searches for charged LFV processes, the most dramatic experimental progress in the near future is expected for the conversion of muons bound on atomic nuclei, known as $\mu^- - e^-$ conversion. With expected sensitivities that improve current limits by up to five/six orders of magnitude, $\mu^- - e^-$ conversion will be the most sensitive LFV probe available, potentially reaching a spectacular sensitivity on the branching ratio of $\mathrm{BR}[\mu^- + {}^{48}\mathrm{Ti} \to e^- + {}^{48}\mathrm{Ti}] = \mathcal{O}(10^{-18})$ [45]. Most experiments searching for $\mu^- - e^-$ conversion can additionally search for the LNV $\mu^- - e^+$ conversion with at most minor modifications of the setup. An analogous improvement on the sensitivity of $\mu^- - e^+$ conversion by several orders of magnitude is expected with sensitivities similar to those for $\mu^- - e^-$ conversion, provided a suitable choice of isotope [46].
For precisely probing charged LFV and LNV, the theoretical treatment of these processes must be thorough, which is a highly non-trivial task due to the nuclear physics involved. Even though these two types of bound muon conversion were proposed decades ago, many details are still unresolved. To help unlock these processes' discovery potential, parts of my research presented in this thesis was devoted to closing several gaps in the required theoretical knowledge. As the prime example, we employed an effective theory involving a doubly charged SU(2) singlet scalar [47], because already such a minimal setting provides a rich phenomenology both at high and low energy scales. This enabled us to demonstrate the importance of complementarity in experimental searches, while avoiding the introduction of a large number of free parameters.

In summary, the discovery of neutrino oscillations has opened a window to study the nature of physics beyond the SM, especially with respect to its LFV and LNV behaviour. To profoundly constrain potential New Physics models, it is essential to combine the complementary constraints from neutrino oscillations, charged LFV and LNV processes, and direct new-particle searches. In order to fully exploit the upcoming experimental progress, this thesis makes substantial contributions to advancing the theoretical knowledge required for both $\mu^- - e^-$ and $\mu^- - e^+$ conversion and to demonstrating the importance of renormalisation group effects when confronting model predictions with low-energy experimental data.

Outline

Chapter 2 will extend the introduction to this thesis by providing an overview of the current status of neutrino physics. It will further motivate the intense research activities, both on the theoretical and on the experimental side. Subsequently, chapter 3 will be devoted to the origin of neutrino masses and leptonic mixing, as well as the connection between neutrinos and other New Physics beyond the Standard Model. To that end, we will review the basic concepts of neutrino model building, address phenomenological consequences concerning lepton flavour and lepton number violation, and introduce the two models predominantly employed in chapters 5 and 6. Chapter 4 will be dedicated to the introduction of the mathematical tools and methods we will apply throughout chapters 5 and 6, namely renormalisation group effects, effective field theories, and the method of least squares. Having laid the theoretical groundwork in chapters 2 through 4, we will turn to the research projects conducted during my doctorate studies. Chapter 5 is devoted to an overall discussion of the lepton flavour violating $\mu^- - e^-$ conversion and the lepton flavour and lepton number violating $\mu^- - e^+$ conversion. For both types of bound muon conversions, we will present our detailed and comprehensive computations which aim at making the treatment of both processes accessible to the particle physics community. In addition, we will assess their respective reach, discuss the benefits of complementarity, and introduce experimental aspects. In chapter 6, we will present our results on the comprehensive renormalisation group analysis of the Littlest Seesaw model. To that end, we will perform a χ^2 analysis of the low-energy neutrino masses and leptonic mixing angles, in the presence of renormalisation group corrections. Finally, we will summarise and conclude this thesis in chapter 7.

Chapter 2

Snapshot – Current Status of Neutrino Physics

The goal of this chapter is to provide an overview of the current status of neutrino physics. We thereby aim to motivate the intense research activities with respect to the nature of neutrinos, both on the theoretical and on the experimental side, and to illustrate their connection to New Physics beyond the Standard Model. To that end, we will address both our current knowledge of neutrino masses and leptonic mixing, and the fundamental questions in neutrino physics that remain unanswered. To brush up on the theoretical foundations, we start by discussing the concept of neutrino oscillations. Note that this chapter is by no means exhaustive. For more comprehensive reviews, see e.g. Refs. [9, 48–55].

In the following, we want to briefly go through the basic principle of neutrino oscillations and discuss their implications by means of slightly simplified scenarios based on Refs. [56, 57].[1] We begin with a scenario generic for neutrino oscillation experiments. We set the scene by producing a flux of (muon) neutrinos from a pion beam decaying into a muon plus a muon neutrino, i.e. $\pi^+ \to \mu^+ + \nu_\mu$, through weak interactions.[2] Simultaneously, we search for neutrino interactions in a target-detector down the beamline. Since the neutrinos in the beam interact weakly in the target-detector, we can learn which flavour of neutrino arrives at the detector from observing the correspondingly produced charged lepton. Therefore, assuming we observe sufficiently many electrons in the final state, this implies that a muon neutrino has to have had transformed itself into an electron neutrino in flight. The question is now,

[1] Note that we closely follow the structure and line of reasoning of chapter 2.3 in Ref. [56]. A detailed discussion of not only neutrino oscillations but more generally neutrino physics can be found in Ref. [57].

[2] Note that pions primarily decay into muons and muon neutrinos, with a branching fraction of more than 99.9 % [52]. We therefore assume that the resulting neutrino flux consists of muon neutrinos exclusively.

if and how this is possible. The short answers would be "yes" and "*quantum mechanics*". The more detailed answer can be outlined as follows, with more information on the notions of mass/ flavour eigenbases and how they are related via a mixing matrix U described in section 3.1. We assume that there are N flavours of charged leptons $\ell = e,\ \mu,\ \tau, \cdots$, their (through weak interactions) associated N neutrino flavour eigenstates $\nu_\ell = \nu_e,\ \nu_\mu,\ \nu_\tau, \cdots$, as well as N neutrino mass eigenstates $\nu_k = \nu_1,\ \nu_2,\ \nu_3, \cdots$.[3] Furthermore, in analogy to the example of the neutrino oscillation experiment, we assume that we have a source at our disposal which produces a pure beam of a specific neutrino flavour ν_ℓ. Realistically, the momentum resolution of such an experiment is too small to resolve the generated neutrino mass eigenstates. Therefore, with the mass and flavour eigenbases not matching and the level of sensitivity to low to determine exactly which mass eigenstate was generated, the flavour eigenstate produced is a coherent superposition of the mass eigenstates, cf. Eq. (3.1.8):

$$\nu_\ell = \sum_{k=1}^{N} U_{\ell k}^* \, \nu_k \,. \tag{2.0.1}$$

To simplify matters, we assume that the neutrino of flavour ν_ℓ is generated with an exactly determined momentum p_ν at the time $t = 0$,[4] which means the wave function is given by:

$$\psi(x, t = 0) = \sum_k U_{\ell k}^* \, \nu_k \, \mathrm{e}^{i p_\nu x} \,. \tag{2.0.2}$$

Evolving in time, each mass component of the wave function accumulates a phase:

$$\begin{aligned} \psi(x,t) =& \sum_k U_{\ell k}^* \, \nu_k \, \mathrm{e}^{i p_\nu x} \, \mathrm{e}^{-i E_k t} \,, \\ \text{with} \quad E_k =& E(\nu_k) = \sqrt{p_\nu^2 + m_k^2} \overset{p_\nu \gg m_k}{\approx} p_\nu + \frac{m_k^2}{2 p_\nu} \,. \end{aligned} \tag{2.0.3}$$

With all neutrino masses being tiny, i.e. $m_k^2 \ll p_\nu^2$, the neutrino flavour state propagates at almost the speed of light. Therefore, with ν_ℓ being produced at $x = 0$, the neutrino will have travelled to about $x = t$ at the time t, resulting in the wave function:

$$\psi(t,t) = \psi(x,x) \simeq \sum_k U_{\ell k}^* \, \nu_k \, \mathrm{e}^{-i \frac{m_k^2}{2 p_\nu} x} \,. \tag{2.0.4}$$

[3] Note that there need not be N neutrino mass eigenstates, but we choose that for the following discussion.

[4] Here, we have set the coordinate system such that the neutrino beam travels along the x-axis, i.e. it is $\vec{p}_\nu = (p_\nu, 0, 0)$. Hence, x describes the distance from where the neutrino was produced to where we try to observe it.

Reversing Eq. (2.0.1), we can express the neutrino mass eigenstates as linear combinations of the flavour eigenstates. This allows us to rewrite Eq. (2.0.4) as:

$$\psi(x,x) \simeq \sum_{\ell'} \left[\sum_k U^*_{\ell k}\, \mathrm{e}^{-i\frac{m_k^2}{2p_\nu}x}\, U_{\ell' k} \right] \nu_{\ell'} \,. \tag{2.0.5}$$

Clearly this wave function, being a superposition of all neutrino flavours, shows that the beam has picked up components of possibly all flavours while travelling along the beamline. The amplitude for a given flavour neutrino ν_ℓ to have transitioned into another flavour neutrino $\nu_{\ell'}$ (travelling a distance of x) can be retrieved from the coefficient of the respective $\nu_{\ell'}$ in Eq. (2.0.5). In other words, massive neutrinos can transition between different flavours in flight.
We can now determine the probability $P(\ell \to \ell', x)$ to find that, at the distance x from the source, the original flavour neutrino ν_ℓ has transformed itself into the flavour neutrino $\nu_{\ell'}$. That way, we finally arrive at the phenomenon referred to as neutrino oscillations. Based on Eq. (2.0.5), we can derive

$$\begin{aligned} P(\ell \to \ell', x) &= \left[\sum_{k'} U_{\ell k'}\, \mathrm{e}^{i\frac{m_{k'}^2}{2p_\nu}x}\, U^*_{\ell' k'} \right] \cdot \left[\sum_k U^*_{\ell k}\, \mathrm{e}^{-i\frac{m_k^2}{2p_\nu}x}\, U_{\ell' k} \right] \\ &\to \sum_k U^2_{\ell k}\, U^2_{\ell' k} + \sum_{k' \neq k} U_{\ell k}\, U_{\ell k'}\, U_{\ell' k'}\, U_{\ell' k}\, \cos\left(2\pi \frac{x}{L_{kk'}}\right) , \end{aligned} \tag{2.0.6}$$

where we have introduced the so-called oscillation length $L_{kk'}$:

$$L_{kk'} \equiv 2\pi \frac{2p_\nu}{\Delta m^2_{kk'}} \,, \quad \text{where} \quad \Delta m^2_{kk'} \equiv |m_k^2 - m_{k'}^2| \,. \tag{2.0.7}$$

The simplified expression in the second line of Eq. (2.0.6) is based on choosing the mixing matrix U to be real.[5] In fact, the simplified expression nicely displays the oscillatory behaviour of the transition probability with the distance x, which is the phenomenon we call *neutrino oscillations*. This phenomenon can be understood by realising that the mass eigenstate components of the flavour ν_ℓ produced at the source travel at slightly different speeds due to their distinct masses. So, at a given p_ν, the lighter mass states propagate faster than the heavier ones. As a consequence, the various ν_k components of the neutrino beam develop relative phase shifts while propagating, which causes them to *not* add up to the original neutrino flavour ν_ℓ anymore but instead to combine to varying superpositions of all flavour eigenstates. In other words, the neutrino beam picks up components that belong to other flavour eigenstates, which vary in relative "strength" with the distance propagated. From Eq. (2.0.6) we learn that, for neutrino oscillations to occur, both distinct neutrino masses and non-vanishing leptonic mixing angles are required.
There are a few implications of neutrino oscillation we want to highlight briefly:

[5] This choice is predicated upon the assumption that CP is conserved. As CP is violated in the quark sector [58–60] and there are hints towards its violation in the lepton sector [48, 49], this assumption is based on simplification only.

- The oscillating terms in the transition probability, be it the simplified version in Eq. (2.0.6) or that of a more realistic scenario, stem from the interferences of the different mass eigenstates in the wave function.

- For $x \ll L_{kk'}$: the original ν_ℓ maintains its flavour.

- For $x \gg L_{kk'}$: at a distance that far exceeds the oscillation length, the oscillation pattern disappears,[6] and the probability is given by $P(\ell \to \ell', x) = \sum_k U_{\ell k}^2 U_{\ell' k}^2 \neq 0$. So, neutrinos produced at the source are still transformed into other flavours, but the probability does not oscillate with the distance any longer.

- The oscillatory behaviour is best observed if the length scale of the experiment is $x = \mathcal{O}(L_{kk'})$. Neutrino oscillation experiments generally fall into one of two categories. They are either *appearance* experiments, searching for the $\nu_{\ell'}$ in $\nu_\ell \to \nu_{\ell'}$, or *disappearance* experiments, looking for the reduction or x-dependence of the flux of original flavour.

Clearly, the phenomenon of neutrino oscillations is intimately related to quantum mechanics. Recall that, at the beginning of this discussion, we assumed the momentum of the initially produced flavour neutrino eigenstate to be known precisely (for reasons of simplification). Due to the uncertainty principle [62, 63], we would completely lose any information on the location of the source, i.e. the decay point where ν_ℓ is produced, the more accurately we want to determine the momentum. However, to observe any oscillations with distance, the uncertainty in the position cannot be larger than the oscillation lengths. Thus, we need to know the location of the source with high enough accuracy, which implies that the momentum cannot be precisely known. To describe a more realistic setting, one rather needs to make use of a wave packet treatment to capture the spread in momentum. Doing so [63], however, leads to the same results as the simplified computation we outlined above. Note that, in the relativistic limit employed for the neutrinos, the energy of the mass eigenstate ν_k can be given in terms of the total energy of the initially produced neutrino E: $E_k \approx p_\nu + m_k^2/(2p_\nu) \approx E + m_k^2/(2E)$. So, the probability of neutrino oscillations is a function of the neutrino energy E, of the source-detector distance x (often referred to as L in the literature), of the parameters of the leptonic mixing matrix U, and of the neutrino mass squared differences $\Delta m_{kk'}^2$ (assuming relativistic neutrinos, i.e. $m_k \ll p_\nu \approx E$).
In principle, we can derive the probability of neutrino oscillations for any number of neutrinos N, cf. Eq. (2.0.6). The corresponding mixing matrix U, defined by Eq. (2.0.1), is a unitary $N \times N$ matrix which, in principle, depends

[6] The oscillation pattern is washed out over long distances due to the spread in momentum within the neutrino beam. This is related to the fact that the average over the oscillating terms becomes smaller the longer the neutrino beam travels as the interference decreases. For more information, see e.g. Ref. [61].

on N^2 independent real parameters. We can divide these parameters into

$$\frac{N(N-1)}{2} \quad \text{mixing angles and} \quad \frac{N(N+1)}{2} \quad \text{mixing phases.} \tag{2.0.8}$$

Note that, however, not all mixing phases are physically observable. Following the discussion in section 4.2 of Ref. [57], $(2N-1)$ mixing phases can be eliminated (in case of the neutrinos being Dirac fermions) by global phase transformations of the associated lepton fields, leaving us with

$$\frac{N(N-1)}{2} \quad \text{mixing angles and} \quad \frac{(N-2)(N-1)}{2} \quad \text{physical mixing phases.} \tag{2.0.9}$$

Expressing the probability of neutrino oscillations in terms of mixing angles and phases becomes increasingly cumbersome as the number of mixing neutrinos N increases. There are, however, a number of scenarios, where only two neutrinos significantly participate in the mixing.[7] The two-neutrino setting solely depends on one mixing angle θ and one mass squared difference Δm^2_{21} (or, interchangeably, one oscillation length L_{21}), with the mixing matrix of Eq. (2.0.1) given by:

$$U = \begin{pmatrix} \cos\theta & \sin\theta \\ -\sin\theta & \cos\theta \end{pmatrix}, \quad \text{such that} \quad \begin{pmatrix} \nu_\alpha \\ \nu_\beta \end{pmatrix} = U^* \begin{pmatrix} \nu_1 \\ \nu_2 \end{pmatrix} = U \begin{pmatrix} \nu_1 \\ \nu_2 \end{pmatrix}. \tag{2.0.10}$$

The probability that would be investigated in an appearance experiment is:

$$P(\alpha \to \beta, x) = \sin^2(2\theta) \sin^2\Big(\underbrace{\frac{x\Delta m^2_{21}}{4E}}_{\equiv \delta_{12}} \Big), \tag{2.0.11}$$

as deduced from Eq. (2.0.6). Consequently, the probability that would be investigated in a disappearance experiment takes the form:

$$P(\alpha \to \alpha, x) = 1 - \sin^2(2\theta) \sin^2(\delta_{12}). \tag{2.0.12}$$

The phase responsible for the oscillation with distance, δ_{12}, is useful to estimate the sensitivity of an experiment. Using SI units, we obtain [56]:

$$\delta_{12} = 1.27 \times \frac{\Delta m^2_{21}[\mathrm{eV}^2] \cdot x[\mathrm{km}]}{E[\mathrm{GeV}]}, \tag{2.0.13}$$

which implies that, in order to probe tiny neutrino masses, the ratio x/E has to be rather large. We thus generally aim at experiments with low-energy neutrinos travelling long distances to study neutrino oscillations. Note that, as neutrino detectors are usually far too large to be moved in order to measure

[7] For example, for the atmospheric mixing $\nu_\mu \leftrightarrow \nu_\tau$, ν_e barely plays a role such that this type of simplified description can be appropriate.

at varying distances, neutrino oscillations are probed by varying the neutrino energy. We will come back to the energy and length scales used in different types of neutrino oscillation experiments later in this chapter, cf. Tab. 2.1. For now, we simply bare in mind that the ratio x/E will be decisive for the detection of oscillation properties.
The number of light active neutrinos N, i.e. neutrinos that couple to the Z-boson via a Standard Model (SM) neutral current and have masses much smaller than $M_Z/2$, can be determined from the production cross-section of $e^+e^- \to$ hadrons by taking a closer look at the Z resonance. The Z resonance of the hadronic production cross-section is rather sensitive to N, and the current best fit matches $N = 3$, with any other integer value excluded [9]. This result agrees with other observations of three generations of leptons, and it implies that there are indeed no further SM-like lepton generations with a light neutrino.[8] In principle, however, the number of massive neutrinos could be larger due to, e.g., so-called sterile right-handed neutrinos, which have no ordinary interactions apart from mixing with the active flavour neutrinos [64]. Since the experimental hints for sterile neutrinos are currently inconclusive [65, 66] and we can accommodate all oscillation data by means of three light neutrinos, we will disregard that scenario hereafter. The leptonic mixing matrix U corresponding to $N = 3$ is also referred to as *PMNS matrix* (after Pontecorvo, Maki, Nakagawa, and Sakata), and it is the leptonic analogue of the Cabibbo-Kobayashi-Maskawa (CKM) matrix, which describes the corresponding mixing among the quarks. In section 3.1, we will discuss the PMNS matrix in detail. At this point, we only briefly list its most important properties. The PMNS matrix is parametrised by means of three mixing angles (θ_{12}, θ_{13}, and θ_{23}), one CP violating Dirac phase (δ), and (in case the neutrinos are Majorana particles) two CP violating Majorana phases (φ_1 and φ_2), cf. Eqs. (3.1.5) and (3.1.6). Although the numbering of the mass eigenstates is in principle arbitrary, we choose a convention for which the mixing angle θ_{12} (in combination with the mass squared difference Δm^2_{21}) drives the oscillation of "solar" neutrinos[9] ν_e into ν_μ and ν_τ, while the mixing angle θ_{23} (in combination with the mass squared difference $|\Delta m^2_{32}|$) drives the oscillation of "atmospheric" neutrinos[10] ν_μ. Then, the mixing angle θ_{13} corresponds to the smallest mixing angle measured in reactor experiments. The probability of neutrino oscillations, cf. Eq. (2.0.6), only depends on the mixing angles and on the Dirac phase, but *not* on the Majorana phases [67, 68], which means that we cannot extract any information on whether neutrinos are Dirac or Majorana from oscillation experiments. Furthermore, as can be seen from Eq. (2.0.6), neutrino oscillations

[8] For a more thorough discussion on the number of neutrino species, see section 5.1.3 of Ref. [57].

[9] The term goes back to first observing flavour conversions by means of the reduced flux of electron neutrinos, produced in the Sun.

[10] When cosmic rays hit the upper atmosphere muon neutrinos are produced. Flavour oscillations were confirmed by comparing the deficit of such atmospheric muon neutrinos reaching the experiment directly and after passing through the Earth.

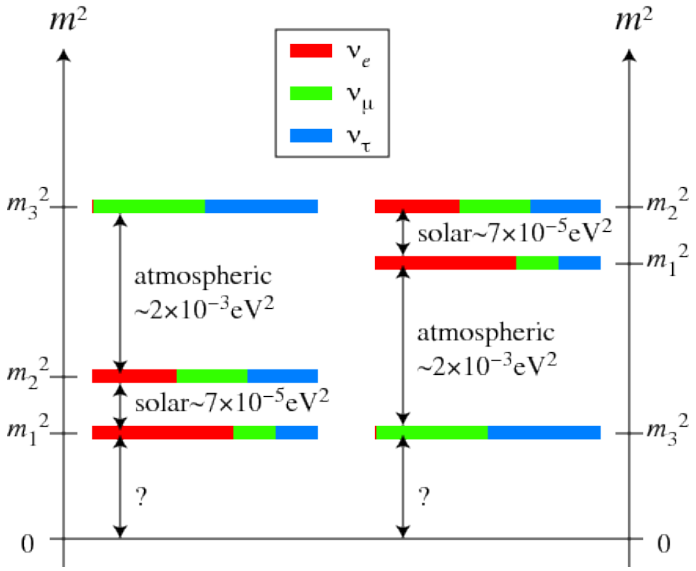

Figure 2.1: Illustration of the potential neutrino mass orderings: (*left*) normal ordering and (*right*) inverted ordering. The figure has been taken from Ref. [55]. Note that the colours represent the probability that a particular mass eigenstate contains a respective flavour eigenstate. The question marks refer to the yet unknown absolute value of the lightest neutrino mass.

are only sensitive to (and thus provide information on) the mass squared differences. They, consequently, do not allow for the determination of the absolute mass scale of neutrinos, see also Fig. 2.1.

After the idea of neutrino oscillations was introduced by Pontecorvo as early as 1957 [64, 69, 70] (and by Maki, Nakagawa, and Sakata in 1962 [71]), their existence was experimentally verified in 1998 by Super-Kamiokande [7] and in 2002 by the Sudbury Neutrino Observatory (SNO) [8]. Furthermore, in 2015, the Nobel prize was awarded for the said discoveries. Since the discovery of neutrino oscillations there have been various developments in the field of neutrino physics, and experiments with solar, atmospheric, reactor, or accelerator neutrinos have provided further compelling evidence for the existence of flavour oscillations.
Revisiting the discussion related to Eq. (2.0.13), the characteristics potentially probed by a given neutrino oscillation experiment depend, in particular, on the average energy of the neutrinos $\overline{E}$ and on the distance between source and detector L. The corresponding minimal value of the mass squared difference, which the experiment is sensitive to, results from $\min(\Delta m^2) \sim 2\overline{E}/L$ [9]. Note that, due to interference effects [72], neutrino oscillation experiments can in fact explore rather small values Δm^2_{ij}. In Tab. 2.1, taken from Ref. [9], we display the respective ballparks of minimal mass squared difference $\min(\Delta m^2)$ characterising the sensitivity of different oscillation experiments. In the follow-

Source	Type of ν	$\overline{E}$ [MeV]	L [km]	$\min(\Delta m^2)$ [eV^2]
Reactor	$\overline{\nu}_e$	~ 1	1	$\sim 10^{-3}$
Reactor	$\overline{\nu}_e$	~ 1	100	$\sim 10^{-5}$
Accelerator	ν_μ, $\overline{\nu}_\mu$	$\sim 10^3$	1	~ 1
Accelerator	ν_μ, $\overline{\nu}_\mu$	$\sim 10^3$	1000	$\sim 10^{-3}$
Atmospheric ν's	$\nu_{\mu,e}$, $\overline{\nu}_{\mu,e}$	$\sim 10^3$	10^4	$\sim 10^{-4}$
Sun	ν_e	~ 1	1.5×10^8	$\sim 10^{-11}$

Table 2.1: Sensitivity of different neutrino oscillation experiments, taken from Ref. [9]. Here, $\overline{E}$ denotes the average energy of the neutrinos, L refers to the source-detector distance, and $\min(\Delta m^2) \sim 2\overline{E}/L$ cites the minimal value for the mass squared difference to which the experiment is sensitive.

ing, we present a selection of neutrino oscillation experiments that correspond to the settings listed in Tab. 2.1:

- Reactor experiment(s) with $L \sim 1$ km: Chooz [10, 11], Daya Bay [12], RENO [13], or Double Chooz [14].
- Reactor experiment(s) with $L \sim 100$ km: KamLAND [15].
- Accelerator experiment(s) with $L \sim 1$ km: E776 [73].
- Accelerator experiment(s) with $L \sim 1000$ km: K2K [16], MINOS [17–20], OPERA [21, 22], T2K [23, 24], or NOνA [25, 26]. Note that the source-detector distance varies in the range of 300 km $\lesssim L \lesssim$ 1000 km between these experiments.
- Experiment(s) studying atmospheric neutrinos: Super-Kamiokande [7], or MINOS [20, 27].
- Experiment(s) studying solar neutrinos: SNO [8], Super-K [28], Borexino [74], or Gallex [75].

The existing data, collected over many years of studying neutrino oscillations experimentally, allow us to determine the neutrino mass squared differences and leptonic mixing angles with a relatively good accuracy, as well as to include first estimates on the CP violating Dirac phase [48, 49]. We have summarised the latest results in Tab. 2.2, with oscillation parameters taken from Ref. [49]. Another analysis of global neutrino oscillation data performed in Ref. [48] provides similar results.

Explaining the oscillation data requires at least three massive but light neutri-

Parameter	Best-fit value	1σ range	3σ range
$\sin^2\theta_{12}$	0.306	$0.294 \to 0.318$	$0.271 \to 0.345$
$\sin^2\theta_{13}$ (NO)	0.02166	$0.02091 \to 0.02241$	$0.01934 \to 0.02392$
$\sin^2\theta_{13}$ (IO)	0.02179	$0.02094 \to 0.02246$	$0.01953 \to 0.02408$
$\sin^2\theta_{23}$ (NO)	0.441	$0.420 \to 0.468$	$0.385 \to 0.635$
$\sin^2\theta_{23}$ (IO)	0.587	$0.563 \to 0.607$	$0.393 \to 0.640$
$\delta[^\circ]$ (NO)	261	$202 \to 312$	$0 - 360$
$\delta[^\circ]$ (IO)	277	$231 \to 317$	$145 - 391$
$\frac{\Delta m^2_{21}}{10^{-5}\mathrm{eV}^2}$	7.50	$7.33 \to 7.69$	$7.03 \to 8.09$
$\frac{\Delta m^2_{31}}{10^{-3}\mathrm{eV}^2}$ (NO)	2.524	$2.484 \to 2.563$	$2.407 \to 2.643$
$\frac{\Delta m^2_{32}}{10^{-3}\mathrm{eV}^2}$ (IO)	-2.514	$-2.555 \to -2.476$	$-2.635 \to -2.399$

Table 2.2: The best-fit values, 1σ and 3σ ranges for the three-flavour oscillation parameters from the fit to global data performed in Ref. [49]. Note that $\Delta m^2_{31} > 0$ for normal mass ordering (NO) and $\Delta m^2_{32} = -\Delta m^2_{23} < 0$ for inverted mass ordering (IO).

nos, which must have different masses. Note that, for the mixing of three neutrinos, there are only two independent mass squared differences Δm^2_{ij}. The sign of the smaller mass squared differences has been determined: $\Delta m^2_{21} > 0$ [28,76]. However, since neutrino oscillation experiments have so far not been sensitive enough to determine the sign of $\Delta m^2_{32(31)}$, we currently cannot distinguish between the following two patterns of mass orderings illustrated in Fig. 2.1:

1. *normal ordering* (NO), presented on the left-hand side of Fig. 2.1, corresponds to $\Delta m^2_{31(32)} > 0$ or, equivalently, $m_1 < m_2 < m_3$.

2. *inverted ordering* (IO), presented on the right-hand side of Fig. 2.1, corresponds to $\Delta m^2_{32(31)} < 0$ or, equivalently, $m_3 < m_1 < m_2$.

Note that, in Fig. 2.1, the colours represent the probability that a particular mass eigenstate contains a respective flavour eigenstate. In addition, Fig. 2.1 indicates by means of question marks that the lightest neutrino mass is currently unknown. So, in summary, the main questions with respect to neutrino masses are [54]:

- What is the mass ordering?
- What is the absolute mass scale of neutrino masses? We can rephrase this question to: what is the value of the lightest neutrino mass?
- What is the nature of neutrino masses: Majorana or Dirac?

There are basically four ways to approach these questions [50, 53]:

1. Obtain more accurate information on the mass squared differences in order to resolve the mass ordering. This is one of the main goals of future neutrino oscillations experiments [52, 77–85].

2. Derive constraints on the sum of neutrino masses (and hence the lightest neutrino mass) by means of cosmology and astrophysics [86]. The upper limits derived are in the range of [87] $\Sigma \equiv \sum_k m_k \lesssim (0.3 - 1.3)$ eV at 95 %C.L., depending on the complexity of the underlying cosmological model and data set used. From the exemplary value of $\Sigma = 0.3$ eV, the absolute neutrino mass scale can be estimated to be $m_k \sim \Sigma/3 \lesssim 0.1$ eV [88]. These upper limits on the absolute mass scale can be lowered by adding further assumptions, such as the validity of the ΛCDM model, or data from, e.g. Baryon Acoustic Oscillations (BAO). However, this enhances the model dependence of the limit. By including further assumptions and data sets, the most stringent limit has been derived in Ref. [89]: $\sum_k m_k \lesssim 0.170$ eV at 95 %C.L.

3. Probe the Majorana nature of neutrinos by searching for lepton number violating (LNV) processes like neutrinoless double beta decay ($0\nu\beta\beta$). Apart from investigating the nature of neutrinos, $0\nu\beta\beta$ could also measure the following element of the Majorana neutrino mass matrix:

$$|(m_\nu)_{ee}| = \left| \sum_k U_{ek}^{*2}\, m_k \right| , \tag{2.0.14}$$

   which, in combination with oscillation data, might provide information on the absolute mass scale of the neutrinos [90]. Note that, however, this is based on the assumption that only the Majorana mass term violates lepton number. Based on this assumption and assuming a suitable nuclear matrix element, the current limit on $0\nu\beta\beta$ leads to $|(m_\nu)_{ee}| \lesssim 10^{-1}$ eV [91], which can be translated into an estimate on the upper limit of neutrino masses: $m_k \lesssim 0.2$ eV [88]. For more details on the information obtained from LNV processes, see section 3.2 and references therein.

4. Information on the absolute mass scale might be obtained from by measuring the electron spectrum of single β-decays near the endpoint [52, 92–95]. Such β-decay experiments measure the quantity:

$$m_{\nu_e}^2 = \sum_k |U_{ek}^*|^2 |m_k|^2 . \tag{2.0.15}$$

The Troitsk experiment currently provides the most stringent limit with $m_{\nu_e} < 2.05$ eV at 95 %C.L. [95] based on ^3H (tritium) β-decays. This limit can be used to derive an estimate on the upper bound on the neutrino masses: $m_k \lesssim m_{\nu_e} \sim 2$ eV [88]. The experiment KATRIN plans to reach sensitivities of $m_{\nu_e} \sim 0.20$ eV also based on tritium β-decays [96].

For more information on the measurements of the absolute neutrino mass scale, see e.g. Ref. [88, 97–99].

In addition, there are several unknowns with respect to the mixing parameters [54]:

- Is the atmospheric angle θ_{23} in the first or second octant?
- Is there CP violation in the leptonic sector? If so, how large is it?
- What are the values of the CP violating Majorana phases, in case they exist?

So far, the octant of the atmospheric angle has not been determined yet, and its precise value is uncertain, cf. Tab. 2.2. While T2K prefers a close-to-maximal atmospheric mixing angle [24], NOνA excludes maximal mixing at 2.6σ [26]. The forthcoming results from T2K and NOνA will hopefully clarify the situation. The CP properties of the leptonic sector are of great interest, as the Dirac and/or Majorana phases might provide the CP violation necessary to generate the baryon asymmetry of the Universe (BAU) [100–102]. In both analyses [48, 49], the best-fit value for the Dirac phase is close to $\delta \sim 3\pi/2$, cf. Tab. 2.2. Due to the large uncertainty, however, and with no other experimental information on either Dirac or Majorana phases available, we practically do not know whether or not the CP symmetry is conserved or violated within the leptonic sector. Due to $\theta_{13} \neq 0$, the Dirac phase can induce CP violation into the neutrino oscillations [67, 103, 104]. As a consequence, we would observe their effects in the probability of neutrino oscillation, $P(\nu_\ell \to \nu_{\ell'}, x) \neq P(\overline{\nu_\ell} \to \overline{\nu_{\ell'}}, x)$, and the magnitude of the CP violation could be determined by means of a so-called rephasing invariant J_{CP} [105]. Nevertheless, the Majorana phases do not appear in the neutrino oscillations. To obtain information on the Majorana phases, we would have to turn to LNV processes like $0\nu\beta\beta$ [106–108], albeit such processes have not been measured yet. The determination of both θ_{23} and δ, however, can be addressed by neutrino oscillation experiments and is, therefore, a priority in future endeavours [82, 83, 85, 109–112].

To subsume, the origin of neutrino mass and leptonic mixing is an outstanding open question, as is the existence of massive neutrinos. The latter follows from the discovery of neutrino oscillations but cannot be accommodated within

the SM of particle physics. The data obtained in neutrino oscillation experiments may provide key information on nature of the New Physics beyond the SM. Neutrino physics might even open up the possibility to study more fundamental questions with respect to the origins of flavour, i.e. what is the source of the patterns we observe in both quark and lepton masses and mixing. These open questions may also imply that the SM is merely an effective low-energy theory of some yet unknown complete high-energy theory. Explaining both the smallness of neutrino masses relative to the charged lepton masses and the large leptonic mixing compared to the mixing in the quark sector sets the main goal for model building in the neutrino sector, different approaches to which will be reviewed in section 3.1. Note that many New Physics settings are defined at high energy scales, whereas experimental oscillation data are measured at low energies. Since the parameters of a theory change with the energy scale under consideration (as will be discussed in section 4.1), it is important to consistently derive the settings' low-energy predictions to compare to experimental oscillation data. As already touched upon above, neutrino oscillations are by far not the only avenue towards unravelling the nature of neutrino physics or, even more general, of physics beyond the SM. Since neutrino oscillations have established lepton flavour violation (LFV), New Physics models have a tendency to introduce additional LFV (and sometimes even LNV) physics, providing a rich phenomenology of both charged LFV and LNV processes.[11] To fully exploit the complementarity and constrain the free input parameters of a respective New Physics model, we need to combine the bounds from neutrino oscillation experiments with those derived from the model being sensitive to experimental probes from both indirect and direct searches at different energy scales. For these purposes, the theoretical treatment of relevant (LFV and LNV) processes and the accurate derivation of predictions for the measurable quantities are crucial. These points are, in fact, the motivation for the research projects presented in chapters 5 and 6, on which this thesis is based.

[11] Both LFV and LNV as well as some of their phenomenological consequences will be discussed in sections 3.2 and 3.3.

Chapter 3

Neutrino Mass Models

This chapter is devoted to the origin of neutrino mass and leptonic mixing. Therefore, section 3.1 is dedicated to reviewing basic concepts of neutrino model building, recapitulating the low-energy limit of neutrino mass models, and introducing the notation used throughout this thesis. Note that section 3.1 is by no means exhaustive. Although we introduce a number of important concepts and ideas in 3.1, we do so focussing our attention on those that are relevant throughout this thesis. In section 3.2, we move on to the phenomenological consequences of neutrino masses and review the concepts of lepton flavour and lepton number violation. After having laid the conceptional groundwork, we turn to the models employed in chapters 5 and 6. We review the effective field theory of a doubly charged scalar singlet in section 3.3, and subsequently recapitulate the Littlest Seesaw in section 3.4.

3.1 Brief Overview on Neutrino Mass Models

According to the Standard Model (SM), neutrinos are exactly massless. This feature can be traced back to the absence of a valid mass generation mechanism under the full SM gauge group. Since the SM does neither contain right-handed (RH) neutrinos nor does its Higgs sector contain anything but $\mathrm{SU}(2)_\mathrm{L}$ doublets (and thus, no triplets), one can generate neither a Dirac nor a Majorana mass after electroweak symmetry breaking (EWSB). The SM, furthermore, is a renormalisable theory, i.e. operators are of dim $= 4$ at most, such that operators like the dim $= 5$ Weinberg operator $\mathcal{L}_{\mathrm{dim}=5} = -c_{ab}/\Lambda\,[\overline{(\ell_{a\mathrm{L}})^c}\tilde{H}^*][\tilde{H}^\dagger \ell_{b\mathrm{L}}]$ [113] are not allowed. Here, $\ell_{a\mathrm{L}} = (\nu_{a\mathrm{L}},\, e_{a\mathrm{L}})$ denotes the left-handed (LH) lepton doublet with lepton flavour $a, b = e,\, \mu,\, \tau$. The SM Higgs $\mathrm{SU}(2)_\mathrm{L}$-doublet is labeled by $H = (H^+,\, H^0)$, $\tilde{H} = i\sigma_2 H^*$, and c_{ab} is a UV-model-dependent coefficient suppressed by the scale of New Physics Λ.[1] Due to the discovery of neutrino oscillations, whose existence implies non-zero neutrino masses, it proves necessary to extend the SM to explain the origin

[1] The term ultraviolet (UV) refers to high energies.

of the neutrino masses required, see chapter 2. This may hint towards the SM only being an effective low-energy theory of some yet unknown theory (prevalent at high energies). And, furthermore, it suggests that neutrinos and their mixing behaviour may provide key information on the nature of the New Physics beyond the SM. Explaining both the smallness of neutrino masses relative to the charged lepton masses and the large leptonic mixing compared to the mixing in the quark sector sets the goal for model building in the neutrino sector. In the literature, there are numerous models, mechanisms, and ideas on how to generate neutrino masses and leptonic mixing; some focusing more on naturally implementing the smallness of the neutrino masses and others on predicting the leptonic mixing pattern. However, note that none of the proposed models have been experimentally substantiated so far.

Approaches focusing an the prediction of the leptonic mixing pattern, referred to as *flavour models*, are based on extending the SM by qualitatively new symmetries. These so-called horizontal symmetries connect the different families. There is a vast number of models employing flavour symmetries, which can be either continuous or discrete, Abelian or non-Abelian. A detailed review on discrete flavour symmetries can be found in Ref. [53]. Papers reviewing discrete non-Abelian symmetries and their application to the generation of neutrino mass and mixing are Refs. [54, 55, 114–116]. Another review that discusses the continuous Abelian U(1) in addition to discrete non-Abelian symmetries is Ref. [117]. While flavour models are designed to predict specific values for the mixing of neutrinos, they often do so by introducing virtually unobservable high-energy physics, which makes testing such models challenging. One popular approach in flavour theory is introducing a so-called family symmetry G_f which acts on the three lepton families in combination with enlarging the scalar sector by Higgs-type fields called flavons, see e.g. Refs. [53, 117]. To deviate from the otherwise trivial structure and generate the observed leptonic mixing pattern, G_f has to be broken. To that end, the scalar sector was extended by the flavons which are neutral under the full SM gauge group. Due to the flavons acquiring a non-vanishing vacuum expectation values (vev), the family symmetry breaks spontaneously. From designated flavon alignments, also called vacuum alignments, the mixing pattern can be predicted. We make use of the theory of flavour symmetries in section 3.4, where we introduce a neutrino mass/flavour model called the Littlest Seesaw (LS) and show how its mixing pattern can be justified by non-Abelian discrete family symmetries.

The other type of theories, referred to as *mass models*, focuses on naturally suppressing neutrino masses. The mass models usually do not predict an absolute scale for neutrino masses but rather a hierarchy among neutrino and charged-lepton masses. There are many different mass models and several mechanisms naturally explaining the smallness of neutrino masses. The reviews in Refs. [51, 118, 119] explore the most popular approaches. Since we will employ mass models in sections 3.3 and 3.4, we discuss a number of basic ideas and strategies in the following. In general, in order to introduce neutrino

masses to the SM in a renormalisable manner, we need to lift the constraints on its particle content.
An obvious way to do so is by extending the SM by RH gauge singlet neutrinos and employ the Higgs mechanism. That way we induce Dirac neutrino masses via EWSB, in analogy to charged-lepton masses. To account for the mass hierarchy, however, the Yukawa couplings to neutrinos have to be tiny,[2] which solely shifts the problem of "why are the neutrino masses so small in comparison to the charged lepton masses?" to "why are the neutrino Yukawa couplings so small in comparison to the charged lepton couplings?", instead of actually explaining it. By introducing RH fermionic *gauge singlets*, we also opened way to Majorana mass terms for said singlets that are not related to the Higgs vev and only restricted by the Planck scale. In order to generate *Dirac* neutrinos, however, this RH Majorana mass term has to vanish. But there is no a priori explanation on why.[3]
Alternative to producing Dirac neutrinos masses via the RH gauge singlets, we can extend the SM by a scalar $\mathrm{SU(2)_L}$ Higgs triplet which couples to two LH lepton doublets, see e.g. Ref. [120], and generate Majorana masses instead. Under these conditions, a Majorana mass term m_L is induced at tree level due to the neutral component of the triplet acquiring a vev v_T. To generate small neutrino masses, either the coupling of the lepton doublets to the Higgs triplet and/or the vev v_T has to be very small. The latter need to be motivated.
Although, we can explain the origin of neutrino masses by either of the two simple extensions above, their smallness remains elusive. We therefore need to elaborate on the mechanisms to include a natural solution to the suppression problem. One possibility is to make use of scale suppressions to naturally implement the mass hierarchy among charged leptons and neutrinos. One way to do exactly that is to take the extension of the SM by RH gauge singlets and require their Majorana masses to be larger than the electroweak scale. That way, the light neutrinos become Majorana and their mass term is approximately given by $-m_D M_\mathrm{R}^{-1} m_D^T$. With $m_D \sim v/\sqrt{2} = \mathcal{O}(100\ \mathrm{GeV})$ and $M_\mathrm{R} \sim \mathcal{O}(10^{14}\ \mathrm{GeV})$, the light neutrino masses are of $\mathcal{O}(0.1\ \mathrm{eV})$ [118]. We discuss this famous mechanism, called Seesaw type I [32–36], in more detail in section 3.4. Another type of Seesaw mechanism, Seesaw type II [121–124], is based on the extension by Higgs triplets, as discussed above. The scale suppression traces back to the triplet vev being connected to the doublet vev due to the Higgs fields' interactions in the potential. As a consequence, one obtains the relation $v_T \sim v^2/M_T$,[4] which for a large triplet mass parameter $M_T \gg v$ accounts for the suppression. The latter is phenomenologically mo-

[2] A neutrino Yukawa coupling of $Y_\nu^{ab} \lesssim 10^{-12}$ is needed for neutrino masses of $\mathcal{O}(0.1\ \mathrm{eV})$ [53] in stark contrast that of the electron of $\mathcal{O}(10^{-6})$, which implies $m_e = 511\ \mathrm{keV}$.

[3] One might argue that vanishing Majorana mass terms increase the symmetry of the Lagrangian, and are therefore favourable. However, this additional symmetry, associated with lepton number conservation, is only realised at the perturbative level for the SM.

[4] Note that this relation is derived based on assumptions. For more information, see e.g. Refs. [125–127].

tivated: since the Higgs triplet also contains electrically charged components and we have not observed them at collider experiments so far, they must be heavier.
Another approach on naturally suppressing neutrino masses is having them arise only at loop level. Such *radiative mass models* forbid tree-level neutrino masses and introduce additional Higgs singlets and doublets at higher energy scales, see e.g. [47, 128–146]. Some well-known examples for producing loop-suppressed neutrino masses are the Scotogenic model [147] (at one-loop), the Zee-Babu model [131, 148, 149] (at two-loop), or the Cocktail model [150, 151] (at three-loop). The effective theory of a doubly charged scalar, which we will introduce in section 3.3, also belongs to that category.
Note that there are many more mass models that work based on scale and/or loop suppressions. Without being exhaustive, we want to name a few more proposals on the origin of small neutrino masses. There are for example Seesaw type III [152, 153], inverse Seesaw [154], R-parity violating supersymmetry [155–180], or models based on extra dimensions [181–187] and string theory [154, 188–200]. More details on these proposals can be found in Ref. [51].
At first glance, it seems like we would only have relocated the problem of naturally suppressing neutrino masses to another yet undetected sector by introducing additional particles and thereby new parameters like their masses and couplings. These mass models, however, should always lead to (preferably testable) predictions which have to be consistent with current data and are, ideally, testable further by near-future experiments. Comparing a certain model's prediction with experimental measurements allows for either excluding the model or continuing to investigate it as a viable candidate. Models providing a rich phenomenology are particularly attractive because they can be tested in many processes and ideally at different energy scales. This is especially true for radiative loop models, as discussed in section 3.3.

Even though the origin of neutrino mass remains unknown, any mass model leads to an effective theory with either Dirac or Majorana neutrinos in the low-energy limit. Assuming neutrinos to be purely Dirac, the effective low-energy Lagrangian for lepton masses below the electroweak scale is given by

$$-\mathcal{L}_m = \overline{\nu_{a\mathrm{L}}} m_\nu^{ab} \nu_{b\mathrm{R}} + \overline{e_{a\mathrm{L}}} m_\ell^{ad} E_{d\mathrm{R}} + \mathrm{h.c.}\,, \tag{3.1.1}$$

where the basis is still arbitrary. Here, $e_{a\mathrm{L}}$ denote the 3 LH charged leptons, and $E_{a\mathrm{R}}$ the 3 RH ones. Consequently, the charged-lepton mass matrix is (3×3). As we want to generate three non-vanishing light neutrino masses, there are 3 RH and 3 LH neutrinos $\nu_{a\mathrm{R,L}}$, respectively, which makes m_ν a (3×3) matrix. Note that, in the literature as well as throughout this thesis, the notation for RH neutrinos is (often) changed in case they are heavy, $\nu_\mathrm{R} \to N_\mathrm{R}$.
In case the mass model provides Majorana neutrinos, its effective low-energy Lagrangian is given by

$$-\mathcal{L}_m = \frac{1}{2}\overline{\nu_{a\mathrm{L}}} m_\nu^{ab} (\nu_{b\mathrm{L}})^c + \overline{e_{a\mathrm{L}}} m_\ell^{ab} E_{b\mathrm{R}} + \mathrm{h.c.}\,, \tag{3.1.2}$$

where $(\nu_{\mathrm{L}})^c = \mathcal{C}\overline{\nu_{\mathrm{L}}}^T = (\nu^c)_{\mathrm{R}}$ is the charge conjugated neutrino, and the remaining quantities are equivalent to the Dirac case.
Starting from an arbitrary basis, we want to switch to the mass eigenbasis, which means that we diagonalise both mass matrices m_ν and m_ℓ.[5] While m_ℓ can be diagonalised by means of a bi-unitary transformation, the neutrino mass matrix is diagonalised by a transformation using the unitary matrix $U_{\nu\mathrm{L}}$. Hence, it is

$$U_{e_{\mathrm{L}}} m_\ell U_{E_{\mathrm{R}}}^\dagger = \mathrm{diag}(m_e,\, m_\mu,\, m_\tau) \quad \text{and} \quad U_{\nu_{\mathrm{L}}} m_\nu U_{\nu_{\mathrm{L}}}^T = \mathrm{diag}(m_1,\, m_2,\, m_3)\,, \tag{3.1.3}$$

where the masses $m_{e,\,\mu,\,\tau}$ and $m_{1,\,2,\,3}$ are real and positive (≥ 0). The (unitary) PMNS matrix is given by the mismatch between the two mass eigenbases,

$$U_{\mathrm{PMNS}} = U_{e_{\mathrm{L}}} U_{\nu_{\mathrm{L}}}^\dagger\,. \tag{3.1.4}$$

In the basis where the charged-lepton mass matrix is diagonal, the unitary PMNS matrix takes the form [201]:

$$U_{\mathrm{PMNS}} = \mathrm{diag}(\mathrm{e}^{i\delta_e},\, \mathrm{e}^{i\delta_\mu},\, \mathrm{e}^{i\delta_\tau})\, V\, \mathrm{diag}(\mathrm{e}^{-i\varphi_1/2},\, \mathrm{e}^{-i\varphi_2},\, 1)\,, \tag{3.1.5}$$

with

$$V = \begin{pmatrix} c_{12}c_{13} & s_{12}c_{13} & s_{13}\mathrm{e}^{-i\delta} \\ -s_{12}c_{23} - c_{12}s_{13}s_{23}\mathrm{e}^{i\delta} & c_{12}c_{23} - s_{12}s_{13}s_{23}\mathrm{e}^{i\delta} & c_{13}s_{23} \\ s_{12}s_{23} - c_{12}s_{13}c_{23}\mathrm{e}^{i\delta} & -c_{12}s_{23} - s_{12}s_{13}c_{23}\mathrm{e}^{i\delta} & c_{13}c_{23} \end{pmatrix}\,. \tag{3.1.6}$$

Here, c_{ij} and s_{ij} denote $\cos\theta_{ij}$ and $\sin\theta_{ij}$ for the mixing angle θ_{ij}, respectively, with $0 \leq \theta_{ij} \leq \pi/2$ [9]. The Dirac phase is labeled δ and the Majorana phases are given by $\varphi_{1,2}$. For a model providing Dirac neutrinos, the Majorana phases are trivial, i.e. $\varphi_{1,2} = 0, \pi$. The phases of the charged-lepton mass eigenstates, $\delta_{e,\mu,\tau}$, are unphysical and can therefore be arranged in an arbitrary manner. As a consequence, they are often removed by phase rotations on the RH charged lepton fields (leaving m_ℓ unchanged). In the standard parametrisation, all phases are within the range $[0, 2\pi[$.
Another useful basis is the so-called flavour basis. In the flavour basis, the charged-lepton matrix is diagonal (with real, positive entries), and the weak charged current interactions are given by

$$\mathcal{L}_{\mathrm{int}} = -\frac{g}{2}\overline{e_{a\mathrm{L}}}\gamma^\rho W_\rho^- \nu_{a\mathrm{L}} + \mathrm{h.c.}\,, \tag{3.1.7}$$

with the flavour indices $a = e,\, \mu,\, \tau$. In other words, flavour and mass eigenbasis are identical for charged leptons, and the neutrino flavour eigenstates are defined according to the physical charged lepton with which they interact

[5] For the following discussion, m_ν can either be a Dirac or a Majorana mass matrix.

in Eq. (3.1.7). Thus, it is the PMNS matrix that relates the (physical) mass eigenstates ν_i with the flavour eigenstates ν_a,

$$\begin{pmatrix} \nu_e \\ \nu_\mu \\ \nu_\tau \end{pmatrix} = U^*_{\text{PMNS}} \begin{pmatrix} \nu_1 \\ \nu_2 \\ \nu_3 \end{pmatrix} . \tag{3.1.8}$$

Upon rotating the charged current interactions from the flavour basis into the basis where all leptons are in their physical mass eigenstate, we obtain

$$\mathcal{L}_{\text{int}} = -\frac{g}{\sqrt{2}} (U^*_{\text{PMNS}})^{aj} \overline{e_{a\text{L}}} \gamma^\rho W^-_\rho \nu_{j\text{L}} + \text{h.c.} , \tag{3.1.9}$$

where the indices $a = e, \mu, \tau$ denote the lepton flavour and $j = 1, 2, 3$ refer to the neutrino mass eigenstates. We will discuss the phenomenological consequences of the mismatch of mass eigenbases in the following section.

3.2 Lepton Flavour and Lepton Number Violation

In the absence of Beyond-the-Standard-Model (BSM) particles which generate non-zero neutrino masses, the SM Lagrangian is invariant under the global $U_e(1) \times U_\mu(1) \times U_\tau(1)$ transformations

$$\ell_{a\text{L}} \to \mathrm{e}^{i\varphi_a} \ell_{a\text{L}} \quad \text{and} \quad E_{a\text{R}} \to \mathrm{e}^{i\varphi_a} E_{a\text{R}} \quad \forall a = e, \mu, \tau , \tag{3.2.1}$$

with generally different phases for each flavour. Due to Noether's theorem, these *accidental symmetries* imply the conservation of lepton flavours L_e, L_μ, and L_τ in the SM [202]. We refer to lepton flavour conservations as accidental symmetries, since they are not integral to the SM and virtually any model introducing neutrino masses automatically violates lepton flavour. To understand how neutrino masses induce lepton flavour violation (LFV) recall that, due to the non-vanishing neutrino masses and the non-zero leptonic mixing angles, there is no shared mass eigenbasis for neutrinos and charged leptons. We choose the flavour basis, i.e. m_ℓ is diagonal, whereas m_ν is not. While both weak interactions and the charged-lepton mass term remain invariant under the transformations in Eq. (3.2.1), it is not generally possible to find a transformation under which the Dirac neutrino mass term in Eq. (3.1.1) and the kinetic neutrino term in the Lagrangian are simultaneously invariant. In case the neutrinos are Majorana, the transformation of $(\nu_{\text{L}})^c$ is already defined by Eq. (3.2.1), and the neutrino mass term in Eq. (3.1.2) itself violates lepton flavour. The non-conservation of lepton flavour also leads to neutrino oscillations,[6] which have been observed in a variety of experiments [7, 8, 12–14, 17, 203, 204].

[6] Note that, in order to observe neutrino oscillations, some of the neutrino masses have to be non-zero and distinct. Furthermore, the leptonic mixing needs to be non-trivial, i.e., U_{PMNS} is not diagonal. For more information, see chapter 2.

By switching between the mass eigenbases of m_ℓ and m_ν, we introduce the LFV mixing to the weak charged current interactions, see Eq. (3.1.9). We therefore expect to also observe LFV in the charged lepton sector. Inherently, these charged lepton flavour violating (cLFV) processes – allowed by all fundamental conservation laws such as energy or charge conservation – should make for a rich phenomenology. That includes charged-lepton decays such as $e_a \to e_b\gamma$ or $e_a \to e_b e_c \overline{e_d}$, meson decays of the form $X \to e_a \overline{e_b}$, or conversion processes like $e_a + N \to e_b + N$. Here, $a, b, c, d = e, \mu, \tau$ denote the lepton flavour, while X, N are states without lepton flavour. The experimental hunt for cLFV is of high priority, and a considerable experimental effort is made towards detecting such processes. As a result, the experimental limits on many cLFV processes are rather strong. Although incomplete, the collection of limits on LFV charged-lepton decays displayed in Tab. 3.1 of section 3.3 provides an insight. Currently, the most stringent bound on cLFV is $\mathrm{BR}(\mu \to e\gamma) < 5.7 \times 10^{-13}$ [205]. Among the rare kaon decays, the maybe most sensitive channel for the moment is $\mathrm{BR}(K_\mathrm{L} \to \mu^\pm e^\mp) < 4.7 \times 10^{-12}$ [206]. In the near future, the conversion of bound muons on atomic nuclei to electrons (μ^-– e^- conversion) is expected to undergo the most dramatic improvement in experimental sensitivity up to $\mathrm{BR} \sim 10^{-17}$ [207, 208], thereby becoming the most sensitive cLFV probe available. As this process will be crucial to probing cLFV, we investigate its experimental aspects and present a detailed computation of the conversion mediated by a doubly charged SU(2) singlet scalar in sections 5.1 and 5.2, respectively. For more information, there are a number of comprehensive reviews on different aspects of cLFV, among others Refs. [207, 209–215].

Although there is no fundamental reason why such cLFV processes should not take place, LFV has up to now not been observed in the charged-lepton sector. To anticipate where to expect cLFV, estimating the rates for the various cLFV processes might be useful. Unfortunately, we cannot reliably estimate these rates in a general manner. While in the neutrino sector, the LFV neutrino oscillations solely depend on the masses and mixing of the neutrinos (which we can extract from the measurements without addressing the mechanism behind), the rates for cLFV processes are highly model-dependent. In other words, the contributions to a cLFV process can vary widely with the mechanism inducing neutrino masses, and therefore need to be computed for each BSM model separately. Consequently, cLFV processes provide a nontrivial insight into the nature of physics beyond the SM.
Nonetheless, we can asses the so-called *standard contribution* to a given cLFV process, which is the contribution contingent on the light neutrinos. As a consequence, these contributions are independent of the origin of the neutrino mass and can be computed based on the measured neutrino parameters alone. To construct a cLFV process from the SM augmented by massive neutrinos, we employ the weak charged current interactions in Eq. (3.1.9), and obtain cLFV processes at one-loop. As an example, we consider cLFV decays such

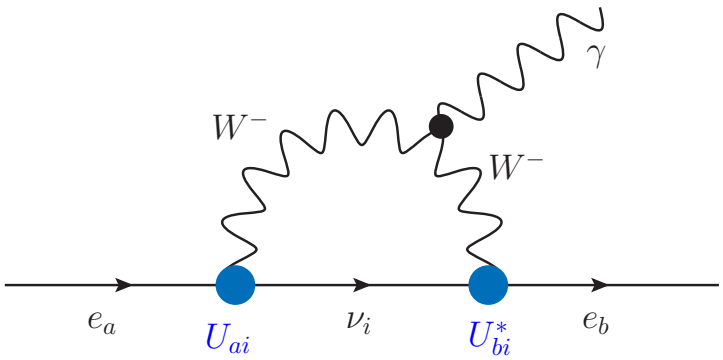

Figure 3.1: Standard contribution to cLFV decays with $a = \mu, \tau$ and $b = e, \mu$, while $a \neq b$.

as $e_a \to e_b + \gamma$, where $a = \mu, \tau$ and $b = e, \mu$ while $a \neq b$. The standard contribution to these decays is displayed in Fig. 3.1. The leading contribution to the respective BR is of the form [216–220]:

$$\mathrm{BR}(e_a \to e_b \gamma) \propto \alpha \left| \sum_{i=1,2,3} U_{ai} U^*_{bi} \frac{m_i^2}{M_W^2} \right|^2 , \tag{3.2.2}$$

which indicates that the standard contribution is strongly suppressed by the factor $(m_i^2/M_W^2)^4$ (with M_W being the W-boson mass). This is the result of the famous Glashow-Iliopoulos-Maiani (GIM) mechanism [44], which is applicable for flavour changing currents in loop diagrams and relies on the mixing matrix U_{PMNS} to be unitary.[7] We can now plug in the measured leptonic mixing parameters and assume a rather optimistic scenario with neutrino masses of $\mathcal{O}(1\ \mathrm{eV})$. Nevertheless, the resulting BR for the rare muon decay is inaccessibly small, $\mathrm{BR}(\mu \to e\gamma) \sim 10^{-47}$ [211, 223]. Since all standard contributions to cLFV processes are subject to the GIM mechanism, their rates are suppressed to similar unmeasurable sizes [209, 212], making detection virtually impossible. Due to their unmeasurably small rates, the standard contribution to cLFV processes avoids detection for good. However, in many neutrino-mass-generating BSM models, there are further sources of LFV [222], see for example the effective model in section 3.3. These additional LFV reactions are referred to as *non-standard contributions*. Hence, any experimental observation of cLFV would unambiguously be a signal for New Physics beyond the SM, and even beyond massive neutrinos. That is what makes the search for cLFV processes a high-priority and a complementary alternative to collider searches for New

[7] Note that this suppression relies on lepton universality. Lepton universality is a key assumption of the SM, implying that leptonic families have identical couplings to the gauge bosons, see e.g. Ref. [221]. In case lepton universality proves to be wrong or if additional non-universal gauge interactions are introduced [222], the mixing matrix will not be unitary anymore, thereby lifting the GIM suppression.

Physics.

By adding Dirac or Majorana neutrino masses to the SM, lepton flavour is generally violated. However, in case the neutrinos are Dirac, the following global U(1) transformation still leaves the Lagrangian invariant:

$$\ell_{a\mathrm{L}} \to \mathrm{e}^{i\varphi}\,\ell_{a\mathrm{L}}\,, \quad E_{a\mathrm{R}} \to \mathrm{e}^{i\varphi}\,E_{a\mathrm{R}}\,, \quad \text{and} \quad \nu_{i\mathrm{R}} \to \mathrm{e}^{i\varphi}\,\nu_{i\mathrm{R}}\,, \tag{3.2.3}$$

with the same phase φ for all leptons. Note that, for phase transformations with a mutual phase for all flavour eigenstates, the transformation property imposed on the RH neutrino "flavour" state $\nu_{a\mathrm{R}} \to \mathrm{e}^{i\varphi}\,\nu_{a\mathrm{R}}$ carries over to its mass eigenstate without further modification. As a consequence, both the Dirac mass term in Eq. (3.1.1) and the kinetic neutrino Lagrangian can simultaneously remain invariant under the transformation. This accidental symmetry is associated with the conservation of lepton number.
While the SM without massive neutrinos or the extension by Dirac neutrinos both seem to conserve lepton number at first view, they only do so in perturbative, low-energy processes. Already within the SM, there are non-perturbative processes that violate lepton number [224, 225], though they do not appear at low-energies. Therefore, it does not come as a surprise that, introducing Majorana neutrinos to the SM, the Lagrangian is no longer invariant under the global U(1) transformation from Eq. (3.2.3): since both $\nu_{a\mathrm{L}}$ and $(\nu_{a\mathrm{L}})^c$ acquire the same phase factor, the mass term in Eq. (3.1.2) violates lepton number by two units. To put it another way, lepton number counts the number of particles and antiparticles. While neutrino and antineutrino are different particles for Dirac type neutrinos, they are the same object for Majorana neutrinos. Hence, there is a fundamental relation between the nature of massive neutrinos, and lepton number violation (LNV). Furthermore, note that neutrino oscillations solely imply the existence of LFV and neutrino masses, but they are not necessarily tied to LNV. As a consequence, the experimental search for LNV processes is of great importance to understand the features of physics beyond the SM.
Even though there are various processes for probing LNV currently under experimental investigation, the nature of neutrinos has not been revealed thus far. The most sensitive test for LNV is probably neutrinoless double beta decay ($0\nu\beta\beta$), which has been studied extensively in the literature, e.g. in Refs. [106, 226–229], and in different experiments, see e.g. Refs. [230–232]. At the moment, the limit on its half-life time, $T_{1/2}^{0\nu\beta\beta} > 5.3 \times 10^{25}$yrs, has been set by GERDA's Phase II [91]. What makes $0\nu\beta\beta$ much more promising than many other LNV processes is a combination of the discriminability of background from mono-energetic signal and the statistical advantage due to the large number of atoms contained in the solid state source. Like $0\nu\beta\beta$, many LNV processes are in fact nuclear physics processes. Understanding how to treat the nuclear structure is therefore essential in order to obtain information on the BSM particle physics involved. Another LNV

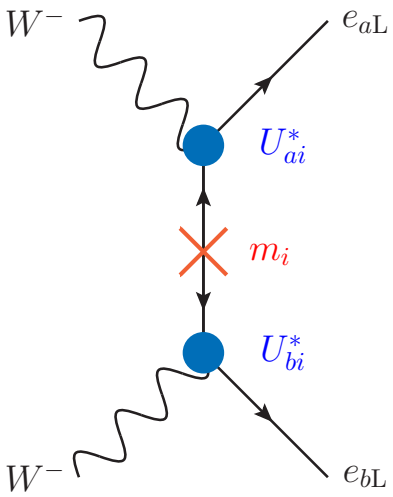

$$\longleftrightarrow \qquad (m_\nu)_{ab} = \sum_{i=1,2,3} U^*_{ai} U^*_{bi} m_i$$

Figure 3.2: Basic module to generate the standard contribution to LNV processes.

process involving nuclear probes is $\mu^- - e^+$ conversion with current limits of $\mathrm{BR}(\mu^- + \mathrm{Ti} \to e^+ + \mathrm{Ca}) < 1.7 \times 10^{-12}$ [233]. This process is particularly interesting to pursue because new experimental advances might dramatically improve its limits in the near future [3, 45, 46, 207]. A detailed discussion on the experimental aspects of the conversion of bound muons can be found in section 5.1. We furthermore discuss the computation of $\mu^- - e^+$ conversion in section 5.3. Limits on other LNV processes like kaon decays (e.g. NA48 [234]: $\mathrm{BR}(K^\pm \to \pi^\mp \mu^\pm \mu^\pm) < 8.6 \cdot 10^{-11}$ at 90% C.L.), B-meson decays (BaBar [235]: $\mathrm{BR}(D^+ \to K^- e^+ \mu^+) < 1.9 \cdot 10^{-6}$ at 90% C.L.; BELLE [236]: $\mathrm{BR}(B^+ \to D^- e^+ \mu^+) < 1.8 \cdot 10^{-6}$ at 90% C.L.), or τ decays (BELLE [237]: $\mathrm{BR}(\tau^- \to e^+ \pi^- \pi^-) < 2.0 \cdot 10^{-8}$ at 90% C.L.) also exist. However, neither these LNV decays nor future limits on $\mu^- - e^+$ conversion are anywhere near the sensitivity on $0\nu\beta\beta$.

As for cLFV processes, the *standard contribution* to LNV processes refers to the contribution that stems solely from the light Majorana masses. A BSM setting in which only the Majorana mass term violates lepton number provides the standard contribution exclusively. And, as a result, all LNV processes have the same underlying mechanism and therefore build upon to the same basic module, see Fig. 3.2. The basic module mediating the standard contribution to LNV processes is $W^- W^- \to e_a e_b$ [238]. As a consequence, the matrix element for a generic $\Delta L = 2$ process is always proportional to $(m_\nu)_{ab}$. In case the standard contribution is the dominant LNV mechanism, all particle physics parameters, including those which depend on the specifics of the BSM model generating neutrino masses, are thus contained within $(m_\nu)_{ab}$. Hence, we can infer an upper limit on the elements of m_ν from LNV processes [227]: the most restrictive (but practically meaningless) limits on $|(m_\nu)_{e\tau}| \lesssim 10^{12}$ eV and $|(m_\nu)_{\mu\tau}| \lesssim 10^{12}$ eV stem from τ decays, while the limit on $|(m_\nu)_{\mu\mu}| \lesssim 10^{8}$ eV is

from kaon decays.[8] Furthermore, a purely Majorana-neutrino-generated μ^-–e^+ conversion would set the limit on $|(m_\nu)_{e\mu}| \lesssim 10^7$ eV, whereas $0\nu\beta\beta$ would result in the limit $|(m_\nu)_{ee}| \lesssim 10^{-1}$ eV. Clearly, the latter beats the limits from other LNV processes by several orders of magnitude, the reasons for which have been discussed above. If we furthermore combine the limit on the effective neutrino mass $(m_\nu)_{ee}$ with the data from neutrino oscillations, we might obtain information on the absolute mass scale of the neutrinos [90]. Note that, however, the effective neutrino mass also depends on the mass ordering and the complex phases, and is affected by the uncertainties on the leptonic mixing angles and neutrino mass squared differences.
Finally, although $0\nu\beta\beta$ is the most promising LNV process, it is vital to continue exploring other LNV processes for the following reasons. First of all, even if the standard contribution was dominating LNV, the effective neutrino mass could still be suppressed due to phase cancellations, leading to $(m_\nu)_{ee} \ll (m_\nu)_{ab}$ with $ab \neq ee$. Second, there is a number of BSM settings that offer alternative LNV mechanisms, see e.g. Refs. [240, 241]. Moreover, these non-standard contributions to LNV could be such that other LNV sectors are enhanced over the ee sector. There are indeed several examples known to strongly suppress or even cancel LNV in the ee sector, while inducing "more" LNV in the other sectors, see e.g. Refs. [47, 242, 243].[9] As we do not know which type of New Physics is realised in Nature, we continue our efforts to probe the character of neutrinos in different channels and LNV sectors.
Recapitulating, with the detection of neutrino oscillations, the existence of neutrino masses and LFV has been established, which demonstrates that the SM is incomplete. Due to lepton flavour not being conserved in Nature, New Physics models tend to introduce additional LFV and sometimes even LNV physics, thereby providing a rich phenomenology of both cLFV and LNV processes, which can be used as a window to New Physics beyond the SM.

3.3 Effective Theory of a Doubly Charged Scalar Singlet

In this section we will introduce an effective theory based on the SM extended by a doubly charged scalar $\mathrm{SU(2)_L}$ singlet and discuss its features along the lines of Ref. [47].
New Physics models that generate neutrino masses at loop level often include a variety of additional Higgs or other scalar fields [128,131,147,149–151,244–246]. Hence, such models combine the perks of providing a rich phenomenology with

[8] Note that this limit is inferred from an outdated experimental bound of $\mathcal{O}(10^{-9})$ [239] in comparison to the current limit of $\mathcal{O}(10^{-11})$ [234], which does however not alter the basic statements.

[9] One such setting introducing relevant non-standard contributions to both cLFV and LNV processes is discussed in the section 3.3.

naturally small neutrino masses. Radiative neutrino mass models with electrically charged particles are particularly interesting, since they allow for testing the model and detecting its new particles not only indirectly, i.e. by means of LFV and LNV processes, but also directly via collider phenomenology. This is especially true for models that introduce doubly charged scalars. There are, however, some drawbacks to radiative neutrino mass models. In order to generate neutrino masses, multiple new particles and parameters need to be introduced. Consequently, concrete phenomenological predictions are difficult to derive. Furthermore, some of the models predict neutrino masses at two or three loops, which makes it challenging – if at all analytically feasible – to compute their mass matrices.

To work around the downsides while keeping the upsides of employing a doubly charged scalar to induce loop neutrino masses, a most minimal framework which captures the main features of said class of models was introduced in Ref. [47]. The proposed setting combines the minimal extension of the SM by just one additional particle (preferably at accessible energy scales), namely the doubly charged $\mathrm{SU(2)_L}$ singlet scalar $S^{\pm\pm}$, with the assumption that all further new particles are heavier than the $S^{\pm\pm}$ and therefore contained within an effective theory. Thus, the number of parameters is reduced drastically. Since the sole minimal extension of the SM by the doubly charged scalar does not generate the desired neutrino masses, we need to add non-renormalisable effective operators containing both SM fields and $S^{\pm\pm}$. Baring in mind that for this class of models the doubly charged scalar is connected to the generation of neutrino masses, the lowest dimensional effective operator, i.e. the Weinberg operator at $d = 5$, is forbidden at tree level, and the relevant effective operator creates the coupling of the doubly charged scalar to two same-sign weak gauge bosons $W^{\pm}W^{\pm}$. The resulting model generates neutrino masses at two-loop level and has several known UV completions [150, 242, 247], for which the required effective operator originates in various ways.

The renormalisable Lagrangian describing the SM extended by only one doubly charged scalar singlet is [1, 2]:

$$\mathcal{L} = \mathcal{L}_{\mathrm{SM}} + (D_\mu S^{++})^\dagger (D^\mu S^{++}) + f_{ab}\, \overline{(E_{\mathrm{R}a})^c} E_{\mathrm{R}b}\, S^{++} + \mathrm{h.c.} - V' \,, \qquad (3.3.1)$$

with the lepton flavour indices a, $b = e$, μ, τ, the symmetric coupling matrix $f^{(*)}_{ab} = f^{(*)}_{ba}$ and the covariant derivative $D_\mu = \partial_\mu + ig'YB_\mu$. Due to the scalar hypercharge of $Y = \pm 2$ for $S^{\pm\pm}$, the covariant derivative can be rephrased into $D_\mu = \partial_\mu \pm 2ieA_\mu \mp 2ig' \sin\theta_W Z_\mu$. Furthermore, the potential is given by $V' = M_S^2\, S^{++}S^{--} + \lambda_S (S^{++}S^{--})^2 + \lambda_{HS}(H^\dagger H)(S^{++}S^{--})$ with $v = 246$ GeV, and the scalar mass M_S.

Allowing for non-renormalisable operators, we can extend the Lagrangian further. As we assume that the doubly charged scalar is involved in the generation of neutrino masses, a tree-level realisation of the Weinberg operator is forbid-

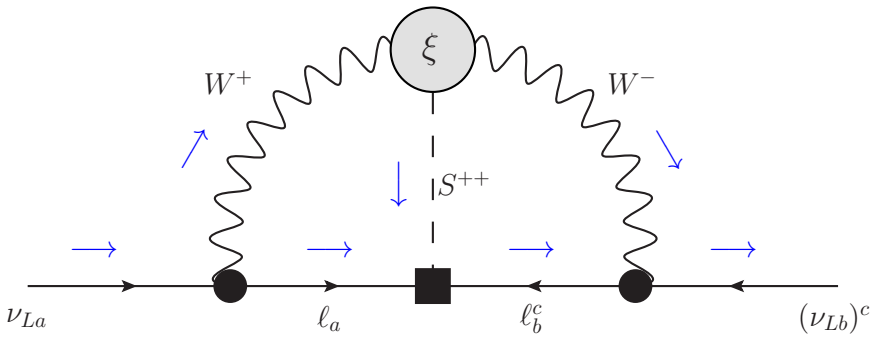

Figure 3.3: Two-loop diagram generating the (Majorana) neutrino masses in the framework of the effective theory with a doubly charged scalar singlet. The blue arrows indicate the direction of the four-momentum.

den by construction. The leading LNV operator[10] allowing for such a scenario appears at $d = 7$ and stems from (see Ref. [47]):

$$\frac{\xi}{\Lambda^3}\left[H^T i\sigma_2 \left(D_\mu H\right)\right]\left[H^T i\sigma_2 \left(D^\mu H\right)\right] S^{--} + \text{h.c.}\,, \tag{3.3.2}$$

which leads to the doubly charged scalars interactions with two W bosons

$$\mathcal{L}_{d=7} \supset -\frac{g^2\, v^4\, \xi}{4\,\Lambda^3} S^{++} W^-_\mu W^{-\mu} + \text{h.c.}\,. \tag{3.3.3}$$

Here, the effective coupling strength is given by ξ, while Λ denotes the cutoff scale below which the effective description is not valid anymore. Without loss of generality, we can choose ξ to be real, because the complex phase can be absorbed into the doubly charged scalar field S^{++}. We furthermore assume that all BSM particles apart from the doubly charged scalar have masses in excess of Λ. All Feynman rules needed for calculations throughout this thesis are given in Appendix A.

The LNV effective vertex in Eq. (3.3.3) in combination with the coupling of the doubly charged scalar to two RH charged leptons allows for the generation of light (Majorana) neutrino masses at the two-loop level, as displayed in Fig. 3.3. A detailed computation of the light neutrino mass matrix was performed in Ref. [47] and resulted in[11]

$$\left(\mathcal{M}_\nu\right)_{ab} = \frac{2\xi m_a m_b M_S^2 f_{ab}(1+\delta_{ab})}{\Lambda^3}\,\tilde{\mathcal{I}}(M_W,\, M_S,\, \mu)\,. \tag{3.3.4}$$

[10] Note that only the combination of the effective operator in Eq. (3.3.3) and the doubly charged scalar coupling to two RH charged leptons in Eq. (3.3.1) violates lepton number.

[11] Note that Ref. [47] uses a different notation for the Feynman rule of the S^{++} coupling to the pair of same-sign RH leptons: $f_{ab}(1+\delta_{ab}) \leftrightarrow 2f_{ab}$. This, however, does not play a significant role since potential discrepancies can be absorbed into a redefinition of the respective f_{ab}.

The result for the integral $\tilde{\mathcal{I}}$ can be simplified to very good approximation to [47]

$$\tilde{\mathcal{I}}(M_W,\, M_S,\, \mu) \simeq \frac{-1}{4(16\pi^2)^2}\left\{\left(1-\frac{2}{\rho}\right)\left[2(C_\gamma - L_W)^2 + \frac{\pi^2}{6} + 1\right] + (2C_\gamma - L_W - L_S)^2 + \frac{\pi^2}{3} + 2\right\}, \tag{3.3.5}$$

where the following abbreviations are employed: $L_{W,S} = \log(M^2_{W,S}/\mu^2)$, $\rho = M_S^2/M_W^2$, and $C_\gamma = 1 - \gamma + \log(4\pi)$. The latter makes use of the Euler-Mascheroni constant $\gamma \approx 0.5771$.
To exploit complementarity it is key that the coupling of the doubly charged scalar to the charged leptons is not arbitrary but enters the light neutrino mass matrix in the following manner [1]:

$$(\mathcal{M}_\nu)_{ab} \propto \begin{pmatrix} m_e^2 f_{ee} & m_e m_\mu f_{e\mu} & m_e m_\tau f_{e\tau} \\ m_e m_\mu f_{e\mu} & m_\mu^2 f_{\mu\mu} & m_\mu m_\tau f_{\mu\tau} \\ m_e m_\tau f_{e\tau} & m_\mu m_\tau f_{\mu\tau} & m_\tau^2 f_{\tau\tau} \end{pmatrix}. \tag{3.3.6}$$

Hence, the constraints on the structure of the light neutrino mass matrix from the experimental measurements of the neutrino mass squared differences and the leptonic mixing angles carry over to the coupling matrix f_{ab} [248–250]. To fully exploit the complementarity and constrain the free input parameters of this model, we combine the bounds from the neutrino parameters with those derived from the doubly charged scalar being sensitive to experimental probes from both low- and high-energy experiments. That way, one can extract benchmark points of $S^{\pm\pm}$ masses and couplings (in combination with the cutoff scale of the theory) that produce suitable neutrino masses and mixing while being consistent with limits from LFV and LNV.
The next step is finding example benchmark scenarios (f_{ab}, M_S, ξ, Λ) that fulfil the bounds from LFV and LNV processes and generate a suitable light neutrino mass matrix. In Ref. [47], the parameter space was scanned numerically based on the following considerations:

- The range of values for the parameters (f_{ab}, M_S, ξ, Λ) is not arbitrary. As stated above, all further BSM particles (besides $S^{\pm\pm}$) have masses above Λ and are thereby embedded in the EFT. Since the doubly charged scalar must not be integrated out, its mass scale needs to be well below the cutoff scale: $M_S \ll \Lambda$. This condition is met to sufficiently good accuracy for $5M_S \approx \Lambda$. Furthermore, couplings have to be below the perturbativity limit of 4π, which in practice leads to effective coupling strengths of $\xi \sim \mathcal{O}(1)$ and symmetric couplings of $f_{ab} \leq \mathcal{O}(0.1)$ [47]. Although there is a number of benchmark points with large scalar masses M_S, they are not included in the following discussion due to them not being within reach of current or future collider experiments like the LHC. We

hence set an analytical upper limit on the scalar mass $M_S \lesssim \mathcal{O}(100\ \text{TeV})$ for practical reasons.

- Taking a closer look at Eqs. (3.3.4) and (3.3.6), it turns out that the only lepton flavour dependent quantity that can be varied is the coupling f_{ab}. Consequently, the flavour structure of the neutrino mass matrix in Eq. (3.3.4) is solely determined by the relative size of the f_{ab}. It is the *relative* size that is crucial for the flavour structure because the other free parameters (M_S, ξ, Λ) are flavour independent and the other flavour dependent quantities (namely the masses of the charged leptons) are known experimentally. In addition, the integral function $\tilde{\mathcal{I}}(M_W, M_S, \mu)$ only varies marginally with the scalar mass [47]. As a consequence, the neutrino mass matrix $\mathcal{M}_\nu$ remains near-constant when altering the parameters (f_{ab}, M_S, ξ, Λ), as long as the relative size of the couplings f_{ab} stays approximately the same and

$$\frac{\xi M_S^2 f_{\max}}{\Lambda^3} \equiv b \simeq \text{const.}\,, \tag{3.3.7}$$

where $f_{\max} \equiv \max|f_{ab}|$. This also implies that, as soon as an appropriate set (f_{ab}, M_S, ξ, Λ) reproducing the neutrino mass matrix is found, one can obtain further valid benchmark points generating roughly the same neutrino mass matrix by rescaling the parameter set accordingly. Keep in mind that, however, parameters can only be varied within the limits stated in the first point, and in a second step they have to pass the limits from LNV and LFV processes. Furthermore, there are rather sizeable suppression factors from e.g. M_S^2/Λ^3 on all entries of the neutrino mass matrix. Hence, generating a mass scale as large as $\mathcal{O}(\sqrt{\Delta m_{31}^2})$ can prove to be non-trivial.

- Since the effective model at hand provides both the effective coupling $S^{--}W^+W^+$ and the renormalisable coupling $\overline{(E_{\text{R}a})^c} E_{\text{R}b}\, S^{++}$, there are non-standard contributions to LNV processes like $0\nu\beta\beta$. In order to extract the limits from the half-life of $0\nu\beta\beta$, we can employ the general formalism derived in Ref. [251, 252]. The energy of this process is $\mathcal{O}(m_\mu) \ll M_W < M_S$ [241],[12] which means that we can integrate out the heavier bosons (first the heavier doubly charged scalar and subsequently the gauge bosons) and map the diagram onto a point-like short-range operator as defined in Ref. [252]:

$$\mathcal{L}_{0\nu\beta\beta}^{\text{short-range}} = \frac{G_F^2}{2m_P}\, \epsilon_3^{\text{LLL}}\, J_{\text{L}\rho} J_{\text{L}}^\rho\, j_{\text{L}} \leftrightarrow \frac{\xi f_{ee}^*}{4 M_S^2 \Lambda^3}\, J_{\text{L}\rho} J_{\text{L}}^\rho\, j_{\text{L}}\,, \tag{3.3.8}$$

with $J_{\text{L}}^\rho = \overline{u}\gamma^\rho(1-\gamma_5)d$ being the hadronic and $j_{\text{L}} = \overline{e}(1-\gamma_5)e^c$ the leptonic current. Here, m_P is the proton mass and $G_F = 1.166 \times 10^{-5}\text{GeV}^{-2}$

[12] And references therein.

is Fermi's constant. From Eq. (3.3.8), the effective coupling ϵ_3^{LLL} can be extracted. To this end, we employ improved nuclear matrix elements given in Refs. [253, 254]. That way, GERDA's Phase I limit[13] on the half-life time $T_{1/2}^{0\nu\beta\beta} > 2.1 \times 10^{25}$yrs (at 90% C.L.) [255] can be translated into a limit on the free parameters

$$\frac{|\xi f_{ee}^*|}{M_S^2 \Lambda^3} < \frac{4.0 \times 10^{-3}}{\text{TeV}^5} \qquad 90\%\,\text{C.L.}\,. \tag{3.3.9}$$

This apparently poses a strong bound on the parameters which can be satisfied by either a tiny product ξf_{ee}^*, a large product $M_S^2 \Lambda^3$, or a more moderate combination of both. Choosing the latter product to be large means either further suppressing the neutrino masses with Λ^3 – and thus further complicating the neutrino mass productions – or pushing the scalar mass to a region that is not accessible for colliders. The limit from $0\nu\beta\beta$ can also be satisfied by a tiny ξ which leads to similar problems as enlargening Λ, namely an additional suppression on the neutrino mass matrix. Finally, this LNV bound can most trivially be satisfied by a vanishing f_{ee}^*, which will turn out to be the case for many benchmark points found.

- Since the doubly charged scalar couples in a lepton flavour violating manner, there are various processes at tree- and one-loop level that additionally constrain the parameter space for the free parameters. Moreover, the doubly charged scalars add to the anomalous magnetic moments of the leptons, which thus provide further constraints. In Tab. 3.1, we display the limits on their branching ratios (BR) and how they translate into bounds on the parameters of the theory as derived in Refs. [47, 256]. The strongest bound emanates from $\mu \to e\gamma$, followed by $\mu \to e^+e^-e^-$, see Tab. 3.1. To comply with the first limit, one either strongly restricts the combination $|f_{ee}^* f_{e\mu} + f_{e\mu}^* f_{\mu\mu} + f_{e\tau}^* f_{\tau\mu}|$ from above or pushes the scalar mass beyond the region of interesting collider phenomenology. The same applies for the second bound which instead restricts the product $|f_{e\mu} f_{ee}^*|$.

A rather simple way to comply with the strong constraints from the LFV and LNV processes discussed above is to only choose tiny couplings f_{ab}. In order to obtain a suitable neutrino mass matrix and reproduce the mass squared differences, however, we cannot suppress all f_{ab} simultaneously. Nonetheless, it is a viable approach to start numericial scans for an appropriate benchmark point (f_{ab}, M_S, ξ, Λ) based on the assumption that certain combinations of couplings f_{ab} almost vanish, and then relax these assumptions to obtain more realistic cases. Pursuing this approach, Ref. [47] found 30 benchmark points

[13] At the time this thesis was written, GERDA Phase II had already improved the limit to $T_{1/2}^{0\nu\beta\beta} > 5.3 \times 10^{25}$yrs (at 90% C.L.) [91]. We will, however, keep on working with the results of Ref. [47] based on Phase I results, because the experimental improvement is not at all critical to the discussion.

Process (Tree)	Experimental Limit	Resulting Bound
$\mu^- \to e^+e^-e^-$	$\mathrm{BR} < 1.0 \times 10^{-12}$ [9]	$\lvert f_{e\mu} f^*_{ee}\rvert < 2.3 \times 10^{-5} M_S^2$
$\tau^- \to e^+e^-e^-$	$\mathrm{BR} < 2.7 \times 10^{-8}$ [9]	$\lvert f_{e\tau} f^*_{ee}\rvert < 8.7 \times 10^{-3} M_S^2$
$\tau^- \to e^+e^-\mu^-$	$\mathrm{BR} < 1.8 \times 10^{-8}$ [9]	$\lvert f_{e\tau} f^*_{e\mu}\rvert < 5.0 \times 10^{-3} M_S^2$
$\tau^- \to e^+\mu^-\mu^-$	$\mathrm{BR} < 1.7 \times 10^{-8}$ [9]	$\lvert f_{e\tau} f^*_{\mu\mu}\rvert < 7.0 \times 10^{-3} M_S^2$
$\tau^- \to \mu^+e^-e^-$	$\mathrm{BR} < 1.5 \times 10^{-8}$ [9]	$\lvert f_{\mu\tau} f^*_{ee}\rvert < 7.0 \times 10^{-3} M_S^2$
$\tau^- \to \mu^+e^-\mu^-$	$\mathrm{BR} < 2.7 \times 10^{-8}$ [9]	$\lvert f_{\mu\tau} f^*_{e\mu}\rvert < 7.0 \times 10^{-3} M_S^2$
$\tau^- \to \mu^+\mu^-\mu^-$	$\mathrm{BR} < 2.1 \times 10^{-8}$ [9]	$\lvert f_{\mu\tau} f^*_{\mu\mu}\rvert < 8.1 \times 10^{-3} M_S^2$
$\mu^+e^- \to \mu^-e^+$	$\mathrm{G}_{\mathrm{M\overline{M}}} < 0.0030\, G_F$ [9]	$\lvert f_{ee} f^*_{\mu\mu}\rvert < 0.2\, M_S^2$
Process (Loop)	**Experimental Limit**	**Resulting Bound**
$(g-2)_e$	$\delta a_e = (1.2 \pm 1.0) \times 19^{-11}$ [256]	$\sum_a \lvert f_{ea}\rvert^2 < 1.4 \times 10^3 M_S^2$
$(g-2)_\mu$	$\delta a_\mu = (2.1 \pm 1.0) \times 10^{-9}$ [256]	$\sum_a \lvert f_{\mu a}\rvert^2 < 2.0\ M_S^2$
$\mu \to e\gamma$	$\mathrm{BR} < 5.7 \times 10^{-13}$ [9]	$\lvert\sum_a f^*_{ea} f_{a\mu}\rvert < 3.2 \times 10^{-4} M_S^2$
$\tau \to e\gamma$	$\mathrm{BR} < 3.3 \times 10^{-8}$ [9]	$\lvert\sum_a f^*_{ea} f_{a\tau}\rvert < 0.18\, M_S^2$
$\tau \to \mu\gamma$	$\mathrm{BR} < 4.4 \times 10^{-8}$ [9]	$\lvert\sum_a f^*_{\mu a} f_{a\tau}\rvert < 0.21\, M_S^2$

Table 3.1: Bounds on the branching ratios of LFV processes and anomalous leptonic magnetic moments, together with limits they imply on the model parameters, as taken from Ref. [47]. Both the experimental limits and the resulting bounds are stated at 90% C.L.. Furthermore, the mass of the doubly charged scalar M_S is measured in TeV, and $a = e,\ \mu,\ \tau$ represents the flavour index.

that predict viable LNV (i.e. $0\nu\beta\beta$) and LFV observables while agreeing with neutrino oscillation data at 3σ, see Tab. 3.1. The set of valid benchmark points found is not necessarily complete, and further numerical scans would most certainly reveal additional benchmark points. However, the scenarios found illustrate both the powers of categorising different regions in the parameter space and of the constraints on the parameters. The 30 points found fall into three categories:

- **red** points: $\lvert f_{ee}\rvert \simeq 0$ and $\lvert f_{e\tau}\rvert \simeq 0$
  For this type of benchmark point, two of the couplings connecting the doubly charged scalar to two RH charged leptons basically vanish. This connotes two approximate texture zeros in the coupling matrix, which in turn carry over to the neutrino mass matrix. To nevertheless allow for phenomenologically viable neutrino masses, the coupling $\lvert f_{e\mu}\rvert$ must be sufficiently large. By means of the nearly vanishing $\lvert f_{ee}\rvert$, we can compensate for a larger $\lvert f_{e\mu}\rvert$ and still satisfy the bound from $\mu \to 3e$. Moreover, $\mu \to e\gamma$ only receives contributions from the combination $\lvert f^*_{e\mu} f_{\mu\mu}\rvert$. Due to $\lvert f_{ee}\rvert \simeq 0$, the non-standard interaction to the neutrinoless double beta

decay vanishes, thus agreeing with the LNV observable. In addition, the standard light neutrino contribution to $0\nu\beta\beta$ also essentially vanishes due to the effective mass $(\mathcal{M}_\nu)_{ee}$ being m_e^2 suppressed. The latter implies normal ordering (NO) with a lightest neutrino mass m_1 of roughly 5 meV [98, 257]. The feature $|f_{e\tau}| \simeq 0$ results in $(\mathcal{M}_\nu)_{e\tau} \simeq 0$, which further constraints the neutrino mixing angles and phases [258].

- **purple** points: $|f_{ee}| \simeq 0$ and the correlation $f_{e\mu} \simeq -\frac{f^*_{\mu\tau}}{f^*_{\mu\mu}} f_{e\tau}$
  As for the red points, the effective mass vanishes for the purple points, hence implying NO and a lightest neutrino mass of $m_1 \sim 5$ meV. In addition to the standard contribution, the non-standard contribution to $0\nu\beta\beta$ vanishes due to $|f_{ee}| \simeq 0$, thereby complying with this strong experimental LNV constraint. The default texture zero of this category further helps evading the limit from $\mu \to 3e$. Consistency with the even stronger constraint from $\mu \to e\gamma$ is realised with aid of the correlation above, which implies the cancellation $f^*_{e\mu} f_{\mu\mu} + f^*_{e\tau} f_{\tau\mu} \simeq 0$ in combination with $|f_{ee}| \simeq 0$. The correlation imposed for the purple category also establishes additional predictivity for lepton flavour phenomenology.

- **blue** points: only the correlation $f_{e\mu} \simeq -\frac{f^*_{\mu\tau}}{f^*_{\mu\mu}} f_{e\tau}$
  For this type of benchmark point, only the correlation above needs to be fulfilled. That means that the coupling $|f_{ee}|$ which is tiny for the other two categories can be as large as $\mathcal{O}(0.1)$. Although $|f_{ee}|$ can be sizeable, the effective mass still approximately vanishes due to the m_e^2 suppression. Hence, NO with a lightest mass of about 5 meV is implied in analogy to the red and purple points [98,257]. In addition, the standard contribution to $0\nu\beta\beta$ is negligible. The non-standard contribution, however, can be considerable. To evade the stringent experimental limit on $0\nu\beta\beta$, M_S and Λ are required to be large enough, see Eq. (3.3.9), which makes for a testable scenario with respect to dedicated low-energy experiments while destroying potentially interesting collider phenomenology. Not to be in conflict with the limits from $\mu \to e\gamma$, the coupling $|f_{e\mu}|$ needs to be small enough to compensate for possibly large $|f_{ee}|$, even though there is already some suppression from the correlation above. Likewise, the limit from $\mu \to 3e$ requires a small enough $|f_{e\mu}|$.

In Fig. 3.4, taken from Ref. [47], the sizes of the couplings $|f_{ab}|$ are displayed in order to illustrate the features of the three categories as discussed above. In chapter 5, we will introduce two more processes, namely μ^-– e^- and μ^-–e^+ conversion. While many bounds discussed so far evade limits from LFV processes due to cancellations within the amplitude, those cancellations cannot appear simultaneously within the amplitudes of e.g. $\mu \to e\gamma$ and the μ– e^- conversion process. Therefore, employing both these processes at the same time strongly restricts the parameter space.

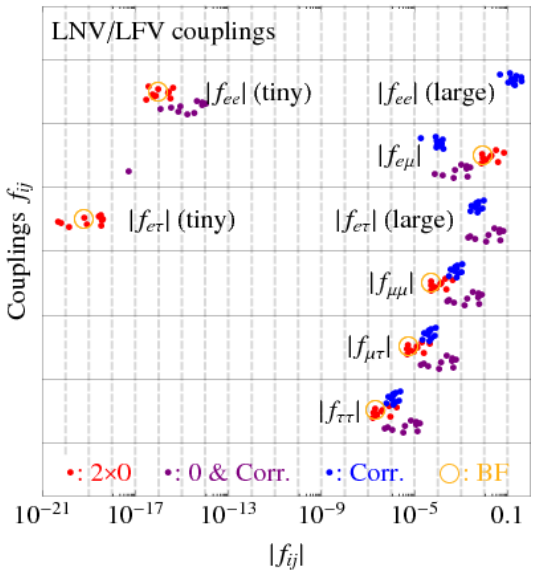

Figure 3.4: Absolute values of f_{ab} which symmetrically couple the doubly charged scalar to two RH same-sign charged leptons. Taken from [47]. Here, BF denotes the best fit benchmark points.

To maximise the benefits from ongoing and near-future experiments, we extend the complementarity analysis by direct searches performed by both ATLAS [259] and CMS [260] collaborations at LHC. To identify signatures from doubly charged scalars, a number of phenomenological studies was presented in Refs. [261–274]. Based on the extensive, model-independent analysis of the production and decay channels of doubly charged scalars in Ref. [275], Ref. [47] gives on overview on the possible phenomenology of an effective theory with a doubly charged scalar, extracting bounds on the three categories of benchmark points. Starting with the production channels, doubly charged scalars are either generated via single- or pair-production mechanisms. The dominant pair-production mode for most scalar masses is called a Drell-Yan (DY) process and mediates a Z-boson/photon in the s-channel. The production of doubly charged scalars via DY provides a lower limit on M_S and is discussed more thoroughly in Ref. [1], where the limits are derived for the three categories of benchmark points for both 7 TeV limits and expected 13 TeV limits. Another pair-production channel is vector boson fusion (VBF), which creates the two doubly scalars in combination with jets. This process, however, is subdominant due to its higher order. While these pair-production channels mostly provide lower bounds on the scalar mass, the VBF single-production mode involves the effective coupling of the doubly charged scalar to two W-bosons, namely SWW. Consequently, its cross section strongly depends on the details of the UV completion which determines the parameters ξ and Λ. Cross sections for both pair-production and single-production with different settings of fixed (ξ, Λ) and varying scalar masses were derived in Ref. [47]. Turning to the

decay channels, Ref. [47] also investigates which decay channels to explore at which scalar masses and effective couplings in order to test the three categories of benchmark points. In principle, the doubly charged scalar decays either via charged leptons or via W-bosons. Which decay channel is preferred correlates not only with the class of benchmark points but also with the parameters ξ and Λ that can enter the BR via the effective coupling SWW and contain the details of the UV completion. Note that the analyses so far are optimised for leptonic decays, and exploring the W-boson decay channels makes for interesting future studies. Ref. [47] demonstrates that already at 7 TeV there are benchmark points which, although allowed by flavour bounds and consistent with neutrino parameters, are excluded by collider experiments.

3.4 The Littlest Seesaw Model

The Littlest Seesaw (LS) is a minimal Seesaw model, proposed in Refs. [29–31], which involves extending the SM by two RH neutrino singlets in combination with a very constrained Dirac neutrino Yukawa coupling matrix. There are a number of UV scenarios using symmetry and vacuum alignment from which such a low-energy theory can hail.

Among the many possibilities to generate light neutrino masses, the Seesaw mechanism (type I) might be one of the simplest and most appealing ideas. For a detailed, pedagogical discussion on the derivation of the Seesaw formula see Ref. [118]. The classic (i.e. type I) Seesaw mechanism [32–36] extends the SM by a number of RH neutrino singlets $N_{i\mathrm{R}}$ (at least two) as:

$$-\mathcal{L}_m = \overline{\ell_{a\mathrm{L}}} Y_l^{ab} H E_{b\mathrm{R}} + \overline{\ell_{a\mathrm{L}}} Y_\nu^{ai} \tilde{H} N_{i\mathrm{R}} + \frac{1}{2} \overline{(N_\mathrm{R})^c} M_\mathrm{R} N_\mathrm{R} + \mathrm{h.c.}\,, \qquad (3.4.1)$$

where $\ell_{a\mathrm{L}} = (\nu_{a\mathrm{L}}, e_{a\mathrm{L}})$ denotes the LH lepton doublet with lepton flavour $a, b = e, \mu, \tau$. The SM Higgs doublet is labeled by $H = (H^+, H^0)$, with $\tilde{H} \equiv \mathrm{i}\sigma_2 H^*$. Furthermore, $E_{a\mathrm{R}}$ and $N_{i\mathrm{R}}$ are the RH charged-lepton and neutrino singlets, Y_l (3×3) and Y_ν $(3 \times k)$ are the charged-lepton and Dirac neutrino Yukawa coupling matrices, M_R $(k \times k)$ is the symmetric Majorana mass matrix of RH neutrino singlets. In Eq. (3.4.1), N_R denotes the k-dimensional vector collecting the k RH neutrino singlets introduced. Furthermore, note that $(\psi_{\mathrm{L,R}})^c = (\psi^c)_{\mathrm{R,L}}$ for any leptonic field or multiplet $\psi = \nu, e, \ell, N, E$. The Dirac neutrino mass matrix is induced by the Higgs mechanism, i.e. from electroweak symmetry breaking generating the vev $\langle H \rangle = (0, v/\sqrt{2})$ with $v = 246$ GeV. That way, we obtain the Dirac neutrino mass term $\overline{\nu_\mathrm{L}} m_D N_\mathrm{R}$, with $m_D = Y_\nu v/\sqrt{2}$ being the $3 \times k$ Dirac neutrino mass matrix and ν_L representing the triplet of LH neutrinos. Starting from

$$-\mathcal{L}_m = \overline{\nu_\mathrm{L}} m_D N_\mathrm{R} + \frac{1}{2} \overline{(N_\mathrm{R})^c} M_\mathrm{R} N_\mathrm{R} + \mathrm{h.c.}\,, \qquad (3.4.2)$$

we combine the following features to rewrite the Lagrangian. First, note that Majorana mass matrices are symmetric, $M_\mathrm{R} = M_\mathrm{R}^T$. Second, the Dirac mass

term can be split up into the sum

$$\overline{\nu_{\rm L}} m_D N_{\rm R} = \frac{1}{2}\overline{\nu_{\rm L}} m_D N_{\rm R} + \frac{1}{2}\overline{(N_{\rm R})^c} m_D^T (\nu_{\rm L})^c \,. \tag{3.4.3}$$

As a consequence, Eq. (3.4.2) can be rephrased into

$$-\mathcal{L}_m = \frac{1}{2}\left(\overline{\nu_{\rm L}} \quad \overline{(N_{\rm R})^c}\right) \underbrace{\begin{pmatrix} 0 & m_D \\ m_D^T & M_{\rm R} \end{pmatrix}}_{\equiv M_\nu} \begin{pmatrix} (\nu_{\rm L})^c \\ N_{\rm R} \end{pmatrix} + \text{h.c.}\,. \tag{3.4.4}$$

The classic Seesaw scenario features no LH neutrino mass matrix, thus the upper left block $m_{\rm L} \equiv (M_\nu)^{11} = 0$ (or at most a tiny one), and the hierarchy $(m_{\rm L} \ll) m_D \ll M_{\rm R}$. Since we are dealing with matrices, the condition on the mass hierarchies actually refers to the eigenvalues of the matrices. In other words, $m_D \ll M_{\rm R}$ means that all eigenvalues of the RH neutrino mass matrix are large in comparison to each and every eigenvalue of the Dirac neutrino matrix. Furthermore, the choice of $M_{\rm R}$ must be such that $\det M_{\rm R} \neq 0$, i.e. is invertible in order to apply the Seesaw formula.
Next, we need to diagonalise M_ν. Due to the strong hierarchy in the different mass matrices, it is sufficient to approximately block-diagonalise M_ν by means of the nearly unitary matrix [118]:

$$\tilde{U} = \begin{pmatrix} \mathbb{1} - \frac{1}{2} b b^\dagger & b \\ -b & \mathbb{1} - \frac{1}{2} b^\dagger b \end{pmatrix} \quad \text{with} \quad \tilde{U}\tilde{U}^\dagger = \mathbb{1} + \mathcal{O}(b^4)\,, \tag{3.4.5}$$

for $b = \mathcal{O}(m_D M_{\rm R}^{-1})$. To determine the matrix b unambiguously, we first perform the approximate block-diagonalisation $\tilde{D}_\nu \equiv \tilde{U}^T M_\nu \tilde{U}$ up to $\mathcal{O}(b^2 M_{\rm R}) = \mathcal{O}(b m_D)$. Since the off-diagonal expressions have to vanish, we can extract $b^* = m_D M_{\rm R}^{-1}$, and obtain the general Seesaw formula

$$\tilde{D}_\nu = \tilde{U}^T M_\nu \tilde{U} \simeq \begin{pmatrix} -m_D M_{\rm R}^{-1} m_D^T & 0 \\ 0 & M_{\rm R} \end{pmatrix} \equiv \begin{pmatrix} m_\nu & 0 \\ 0 & M_{\rm R} \end{pmatrix}\,. \tag{3.4.6}$$

As neither m_ν nor $M_{\rm R}$ are diagonal yet, we subsequently need to diagonalise both blocks individually. We can use the methods from section 3.1 to diagonalise the former, since the light Majorana neutrino mass m_ν in Eq. (3.4.6) is equivalent to the low-energy limit m_ν displayed in Eq. (3.1.2). From Eq. (3.4.6), we extract the light LH Majorana neutrino mass matrix,

$$m_\nu = -m_D M_{\rm R}^{-1} m_D^T = -\frac{v^2}{2} Y_\nu M_{\rm R}^{-1} Y_\nu^T\,, \tag{3.4.7}$$

which generates the physical light effective Majorana neutrino masses. The Feynman diagram corresponding to the classic Seesaw mechanism is displayed in Fig. 3.5, and results in Eq. (3.4.7) upon integrating out the heavy RH neutrinos.

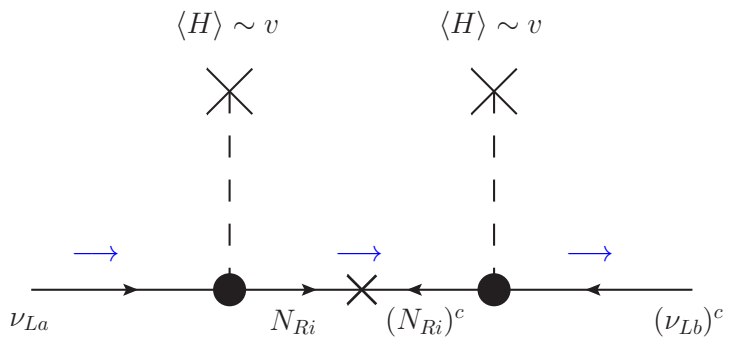

Figure 3.5: Feynman diagram generating light neutrino matrix m_ν for the Seesaw type I mechanism. Here, the mass eigenstates of the RH neutrinos propagate with masses $M_i \gg v$, i.e. we have chosen a basis where M_R is diagonal.

Although the Seesaw mechanism motivates the smallness of neutrino masses, it fails to predict both the mass ordering – inverted or normal (IO/NO) – and the leptonic mixing angles and phases. To eradicate these shortcomings, we complement the Seesaw mechanism by implementing *constrained sequential dominance* (CSD) [37–43] on the couplings of the RH neutrinos to the LH flavour eigenstate neutrinos (ν_e, ν_μ, ν_τ). In practice, this means imposing a certain pattern onto the Dirac neutrino mass matrix m_D (or, for that matter, onto the neutrino Yukawa coupling matrix Y_ν), which in turn leads to an accurate prediction of the leptonic mixing angles and phases employing only a few input parameters. CSD takes sequential dominance (SD) [29,276,277] and additionally fixes relevant Yukawa coupling ratios. The idea of SD is that one of the RH neutrinos (with mass M_atm) dominates the Seesaw mechanism and mainly accounts for the atmospheric neutrino mass m_3 and mixing [276–278]. A second RH neutrino (with mass M_sol) contributes subdominantley and is responsible for the solar neutrino mass m_2 and mixing [29, 30, 278] and, in case a third RH neutrino is included, it generates a non-zero lightest neutrino mass m_1 while being almost decoupled from the theory. The SD immediately implies NO [31, 276, 277]. However, note that the mass ordering of the RH neutrinos has not yet been specified. In case the third RH neutrino is the heaviest one, the three RH neutrino scenario effectively equals the scenario with only two RH neutrinos [29, 39, 277]. This is true for both $M_\mathrm{atm} < M_\mathrm{sol}$ and $M_\mathrm{sol} < M_\mathrm{atm}$ [279]. Since the LS model consists of only two heavy RH neutrinos, we restrict the discussion hereafter to this scenario. We start with the case that $M_\mathrm{atm} < M_\mathrm{sol}$, i.e. the lightest RH neutrino dominates the Seesaw mechanism. In the basis where the charged-lepton and the RH neutrino mass matrices are diagonal, i.e. $M_\mathrm{R} = \mathrm{diag}(M_\mathrm{atm}, M_\mathrm{sol})$, we write down the Dirac neutrino mass matrix in terms of its two columns, $m_D = (m_D^\mathrm{atm}, m_D^\mathrm{sol})$ with $(m_D^\mathrm{atm})^T = (a_1, a_2, a_3)$ and $(m_D^\mathrm{sol})^T = (b_1, b_2, b_3)$. In general, the param-

eters a_i and b_i are complex.[14] We obtain the light neutrino mass matrix from Eq. (3.4.7):

$$\begin{aligned} -m_\nu &= \begin{pmatrix} \frac{a_1^2}{M_{\rm atm}}+\frac{b_1^2}{M_{\rm sol}} & \frac{a_1a_2}{M_{\rm atm}}+\frac{b_1b_2}{M_{\rm sol}} & \frac{a_1a_3}{M_{\rm atm}}+\frac{b_1b_3}{M_{\rm sol}} \\ \frac{a_1a_2}{M_{\rm atm}}+\frac{b_1b_2}{M_{\rm sol}} & \frac{a_2^2}{M_{\rm atm}}+\frac{b_2^2}{M_{\rm sol}} & \frac{a_2a_3}{M_{\rm atm}}+\frac{b_2b_3}{M_{\rm sol}} \\ \frac{a_1a_3}{M_{\rm atm}}+\frac{b_1b_3}{M_{\rm sol}} & \frac{a_2a_3}{M_{\rm atm}}+\frac{b_2b_3}{M_{\rm sol}} & \frac{a_3^2}{M_{\rm atm}}+\frac{b_3^2}{M_{\rm sol}} \end{pmatrix} \\ &= \underbrace{\begin{pmatrix} \frac{a_1^2}{M_{\rm atm}} & \frac{a_1a_2}{M_{\rm atm}} & \frac{a_1a_3}{M_{\rm atm}} \\ \frac{a_1a_2}{M_{\rm atm}} & \frac{a_2^2}{M_{\rm atm}} & \frac{a_2a_3}{M_{\rm atm}} \\ \frac{a_1a_3}{M_{\rm atm}} & \frac{a_2a_3}{M_{\rm atm}} & \frac{a_3^2}{M_{\rm atm}} \end{pmatrix}}_{\frac{m_D^{\rm atm}(m_D^{\rm atm})^T}{M_{\rm atm}}} + \underbrace{\begin{pmatrix} \frac{b_1^2}{M_{\rm sol}} & \frac{b_1b_2}{M_{\rm sol}} & \frac{b_1b_3}{M_{\rm sol}} \\ \frac{b_1b_2}{M_{\rm sol}} & \frac{b_2^2}{M_{\rm sol}} & \frac{b_2b_3}{M_{\rm sol}} \\ \frac{b_1b_3}{M_{\rm sol}} & \frac{b_2b_3}{M_{\rm sol}} & \frac{b_3^2}{M_{\rm sol}} \end{pmatrix}}_{\frac{m_D^{\rm sol}(m_D^{\rm sol})^T}{M_{\rm sol}}} . \end{aligned} \tag{3.4.8}$$

Note that, in Eq. (3.4.8), the determinant vanishes, $\det m_\nu = 0$, which implies that the lightest neutrino mass eigenstate is zero, $m_1 \equiv 0$. Realising the idea of SD, we want the RH neutrino with $M_{\rm atm}$ to dominate the Seesaw, and the second RH neutrino to act as a perturbation (generating a non-zero m_2) , which implies the condition

$$\frac{|a_i a_j|}{M_{\rm atm}} \gg \frac{|b_i b_j|}{M_{\rm sol}} \,. \tag{3.4.9}$$

Hence, we have $-m_\nu \approx [m_D^{\rm atm}(m_D^{\rm atm})^T]/M_{\rm atm}$ to leading order under the SD condition from Eq. (3.4.9), which coincides with the scenario introducing only one RH neutrino [276, 277]. Therefore, we investigate this scenario for a start. A scenario with only one RH neutrino generates two vanishing light neutrino mass eigenstates (which is why it is already excluded) and a third mass eigenstate with $m_3 = (|a_1|^2+|a_2|^2+|a_3|^2)/M_{\rm atm}$ [29, 30, 279]. Furthermore, the atmospheric and reactor angles are predicted to be [29, 30, 279]:

$$\tan\theta_{23} = \left|\frac{a_2}{a_3}\right| \quad \text{and} \quad \tan\theta_{13} = \frac{|a_1|}{\sqrt{|a_2|^2+|a_3|^2}} \,, \tag{3.4.10}$$

whereas no prediction can be derived for the solar angle θ_{12}. From the experimental results for the mixing angles, we can deduce $|a_1| \ll |a_2| \sim |a_3|$. Clearly, this scenario fails to predict a non-zero m_2 and θ_{12}. We thus use the perturbation by the second matrix $[m_D^{\rm sol}(m_D^{\rm sol})^T]/M_{\rm sol}$ in Eq. (3.4.8) to generate the missing neutrino parameters, i.e. we introduce a second RH neutrino [29, 30]. That way, we additionally obtain a prediction for the solar angle and for the neutrino mass m_2, which both depend on the phases of the couplings [30, 279].

[14] Note that many results derived in the literature, e.g. [29, 276, 277], do ignore the phases of these parameters. Refs. [30, 39, 278, 279], however, discuss SD based on complex Yukawa couplings.

For now, we keep to the solar angle derived in Ref. [29] which, making use of the measured mixing angles, can be simplified to the "real" condition [43]:

$$\tan\theta_{12} \approx \frac{\sqrt{2}|b_1|}{|b_2|-|b_3|}\,. \tag{3.4.11}$$

Using the condition for the solar angle which includes the phases of the couplings a_i and b_i becomes relevant in case phase-dependent cancellations arise, see Refs. [30, 279]. Otherwise, working with the "real" condition is sufficient. At this point, it becomes apparent why we want to extend the concept of SD by fixing certain relevant Yukawa ratios: the hereby defined CSD specifies the predictions for the leptonic mixing angles based on a smaller number of input parameters.

The original CSD framework [37] was proposed to generate a tribimaximal mixing matrix (TBM) [280–283] from the Seesaw mechanism, thus predicting a zero reactor angle $\theta_{13} = 0^\circ$ ($\tan\theta_{13} = 0$), a maximal atmospheric angle $\theta_{23} = 45^\circ$ ($\tan\theta_{23} = 1$), and a trimaximal solar angle of $\theta_{12} \approx 35.3^\circ$ ($\tan\theta_{12} = 1/\sqrt{2}$) [31]. To obtain these mixing angles from the relations in Eqs. (3.4.10) and (3.4.11), the input parameters a_i and b_i can take on the values $a_1 = 0$, $a_2 = a_3$, $2b_1 = b_2 - b_3$. To minimise the number of input parameters, we further fix $b_2 = b_1$ and $b_3 = -b_1$. That way, we also achieve *form dominance* [284–286], which means that the columns of the Dirac mass matrix m_D are proportional to the respective columns of the PMNS mixing matrix. The latter equates the TBM matrix, since we choose a basis of diagonal charged lepton and RH neutrino mass matrices. As the original CSD does not comply with the measurement of the non-zero θ_{13}, we generalise the approach.

We are still aiming at minimising the number of input parameters, while obtaining mixing angles in agreement with experimental data. We further assume $\tan\theta_{23} \sim 1$. We also keep the texture zero $a_1 = 0$, and the solar angle close to trimaximal, so $\tan\theta_{12} \sim 1/\sqrt{2}$. What we change in contrast to the original CSD is that we allow for more degrees of freedom and drop form dominance, while still satisfying $a_2 = a_3$ and $2b_1 = b_2 - b_3$. As a result, we obtain [31]:

$$m_D = \begin{pmatrix} 0 & b_1 \\ a_2 & nb_1 \\ a_2 & (n-2)b_1 \end{pmatrix}\,, \tag{3.4.12}$$

which is the Dirac neutrino mass matrix defining CSD(n), for a positive integer n. Although $a_1 = 0$, the structure of m_D implies a non-zero reactor angle, $\theta_{13} \sim (n-1)\sqrt{2}m_2/(3m_3)$ [31]. For $n = 1$, the reactor angle still vanishes, and we obtain the original CSD scenario discussed above. Since one of the phases of the complex parameters a_2 and b_1 is unphysical, we can rewrite Eq. (3.4.12) in terms of three real parameters $\tilde{a}$, $\tilde{b}$, and η with $\tilde{a} = |a_2|$, $\tilde{b} = |b_1|$ and $\eta = \arg(\tilde{b}/\tilde{a})$, which corresponds to the Yukawa coupling matrix for Case

A in Eq. (3.4.15).[15]
Another way to realise Eq. (3.4.11) with $\tan\theta_{12} \sim 1/\sqrt{2}$ is for the parameters b_i to take on values satisfying $2b_1 = b_3 - b_2$. In analogy to the scenario discussed above, we can fix $b_2 = (n-2)b_1$ and $b_3 = nb_1$ [287], and obtain the Dirac neutrino matrix which corresponds to the Case B [39,287] in Eq. (3.4.15) (using the translation to real parameters employed for Case A).
So far, we have motivated two structures for m_D based on $M_{\rm atm} < M_{\rm sol}$. Moving on to the case for which the heavier RH neutrino dominates the Seesaw [39, 288], $M_{\rm sol} < M_{\rm atm}$, we need to take into account that the texture zero always couples ν_e to the dominant RH neutrino (with mass $M_{\rm atm}$) [39], independent of the RH neutrino mass ordering. Due to the reverted RH mass ordering, we have $M_{\rm R} = {\rm diag}(M_{\rm sol}, M_{\rm atm})$ in the diagonal charged lepton and RH neutrino mass basis. Consequently, we have to interchange the columns in Eq. (3.4.8) in order to keep the derivation and rephrasing of the parameters a_i and b_i applicable. Thus, by changing the RH mass ordering, we obtain two more structures for m_D that are given by commuting the columns for Case A (given in Eq. (3.4.12)) or Case B, respectively. The resulting m_D correspond to the Cases C and D in Eq. (3.4.16) and cannot be distinguished from Cases A and B at tree level.

Since the original CSD was motivated on the basis of inducing TBM mixing, we address the connection of m_D and the neutrino mixing matrix $U_{\rm PMNS}$, as parametrised in Eq. (3.1.5), below. The TBM is defined by setting the values $U_{e3} = 0$, $|U_{\mu 3}|^2 = 1/2$ and $|U_{e2}|^2 = 1/3$ [280].[16] Due to unitarity constraints, we obtain $|U_{\tau 3}|^2 = 1/2$ for the last column of U. Combining unitarity with orthogonality the centre column has to comply with $|U_{\mu 2}|^2 = |U_{\tau 2}|^2 = 1/3$. The entries of the first column are fixed to $|U_{e1}|^2 = 2/3$ and $|U_{\mu 1}|^2 = |U_{\tau 1}|^2 = 1/6$ by applying unitarity to the rows. As only the absolute values of the TBM mixing matrix entries are constrained, there are several realisations of the TBM mixing matrix $U_{\rm TBM}$ [280–283]. Within the context of the LS, one usually opts for the convention [31, 282]:

$$U_{\rm TBM} = \begin{pmatrix} \sqrt{\frac{2}{3}} & \frac{1}{\sqrt{3}} & 0 \\ -\frac{1}{\sqrt{6}} & \frac{1}{\sqrt{3}} & \frac{1}{\sqrt{2}} \\ \frac{1}{\sqrt{6}} & -\frac{1}{\sqrt{3}} & \frac{1}{\sqrt{2}} \end{pmatrix} . \tag{3.4.13}$$

This version of $U_{\rm TBM}$ is equivalent to choosing a basis where the charged-lepton mass matrix is not only diagonal but also real, i.e. setting the unphysical phases $\delta_i = 0$. Since the mixing angles by convention are real and $0 \leq \theta_{ij} \leq \pi/2$, it is $|U_{e3}| = s_{13} = 0$. Due to the vanishing mixing angle, leptonic CP violating effects cannot be measured.[17] We thus choose $\delta = \varphi_{1,2} = 0$. We furthermore

[15] This means that $\tilde{a} = va/\sqrt{2}$, $\tilde{b} = vb/\sqrt{2}$, and $\eta = \arg(\tilde{b}/\tilde{a}) = \arg(b/a)$.

[16] For brevity, we refer to the PMNS matrix by U instead of $U_{\rm PMNS}$ for the following discussion.

[17] The Dirac phase always enters the flavour oscillation probabilities $P(\nu_l \to \nu_{l'})$ and

obtain $|s_{12}|= 1/\sqrt{3}$, $|c_{12}|= \sqrt{2/3}$, and $|s_{23}|= |c_{23}|= 1/\sqrt{2}$, which due to the convention for the range of mixing angles translates into $\theta_{12} \approx 35.3^\circ$ and $\theta_{23} = 45^\circ$. The light effective neutrino mass originating from m_D in Eq. (3.4.12) with $n = 1$ predicts the TBM matrix in Eq. (3.4.13). For $n > 1$, however, Eq. (3.4.13) will only block-diagonalise the corresponding m_ν. What does that mean for the PMNS mixing matrix in case $n > 1$? For $n = 1$ the columns of $U_{\rm TBM}$ are eigenvectors of m_ν to the eigenvalues $m_1 = 0$, m_2, m_3 with the first column corresponding to the eigenvalue $m_1 = 0$. For $n > 1$, $m_1 = 0$ is still an eigenvalue of the light neutrino mass matrix m_ν. Moreover, the corresponding eigenvector continues to be the first column of TBM matrix in Eq. (3.4.13), which eventuates in the block diagonalisation of $m_\nu(n > 1)$. This also means that the PMNS matrix for $n > 1$ and $U_{\rm TBM}$ share the first column but differ in the other two columns, i.e. CSD($n > 1$) leads to the less restrictive so-called $\rm TM_1$ mixing [289–291]. A useful feature to test $\rm TM_1$ mixing are its sum rules [31]. In general, sum rules interrelate the physical observable quantities (like the neutrino parameters), without entering the input parameters of a given model into the equation. Sum rules can arise in case there are fewer input than observable parameters, i.e. the observables are over-determined. Albeit, deriving such sum rules might turn out not to be technically feasible. The sum rules for $\rm TM_1$ mixing given in Ref. [31] express δ in terms of the mixing angles [290, 291] and relate θ_{12} to θ_{13} [53].
The TBM realisation in Eq. (3.4.13) is directly linked to the m_D structure in Eq. (3.4.12), referred to as Case A. Changing the structure of m_D to generate the so-called Case B – i.e. interchanging the two lower rows – leads to an effective light neutrino mass that cannot be diagonalised neither by means of Eq. (3.4.13) for $n = 1$ nor by means of the kind of $\rm TM_1$ matrix introduced above for $n > 1$. Nevertheless, this does not imply that Case B does not predict such mixing scenarios. What it does mean, on the other hand, is that we need to invoke another convention, namely [287]

$$U_{\rm TBM}^{\rm B} = \begin{pmatrix} \sqrt{\frac{2}{3}} & \frac{1}{\sqrt{3}} & 0 \\ \frac{1}{\sqrt{6}} & -\frac{1}{\sqrt{3}} & -\frac{1}{\sqrt{2}} \\ -\frac{1}{\sqrt{6}} & \frac{1}{\sqrt{3}} & -\frac{1}{\sqrt{2}} \end{pmatrix} , \tag{3.4.14}$$

which stems from combining the neutrino mixing angles and physical phases used for Eq. (3.4.13) with the unphysical phases $\delta_\mu = \delta_\tau = \pi$. Clearly, both realisations of the TBM matrix only differ in the choice of the unphysical phases. It is therefore hardly surprising that Case B with $n > 1$ leads to a version of $\rm TM_1$ mixing that is associated with the TBM choice in Eq. (3.4.14). Since the $\rm TM_1$ mixing for Case B solely differs from the one of Case A in terms of an unphysical phase, the corresponding set of sum rules is identical. Another

$P(\overline{\nu}_l \to \overline{\nu}_{l'})$ in combination with s_{13}, whereas the Majorana phases do not appear at all [67, 68]. The Majorana phases can play an important role for LNV processes but cannot be probed thus far.

way to validate this statement is by realising that the sum rules we refer to are equivalent to either $|U_{e1}|= \sqrt{2/3}$ or $|U_{\mu 1}|= |U_{\tau 1}|= 1/\sqrt{6}$ [31], which is always satisfied independent of unphysical phases. Since we have not included renormalisation group (RG) effects thus far, Cases A and C as well as Cases B and D are degenerate and the discussion above carries over.

Lastly, having motivated CSD(n) in a bottom-up manner, it remains to justify such patterns from a more fundamental theory at high energies. A popular approach in literature is augmenting the neutrino mass model by a discrete, non-Abelian family symmetry group G_f of the Lagrangian, see e.g. Refs. [31,292] and references therein. The relation between the observed flavour symmetry of m_ν and the underlying family symmetry G_f is used to classify the respective model as direct or indirect. This classification depends on whether the neutrino flavour symmetry is a residual subgroup of the family symmetry (direct) or an accidental symmetry (indirect). The TBM neutrino mass matrix is invariant under Klein's four-group $\mathbb{Z}_2 \times \mathbb{Z}_2$ [292,293]. Direct models for which G_f leads to TBM mixing can arise from family symmetries such as S_4 [294–296] or A_4 [297–303]. Direct models producing TM_1 can for example be based on S_4 [31, 304] or $S_4 \times U(1)$ [287]. Usually, direct models allow for an $SU(5)$ type unification [301, 303, 305–307]. For indirect models, the family symmetry G_f is broken completely by flavons. The accidental symmetry is nevertheless an (indirect) effect of G_f as it emerges due to the vacuum alignment of said flavons proportional to the columns of m_D [292]. A number of viable choices G_f for indirect models is discussed in Ref. [292]. Furthermore, such indirect models normally permit $SO(6)$ type unification [308, 309]. This discussion illustrates that CSD(n) is not only motivated from a natural and minimal implementation of the Seesaw mechanism but also more fundamentally from symmetry arguments.

Having established the underlying concepts and motivations, we are ready to introduce the LS based on Sec. 2 of Ref. [5] (by the author of this thesis). Note that parts of this discussion are thus taken par for par from the reference. The LS model [31, 39, 43, 287, 306] extends the SM by two heavy RH neutrino singlets with masses M_{atm} and M_{sol} and imposes CSD(n) on the Dirac neutrino Yukawa couplings. The type of LS is defined by the particular choice of structure of $Y_\nu^{\mathrm{A,B,C,D}}$ and heavy mass ordering $M_{\mathrm{R}}^{\mathrm{A,B,C,D}}$, as discussed above. All four LS cases predict a NO for the light neutrinos with a massless neutrino $m_1 = 0$.

In the flavour basis, where the charged leptons and RH neutrinos are diagonal, the **Cases A, B** are defined by the mass hierarchy $M_{\mathrm{atm}} \ll M_{\mathrm{sol}}$, and hence $M_{\mathrm{R}} = \mathrm{diag}(M_{\mathrm{atm}}, M_{\mathrm{sol}})$, and the structure of the respective Yukawa coupling matrix by

$$\textbf{Case A}: \; Y_\nu^{\mathrm{A}} = \begin{pmatrix} 0 & be^{\mathrm{i}\eta/2} \\ a & nbe^{\mathrm{i}\eta/2} \\ a & (n-2)be^{\mathrm{i}\eta/2} \end{pmatrix}, \; \textbf{Case B}: \; Y_\nu^{\mathrm{B}} = \begin{pmatrix} 0 & be^{\mathrm{i}\eta/2} \\ a & (n-2)be^{\mathrm{i}\eta/2} \\ a & nbe^{\mathrm{i}\eta/2} \end{pmatrix} \tag{3.4.15}$$

with a, b, η being three real parameters and n is an integer. These scenarios together with their RG behaviour were analysed in Ref. [310] with heavy neutrino masses of $M_{\rm atm} = M_1 = 10^{12}$ GeV and $M_{\rm sol} = M_2 = 10^{15}$ GeV.

Considering an alternative mass ordering of the two heavy Majorana neutrinos – $M_{\rm atm} \gg M_{\rm sol}$, and consequently $M_{\rm R} = {\rm diag}(M_{\rm sol}, M_{\rm atm})$ – we have to exchange the two columns of Y_ν in Eq. (3.4.15), namely,

$$\textbf{Case C}: Y_\nu^{\rm C} = \begin{pmatrix} be^{{\rm i}\eta/2} & 0 \\ nbe^{{\rm i}\eta/2} & a \\ (n-2)be^{{\rm i}\eta/2} & a \end{pmatrix}, \ \textbf{Case D}: Y_\nu^{\rm D} = \begin{pmatrix} be^{{\rm i}\eta/2} & 0 \\ (n-2)be^{{\rm i}\eta/2} & a \\ nbe^{{\rm i}\eta/2} & a \end{pmatrix}, \tag{3.4.16}$$

which we refer to as **Cases C, D**. For $M_{\rm atm} = M_2 = 10^{15}$ GeV and $M_{\rm sol} = M_1 = 10^{12}$ GeV, both these cases (and their RG behaviour) were studied in Ref. [310].

We apply the Seesaw formula in Eq. (3.4.7), for **Cases A, B, C, D** using the Yukawa coupling matrices $Y_\nu^{\rm A,B}$ in Eq. (3.4.15) with $M_{\rm R}^{\rm A,B} = {\rm diag}({\rm M_{atm}}, {\rm M_{sol}})$ and $Y_\nu^{\rm C,D}$ in Eq. (3.4.16) with $M_{\rm R}^{\rm C,D} = {\rm diag}({\rm M_{sol}}, {\rm M_{atm}})$, to give (after rephrasing) the light neutrino mass matrices in terms of the real parameters $m_a = a^2v^2/(2M_{\rm atm})$, $m_b = b^2v^2/(2M_{\rm sol})$,[18]

$$m_\nu^{\rm A,C} = m_a \begin{pmatrix} 0 & 0 & 0 \\ 0 & 1 & 1 \\ 0 & 1 & 1 \end{pmatrix} + m_b {\rm e}^{{\rm i}\eta} \begin{pmatrix} 1 & n & (n-2) \\ n & n^2 & n(n-2) \\ (n-2) & n(n-2) & (n-2)^2 \end{pmatrix}, \tag{3.4.17}$$

$$m_\nu^{\rm B,D} = m_a \begin{pmatrix} 0 & 0 & 0 \\ 0 & 1 & 1 \\ 0 & 1 & 1 \end{pmatrix} + m_b {\rm e}^{{\rm i}\eta} \begin{pmatrix} 1 & (n-2) & n \\ (n-2) & (n-2)^2 & n(n-2) \\ n & n(n-2) & n^2 \end{pmatrix}. \tag{3.4.18}$$

Note the Seesaw degeneracy of **Cases A, C** and **Cases B, D**, which yield the same effective neutrino mass matrices, respectively. Studies which ignore RG running effects do not distinguish between these degenerate cases. Of course, in the RG study discussed in chapter 6 the degeneracy is resolved and we have to separately deal with the four physically distinct cases.

The neutrino masses and lepton flavour mixing parameters at the electroweak scale $\Lambda_{\rm EW} \sim \mathcal{O}(1000$ GeV) can be derived by diagonalising the effective neutrino mass matrix as defined in Eq. (3.1.3). From a neutrino mass matrix as given in Eqs. (3.4.17) and (3.4.18), one immediately obtains NO with $m_1 = 0$. Therefore, these scenarios only provide one physical Majorana phase σ. Since we choose to start in a flavour basis, where the RH neutrino mass matrix $M_{\rm R}$ and the charged-lepton mass matrix m_ℓ are diagonal, the PMNS matrix is given by $U_{\rm PMNS} = U_{\nu{\rm L}}^\dagger$. We use the PMNS standard parametrisation

[18] Note that Ref. [5] makes use of the vev $v = 174$ GeV. Consequently, Eq. (3.4.7) differs by $v \leftrightarrow v/\sqrt{2}$ as do the definitions of the real parameters $m_{a,b}$.

in Eq. (3.1.5),[19] which implies that the standard Majorana phase φ_1 vanishes, and we define $\sigma \equiv -\varphi_2/2$.

For LS Case A, exact analytical expressions for all 8 neutrino parameters $\{\theta_{ij},\, m_i, \delta,\, \sigma\}$ in terms of the four input parameters $\{m_a,\, m_b,\, \eta,\, n\}$ were derived in Ref. [31]. It was also shown in Ref. [31] that there are more sum rules for the LS than are specific to TM_1 mixing. We can extract the exact neutrino parameters for Case B from Case A since both scenarios are related by means of interchanging the second and third rows of m_D and by association m_ν. As a result, we can phrase the light neutrino mass matrix of Case B via the one of Case A and a transformation matrix P_{23} [310]:

$$m_\nu^{\mathrm{B}} = P_{23} m_\nu^{\mathrm{A}} P_{23}^T \quad \text{with} \quad P_{23} = \begin{pmatrix} 1 & 0 & 0 \\ 0 & 0 & 1 \\ 0 & 1 & 0 \end{pmatrix} . \tag{3.4.19}$$

That way, the PMNS matrices for Cases A and B are linked, via $U^{\mathrm{B}} = P_{23} U^{\mathrm{A}}$ for the same neutrino mass eigenstates. The mixing parameters of Case B are hence deduced from those of Case A [310]: $\theta_{12}^{\mathrm{B}} = \theta_{12}^{\mathrm{A}}$, $\theta_{13}^{\mathrm{B}} = \theta_{13}^{\mathrm{A}}$, $\theta_{23}^{\mathrm{B}} = \pi/2 - \theta_{23}^{\mathrm{A}}$, $\delta^{\mathrm{B}} = \pi - \delta^{\mathrm{A}}$ and $\sigma^{\mathrm{B}} = \pi - \sigma^{\mathrm{A}}$. As long a RG effects are not included, Cases C and D are covered by the expressions for A or B, respectively.

The low-energy phenomenology in the LS model Case A has been studied in detail both numerically [39,43] and analytically [31], where it has been found that the best fit to experimental data of neutrino oscillations is obtained for $n = 3$ for a particular choice of phase $\eta \approx 2\pi/3$, while for Case B the preferred choice is for $n = 3$ and $\eta \approx -2\pi/3$ [39, 287]. Due to the degeneracy of Cases A, C and Cases B, D at tree level, the preferred choice for n and η carries over, respectively. The prediction for the baryon number asymmetry in our Universe via leptogenesis within Case A is also studied [306], while a successful realisation of the flavour structure of Y_ν for Case B in Eq. (3.4.15) through an $S_4 \times U(1)$ flavour symmetry is recently achieved in Ref. [287], where the symmetry fixes $n = 3$ and $\eta = \pm 2\pi/3$.

With the parameters $n = 3$ and $\eta = \pm 2\pi/3$ fixed, there are only two remaining real free Yukawa parameters in Eqs. (3.4.15) and (3.4.16), namely a and b, so the LS predictions then depend on only two real free input combinations $m_a = a^2 v^2/(2M_{\mathrm{atm}})$ and $m_b = b^2 v^2/(2M_{\mathrm{sol}})$, in terms of which all neutrino masses and the PMNS matrix are determined. For instance, if m_a and m_b are chosen to fix m_2 and m_3, then the entire PMNS mixing matrix, including phases, is determined with no free parameters. Using benchmark parameters ($m_a = 26.57$ meV, $m_b = 2.684$ meV, $n = 3$, $\eta = \pm 2\pi/3$), it turns out that the LS model predicts close to maximal atmospheric mixing at the high scale, $\theta_{23} \approx 46^\circ$ for Case A , or $\theta_{23} \approx 44^\circ$ for Case B [287], where both predictions are challenged by the latest NOνA results [26] which indicates that $\theta_{23} = 45^\circ$ is excluded at the 2.6 σ, although T2K measurements

[19] Note that one can interchangeably use different ranges for the phases, depending on the definition used. For more information, see section 6.1.

continue to prefer close-to-maximal mixing [24,311]. Since no RG running has been included so far, Cases C and D predict the same atmospheric angles upon inserting the benchmark parameters.

Chapter 4

Tools, Concepts, and Methods

This chapter is dedicated to the introduction of theoretical concepts and methods we apply throughout chapters 5 and 6 of this thesis. We start by recapitulating the concepts of regularisation, renormalisation, and renormalisation group equations, which are used to treat infinities that can arise from including quantum effects in section 4.1. Subsequently, we review the basics of effective field theories (as well as some applications) in section 4.2. Finally, in section 4.3, we turn to the method of least squares, which is a statistical tool used to identify the level of agreement between the measured data and the predictions of a specific model based on a set of input parameters.

4.1 Renormalisation Group Effects

The Standard Model (SM) of particle physics is an almost perfect description of the smallest building blocks we know of the Universe. It is based on depicting Nature by means of quantum field theories (QFTs), collecting the elementary fields and their fundamental interactions in a Lagrangian. In general, as soon as interactions are included in a QFT, the resulting amplitudes may no longer be exactly calculable. Nevertheless, we are able to provide good approximations to the results by employing perturbation theory. For many phenomenological processes, the leading order contribution to the amplitude emerges at *tree-level*, which corresponds to the classical description of the respective process. For higher accuracy and/or to include quantum effects, we need to go beyond tree-level to higher order in the perturbation series, where *loop-level* contributions are generated. The loop-level contributions to an amplitude involve the integration over internal/virtual momenta. Since these loop-momenta are not specified by momentum conservation, the loop integrals may not converge, resulting in divergent expressions. This raises two questions. First, how can we technically perform the momentum integration and separate divergences from finite contributions? Second, how can we make sense of diverging contributions? The latter seems particularly unsettling because

employing perturbation series is based on small coefficients. We will address these fundamental issues by means of renormalisation group (RG) methods throughout this section. It will turn out that, as a consequence of including quantum effects, the coupling "constants" and masses of the QFT are predicted to depend on the energy scale under consideration. This phenomenon is referred to as *RG running*, and it has indeed been verified experimentally e.g. by the discovery of asymptotic freedom[1] in the QFT of strong interactions (QCD) [312–314].
When discussing how to compute amplitudes, the one-particle-irreducible (OPI) Green's functions with n external legs, also referred to as n-point vertex-functions $\Gamma^{(n)}$, are a useful tool. In Feynman diagram language, they correspond to OPI diagrams. Considering an amputated Feynman diagram, the diagram is called reducible if it is possible to create two disconnected diagrams by cutting an inner line. An OPI diagram is an amputated Feynman diagram for which this is not possible. Furthermore, the generating functional of the n-point vertex-functions is the effective action (in real space) $\Gamma[\phi_c]$, such that:

$$\Gamma^{(n)}(x_1, \ldots, x_n) \equiv \frac{\delta^n \Gamma[\phi_c]}{\delta\phi_c(x_1) \cdots \delta\phi_c(x_n)} \,. \tag{4.1.1}$$

We will mostly employ the n-point vertex-functions in momentum space, which are defined as the Fourier transform of Eq. (4.1.1) net of the energy-momentum conserving δ-function.

We illustrate how to treat emerging divergences in a self-consistent manner introducing the concepts of regularisation, renormalisation, and renormalisation group equations by means of the standard example of the ϕ^4-theory. This simple setting consists of a real scalar field ϕ of mass m, which self-interacts via quartic couplings λ, and is discussed throughout the literature [202, 315–317] and in many advanced QFT lectures. Albeit being simplistic in a sense, this example model can be employed to adequately explain the concepts needed and it can easily be generalised to more realistic settings. The ϕ^4-theory Lagrangian is given by

$$\mathcal{L} = \frac{1}{2}(\partial_\rho \phi)(\partial^\rho \phi) - \frac{1}{2} m^2 \phi^2 - \frac{\lambda}{4!}\phi^4 \,. \tag{4.1.2}$$

For a start, we consider the one-loop corrections to both two-point and four-point vertex-function[2] displayed in Fig. 4.1. For the one-loop correction to the amputated propagator in momentum space, we obtain the so-called self-energy,

$$-i\Sigma^{(1)} = -\frac{i\lambda}{2} \int \frac{\mathrm{d}^4 q}{(2\pi)^4} \frac{i}{q^2 - m^2} \,, \tag{4.1.3}$$

[1] Asymptotic freedom refers to the property in a QFT that causes the interaction strength to asymptotically decrease with the length scale (or, analogously, the inverse energy scale).
[2] Note that the propagator is given by the inverse of the two-point vertex-function $\Gamma^{(2)}$.

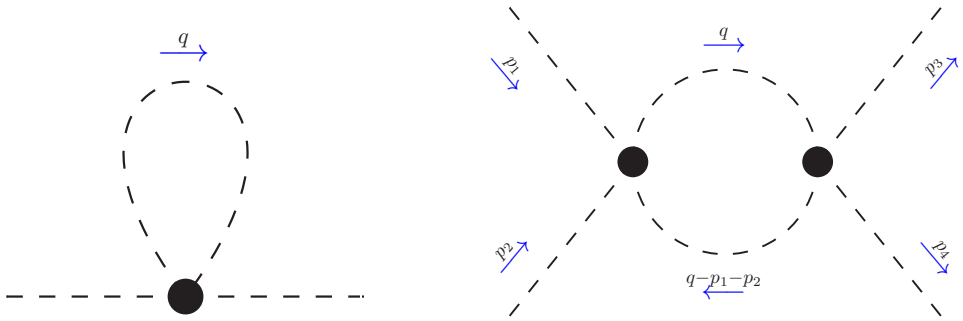

Figure 4.1: One-loop corrections to the (*left*) propagator and the (*right*) quartic coupling in ϕ^4-theory.

with the symmetry factor 1/2. The one-loop correction to the four-point vertex function can be determined from the amputated Feynman diagram on the right-hand side of Fig. 4.1,

$$\begin{aligned} -i\Gamma^{(4)}_{1-\text{loop}} &= \frac{(-i\lambda)^2}{2}\int \frac{\mathrm{d}^4q}{(2\pi)^4}\frac{i}{q^2-m^2}\frac{i}{(q-p_1-p_2)^2-m^2} + \text{permutations} \\ &\xrightarrow{p_i=0} \frac{3\lambda^2}{2}\int \frac{\mathrm{d}^4q}{(2\pi)^4}\frac{1}{(q^2-m^2)^2}\,, \end{aligned} \tag{4.1.4}$$

where the factor 3 arises from different permutations possible, by interchanging the external legs.

Regularisation. We begin by addressing the question of how to technically perform the momentum integration of integrals such as the one displayed in Eq. (4.1.4) and separate the divergence from finite contributions. To that end, we rewrite the integrals using the Feynman parametrisation,

$$\frac{1}{AB} = \int_0^1 \mathrm{d}x\,\frac{1}{\left[Ax+B(1-x)\right]^2}\,, \tag{4.1.5}$$

and subsequently perform a so-called Wick rotation. The Wick rotation is used to switch from Minkowski to Euclidean space, and it is based on the idea of computing the q_0-integration by means of the residue theorem. To allow for the use of the residue theorem, the integrand's pole cannot be on the real axis. Consequently, we add an infinitesimal imaginary term, $q^2-m^2 \to q^2-m^2+i\eta$, to fix the pole structure.[3] Based on the pole structure in the q_0-plane, we then rotate the integration contour such that $q_0 = iq_{E0}$ and $q_i = q_{Ei}$ $(i=1,2,3)$, and subsequently switch to spherical coordinates. This leads to

$$\int_{-\infty}^{\infty}\mathrm{d}^4q\frac{1}{(q^2-\Delta)^n} = \frac{i}{(-1)^n}\int \mathrm{d}\Omega_4\int_0^\infty \mathrm{d}q_E\frac{q_E^3}{(q_E^2+\Delta)^n}\,, \tag{4.1.6}$$

[3]Note that the $\pm i\eta$ term can also be motivated from quantum mechanics (QM), where it is used to carry out the projection to ground states for large absolute values of time.

where $\int \mathrm{d}\Omega_4$ is the 3-dimensional surface area of the 4-dimensional unit sphere, and q_E is the absolute value of the momentum four-vector in Euclidean space. Applied to Eqs. (4.1.3) and (4.1.4), this procedure yields:

$$\begin{aligned} -i\Sigma^{(1)} &= -i\frac{\lambda}{2}\frac{1}{(2\pi)^4}\int \mathrm{d}\Omega_4 \int_0^\infty \mathrm{d}q_E \frac{q_E^3}{q_E^2+m^2} \\ \text{and} \quad -i\Gamma^{(4)}_{1-\text{loop}} &= i\frac{\lambda^2}{2}\frac{1}{(2\pi)^4}\int_0^1 \mathrm{d}x \int \mathrm{d}\Omega_4 \int_0^\infty \mathrm{d}p_E \frac{p_E^3}{(p_E^2+\Delta)^2}\,, \end{aligned} \tag{4.1.7}$$

where we have shifted the four-momentum $q \to p = q-(p_1+p_2)x$ and absorbed parameters into $-\Delta \equiv (p_1+p_2)^2 x(1-x) - m^2$ for brevity. Having rephrased the loop integrals, the divergent behaviour becomes explicit. For the self-energy, the divergence is quadratic due to $\int_0^\infty \mathrm{d}q_E \mathcal{O}(q_E)$, whereas we obtain a logarithmic divergence for the four-point vertex owing to $\int_0^\infty \mathrm{d}p_E \mathcal{O}(1/p_E)$.
There are various ways to come to grips with the ultraviolet (UV) divergences[4] that lurk within Eqs. (4.1.3) and (4.1.4), which all rely on the concept of *regularisation*. A diverging integral poses an ill-defined problem, which we can solve by adding information. In other words, each regularisation approach introduces additional information by which the integral is made finite, and the divergence can be recovered in some regularisation-approach-dependent limit. One straightforward way to regularise these diverging integrals is to introduce an ad hoc momentum cut-off Λ, which corresponds to the assumption that the description becomes invalid at Λ. Applying this *cut-off regularisation*, we obtain

$$\begin{aligned} -i\Sigma^{(1)} &\propto \int_0^\Lambda \mathrm{d}q_E\, \mathcal{O}(q_E) \sim \Lambda^2 \\ \text{and} \quad -i\Gamma^{(4)}_{1-\text{loop}} &\propto \int_0^\Lambda \mathrm{d}p_E\, \mathcal{O}(1/p_E) \sim \ln\left[\frac{\Lambda^2}{s}\right] + \ln\left[\frac{\Lambda^2}{u}\right] + \ln\left[\frac{\Lambda^2}{t}\right], \end{aligned} \tag{4.1.8}$$

where s, t, and u are the Mandelstam variables. Although being a valid regularisation method, the cut-off regularisation can break gauge and Lorentz invariance [318] and is therefore less fit for our purposes. Another valid and even handier approach is the so-called *Pauli-Villars regularisation* [319], which does not destroy Lorentz invariance and also has a straightforward interpretation: we introduce another heavy degree of freedom with mass Λ which contributes to each loop correction with an opposite sign. In other words, we substitute

$$\frac{1}{q^2-m^2} \to \frac{1}{q^2-m^2} - \frac{1}{q^2-\Lambda^2}\,. \tag{4.1.9}$$

As a consequence, the heavy auxiliary "particle" cannot be produced for small q, whereas the contributions cancel for large q, making the integral finite.

[4] The term UV refers to divergences that appear at high energies. In contrast, divergences that arise for $p_E \to 0$ are referred to as infrared (IR).

Unfortunately, this approach can also violate gauge invariance, and will hence not be employed further.
Since gauge invariance is important in order to address renormalisation, we turn to the method of *dimensional regularisation* [320], on which we will base the remainder of this discussion. Using dimensional regularisation, we switch from 4 to an arbitrary number of space-time dimensions $d \equiv 4-\epsilon$.[5] In general, the integrals converge to well-defined values for $d \neq 4$, whereas we encounter poles for $d \to 4$ (or analogously $\epsilon \to 0$). Note that this approach is also valid for non-integer, even complex d through analytical continuation. Before computing the integrals applying dimensional regularisation, we perform a dimensional analysis of the Lagrangian and examine whether any coupling constant has acquired a mass dimension upon switching to $d \neq 4$. Since the action $\mathcal{S} = \int \mathrm{d}^d x\, \mathcal{L}(x)$ is dimensionless, the Lagrangian itself has mass dimension $\dim[\mathcal{L}] = d$. Consequently, both the kinetic and the mass term have mass dimension d, which leads to $\dim[\phi] = (d-2)/2$. As the quartic self-interaction is also required to have overall mass dimension d, we obtain $\dim[\lambda] = 4-d = \epsilon$. Aiming at a dimensionless coupling constant, we introduce the parameter μ with $\dim[\mu] = 1$, which can be associated with an arbitrary energy scale, and rephrase the coupling, $\lambda \to \mu^{4-d}\lambda$. Making use of dimensional regularisation, we can compute the integrals in Eqs. (4.1.3) and (4.1.4) and isolate their divergences by expanding around the pole at $\epsilon = 0$:

$$\begin{aligned} -i\Sigma_d^{(1)} &= \frac{\mu^{4-d}\lambda}{2} \int \frac{\mathrm{d}^d q}{(2\pi)^d} \frac{1}{q^2 - m^2 + i\eta} \\ &= i\frac{\lambda}{32\pi^2} m^2 \left(\frac{2}{\epsilon} + 1 - \gamma_E + \ln\left[4\pi\right] + \ln\left[\frac{\mu^2}{m^2}\right] + \mathcal{O}(\epsilon) \right) \end{aligned} \tag{4.1.10}$$

and

$$\begin{aligned} -i\Gamma^{(4)}_{d,\,1-\mathrm{loop}} &= \frac{\mu^{2(4-d)}\lambda^2}{2} \int \frac{\mathrm{d}^d q}{(2\pi)^d} \frac{1}{q^2 - m^2} \frac{1}{(q - p_1 - p_2)^2 - m^2} + \text{permutations} \\ &= i\frac{3\lambda^2}{32\pi^2} \left(\frac{2}{\epsilon} - \gamma_E + \frac{1}{3} F(m,\, \mu,\, \{p_i\}) + \mathcal{O}(\epsilon) \right). \end{aligned} \tag{4.1.11}$$

Here, $\gamma_E \approx 0.57722$ denotes the Euler-Mascheroni constant, and we use the finite function

$$\begin{aligned} F(m,\, \mu,\, \{p_i\}) &= -\int_0^1 \mathrm{d}x\, \ln\left[\frac{m^2 - (p_1 + p_2)^2 x(1-x)}{4\pi\mu^2} \right] + \text{permutations} \\ &\xrightarrow{\{p_i\}=0} -3\ln\left[\frac{m^2}{4\pi\mu^2}\right]. \end{aligned} \tag{4.1.12}$$

[5] Note that, in case the gamma matrix structure is more involved, we need to adapt the Clifford (Dirac) algebra for d dimensions.

Note that we need to proceed with caution in the absence of external scales, which would be the case if e.g. $m = 0$ for the self-energy integral. To avoid any ambiguity and neatly handle problematic cases, we set integrals of polynomials of momenta (without external scale) to zero in the framework of dimensional regularisation (as conjectured in Ref. [320]),

$$\int \frac{\mathrm{d}^d q}{(2\pi)^d} \, (q^2)^n = 0 \qquad \forall n \in \mathbb{R} \,. \tag{4.1.13}$$

This is supported by, for example, Refs. [321–323].

Renormalisation. By including quantum corrections in the form of loop-diagrams, it almost seems as if we obtained infinite contributions to amplitudes and cross sections. Evidently, this is at odds with reality. In other words, physically meaningful quantities like the masses or couplings we obtain from experiments, are finite, even though they contain all quantum corrections, i.e. loop corrections to all orders of perturbation theory. We therefore need to modify our description such that singularities are removed and finite amplitudes and cross sections are predicted. In practice this means that, after extracting the divergent contributions from the diagrams, we simply subtract them. The latter is referred to as *renormalisation* and is realised by introducing so-called *counter terms* to the Lagrangian. These counter-terms give rise to additional "counter" diagrams that cancel divergences emerging from ordinary diagrams of the respective theory. Note that we have already resolved the computability of the divergent loop-integrals and separated finite from infinite contributions using regularisation. To avoid confusion, we refer to the finite quantities as "renormalised", denoted by the subscript "R", whereas we call the yet unrenormalised quantities "bare" fields or parameters, for which we use the label "B". In order to illustrate how to remove the divergences and to discuss the physical implications of including quantum corrections, we continue the discussion by means of the ϕ^4-theory. Starting from the "bare" Lagrangian in Eq. (4.1.2), which coincides with the classical Lagrangian, we replace the bare quantities according to:

$$\phi_\mathrm{B} = Z_\phi^{1/2} \phi_\mathrm{R} \,, \quad m_\mathrm{B}^2 = Z_\phi^{-1} (m_\mathrm{R}^2 + \delta m^2) \,, \quad \text{and} \quad \lambda_\mathrm{B} = Z_\phi^{-2} \mu^\epsilon Z_\lambda \lambda_\mathrm{R} \,. \tag{4.1.14}$$

We furthermore split $Z_i = 1 + \delta Z_i$ and arrive at

$$\begin{aligned} \mathcal{L} &= \frac{1}{2} (\partial_\rho \phi_\mathrm{B})(\partial^\rho \phi_\mathrm{B}) - \frac{1}{2} m_\mathrm{B}^2 \phi_\mathrm{B}^2 - \frac{\lambda_\mathrm{B}}{4!} \phi_\mathrm{B}^4 \\ &= \frac{1}{2} (\partial_\rho \phi_\mathrm{R})(\partial^\rho \phi_\mathrm{R}) - \frac{1}{2} m_\mathrm{R}^2 \phi_\mathrm{R}^2 - \frac{\mu^\epsilon \lambda_\mathrm{R}}{4!} \phi_\mathrm{R}^4 \\ &\quad + \underbrace{\frac{\delta Z_\phi}{2} (\partial_\rho \phi_\mathrm{R})(\partial^\rho \phi_\mathrm{R}) - \frac{1}{2} \delta m^2 \phi_\mathrm{R}^2 - \frac{\mu^\epsilon \lambda_\mathrm{R} \delta Z_\lambda}{4!} \phi_\mathrm{R}^4}_{= \mathcal{L}_\mathrm{ct}} \,, \end{aligned} \tag{4.1.15}$$

which looks like the original Lagrangian extended by the counter-terms, also of the same form but with different factors, in $\mathcal{L}_{\rm ct}$. From the latter, we obtain "counter" diagrams, which translate into the following Feynman rules:

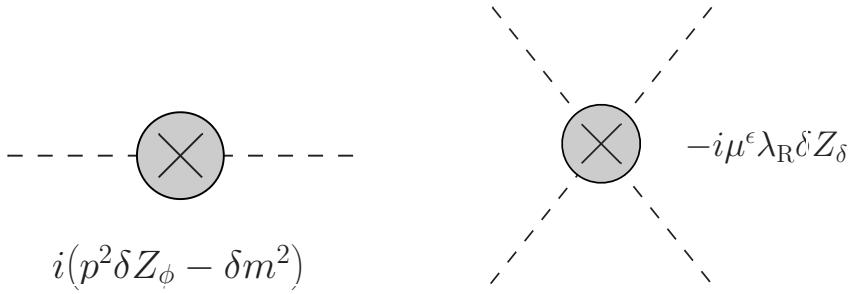

We then specify the coefficients of the counter-terms such that they cancel all divergences at a given order in perturbation theory. At one-loop level, we find:

$$\begin{aligned} \delta m^2 &= \frac{\lambda_{\rm R}}{16\pi^2} m_{\rm R}^2 \left(\frac{1}{\epsilon} + c_m \right) m_{\rm R}^2 \,, \\ \delta Z_{\phi} &= 0 \,, \\ \delta Z_{\lambda} &= \frac{3\lambda_{\rm R}}{16\pi^2} \left(\frac{1}{\epsilon} + c_{\lambda} \right) , \end{aligned} \tag{4.1.16}$$

from the divergent parts of the self-energy in Eq. (4.1.10) and the four-point vertex-function in Eq. (4.1.11). The fact that $c_{m,\,\lambda}$ are arbitrary reflects the freedom in choosing the finite contributions to the counter-terms. Hence, in $d = 4$ dimensions, the renormalised self-energy is given by:

$$\begin{aligned} -i\Sigma_{\rm R}^{(1)} &= \lim_{\epsilon\to 0} \Big[-i\Sigma_d^{(1)} + i(p^2\delta Z_{\phi} - \delta m^2) \Big] \\ &= i\frac{\lambda_{\rm R}}{32\pi^2} m_{\rm R}^2 \left(-2c_m + 1 - \gamma_E + \ln\left[4\pi\right] + \ln\left[\frac{\mu^2}{m_{\rm R}^2}\right] \right) , \end{aligned} \tag{4.1.17}$$

and the renormalised four-point vertex-function by:

$$\begin{aligned} -i\Gamma^{(4)}_{{\rm R},\,1-{\rm loop}} &= \lim_{\epsilon\to 0} \Big[-i\Gamma^{(4)}_{d,\,1-{\rm loop}} - i\mu^{\epsilon}\lambda_{\rm R}\delta Z_{\lambda} \Big] \\ &= i\frac{3\lambda_{\rm R}^2}{32\pi^2} \left(-2c_{\lambda} - \gamma_E + \frac{1}{3} F(m_{\rm R},\, \mu,\, \{p_i\}) \right) . \end{aligned} \tag{4.1.18}$$

Note that, for ϕ^4-theory, $\Sigma_d^{(1)}$ is independent of p^2 by chance, resulting in $\delta Z_{\phi} = 0$; $\delta Z_{\phi} \neq 0$ only arises at two-loop level.[6] Choosing the parameters

[6] The self-energy at two-loop level arises from including its one-particle-irreducible (OPI) contributions at two-loop. It is not enough, however, to only string together two one-loop-level OPI contributions.

δm^2, δZ_ϕ, and δZ_λ in compliance with Eq. (4.1.16), the renormalised theory generated from the Lagrangian in Eq. (4.1.15) is completely finite at one-loop level. That is to say, every physical, observable quantity computed based on Eq. (4.1.15) has finite predictions at one-loop.
Apparently, there is an ambiguity when it comes to the choice of the counter-term factors in Eq. (4.1.16), which manifests in the arbitrary but finite constants c_m and c_λ. This ambiguity is directly linked to the question of how to assign finite loop-contributions to the renormalised Lagrangian and the counter-terms. Thus, by making a choice for specific constants c_m and c_λ, we can define a unique *renormalisation scheme*. Each renormalisation scheme can also be obtained by imposing *renormalisation conditions*. Note that the relation between renormalised (and thus scheme-dependent) quantities and measured (and therefore renormalisation-invariant) quantities differs for each renormalisation scheme.
A conventional choice of renormalisation scheme is the so-called on-shell (OS) scheme, which aims at predicting measurable quantities. We obtain this scheme from the following two conditions. First, we require the renormalised mass m_R to be the physical, measured mass. In terms of renormalisation conditions, this correlates with

$$\begin{aligned}&\Gamma^{(2)}_\mathrm{R}\Big|_{p^2=m^2_\mathrm{R}} = p^2\Big|_{p^2=m^2_\mathrm{R}} - m^2_\mathrm{R} - \Big(\Sigma^{(1)}_\mathrm{R} + \cdots + \Sigma^{(\ell)}_\mathrm{R}\Big)(p^2 = m^2_\mathrm{R}, m^2_\mathrm{R}, \mu) = 0\\ &\Leftrightarrow\ \Sigma^{(1)}_\mathrm{R}(p^2 = m^2_\mathrm{R}, m^2_\mathrm{R}, \mu) + \cdots + \Sigma^{(\ell)}_\mathrm{R}(p^2 = m^2_\mathrm{R}, m^2_\mathrm{R}, \mu) = 0 \quad \forall \ell\,,\end{aligned} \tag{4.1.19}$$

for the two-point vertex-function, which is given by the inverse of the propagator, at ℓ-loop level. Or, in other words, this condition ensures that the propagator has its pole[7] at $p^2 = m^2_\mathrm{R}$. Here, $\Sigma^{(\ell)}_\mathrm{R}$ denotes the self-energy contributions based on the OPI diagrams at ℓ-loop level, which means that the renormalisation conditions must be fulfilled to a given order in perturbation theory.
In order to comprehend how to properly relate $\Gamma^{(2)}_\mathrm{R}$ to the renormalised propagator $S_\mathrm{R}(p^2)$, we decompose the "full" propagator[8] of ϕ_R into its OPI contributions at one-loop level:

[7] We also set the pole's residue to one.

[8] Note that, for a genuinely complete propagator, one needs to include all loop contributions; not only string together the one-loop-level OPI contributions.

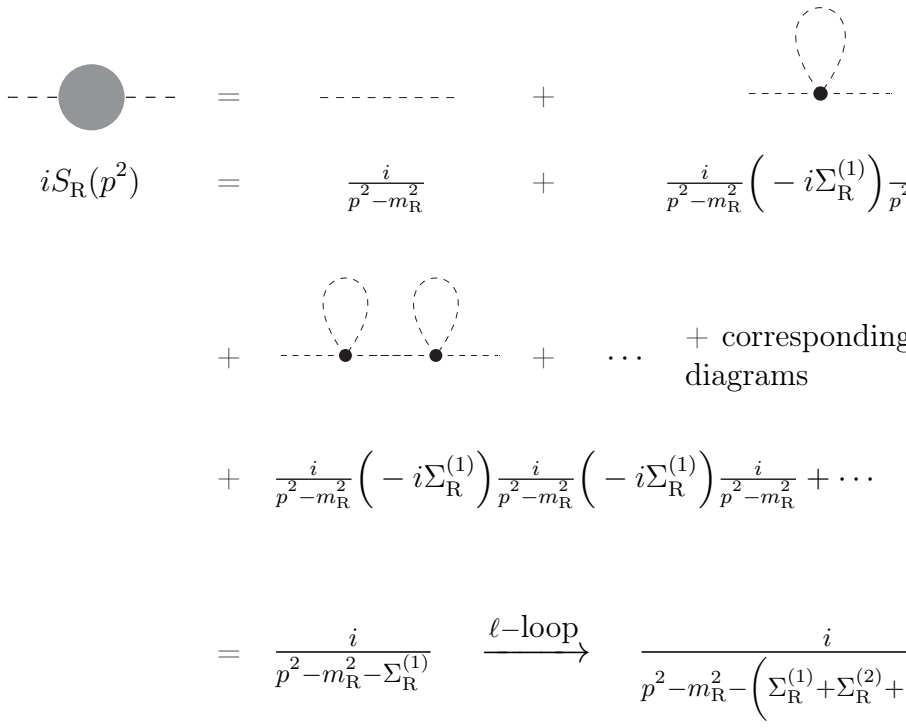

Now that we have justified the form in which we state the first renormalisation condition of the OS scheme in Eq. (4.1.19), we turn to the second condition. The second OS renormalisation condition demands that the renormalised coupling λ_{R} matches the physical coupling constant for vanishing momenta. This corresponds to the following condition on the four-point vertex-function:

$$\begin{aligned} -i\Gamma_{\mathrm{R}}^{(4)}(\{p_i=0\}) = -i\lambda_{\mathrm{R}} - i\Big(\Gamma_{\mathrm{R},\,1-\mathrm{loop}}^{(4)} + \cdots + \Gamma_{\mathrm{R},\,\ell-\mathrm{loop}}^{(4)}\Big)(\{p_i=0\}) \stackrel{!}{=} -i\lambda_{\mathrm{R}} \\ \Leftrightarrow\ \Gamma_{\mathrm{R},\,1-\mathrm{loop}}^{(4)}(\{p_i=0\}) + \cdots + \Gamma_{\mathrm{R},\,\ell-\mathrm{loop}}^{(4)}(\{p_i=0\}) = 0\,, \end{aligned} \tag{4.1.20}$$

to a given order in perturbation theory. Here, $\{p_i\}$ refer to the four external momenta. From the OS renormalisation conditions in Eqs. (4.1.19) and (4.1.20), in combination with the renormalised one-loop corrections displayed in Eqs. (4.1.17) and (4.1.18), we can extract the finite constants that define the OS renormalisation scheme at one-loop level:

$$c_m^{\mathrm{OS}} = \frac{1}{2}\Big(1-\gamma_E+\ln[4\pi]\Big) \quad \text{and} \quad c_\lambda^{\mathrm{OS}} = \frac{1}{2}\Big(-\gamma_E+\ln[4\pi]\Big)\,. \tag{4.1.21}$$

Here, we have used the freedom to choose the arbitrary scale $\mu = m_{\mathrm{R}}$, where we determine the renormalised parameters from experiment. Bear in mind that the scale μ was fixed in addition to specifying the renormalisation scheme, which will play an essential role for the renormalisation group discussion later on.

Next, we want to introduce yet another renormalisation scheme, called the Minimal Subtraction (MS) scheme, which is among the most common schemes. The MS scheme takes an alternative approach to renormalisation, and solely removes the infinities themselves. As a consequence, the constants defining MS vanish:

$$c_m^{\mathrm{MS}} = 0 \quad \text{and} \quad c_\lambda^{\mathrm{MS}} = 0\,. \tag{4.1.22}$$

The MS scheme is a rather natural choice considering that, using dimensional regularisation, the isolated divergences are omnipresent. In the MS scheme, the renormalised propagator assumes a form for which the pole of the propagator does not occur at $p^2 = m_{\mathrm{R}}^2$ anymore, which means that the renormalised mass cannot be identified with the physical mass m_{pole}. Note that, however, the physical mass can be calculated in terms of m_{R} by means of $\Gamma_{\mathrm{R}}^{(2)}|_{p^2=m_{\mathrm{pole}}^2} = 0$. One can proceed analogously for the renormalised versus the physical coupling. By slightly modifying the MS scheme, we obtain the maybe most widely used renormalisation scheme in QFT altogether. This so-called $\overline{\mathrm{MS}}$ scheme absorbs a universal constant, which always arises alongside the divergence in dimensional regularisation, in addition to the divergences. Changing from the MS to the $\overline{\mathrm{MS}}$ scheme corresponds to rescaling $\mu \to \mathrm{e}^{\gamma_E}/(4\pi)\mu$. As a result, the $\overline{\mathrm{MS}}$ scheme is specified by:

$$c_m^{\overline{\mathrm{MS}}} = \frac{1}{2}\Big(1 - \gamma_E + \ln\left[4\pi\right]\Big) \quad \text{and} \quad c_\lambda^{\overline{\mathrm{MS}}} = \frac{1}{2}\Big(-\gamma_E + \ln\left[4\pi\right]\Big)\,. \tag{4.1.23}$$

Note that, due to the absence of p^2-dependent terms in the self-energy at one-loop level, the OS and the $\overline{\mathrm{MS}}$ scheme coincide for ϕ^4-theory.
In general, all MS-like renormalisation schemes take the form

$$\delta Z_i = \sum_{k=1}^{\infty} \frac{\delta Z_{i,k}(\lambda_{\mathrm{R}},\, m_{\mathrm{R}}, \mu)}{\tilde{\epsilon}^k} \quad \text{and} \quad \delta m^2 = \sum_{k=1}^{\infty} \frac{\delta m_k^2(\lambda_{\mathrm{R}},\, m_{\mathrm{R}}, \mu)}{\tilde{\epsilon}^k}\,, \tag{4.1.24}$$

where $\delta Z_{i,k}(\lambda_{\mathrm{R}},\, m_{\mathrm{R}}, \mu)$ and $\delta m_k^2(\lambda_{\mathrm{R}},\, m_{\mathrm{R}}, \mu)$ are independent of $\tilde{\epsilon}$ but may depend on the scale μ. Furthermore, $\tilde{\epsilon}$ is dimensionless and $\tilde{\epsilon} \xrightarrow{d\to 4} 0$.

Remark: The goal of a theory is to make predictions for experiments. Based on the discussion above, we now have the tools at hand to do just that. We start by picking a renormalisation scheme. Then we compute as many physical quantities $\sigma_i^{(\mathrm{calc})}$ as there are renormalised parameters, based on the very same ones. At the same time, we also measure $\sigma_i^{(\mathrm{exp})}$. By setting all $\sigma_i^{(\mathrm{calc})} = \sigma_i^{(\mathrm{exp})}$, we can solve for the renormalised parameters and obtain explicit values for this specific configuration (i.e. the scheme and energy scale considered). Based on these "measured" renormalised parameters, we can now predict other processes up to the same accuracy. Note that the adjustment of the theory, i.e. the determination of the parameters' values, takes places at the level of observables.

Renormalisability. A theory is called (perturbatively) *renormalisable* in case all divergences (at a given loop-order) can be eliminated by redefining a *finite* number of parameters of the theory, which in turn generates the counter-terms required. As a result, introducing counter-terms (which remove the divergences) leaves the form of the Lagrangian invariant and merely modifies the parameters. In other words, $\mathcal{L}_{\mathrm{B}}$, $\mathcal{L}_{\mathrm{R}}$, and $\mathcal{L}_{\mathrm{ct}}$ share the same form, and they only differ in terms of their factors. This means that, for a renormalisable theory, we can always absorb the counter-terms into multiplicative factors, the so-called Z-factors. Our example of ϕ^4-theory is renormalisable with the following Z-factors:

$$\begin{aligned}
\phi_{\mathrm{B}} =& Z_\phi^{1/2}\phi_{\mathrm{R}}\,, \\
m_{\mathrm{B}}^2 =& Z_m m_{\mathrm{R}}^2 \quad \text{with} \quad Z_m = Z_\phi^{-1}\Big(\frac{m_{\mathrm{R}}^2+\delta m^2}{m_{\mathrm{R}}^2}\Big)\,, \\
\lambda_{\mathrm{B}} =& \tilde{Z}_\lambda \mu^\epsilon \lambda_{\mathrm{R}} \quad \text{with} \quad \tilde{Z}_\lambda = Z_\phi^{-2} Z_\lambda\,.
\end{aligned} \tag{4.1.25}$$

By counting the degrees of divergence, it can be shown that the necessary requirements for a renormalisable theory can be expressed in terms of conditions on the mass dimensions of the coupling constants [223, 324]. The latter yield the following classification:

$$\begin{aligned}
\dim[\lambda] > 0 \quad &\Leftrightarrow \quad \text{super-renormalisable}\,, \\
\dim[\lambda] = 0 \quad &\Leftrightarrow \quad \text{renormalisable}\,, \\
\text{and } \dim[\lambda] < 0 \quad &\Leftrightarrow \quad \text{non-renormalisable}\,.
\end{aligned} \tag{4.1.26}$$

Note that, in a super-renormalisable theory, the degree of divergence decreases with higher orders in perturbation theory. Therefore, going to higher orders, there will be a point where all diagrams are already finite. For a renormalisable theory, the degree of divergence does not increase with the order in perturbation theory. As a consequence, we need to extend the counter-terms order by order in perturbation theory. However, for non-renormalisable theories, the degree of divergences grows with perturbation theory, which implies that we would need an infinite number of counter-terms. Within the framework of effective field theories (EFTs) we encounter such non-renormalisable terms on a regular basis. For more information on renormalisability including comprehensive proofs, see e.g. Refs. [325–327].

Renormalisation Group Equations. In general, the renormalised quantities are nothing but mathematical parameters, which can be modified by arbitrarily changing the renormalisation scheme, i.e. the constants c_i, as long as the infinities are subtracted appropriately. Furthermore, even after specifying a renormalisation scheme, both the renormalised field $\phi_{\mathrm{R}}(\mu)$ and the renormalised parameters, mass $m_{\mathrm{R}}(\mu)$ and coupling $\lambda_{\mathrm{R}}(\mu)$, usually still depend on the renormalisation scale μ. So do the predicted n-point vertex-functions $\Gamma_{\mathrm{R}}^{(n)}(\{p_i\},\, \lambda_{\mathrm{R}},\, m_{\mathrm{R}},\, c_i,\, \mu)$, and consequently the predicted amplitudes. This

means that, in addition to fixing the renormalisation scheme, we must specify the *renormalisation point* μ_0 when relating the renormalised to experimentally determined parameters. Nevertheless, how we fix μ_0 is a priori entirely arbitrary, and we might vary it, too. Yet, physics must be independent of an arbitrary scale μ and directly measurable quantities are always renormalisation-invariant. Therefore, any change in μ has to be compensated by simultaneous changes in the renormalised parameters. To ensure that physical quantities remain invariant under μ, we make use of so-called *renormalisation group equations* (RGEs), which are differential equations used to describe how changing μ induces modifications in, e.g., m_R and λ_R. We want to briefly illustrate how to derive the said RGE in the following.
We start by relating the renormalised n-point vertex-function to its bare counterpart:[9]

$$\Gamma^{(n)}_\mathrm{B}(\{p_i\},\, \lambda_\mathrm{B},\, m_\mathrm{B},\, \epsilon) = Z_\phi^{-n/2}(\lambda_\mathrm{R},\, m_\mathrm{R},\, c_i,\, \mu,\, \epsilon)\, \Gamma^{(n)}_\mathrm{R}(\{p_i\},\, \lambda_\mathrm{R},\, m_\mathrm{R},\, c_i,\, \mu)\,. \tag{4.1.27}$$

As the bare function is independent of the renormalisation scale μ, the derivative of $\Gamma^{(n)}_\mathrm{B}$ with respect to μ vanishes. Applying the derivate to Eq. (4.1.27), we obtain the sought RGE:

$$\left(\mu\frac{\partial}{\partial\mu} + \beta(\lambda_\mathrm{R},\, m_\mathrm{R},\, \mu)\frac{\partial}{\partial\lambda_\mathrm{R}} - n\gamma(\lambda_\mathrm{R},\, m_\mathrm{R},\, \mu) + m_\mathrm{R}\gamma_m(\lambda_\mathrm{R},\, m_\mathrm{R},\, \mu)\frac{\partial}{\partial m_\mathrm{R}}\right) \Gamma^{(n)}_\mathrm{R}(\{p_i\},\, \lambda_\mathrm{R},\, m_\mathrm{R},\, \mu) = 0\,, \tag{4.1.28}$$

which is also referred to as Callan-Symanzik Equation [328–330]. Here, we suppress the parameters c_i specifying the renormalisation scheme for brevity. Note that, however, all renormalised quantities can generally be subject to the choice of c_i. Furthermore, we employ

$$\begin{aligned}
\beta(\lambda_\mathrm{R},\, m_\mathrm{R},\, \mu,\, \epsilon) \equiv \mu\frac{\mathrm{d}\lambda_\mathrm{R}}{\mathrm{d}\mu} &\xrightarrow{\epsilon\to 0} \beta(\lambda_\mathrm{R},\, m_\mathrm{R},\, \mu) && \text{denoting the } \beta \text{ function,}\\
\gamma(\lambda_\mathrm{R},\, m_\mathrm{R},\, \mu,\, \epsilon) \equiv \frac{\mu}{2}\frac{\mathrm{d}\ln Z_\phi}{\mathrm{d}\mu} &\xrightarrow{\epsilon\to 0} \gamma(\lambda_\mathrm{R},\, m_\mathrm{R},\, \mu) && \text{the anomalous dimension of the field, and}\\
\gamma_m(\lambda_\mathrm{R},\, m_\mathrm{R},\, \mu,\, \epsilon) \equiv \mu\frac{\mathrm{d}m_\mathrm{R}}{\mathrm{d}\mu} &\xrightarrow{\epsilon\to 0} \gamma_m(\lambda_\mathrm{R},\, m_\mathrm{R},\, \mu) && \text{the anomalous mass dimension,}
\end{aligned} \tag{4.1.29}$$

which describe the change of the coupling, the field renormalisation, and the mass with the renormalisation scale μ, respectively. Note that, in case we explore a theory involving more fields and interactions, the RGE needs to be enlarged by corresponding expressions for each field, mass or coupling. This

[9] See Eq. (4.1.1).

can lead to rather elaborate systems of coupled differential equations, which often cannot be solved analytically and therefore require numerical treatment.[10] The solution of Eq. (4.1.28) has the property [317]:

$$\begin{aligned}\Gamma_{\mathrm{R}}^{(n)}(\{p_i\},\,\lambda_{\mathrm{R}},\,m_{\mathrm{R}},\,\mu_0) =& \Gamma_{\mathrm{R}}^{(n)}(\{p_i\},\,\overline{\lambda_{\mathrm{R}}}(t),\,\overline{m_{\mathrm{R}}}(t),\,\mathrm{e}^t\mu_0) \\ & \times \exp\Big[-n\int_0^t \mathrm{d}\tau\,\gamma(\overline{\lambda_{\mathrm{R}}}(\tau),\,\overline{m_{\mathrm{R}}}(\tau),\,\tau)\Big]\,,\end{aligned} \tag{4.1.30}$$

where $t \equiv \ln[\mu/\mu_0]$. Plus, $\overline{\lambda_{\mathrm{R}}}(t)$ and $\overline{m_{\mathrm{R}}}(t)$ are the solutions to

$$\frac{\partial\overline{\lambda_{\mathrm{R}}}(t)}{\partial t} = \beta(\overline{\lambda_{\mathrm{R}}}(t),\,\overline{m_{\mathrm{R}}}(t),\,t) \quad \text{and} \quad \frac{\partial\overline{m_{\mathrm{R}}}(t)}{\partial t} = \overline{m_{\mathrm{R}}}(t)\gamma_m(\overline{\lambda_{\mathrm{R}}}(t),\,\overline{m_{\mathrm{R}}}(t),\,t)\,, \tag{4.1.31}$$

with boundary conditions $\overline{\lambda_{\mathrm{R}}}(\lambda_{\mathrm{R}}, m_{\mathrm{R}},\, t=0) = \lambda_{\mathrm{R}}$ and $\overline{m_{\mathrm{R}}}(\lambda_{\mathrm{R}}, m_{\mathrm{R}},\, t=0) = m_{\mathrm{R}}$. So, another way to interpret Eqs. (4.1.28) and (4.1.30) is by considering what they reveal regarding the connection between different renormalisation schemes. To that end, recall that changing the renormalisation scheme is equivalent to re-distributing the finite contributions between counter-term and renormalised Lagrangian. This results in distinct renormalisation-scheme-dependent parameters and fields. Say, we have a scheme R and another yet unidentified scheme R′. Then, Eq. (4.1.30) describes the relation between scheme R on the left-hand side and scheme R′ on the right-hand side. This means that using scheme R at renormalisation point μ_0 is equivalent to using some scheme R′ at $\mu = \mathrm{e}^t\mu_0$, identified by its renormalised quantities $\lambda_{\mathrm{R}'} = \overline{\lambda_{\mathrm{R}}}(t)$, $m_{\mathrm{R}'} = \overline{m_{\mathrm{R}}}(t)$ and a field renormalisation $Z_{\phi,\,R'}$ stemming from $Z_{\phi,\,R}$ modified by the exponential function on the right-hand side. Looking at it the other way around, a shift between renormalisation schemes can be compensated by altering the renormalisation scale μ accordingly.
Next, we take a closer look at how the coupling evolves with the renormalisation scale. We consider a theory for which the relation between the bare and the renormalised coupling can be put in the form:

$$\lambda_{\mathrm{B}} = \mu^{D_\lambda\epsilon} Z_\lambda \lambda_{\mathrm{R}}\,, \tag{4.1.32}$$

with D_λ being the additional mass dimensionality that the coupling acquires in $d = 4-\epsilon$ dimensions. This corresponds to renaming $\tilde{Z}_\lambda \to Z_\lambda$ in Eq. (4.1.25), which means that λ is renormalised multiplicatively. Furthermore, we choose to use an MS-like renormalisation scheme, so that

$$Z_\lambda = 1 + \sum_{k=1}^{\infty} \frac{\delta Z_{\lambda,\,k}}{\epsilon^k} = 1 + \delta Z_\lambda\,. \tag{4.1.33}$$

Note that MS-like schemes are also referred to as mass-independent schemes, i.e. the subtraction of UV-poles through e.g. δZ_λ is not connected to a specific

[10] For more involved RGE systems, one generally employs numerical solvers, like the *Mathematica* package `REAP` [331].

scale. As a consequence, δZ_λ solely depends on λ_R and ϵ. The dependence on the renormalisation scale μ is implicit and enters via $\lambda_\mathrm{R}(\mu)$. Since the bare coupling is independent of μ, it is $\mathrm{d}\lambda_\mathrm{B}/\mathrm{d}\mu = 0$. Taking into account that $\delta Z_{\lambda,\,k}(\lambda_\mathrm{R}(\mu))$, we apply the derivative to Eq. (4.1.32) and obtain:

$$\beta(\lambda_\mathrm{R},\,\mu,\epsilon)\left(Z_\lambda + \lambda_\mathrm{R}\frac{\partial\delta Z_\lambda}{\partial\lambda_\mathrm{R}}\right) + \lambda_\mathrm{R} D_\lambda \epsilon Z_\lambda = 0\,. \tag{4.1.34}$$

As $\beta(\lambda_\mathrm{R},\,\mu,\epsilon)$ is finite in the limit $\epsilon \to 0$, we write β as polynomial in ϵ with zeroth order coefficient $\beta(\lambda_\mathrm{R})$ as given in Eq. (4.1.29). Entering the polynomial version of the β function as well as the Z-factor ansatz for MS-like schemes in Eq. (4.1.33) into Eq. (4.1.34), we can compare coefficients, and extract

$$\beta(\lambda_\mathrm{R}) = D_\lambda \lambda_\mathrm{R}^2 \frac{\partial\delta Z_{\lambda,\,1}}{\delta\lambda_\mathrm{R}} \quad \xrightarrow{\phi^4\text{-theory at 1-loop}} \quad \frac{3}{16\pi^2}\lambda_\mathrm{R}^2 \tag{4.1.35}$$

in $d = 4$ dimensions.[11] Now that we have determined the β function, we want to use it to derive the running of the coupling. We start by separating the variables:

$$\beta(\lambda_\mathrm{R}) = \mu\frac{\mathrm{d}\lambda_\mathrm{R}}{\mathrm{d}\mu} \quad \Leftrightarrow \quad \frac{\mathrm{d}\mu}{\mu} = \frac{\mathrm{d}\lambda_\mathrm{R}}{\lambda_\mathrm{R}}\,, \tag{4.1.36}$$

which leads to

$$\ln\left[\frac{\mu}{\mu_0}\right] = \int_{\lambda_\mathrm{R}(\mu_0)}^{\lambda_\mathrm{R}(\mu)} \mathrm{d}\lambda_\mathrm{R}\,\beta^{-1}(\lambda_\mathrm{R})\,. \tag{4.1.37}$$

For small λ_R, we can always assume a power law, i.e. $\beta(\lambda_\mathrm{R}) = b_f \lambda_\mathrm{R}^f$. As a result, the evolution of the renormalised coupling in terms of the renormalisation scale is described by

$$\begin{aligned} \lambda_\mathrm{R}^{f-1}(\mu) &= \frac{\lambda_\mathrm{R}^{f-1}(\mu_0)}{1-(f-1)b_f\lambda_\mathrm{R}^{f-1}(\mu_0)\ln\left[\mu/\mu_0\right]} \\ \xrightarrow{\phi^4\text{-theory at 1-loop}} \quad \lambda_\mathrm{R}(\mu) &= \frac{\lambda_\mathrm{R}(\mu_0)}{1-3/(16\pi^2)\lambda_\mathrm{R}(\mu_0)\ln\left[\mu/\mu_0\right]}\,. \end{aligned} \tag{4.1.38}$$

Note that, however, this equation describes only how the coupling changes with μ. It does *not* state the dependence on the energy scale of the measured process.

Rescaling of External Momenta. RGEs are most commonly used in the context of how rescaling external momenta, i.e. the energy scale of a given process, modifies the n-point vertex-functions and thereby the amplitudes (while

[11] Only in mass-independent renormalisation schemes or for massless theories do β, γ, and γ_m depend solely on the coupling. In general, these functions can also depend on the ratio m_R/μ (see e.g. the OS scheme).

keeping the renormalisation point μ fixed). Before we study this in more detail, we take a look at the concept of *scale invariance*, which is closely related to the running behaviour of renormalised parameters. In general, scale transformations simultaneously scale both the coordinates and the fields of a theory (i.e. the dynamical variables), and the multitude of such scale transformations form an Abelian group. A classical (tree-level), massless Lagrangian in $d = 4$ dimensions is form-invariant under scale changes. This is to say that, for a Lagrangian without dimensionful parameters, the theory is invariant under scale transformations. Consequently, introducing a mass term to the Lagrangian breaks scale invariance explicitly (already at tree-level), which manifests in dependencies of the form p^2/m^2 in the amplitudes. Clearly such terms, and thereby the resultant amplitudes, cannot be invariant if only the dynamical p^2 is scale-transformed while the dimensionful parameters like the mass need to remain the same for the same physical theory. However, even without introducing a mass term, an otherwise scaleless theory acquires a scale by going from the classical to the quantum level. Due to the necessity of regularisation and renormalisation when including quantum effects, we must introduce the dimensionful renomalisation scale μ,[12] which in general leads to an anomalous breaking of scale invariance. In other words, by introducing μ we distinguish a scale at which the theory is renormalised. This contradicts scale invariance. Moreover, introducing the dimensionful scale μ to an otherwise scaleless theory, we can encounter terms like $\ln[p^2/\mu^2]$ in the amplitudes. In a nutshell, scale invariance (in the context of field theories) implies that there is no characteristic length or energy scale, which means that rescaling the energy of an experimental process does not change the interaction strengths of the theory. In turn, breaking scale invariance leads to scale-dependent theories, i.e. the "strength" of the renormalised parameters changes with the energy scale of a given process. In order to describe the response of the *quantum* field theory to scale transformations, we now explore how the n-point vertex-function changes under the rescaling of external momenta.

We can assign a mass dimension to each n-point vertex-function, which depends on n times the mass dimension of the field ϕ, $\dim[\phi] \equiv D_\phi$:

$$\dim[\Gamma_{\mathrm{R}}^{(n)}(\{p_i\})] = 4 - nD_\phi \equiv D_{\Gamma^{(n)}} \,. \tag{4.1.39}$$

Rescaling the external momenta by

$$\{p_i\} \to \{\zeta p_i\} \,, \tag{4.1.40}$$

we can make use of dimensional arguments and put the n-point vertex-function in the form

$$\Gamma_{\mathrm{R}}^{(n)}(\{\zeta p_i\},\, \lambda_{\mathrm{R}}(\mu),\, m_{\mathrm{R}}(\mu),\, \mu) = \mu^{D_{\Gamma^{(n)}}} f\Big(\zeta^2 \frac{p_i \cdot p_j}{\mu^2},\, \frac{m_{\mathrm{R}}}{\mu},\, \lambda_{\mathrm{R}}\Big) \,, \tag{4.1.41}$$

[12] Note that introducing the scale μ in form of a dimensionful coupling is the result of using dimensional regularisation. Other regularisation procedures introduce the new scale by other means. For example, cut-off regularisation introduces the dimensionful cut-off scale Λ.

where f is a dimensionless function. That is to say that $\Gamma_{\mathrm{R}}^{(n)}$ is a homogeneous function of order $D_{\Gamma^{(n)}}$ on the dimensionful variables m_{R}, ζ and μ. As a consequence, due to the properties of homogeneous functions, $\Gamma_{\mathrm{R}}^{(n)}$ needs to satisfy:

$$\left(\zeta\frac{\partial}{\partial\zeta}+m\frac{\partial}{\partial m_{\mathrm{R}}}+\mu\frac{\partial}{\partial\mu}-D_{\Gamma^{(n)}}\right)\Gamma_{\mathrm{R}}^{(n)}(\{\zeta p_i\},\,\lambda_{\mathrm{R}}(\mu),\,m_{\mathrm{R}}(\mu),\,\mu)=0\,. \tag{4.1.42}$$

In combination with the RGE in Eq. (4.1.28), Eq. (4.1.42) leads to

$$\begin{aligned}\Bigg(&-\frac{\partial}{\partial t}+\beta(\lambda_{\mathrm{R}},\,m_{\mathrm{R}},\,\mu)\frac{\partial}{\partial\lambda_{\mathrm{R}}}+(\gamma_m(\lambda_{\mathrm{R}},\,m_{\mathrm{R}},\,\mu)-1)m_{\mathrm{R}}\frac{\partial}{\partial m_{\mathrm{R}}}\\&-n\gamma(\lambda_{\mathrm{R}},\,m_{\mathrm{R}},\,\mu)+D_{\Gamma^{(n)}}\Bigg)\Gamma_{\mathrm{R}}^{(n)}(\{\mathrm{e}^t p_i\},\,\lambda_{\mathrm{R}},\,m_{\mathrm{R}},\,\mu)=0\,,\end{aligned} \tag{4.1.43}$$

where we set $t\equiv\ln\zeta\,(=\ln[\mu/\mu_0])$. The general result to this differential equation reads

$$\begin{aligned}\Gamma_{\mathrm{R}}^{(n)}(\{\mathrm{e}^t p_i\},\,\lambda_{\mathrm{R}},\,m_{\mathrm{R}},\,\mu)=&\exp\left[D_{\Gamma^{(n)}}t-n\int_0^t\mathrm{d}\tau\,\gamma(\overline{\lambda_{\mathrm{R}}}(\tau))\right]\\&\times\Gamma_{\mathrm{R}}^{(n)}(\{p_i\},\,\overline{\lambda_{\mathrm{R}}}(t),\,\overline{\overline{m_{\mathrm{R}}}}(t),\,\mu)\,,\end{aligned} \tag{4.1.44}$$

where $\overline{\overline{m_{\mathrm{R}}}}(t)\equiv\overline{m_{\mathrm{R}}}(t)/\zeta$ and the parameters $\overline{m_{\mathrm{R}}}(t)$ and $\overline{\lambda_{\mathrm{R}}}(t)$ are the solutions to Eqs. (4.1.31), respectively. This exact RGE solution governs the scaling behaviour with the external momenta. Furthermore, it provides us with the origin of the momentum-dependent running of physical quantities. To understand how this comes about, note that Eq. (4.1.44) relates vertex-functions with different values of renormalised parameters and it does so at the same renormalisation point μ. This implies that an amplitude scaled to a different energy scale corresponds to a theory with modified renormalised masses and couplings. Note that these modifications solely stem from changing the external, physical momenta, while keeping both renormalisation scheme and point fixed. Hence, the running behaviour is a physical phenomenon which, though independent of the details of the renormalisation prescription, is a direct consequence of requiring renormalisation in the first place.[13] Moreover, the scaling behaviour of the physical quantities with the typical energy scale of a given process is controlled by the functions β, γ, and γ_m, which is why the corresponding corrections to physical parameters are referred to as RG

[13] To put it another way, recall that we have to correlate the renormalised parameters to measurements at specific momentum configurations, i.e. energy scales, to extract the values, based on which we can predict amplitudes. Due to the breaking of scale invariance, the four-point vertex function $\Gamma_{\mathrm{R}}^{(4)}$ in Eq. (4.1.18), for example, depends on ratios like $p_i\cdot p_j/\mu^2$ and m_{R}^2/μ^2. As a consequence, the value λ_{R} extracted from measurement for a certain choice of momenta generally does not resemble the physical coupling at all other energy scales.

corrections. In case the theory is massless, the RGE simplifies and its solution reveals that the μ-dependence of the coupling λ also describes the scaling behaviour with the energy/momentum scale of the process, i.e. $\lambda_{\mathrm{R}}(\mu \to \sqrt{Q^2})$.

Choosing the renormalisation point μ. In general, one can encounter logarithms of the form $\ln[p^2/\mu^2]$ when computing radiative corrections. Although μ is arbitrary, the logarithmic corrections should not be large in order to comply with perturbation theory. By choosing the renormalisation scale $\mu \sim E$, where E is the typical energy scale of the process,[14] we can naturally prevent potentially large (unphysical) corrections. Hence, we will from now on identify μ with the energy scale under consideration (in particular throughout chapter 6).

In conclusion, the parameters of a theory change with the typical energy scale of the process under consideration when including quantum effects. Incorporating RG effects is particularly important in order to consistently describe New Physics theories, which often comprise several orders of magnitude. Take, for example, the Littlest Seesaw model analysed in chapter 6, which is defined at the scale of some grand unified theory, $\mathcal{O}(10^{16}$ GeV). Since the scales accessible to experiment, $\mathcal{O}(10^2 - 10^3$ GeV), are orders of magnitude below, we must include RG corrections to adequately derive the physical parameters measured. In principle, we can describe the evolution of physical parameters for a specific model straightforwardly once we have solved the corresponding set of RGEs. However, we have not considered so far what happens in case we fall below the mass of a particle when running down the energy scale. Since, by crossing below this so-called *threshold*, the number of particles that can be produced on-shell changes, there is a need for a modified theory description below the threshold. We will discuss how to consistently describe the running across thresholds by means of effective field theories in the next section.

4.2 Effective Field Theories

In physics, it is a well-established procedure to describe Nature in limiting cases by means of simplified theories. These so-called *effective theories* are good approximations to the real world (for the respective limit) and generally offer considerable simplifications in practical calculations. Note that we can make use of an effective theory regardless of whether the full theory is known, or not. Take Newtonian mechanics for example, which we use to describe among other things engineering mechanics. Although we do have special or even general relativity at our disposal, employing classical mechanics in the limit of non-relativistic velocities is a perfectly good approximation and leads to sig-

[14] The "typical" energy of a process can e.g. refer to its centre-of-mass energy for a scattering process.

nificantly simplified computations. And even long before relativistic mechanics was known, classical mechanics was used and provided reliable predictions.
Within the framework of QFT, effective theories – referred to as *effective field theories* (EFTs) – are an important tool, mostly used to describe multiscale problems such as the decoupling of high-energy degrees of freedom. For the latter, the perhaps best-known example is the Fermi theory of weak interactions, i.e. the low-energy EFT, which describes processes mediated by W-bosons at energies well below the bosons' mass. As there are many applications for EFTs, also throughout this thesis, this section is dedicated to the introduction of EFTs, based on Refs. [332–334].

EFTs arise naturally when considering multiscale problems. Say we have a scenario which is characterised by two scales: a large scale M and a much smaller scale E, each of which can, e.g., be a mass, an energy, or a momentum transfer. The EFT description will then be employed when describing the physics at the low scale $\mathcal{O}(E)$ while incorporating effects from the high scale $\mathcal{O}(M)$, resulting in physical quantities which can be approximated by series in $E/M \ll 1$, truncated at intended accuracy.
To illustrate how we arrive at the low-scale EFT, we consider the simplified example of having a full theory made up of quantum fields ϕ. Next, we introduce a cutoff scale Λ, which separates the low from the high scale: $E \ll \Lambda < M$. The cutoff scale is used to divide the fields into low- and high-frequency modes, such that $\phi = \phi_l + \phi_h$. Here, $\phi_{l/h}$ includes the modes with frequency ω lower/higher than the cutoff, respectively. In general, all observable physics quantities, such as decay rates or cross sections as well as the Feynman rules leading to them, can be derived from the so-called *generating functional* within the path integral formalism.[15] For our example theory, the generating functional takes the form:

$$\mathcal{Z}[J_l] = \int \mathcal{D}\phi_l \, \mathcal{D}\phi_h \, \mathrm{e}^{i\mathcal{S}(\phi_l,\, \phi_h) + i \int \mathrm{d}^d x J_l(x) \phi_l(x)} \,, \tag{4.2.1}$$

where J_l denotes the sources of the low-frequency mode fields. Note that, as we only care for low-energy physics, we omit the sources of the high-energy mode fields. Furthermore, the action is given by means of the full theory Lagrangian:

$$\mathcal{S}(\phi_l,\, \phi_h) = \int \mathrm{d}^d x \, \mathcal{L}_{\text{full}}(\phi_l(x),\, \phi_h(x)) \,. \tag{4.2.2}$$

We still aim at describing physics at the low scale E. For this purpose, we do not have to know the theory above the cutoff scale Λ, because the corresponding degrees of freedom cannot be produced on-shell. We can therefore further

[15] Note that the n-point correlation functions, i.e. the Green's functions of the theory, are obtained from the functional derivative of this type of generating functional with respect to the sources. In contrast, the n-point vertex-functions, i.e. the OPI Green's functions employed throughout section 4.1, are related to the effective action as their generating functional.

simplify the generating functional in Eq. (4.2.1) by performing the path integral over ϕ_h. This is referred to as *integrating out* the high-frequency degrees of freedom and results in

$$\mathcal{Z}[J_l] = \int \mathcal{D}\phi_l \, \mathrm{e}^{i\mathcal{S}_\Lambda(\phi_l) + i\int \mathrm{d}^d x J_l(x)\phi_l(x)} \,. \tag{4.2.3}$$

Here, we make use of the so-called Wilsonian action, as defined by

$$\mathrm{e}^{i\mathcal{S}_\Lambda(\phi_l)} = \int \mathcal{D}\phi_h \, \mathrm{e}^{i\mathcal{S}(\phi_l,\phi_h)} \,. \tag{4.2.4}$$

As the choice of cutoff scale is somewhat arbitrary – as long as $E \ll \Lambda < M$ is satisfied – the Wilsonian action depends on Λ. Furthermore, the Wilsonian action describes physics at the low scale *after* having removed the high-frequency modes. As a consequence, it is non-local on distances $\Delta x^\rho \sim 1/\Lambda$. Nevertheless, we can write the non-local action as an expansion in terms of local operators composed of the low-frequency degrees of freedom. This ansatz is referred to as *operator product expansion* (OPE):

$$\mathcal{S}_\Lambda(\phi_l) = \int \mathrm{d}^d x \, \mathcal{L}_{\text{eff}}(x) \,, \quad \text{where} \quad \mathcal{L}_{\text{eff}}(x) = \sum_i C_i \widehat{\mathcal{O}}_i(x) \,. \tag{4.2.5}$$

Within our example model, we employ the *effective Lagrangian* $\mathcal{L}_{\text{eff}}(x) = \mathcal{L}_{\text{eff}}[\phi_l(x)]$ as well as the local (also referred to as *effective*) *operators* $\widehat{\mathcal{O}}_i(x) = \widehat{\mathcal{O}}_i[\phi_l(x)]$. The effective couplings C_i of these operators are called Wilson coefficients. The effective Lagrangian a priori comprises all operators that can be build from the degrees of freedom below the cutoff and which, at the same time, comply with the symmetry requirements of the respective full theory. Therefore, to reproduce the full theory, we would have to include operators to all orders, which results in an infinite series. As our goal is to find a simplified theory which is a good approximation to the full theory at low scales, we only need to reproduce the full theory to a certain accuracy. As suggested above, this will be done by organising the effective Lagrangian in powers of E/M, and truncating the series at the desired accuracy.

The cutoff Λ separates the contributions to, for example, an amplitude into contributions from the "light" (low-scale) degrees of freedom and the "heavy" (high-scale) degrees of freedom. The former appear in form of fields in the effective Lagrangian and describe the long-range contributions from scales below Λ. They can still be produced as external, physical states. The latter, however, are too heavy to be produced on-shell and thus only enter the amplitude through the effective couplings C_i, which approximate the short-range contributions to a given low-scale process. Since the cutoff is, within limits, arbitrary, we can lower or raise it. By doing so, we shift physics contributions from being part of the description above/below the cutoff to begin part of the description below/above the cutoff. In other words, by lowering Λ we simply

integrate out additional high-frequency modes, which means that physics contributions are moved from the effective operators into the Wilson coefficients.[16] Thereby, the structure of the EFT remains the same and cutoff dependence cancels between the short- and long-range contributions. This implies that both Wilson coefficients and effective operators change with the cutoff scale, which implicates some sort of running behaviour.

In practice, the full theory is usually more elaborate such that performing the path integral in order to integrate out high-scale degrees of freedom becomes too difficult. Therefore, instead of employing the path integral formalism, we turn to the so-called *matching procedure*, where we decouple high-scale degrees of freedom by hand. To that end, we need to formulate the EFT by listing all effective operators that are allowed by the symmetries of the full theory (including gauge invariance) and which are made up of the remaining low-scale degrees of freedom. As mentioned above, a priori there are infinitely many effective operators, but we truncate the series based on the precision intended. We then obtain the Wilson coefficients from actually matching the EFT to the full theory via the condition $\mathcal{A}_{\text{eff}} = \mathcal{A}_{\text{full}}$ based on explicit processes (and corresponding energy scales). Each Wilson coefficient only needs to be determined once, as they are process-independent.
The fact that this procedure works is based on the so-called *decoupling theorem*, which states that, in case the mass of a field goes to infinity, the (renormalised) amplitudes that include the said field as external state vanish. This implies what we had already assumed before: "heavy" degrees of freedom with energies/masses much higher than the scale available do not appear as external states but are incorporated into the Wilson coefficients. Although there are numerous applications to the decoupling theorem throughout the literature, see e.g. Refs. [335–344], we will only focus on settings, where the EFT aims at describing low-energy effects of heavy fields. For that reason, we take a closer look at the decoupling of heavy fields,[17] which was first proven in Ref. [335]. Hence, the high scale M corresponds to the mass of the heavy field(s) and the low scale E refers to the energy scale of the experiments under consideration. Well below M, the heavy fields only contribute to an amplitude by means of internal lines in Feynman diagrams. The structure of the propaga-

[16] By lowering the cutoff scale, we should *not* cross the mass threshold of a particle, since this would imply generating new types of effective operators. Although doing so is in principle fine, it does correspond to generating yet another EFT, which is not what we are aiming for with this paragraph.

[17] As stated above, the decoupling theorem holds true even after renormalisation (Appelquist-Carazonne decoupling theorem [325, 335]). Although decoupling is taken care of naturally in some renormalisation schemes such as the OS, this is not necessarily the case. Particularly for mass-independent renormalisation schemes like the MS-like schemes, introduced in section 4.1, we may encounter large logarithms in the regime $p^2 \ll M^2$. Nevertheless, it suffices that there exists a scheme in which decoupling works, since we can change in between schemes as we like. We can avoid any renormalisation-scheme-dependent issues by decoupling the heavy fields *by hand*, to which we resume in the following.

tors in momentum space is given by either $(p^2 - M^2)^{-1}$ for bosonic fields or $(\not{p} - M)^{-1}$ for fermionic fields. As a consequence, the heavy field propagators can be expanded in terms of the ratio "energy of the process over heavy mass", $p^2/M^2 = \mathcal{O}(E^2/M^2)$:

$$\frac{1}{p^2 - M^2} = \frac{-1}{M^2} \sum_{n=0}^{\infty} \left(\frac{p^2}{M^2}\right)^n \quad \text{or} \quad \frac{1}{\not{p} - M} = \frac{\not{p} + M}{p^2 - M^2} = \underbrace{\frac{\not{p} + M}{-M^2}}_{\approx -1/M} \sum_{n=0}^{\infty} \left(\frac{p^2}{M^2}\right)^n . \tag{4.2.6}$$

Subsequently, the Feynman amplitudes, which contain any number of the above heavy propagators, can be matched to the respective effective operators. That way, the effects of the heavy field(s) are "hidden" inside the couplings C_i, and the desired level of accuracy can easily be achieved by truncating the geometric series. The matching procedure is usually performed on the level of Feynman diagrams and matrix elements. Note that this is exactly what we do in section 5.3 upon matching the different models onto the effective Lagrangian in Eq. (5.3.1), or in section 5.2 when mapping the short-range contributions to the effective vertices in Eq. (5.2.28).

In EFTs, we routinely encounter operators with mass dimension greater than four, cf. Eqs. (5.3.1) or (5.2.28). Since the mass dimension of the effective Lagrangian is four, this results in Wilson coefficients of negative mass dimension: $C_i \sim 1/\Lambda^k$, which implies that these interactions are non-renormalisable. Nevertheless, the EFT is only valid at energies below the cutoff and the corresponding UV completing full theory, which applies for energies above Λ, must be renormalisable. Furthermore, note that the effective low-energy description is comprised of both renormalisable remnants of the full theory (e.g. interactions of light fields or their respective kinetic and mass terms) as well as non-renormalisable effective operators (approximately describing the effects from the heavy fields). We therefore rewrite the effective Lagrangian as the sum of renormalisable and non-renormalisable contributions, the latter being given by

$$\mathcal{L}_{\text{non-ren}}(x) = \sum_i \frac{\tilde{C}_i}{\Lambda^{n-4}} \widehat{\mathcal{O}}_i^{(n)}(x) \,. \tag{4.2.7}$$

This implies $C_i = \tilde{C}_i/\Lambda^{n-4}$, where $\tilde{C}_i$ is now a dimensionless coupling and n denotes the mass dimension of the corresponding effective operator, which explicitly displays the suppression of higher-dimensional operators with Λ.[18] We want to emphasise that the non-renormalisable effective operators can be organised in orders of p^2/M^2 [$= \mathcal{O}(E^2/M^2) = \mathcal{O}(E^2/\Lambda^2)$]. In other words, the more orders in p^2/M^2 we include, the more internal heavy propagators we can have in a diagram, and the higher dimensional operators we can generate. Therefore, it is important to consider both the mass dimension of the operator

[18] Recall that only operators with $n \geq 5$ need to be considered at low energies.

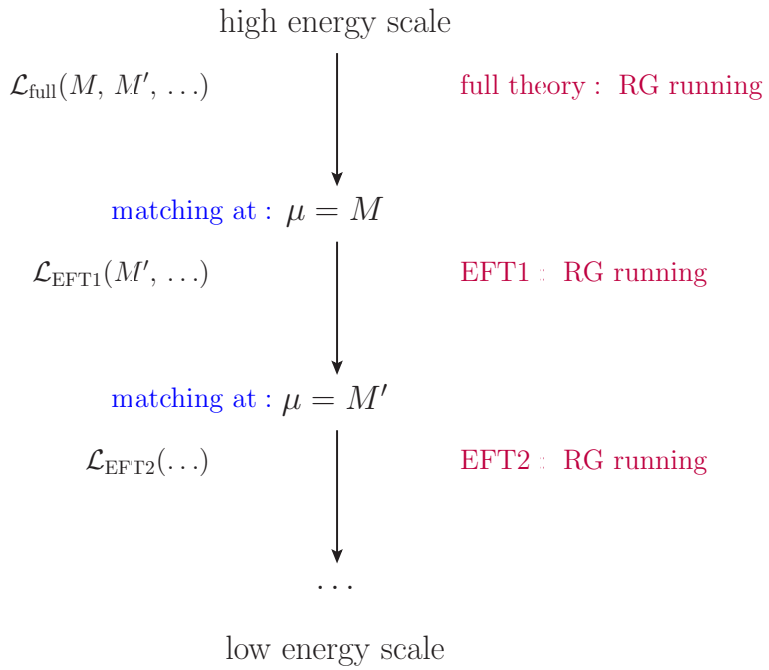

Figure 4.2: Illustration of how to obtain a consistent EFT description at low energies based on the matching procedure [334].

as well as the accuracy per operator in order to consistently truncate the series.

As indicated at the end of section 4.1, EFTs are particularly important when describing the evolution of physical parameters based on RG corrections. Suppose, we have a renormalisable full UV-completing theory, which includes multiple heavy fields far above the energy scale accessible to realistic experiments. We will encounter such settings on a regular basis in the context of neutrino mass models, as discussed in section 3.1. If we want to consistently describe the parameters measured, including quantum effects, we need to combine RG corrections with the use of "different theories at different energy regimes" to account for the change in active degrees of freedom. As this line of action is relevant for the analysis of the Littlest Seesaw model in chapter 6, we want to briefly illustrate how to proceed along the lines of the illustration in Fig. 4.2. In analogy to section 4.1, we start at an energy scale, where all particles of the full theory are kinematically accessible, i.e. they can be produced on-shell. This could be, for example, the energy scale where the full theory is defined. In the energy regime of the full theory, we derive and solve the RGEs. Based on these, we can consistently describe the evolution of the renormalised parameters when running the energy scale down to the mass of the heaviest particle of the theory, M. When crossing below the threshold $\mu = M$, the number of active degrees of freedom, i.e. particles that can be

produced on-shell, changes.[19] The Lagrangian description below M has to reflect that change. Consequently, we "integrate out" the field of mass M and "switch on" effective operators. That way, we derive the corresponding EFT valid in the energy regime below M but above the mass of the next heaviest particle, M'. We refer to this EFT by "EFT1". By equating amplitudes derived from the full theory and EFT1 at the threshold, we can relate the parameters of both theories, resulting in the so-called *matching conditions*, from which we determine the Wilson coefficients of EFT1. Employing a modified theory description calls for a new set of adapted RGEs to adequately describe the RG-induced evolution of parameters within the energy regime described by EFT1.[20] Based on the adapted RGEs, we scale the parameters of EFT1 down to the next threshold at the mass of the second heaviest field, $\mu = M'$. Here, we integrate out the particle of mass M', compute the Wilson coefficients for the resulting EFT2 from the matching conditions at $\mu = M'$ and derive the modified RGEs. By repeating this procedure for every threshold we cross until we reach the energy scale of the experiment, we obtain an appropriate EFT description at the low energy scale. In other words, by means of RGEs, EFTs and the matching procedure, we can consistently describe the evolution of parameters across an arbitrary order of magnitudes, even including thresholds.

EFTs are not only employed to integrate out particles. They can also be useful to describe processes which typically occur at specific energy configurations and/or for which we can describe interactions based on bound systems rather than elementary particles. Well-known examples are non-relativistic EFTs, or the so-called soft-collinear effective theory (SCET) [345–349].[21] Within the context of the conversion of bound muons into electrons, see section 5.2, we will make use of such an effective treatment: starting from the Lagrangian in Eq. (5.2.28), we switch the description from the muon/electron coupling to the nucleus at the quark-level to doing so at the nucleon-level,

[19] Note that, as discussed in section 4.1, we identify the renormalisation scale with the energy scale under consideration in order to avoid large logarithms due to a poorly chosen renormalisation scale μ. Consequently, the evolution from the energy scale of the full theory to lower scales can be interpreted as a running with the renormalisation scale μ. Hence, we perform the matching at each threshold using $\mu = \mathcal{O}(\text{threshold energy})$.

[20] Recall that varying the cutoff scale Λ is connected to reshuffling contributions from the effective operators into the Wilson coefficients and vice versa. As the energy scale under consideration in a sense decides what can be considered as high- or low-scale contributions, we should scale the cutoff together with the said energy scale. That way, logarithmic corrections, due to the RG effects depending on the scale $\mu \simeq \Lambda$, are induced into both Wilson coefficients and effective operators.

[21] Both non-relativistic quantum chromodynamics (NRQCD) [350–352], which has been proven useful to describe hadrons made up of two heavy quarks, and non-relativistic quantum electrodynamics (NRQED) [350,353,354], which describes the interaction of a non-relativistic (composite) spin-1/2 particle with an electromagnetic field, are well-known examples for non-relativistic EFTs. On the other hand, SCET is used to describe highly energetic quarks interacting with either soft, i.e. low energy/momentum, or collinear, i.e. emitted parallel to another particle of the process, gluons.

introducing the so-called nucleon form factors in the process.

In the discussion above as well as in chapters 5 and 6, we have made/will make use of EFT descriptions based on (mostly) known UV completions. Consequently, we determine the effective operators realised by matching them to the parameters of the respective full theory. This approach is called *top-down*. However, as mentioned before, the underlying theory does not have to be known in order to employ EFTs. We can instead construct an EFT from listing all possible non-renormalisable effective operators that 1) respect the symmetries of our low-energy theory, 2) are made up of the fields of the low-energy theory, and 3) need to be included at the intended level of precision. The latter is achieved by organising the effective operators in terms of Λ^{-1}, with Λ being the scale of New Physics, and truncating the series at the desired order. This approach is called *bottom-up*. Bottom-up EFTs can be useful to gain insights into generic features of potential UV completions. For example, the SM is often treated as an EFT[22] and extended by possible effective operators used to describe New Physics effects such as neutrino masses. We also employ such a bottom-up approach in section 3.3 and throughout chapter 5 by using the effective theory of a doubly charged scalar. Using a bottom-up approach, we can consider the type of prediction the realisation of certain effective operators would imply; and thereby study potential UV completions experimentally without specifying the underlying theory. By choosing a bottom-up approach, computations can be significantly simplified, which is actually part of the motivation for the effective theory introduced in section 3.3. Finally, note that, for both the top-down and the bottom-up approach, not all effective operators that are allowed in principle have to be realised in the full theory.

4.3 The Method of Least Squares

The method of least squares is a standard tool for over-determined systems in high-energy data analysis, discussed in standard works covering data analysis and reviewing statistical methods in high-energy physics, see e.g. Refs. [9,356–358]. The method of least squares can be used to identify the level of agreement between the measured data and the predictions of a specific model based on a set of input parameters. That way, one can either assess how valid the model is, or determine the optimal set of input parameters. For the method of least squares, we employ the χ^2 function/ statistic as an estimator. Suppose we have a set of independently measured values μ_i with corresponding variances σ_i^2, and a set of model-dependent input parameters x_i leading to the predicted values of measurement $P_i(x_1, \cdots, x_N)$. To find the best input set, we minimise the sum of the squared errors, i.e. the differences between measured and predicted values, weighted by how precise each measurement is. This sum is the χ^2

[22] See e.g. Ref. [355] for a guide on how to use the SM as EFT.

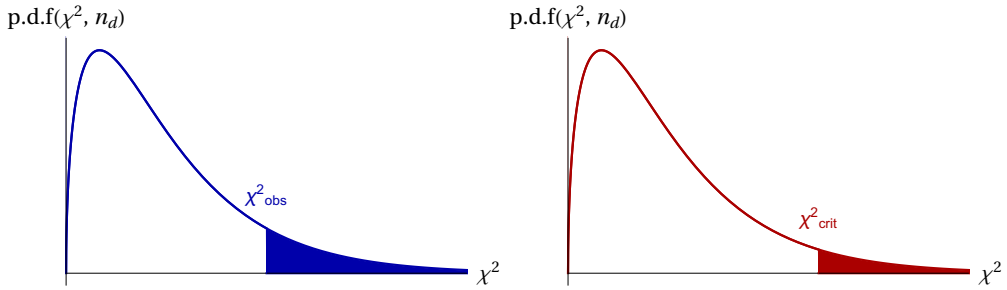

Figure 4.3: Illustrative example of the χ^2 p.d.f for the number of degrees of freedom $n_d = 3$: (*left*) the blue region corresponds to the p-value; (*right*) the red region corresponds to "rejection region" α.

function.
Under the assumption that the μ_i are Gaussian distributed, we can also obtain the χ^2 function from the likelihood function. The likelihood function gives the probability of measuring the set of μ_i under the assumption that the input parameters x_i are true, i.e. it multiplies the probability for each measured value μ_i:

$$c \cdot \prod_i \exp\left[-\frac{(\mu_i - P_i(x_1, \cdots, x_N))^2}{2\sigma_i^2}\right] = c \cdot \exp\left[-\sum_i \frac{(\mu_i - P_i(x_1, \cdots, x_N))^2}{2\sigma_i^2}\right]. \tag{4.3.1}$$

Varying the input parameters, we obtain the optimum set by maximising the likelihood, which is equivalent to minimising twice its negative exponent. The latter coincides with the χ^2 function. Note that the method of least squares is also valid for non-Gaussian distributed μ_i, as long as the measurements are independent. It is, however, no longer equivalent to maximising the likelihood, and will hence yield a result different from a maximum likelihood estimate.

To assess the goodness-of-fit, we start with the hypothesis H_0 that the given model using the optimum input set describes reality well. Imagine we would be able to repeat the "data taking" as often as we wanted. Then, we could determine the χ^2 function's minimum for each data set and the corresponding new optimum input set. From the large number of minimum values $\chi^2(\mu_i, x_i)$, we could deduce the probability density function (p.d.f.) of the statistic χ^2 given the hypothesis is true. In case the estimator is the χ^2 function, the p.d.f. is known to be the χ^2 distribution with expectation value n_d, which is the number of degrees of freedom. The latter is given by the number of measured parameters minus the number of (real) input parameters. As we know the p.d.f. of the estimator, we can derive a criterion on whether or not to reject the hypothesis H_0. Say, we have an experiment that provides a data set with corresponding estimator minimum χ^2_{obs}. We then compute the probability to find a data set equally or less compatible with the predictions of H_0 than our

observed data set (given that the hypothesis is true),

$$p = \text{prob}(\chi^2 \geq \chi^2_{\text{obs}}) = \int_{\chi^2_{\text{obs}}}^{\infty} \text{p.d.f.}(\chi^2,\, n_d)\, \text{d}(\chi^2)\,. \tag{4.3.2}$$

This probability is called the p-value, and it corresponds to the blue region under the p.d.f. curve for estimator values $\chi^2 \geq \chi^2_{\text{obs}}$ on the left-hand side of Fig. 4.3. To test the hypothesis H_0, we decide upon the confidence level (C.L.) at which to reject H_0 before looking at our observed data set. This means, we divide the curve under the p.d.f. into two regions, as illustrated on the right-hand side of Fig. 4.3. In the red region, which corresponds to

$$\alpha = \int_{\chi^2_{\text{crit}}}^{\infty} \text{p.d.f.}(\chi^2,\, n_d)\, \text{d}(\chi^2)\,, \tag{4.3.3}$$

H_0 is rejected at C.L. $(1-\alpha)$. As the p.d.f. is known, we can also infer χ^2_{crit} from α. The resulting criterion on H_0 can be stated as: reject H_0 at C.L. $(1-\alpha)$ if $p < \alpha$ (or, analogously, $\chi^2_{\text{obs}} > \chi^2_{\text{crit}}$). If, on the other hand, $p > \alpha$ (or $\chi^2_{\text{obs}} < \chi^2_{\text{crit}}$), do not reject. Note that not rejecting a hypothesis does *not* mean accepting it.

In chapter 6, we will use the χ^2 function to determine the optimum set of input parameters (m_a, m_b, n, η) for the Littlest Seesaw (LS) model, introduced in section 3.4. The analysis we conduct thereafter is not at the level of hypothesis testing but rather at the level of getting a feel for the suitability of the LS. We therefore do not perform a complete goodness-of-fit hypothesis testing, but instead use a well-established common rule of thumb as measure for the goodness-of-fit.[23] Since the mean of the χ^2 p.d.f. matches n_d, we expect the minimum of the estimator to be $\chi^2 \approx n_d$ for a good fit (given the variances are properly determined) and a large number of measured parameters.[24] Consequently, we will use the estimator to preliminarily assess the goodness-of-fit and sift out tendencies in the LS. We review the necessary definitions and data for that specific case hereafter. The discussion is based on section 4 in Ref. [5], and parts thereof are taken par for par.

Since we can fix $n = 3$ and $\eta = \pm 2\pi/3$ (see section 3.4), there are only two free real parameters remaining to predict the entire neutrino sector in practice. In order to find the best-fit input parameters m_a and m_b while keeping $\eta = \pm 2\pi/3$ and $n = 3$ fixed, we perform a global fit using the χ^2 function [43],

$$\chi^2 = \sum_{i=1}^{N} \left(\frac{P_i(x) - \mu_i}{\sigma_i} \right)^2 . \tag{4.3.4}$$

[23] We will, however, refer to the rule of thumb as being a measure for the goodness-of-fit throughout this thesis.

[24] Another way to motivate this approach is the following: on average, the measured parameters will differ from their true value by the standard deviation. This means that, for a large number of measured parameters N, the statistical variations compensate and we would expect $\chi^2 \approx N$. However, the input parameters are additional degrees of freedom which by adjustment minimise the deviations. Consequently, $\chi^2 \approx n_d$.

Parameters from Ref. [49]	best-fit-values $\pm 1\sigma$
$\sin^2\theta_{12}$	$0.306^{+0.012}_{-0.012}$
$\sin^2\theta_{13}$	$0.02166^{+0.00075}_{-0.00075}$
$\sin^2\theta_{23}$	$0.441^{+0.027}_{-0.021}$
Δm^2_{21}	$(7.50^{+0.19}_{-0.17})\ 10^{-5}\ \text{eV}^2$
Δm^2_{31}	$(2.524^{+0.039}_{-0.040})\ 10^{-3}\ \text{eV}^2$
δ	$-99^\circ\,^{+51^\circ}_{-59^\circ}$

Table 4.1: Best-fit values with 1σ uncertainty range from global fit to experimental data for neutrino parameters in case of normal ordering, taken from [49].

Here, we collect our model parameters in $x = (m_a, m_b, n, \eta)$, and predict the physical values $P_i(x)$ from the LS model. The latter are compared to the μ_i that correspond to the "data", which we take to be the global fit values of [49],

$$\mu_i = \{\sin^2\theta_{12}, \sin^2\theta_{13}, \sin^2\theta_{23}, \Delta m^2_{21}, \Delta^2_{31}(, \delta)\}\,. \tag{4.3.5}$$

Furthermore, σ_i are the standard deviations for each of the neutrino observables. In case the distribution is Gaussian, the 1σ uncertainty matches the standard deviation, which is approximately the case for several of the neutrino parameters depicted in Tab. 4.1. However, there are a few cases where the deviations are asymmetric, i.e. non-Gaussian. To obtain conservative results, we assume the distribution surrounding the best fit to be Gaussian, and choose the smaller uncertainty, respectively. That way, we slightly overestimate the χ^2 values.
A χ^2 function is required to have a well-defined and generally stable global minimum in order to be an appropriate estimator as well as measure for the goodness-of-fit. This is the case for all constrained sequential dominance CSD(n) models under the assumption that the sign of η is fixed [43].
Since the *CP*-violating phases δ and σ are either only measured with large uncertainties or not at all, we define two distinct estimators:

- χ^2 for which $N = 5$, i.e., δ is *not* included in Eq. (4.3.5),
- χ^2_δ for which $N = 6$, i.e., δ is included when performing the global fit.

For a large number of parameters, we would therefore expect $\chi^2 \to 1$ and $\chi^2_\delta \to 2$ to be the benchmark for the goodness-of-fit, which would enable the comparison of $\chi^2/(n_d = 1) \leftrightarrow \chi^2_\delta/(n_d = 2)$. Since we do not have that many parameters, however, the absolute values of both estimators should not be

compared among each other. And taking n_d as a measure for the goodness-of-fit works on an approximate level only. Nevertheless, both estimators should point towards the same set of input parameters, which they do according to the study in chapter 6.
From former analyses of the LS [43, 310], we know in which ballpark the best-fit values of $m_{a,b}$ are to be expected, respectively. That way, we can define a grid in the (m_a, m_b)-plane over which we scan – meaning that we pass on the respective input parameters $x = (m_a,\, m_b,\, n = 3,\, \eta = \pm 2\pi/3)$ at each point of the grid to the *Mathematica* package `REAP` [331, 359]. `REAP` numerically solves the RGEs and provides the neutrino parameters at the electroweak scale, i.e. the $P_i(x)$ in Eq.(4.3.4). The latter are used to determine how good the fit is with respect to the input parameters $(m_a,\, m_b)$, by giving an explicit value for $\chi^2_{(\delta)}$. In the next step, we identify the region of the global $\chi^2_{(\delta)}$ minimum, choose a finer grid for the corresponding region in the $(m_a,\, m_b)$-plane and repeat the procedure until we determine the optimum set of input values.

Chapter 5

Conversion of Bound Muons: $\mu - e$ Conversions

This chapter is devoted to an overall discussion of both the lepton flavour violating $\mu^- - e^-$ conversion and the lepton flavour *and* lepton number violating $\mu^- - e^+$ conversion. For both types of bound muon conversions, we will present detailed and comprehensive computations which aim at making them accessible to the particle physics community. In addition, we will illustrate their respective physics potential. Furthermore, we will discuss the benefits of complementarity, introduce experimental aspects, and address open issues. Note that this chapter is based on Refs. [1–4]. Consequently, parts of the chapter at hand are adopted from parts of those references.

The Standard Model (SM) of particle physics is an almost perfect description of the smallest building blocks we know of the Universe. With the only exception of neutrino oscillations [7–9] (and possibly the anomalous magnetic moment of the muon [360–363]), the SM passes all experimental tests. We can turn around the logic, too, and instead derive predictions from the SM which we can test. Among these predictions are the absence of lepton flavour and lepton number violation (abbreviated LFV and LNV, respectively) at the perturbative level, arising from an accidental symmetry. We discuss the concepts and consequences of both LFV and LNV in section 3.2. Experimentally, LFV is in fact already proven by neutrino oscillations, which imply both neutrino masses and leptonic mixing. Yet, in the charged lepton sector, we have not directly observed any flavour changing reaction – even though all fundamental conservation laws such as energy, momentum, or angular momentum would not forbid LFV processes. Since the rates for LFV processes in the charged lepton sector are suppressed to unmeasureable sizes when only taking into account standard contributions, i.e. from solely augmenting the SM by massive neutrinos, experimentally observing any type of LFV process would be an unambiguous and groundbreaking signal for New Physics beyond the SM – and even beyond massive neutrinos. In addition to LFV, several New

Physics models also introduce LNV at the perturbative level, which has not been observed for the SM so far. Its detection might be considered an even more fundamental discovery regarding the properties of Nature.
Thus, the experimental hunt for both LFV and LNV reactions is regarded to be a high-priority matter in experimental advances alternative to high-energy colliders, as discussed in sections 3.2 and 3.3. While experiments like MEG [205] ($\mu \to e\gamma$), BaBar [205] ($\tau \to e\gamma$, $\tau \to \mu\gamma$), SINDRUM [364] ($\mu \to 3e$), or Belle [365] ($\tau \to 3e$, $\tau \to 3\mu$, $\tau^- \to \mu^- e^+ e^-$, $\tau^- \to e^- \mu^+ \mu^-$) obtain their best limits by triggering for "clean" decays with initial and final states only containing elementary particles, in the near future the most dramatic experimental advances are expected for the conversion of muons bound on atomic nuclei, known as $\mu^- - e^-$ conversion. Sensitivities quoted in experimental proposals would improve current limits up to about five to six orders of magnitude – possibly even reaching an incredible sensitivity of $\mathrm{BR}[\mu^- + (A,Z) \to e^- + (A,Z)] = \mathcal{O}(10^{-18})$ [45]. In the upcoming experiments COMET and Mu2e, sensitivities are expected to reach $\mathcal{O}(10^{-17})$ [208, 366]. For most experiments aiming to measure the LFV $\mu^- - e^-$ conversion, the additional measurement of the LNV $\mu^- - e^+$ conversion comes practically *for free* – or with very minor modifications of the setup – because the signatures of both processes can be distinguished clearly due their respective charge. Thus, with sensitivities not identical but at least similar to those for $\mu^- - e^-$ conversion, we can also expect an improvement on the bounds on $\mu^- - e^+$ conversion by several orders of magnitude – reaching sensitivities of $\mathrm{BR}[\mu^- + (A,Z) \to e^+ + (A,Z-2)] = \mathcal{O}(10^{-16})$ within the coming years (but only by selecting designated isotopes) [46].[1]
Though there are well-motivated scenarios for the generation of neutrino masses and leptonic mixings, see section 3.1, which predict signatures at both the intensity and high-energy frontiers, these scenarios generically predict the existence of multiple new particles, making concrete predictions for phenomenology difficult to extract. However, a common element is a doubly charged scalar particle S^{++}, which is predicted in a sizeable class of these scenarios in connection to LNV and the generation of neutrino masses. An extension of the SM by *just one new particle* at accessible energy, S^{++} (being $\mathrm{SU(2)_L}$ singlet to avoid the introduction of extra degrees of freedom from an $\mathrm{SU(2)_L}$ multiplet), and in the presence of effective operators giving rise to LNV, provides *the most minimal framework* which captures the main features of a large class of neutrino mass models [47]. This setting, to which we refer to as the effective theory of a doubly charged scalar, is introduced in section 3.3 and will be used as the prime example throughout this chapter.
While $\mu^- - e^-$ conversion was proposed more than fifty years ago [367,368], and has since then been repeatedly studied experimentally, it is surprising that it

[1] Note that, although $\mu^- - e^\pm$ conversions do intrinsically contain nuclear physics uncertainties which make it more difficult to interpret experimental limits, it is nevertheless clear that both processes will yield limits by far better than what we could possibly expect from experiments on, e.g., $\mu \to e\gamma$.

has not even been computed explicitly for some relatively generic settings. The rate for $\mu^- - e^-$ conversion has been calculated for channels like light or heavy Majorana neutrino exchange [369], Z'-exchange [370], some specific extended scalar sectors [371], or several supersymmetric settings [372–374], however, the generic example of this decay being mediated by a doubly charged $\mathrm{SU}(2)_\mathrm{L}$ singlet scalar had only been briefly estimated [375] until we performed an explicit calculation [2]. In section 5.2, we will show how to close this gap by presenting the first detailed computation of that very process. Up to that point, not much technical information had been available in the literature, which is why we chose to present the computation in great detail and illustrate all important steps and subtleties involved. Our results are fully general and hold for *any* doubly charged singlet scalar S^{++} coupling to pairs of right-handed (RH) charged leptons (such a coupling is usually allowed as it does not violate any gauge symmetries). Furthermore, even if the doubly charged scalar was, say, the doubly charged component of a Higgs triplet field, the principal computation would not change very significantly, so that our results could easily be extended to this case.
The process of $\mu^- - e^+$ conversion has already been both theoretically proposed [64, 376, 377] and experimentally studied [233, 378–383] decades ago. However, nowadays most of this expertise seems to be "lost", and it is worth reconsidering $\mu^- - e^+$ conversion in the light of the newest technology. As we will point out in section 5.3, advances are necessary on different frontiers, i.e. particle, nuclear, and experimental physics, in order to to fully assess the potential of $\mu^- - e^+$ conversion. What has been unavailable in particular so far, is a detailed computation of $\mu^- - e^+$ conversion on a level accessible to particle physicists. In section 5.3, we will try to make the first step to remedy the situation by presenting a detailed computation of the process when based on one specific effective operator for which the corresponding nuclear matrix element (NME) is currently known. In addition, we relate the said operator to concrete New Physics scenarios. That way, we add several decisive bits needed in order to make use of already existing results [6]: 1.) we provide a guideline on how to realise effective operators by concrete New Physics scenarios; 2.) we provide the tools to compare different particle physics models to each other, which is the key to understanding which settings could be constrained by $\mu^- - e^+$ conversion; 3.) last but not least, we provide a much more explicit computation than presented in Ref. [6], which will make the technical aspects much easier to grasp. Thus, at least for the one effective operator for which NMEs have already been computed, we will make it understandable which elements go into the computation. Should further NME computations become available and should more effective operators be matched to particle physics settings, with an eye on the comparison between different New Physics scenarios, the present work will provide the glue necessary to connect all these efforts.

As indicated above, the remainder of this chapter is organised as follows.

In section 5.1, we review the experimental aspects of both types of bound muon conversions. We focus on the key aspects with regard to sensitivities, backgrounds and nuclear physic aspects. In section 5.2, we present a detailed computation of the conversion of bound muons to electrons being mediated by a doubly charged $\mathrm{SU(2)_L}$ singlet scalar and we illustrate the benefits from exploiting complementarity in order to test New Physics models. In section 5.3, we present a detailed computation of μ^-– e^+ conversion on a level accessible to particle physicists. In addition to the technical aspects of the computation, we present an illustrative discussion of the physics potential of μ^-– e^+ conversion based on a number of New Physics scenarios and point out issues that need to be addressed as to fully embrace the opportunities presented by near-future experiments.

5.1 Experimental Aspects

This section is devoted to presenting the key experimental aspects of both μ^-– e^- and μ^-– e^+ conversion. This will include reviewing backgrounds, experimental sensitivities, nuclear physics aspects, and open questions. Note that the section at hand borrows from section 2.3 of Ref. [2] as well as section 3 of Ref. [3]. Therefore, parts of this section are adopted from those references.

Experimentally, both types of bound muon conversion are two-step processes. First, a μ^- is captured in an atomic shell of higher principal quantum number, $n \sim 10$, before it quickly de-excites to the $1s$ ground state. The emission of the corresponding de-excitation photons (in case of muonic atoms these will carry more than 100 keV of energy) serves as indicator for a shell capture. In case of Al (100% of Al-27), which will be used in the next generation of experiments, the $2p \to 1s$ transition with the emission of a 346.8 keV photon with 79.7(6)% intensity will serve as signal. After that the muon either decays in orbit (DIO), experiences a standard (or radiative) muon capture with the emission of a neutrino (possibly accompanied by an electron and a positron via pair-production), or it undergoes μ– e conversion in which it is captured by the nucleus and reemits a positron or electron. Assuming only "coherent"[2] conversion – which means that both initial and final state nucleus are in ground state – the positron/electron created is fast, and thus escapes the final-state atom. The positron/electron energy is then given by

$$E_e = m_\mu + M_i - M_f - \epsilon_b - E_{\mathrm{rec}}\,, \tag{5.1.1}$$

with m_μ being the muon mass, ϵ_b the binding energy of the $1s$-state in the muonic atom, and E_{rec} the nuclear recoil energy. Furthermore, $M_{i,f}$ denote

[2]Please note that the quotation marks are added here, since *coherent* technically refers to a process that has *the same* initial and final nucleus in the ground state, which cannot be the case for μ^-– e^+ conversion.

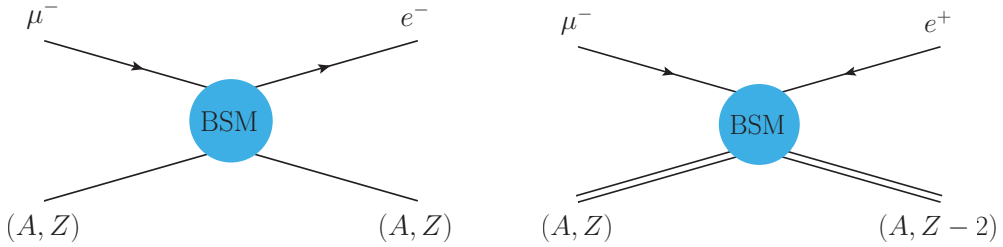

Figure 5.1: Schematic illustration of (*left*) μ^-– e^- conversion and (*right*) μ^-–e^+ conversion. Here, the initial and final state nuclei are characterised by their mass number A and their atomic number Z.

the mass of the (initial state) target nucleus and the mass of the final state nucleus in the ground state, respectively. For μ^-– e^- conversion, it is $M_i = M_f = M(A, Z)$, cf. Fig. 5.1, such that Eq. (5.1.1) simplifies to $E_e = m_\mu - \epsilon_b - E_{\text{rec}}$. In contrast, the final state nucleus in μ^-– e^+ conversion has to compensate for the charge change of $\Delta Q = 2$ due to the muon being transformed into a positron. As a consequence, the mass of the (final state) daughter nucleus is $M_f = M(A, Z-2)$ based on the target (initial state) nucleus $M_i = M(A, Z)$, cf. Fig. 5.1, and the expected energy of the emitted positron further depends on the mass difference between target and daughter nucleus. In general, the last two terms in Eq. (5.1.1) are small compared to the muon mass so that, in the exemplary case of Al-27, the expected energy of the electron/positron is 104.97 MeV. Note that, while it is known that μ^-– e^- conversion is dominated by coherent conversion [211], this may be very different for μ^-– e^+ conversion where several states can be excited and the resulting positrons will therefore have a more involved spectrum [380]. We will come back to this point towards the end of this section.

The success of experimental searches for the conversion of bound muons critically depends on understanding the background spectrum. Although, in "coherent" conversions, a fast and mono-energetic electron/positron is emitted, there exist competing processes leading to background signals at $E_e \sim m_\mu$. The main sources for background signals are DIO and radiative muon capture [46, 233, 378, 380, 382, 384, 385]. In case the muon undergoes DIO, i.e. the muon decays via $\mu^- \to e^- \nu_\mu \overline{\nu}_e$ while being bound in the $1s$-state, the emitted electron can reach energies up to $\mathcal{O}(m_\mu)$. In other words, the DIO spectrum has basically the same endpoint energy as the μ^-– e^- conversion. Hence, the high-energy tail of the DIO spectrum poses an inherent background for μ^-–e^- conversion detection. The background spectrum stemming from DIO, including the high-energy end of the spectrum, has been studied throughout the literature, see e.g. Refs. [386–393]. Note that DIO could in principle also become a background for μ^-– e^+ conversions if the charge is misidentified which is, however, expected to occur very rarely in upcoming experiments.[3]

[3]The positron detection with respect to electrons should have a very high discrimination

In contrast to DIO, the background from radiative muon capture is equally relevant to the detection of both $\mu^- - e^-$ and $\mu^- - e^+$ conversion. Radiative muon capture can induce a high-energetic electron or positron from the emitted photon by means of asymmetric pair-production. Since the endpoint energy of radiative muon capture depends on the difference between the mass of the target nucleus $M(A, Z)$ and the mass of the daughter nucleus $M(A, Z-1)$, this background can be suppressed (or even eliminated) by requiring certain mass relations for the nuclei involved [46]: $M(A, Z-2) < M(A, Z-1)$ for $\mu^- - e^+$ conversion and $M(A, Z) < M(A, Z-1)$ for $\mu^- - e^-$ conversion. The second requirement is commonly satisfied for stable nuclei. The first requirement, however, is harder to fulfil. Consequently, the main limitation to translating improvements on the sensitivity for $\mu^- - e^-$ conversion to the sensitivity for $\mu^- - e^+$ conversion originates from an unsuitable choice of material, giving rise to non-negligible backgrounds. To maximise the sensitivity of $\mu^- - e^+$ conversion by choosing a suitable material, Ref. [46] investigated several promising isotopes, and estimated their experimental sensitivities. They found that the improvement on current limits on $\mu^- - e^+$ conversion using an Al-27 target, which is planned for both COMET and Mu2e, may not even exceed a factor of ten. In contrast, employing one of the most promising isotopes, Ca-40 or S-32, can even lead to sensitivity improvements of four orders of magnitude.

$\mu^- - e^-$ conversion. Having recapitulated the key aspects with respect to experimental searches and backgrounds for both types of muon conversion, we now turn to the nuclear physics aspects of $\mu^- - e^-$ conversion. The main nuclear physics quantities entering the branching ratios for $\mu^- - e^-$ conversion in Eqs. (5.2.2), (5.2.35), and (5.2.43) are Z, Z_{eff}, and F_p. Out of those, the atomic number Z can be trivially looked up, however, the computation of the effective atomic charge Z_{eff} and of the NME F_p require knowledge of the proton charge density $\rho_p(r)$, with r being the distance to the centre of the nucleus. A good reference summarising the nuclear physics aspects is Ref. [394]: based on the classic Refs. [395,396], they assign different simplified nuclear models (such as harmonic oscillator models as well as different Fermi- and Gaussian-type models) to the different nuclei. In order to use values as up to date as possible, we have however instead relied on the online database called *The Nuclear Charge Density Archive* [397], whose data are to the greatest extent identical to those used in the previous references, while they nevertheless contain some updates or smaller corrections. We would like to stress that, from a nuclear physics point of view, the process of $\mu^- - e^-$ conversion would certainly deserve more attention. Although some example computations of NMEs exist [398–402], they still seem not as advanced and/or up to date as the comparatively involved computations of NMEs for neutrinoless double beta decay (see, e.g., Refs. [403–410]), and in particular they do not cover all relevant cases. On the

power due to the different orientation of the helical path in the magnetic field in combination with the high resolution of tracking detectors.

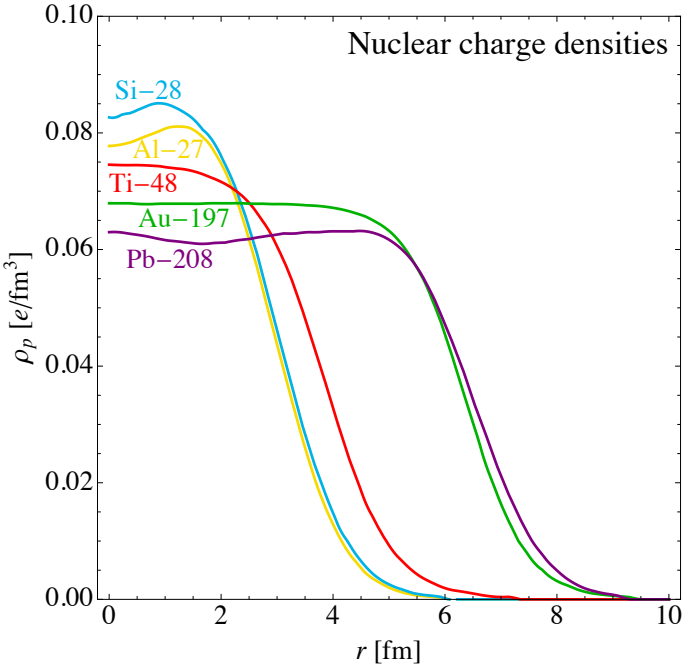

Figure 5.2: Electric charge densities of the isotopes under consideration. The normalisations are chosen such that $\int \mathrm{d}^3 r\ \rho_p(r) = Z$ for each isotope.

other hand, the process of $\mu^- - e^-$ conversion was recognised by parts of the nuclear physics community also in recent years [398] so that hopefully, in the near future, it will be clear how safe the bounds obtained truly are.
The relevant nuclear charge densities are displayed in Fig. 5.2 for the isotopes under consideration. The corresponding effective atomic charges and NMEs are displayed in Tab. 5.1. Note that, as long as the particle physics and nuclear physics parts factorise, cf. Eq. (5.2.2), all nuclear physics dependence can be absorbed into the experimental bounds. Hence, we can conveniently compare bounds from different experiments which constrain the same particle physics amplitude.

The relevant nuclei we have taken into consideration are those for which either existing limits can be found or which are planned to be used in future experiments. The best existing limits were all obtained by the SINDRUM II experiment: $\mathrm{BR}(\mu^-\mathrm{Ti} \to e^-\mathrm{Ti}) < 4.3{\cdot}10^{-12}$@90% C.L. on ^{48}Ti [385], $\mathrm{BR}(\mu^-\mathrm{Au} \to e^-\mathrm{Au}) < 7 \cdot 10^{-13}$@90% C.L. on ^{197}Au [383], and $\mathrm{BR}(\mu^-\mathrm{Pb} \to e^-\mathrm{Pb}) < 4.6 \cdot 10^{-11}$@90% C.L. on ^{208}Pb [411]. Projections for future sensitivities are announced by DeeMe [412] for ^{28}Si, $\mathrm{BR}(\mu^-\mathrm{Si} \to e^-\mathrm{Si}) < 1 \cdot 10^{-14}$, by COMET [208] for ^{27}Al, $\mathrm{BR}(\mu^-\mathrm{Al} \to e^-\mathrm{Al}) < 2.6 \cdot 10^{-17}$,[4] and by PRISM/PRIME [45] for ^{48}Ti, $\mathrm{BR}(\mu^-\mathrm{Ti} \to e^-\mathrm{Ti}) < 1 \cdot 10^{-18}$. However, due to nuclear physics increasing or decreasing the rate for certain nuclei, it is not a priori clear whether the nuclei used in actual experiments have the greatest

[4]Note that a slightly worse sensitivity of $\mathrm{BR}(\mu^-\mathrm{Al} \to e^-\mathrm{Al}) < 6 \cdot 10^{-17}$ is announced by Mu2e [366].

Isotope	Z	Z_{eff}	F_p	$\Gamma_{\text{capt}}[10^6/\text{s}]$
Al-27	13	22.79	0.633	0.7054
Si-28	14	24.37	0.621	0.8712
Ti-48	22	35.85	0.504	2.59
Au-197	79	75.86	0.180	13.07
Pb-208	82	75.44	0.151	13.45

Table 5.1: Atomic numbers Z, effective atomic charges Z_{eff} according to Eq. (127) of Ref. [211], and NMEs F_p according to Eq. (129) of Ref. [211] for the isotopes under consideration. We also quote the rates for ordinary muon capture, cf. Tab. 8 in Ref. [394] (note the typo "Pb-207" in that reference).

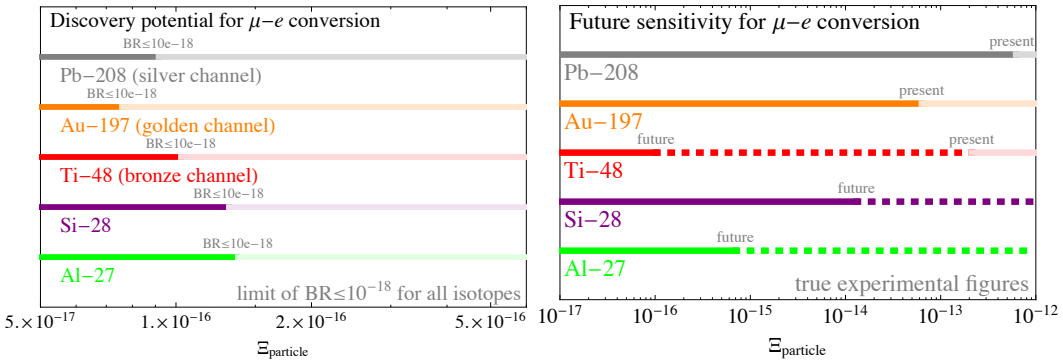

Figure 5.3: Discovery potential and future sensitivities/current limits on Ξ_{particle} for different isotopes under consideration for $\mu^- - e^-$ conversion.

discovery potential. In order to disentangle these tendencies, we have depicted in Fig. 5.3 both the general discovery potential for a given limit on the branching ratio versus the actual future sensitivities and past limits. Here, limits on the branching ratio have been translated into possible limits on the parameter Ξ_{particle}, cf. Eqs. (5.2.2) [in combination with Eq. (5.2.5)], (5.2.35), and (5.2.43), which contains all particle-physics-model-dependent contributions. The left panel exhibits how far down a limit on Ξ_{particle} could go for a hypothetical bound of $1 \cdot 10^{-18}$ on the branching ratio assumed for *all* isotopes (which is identical to the quoted future sensitivity by PRISM/PRIME for ^{27}Ti). As one can see, the best isotope for $\mu^- - e^-$ conversion and thus the (quite literally) golden channel would be the transition on ^{197}Au, followed by ^{208}Pb and ^{48}Ti. Glancing at the right panel, the true best future sensitivity is in fact expected to be reached for ^{48}Ti by PRISM/PRIME. These simple considerations imply that, if it was possible to build a future experiment with $\text{BR}(\mu^-\text{Au} \to e^-\text{Au}) < 1 \cdot 10^{-18}$ instead of $\text{BR}(\mu^-\text{Ti} \to e^-\text{Ti})$, we might be able to boost our limit on Ξ_{particle} even further than currently planned.

$\mu^- - e^+$ conversion. In contrast to coherent $\mu^- - e^-$ conversion, which can occur at a single nucleon and is mediated via the ground state of the nucleus,

$\mu^- - e^+$ conversion has to occur on two nucleons to allow for a $\Delta Q = 2$ process (see section 3.5.1 of Ref. [210] for a pedagogical summary of theoretical and experimental aspects). This also implies that the atomic number of the final state nucleus changes by two units. Therefore, although both types of conversion processes are very similar from an experimental point of view, they differ fundamentally with respect to the nuclear physics involved. For instance, the nuclear interactions, described by the NMEs derived in section 5.3.2, include the transition via virtual intermediate states of the nucleus. Hence, the NMEs for $\mu^- - e^+$ conversion are far more involved than those for $\mu^- - e^-$ conversion explored above. As we will discuss in section 5.3, hardly any NMEs for $\mu^- - e^+$ conversion are currently available, which is one of several open issues that, at this stage, prevent us from unlocking this process's full potential. From Fig. 3.2 and from the corresponding discussion in section 3.2, we know that both $\mu^- - e^+$ conversion and neutrinoless double beta decay $0\nu\beta\beta$ are mediated by the same underlying mechanism in case only the standard contribution mediates LNV processes. In other words, taking the simplest case of Majorana neutrino exchange [6], the effective mass obtained from $0\nu\beta\beta$ contains terms proportional to U_{ei}^{*2}, with U_{ei}^* being the i-th element of the first row in the leptonic mixing matrix, whereas $\mu^- - e^+$ conversion is sensitive to $U_{\mu i}^* U_{ei}^*$, cf. Eq. (5.3.39), therefore providing complementary information. So, in a way, $\mu^- - e^+$ conversion is very similar to $0\nu\beta\beta$, just with a muon instead of an electron. In fact, even if non-standard contributions are relevant, we can turn to an effective field theory treatment analogous to the one used for $0\nu\beta\beta$ in order to consider $\mu^- - e^+$ conversions in a particle-physics-model-independent way, cf. Eq. (5.3.1). Note that, even if the process is not mediated by Majorana neutrino exchange, there will always be some connection between μ and e (which is absent for $0\nu\beta\beta$), thus allowing to probe LNV in another sector. To subsume, we have illustrated how $\mu^- - e^+$ conversion compares to both $\mu^- - e^-$ conversion and $0\nu\beta\beta$ in Fig. 5.4: while $\mu^- - e^-$ conversion can only detect lepton *flavour* violation – which we already know exists from neutrino oscillation experiments – and not the much more fundamental lepton *number* violation, $0\nu\beta\beta$ can detect LNV but only in the ee-sector. Instead, $\mu^- - e^+$ conversion is in some sense the best of both worlds, being able to detect LNV in the $e\mu$ sector. This is a great benefit given that there are models in which LNV is much more prevalent in flavour non-diagonal transitions. On top of that, as discussed at the beginning of this section, most experiments searching for ordinary $\mu^- - e^-$ conversion can, possibly even without significant modifications, *simultaneously* look for $\mu^- - e^+$ conversion.

Another important issue, still unresolved for $\mu^- - e^+$ conversion, is the momentum spectrum of the final state positrons. In order to fully exploit the discovery potential that lies within the next generation of bound muon experiments, it is essential to understand which percentage of the conversion takes places via "coherent" transitions and how the momentum spectrum for excited final state positrons looks like. Since some of the energy is transferred to the

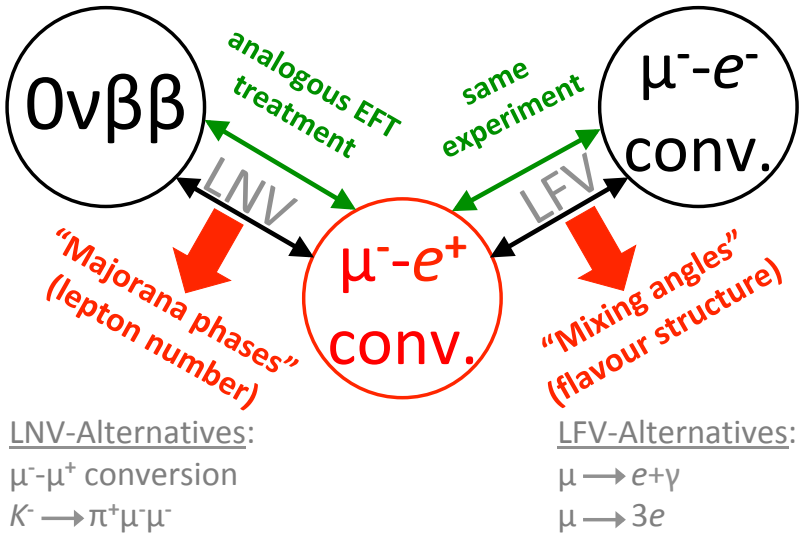

Figure 5.4: Schematic illustration of the profound role of $\mu^- - e^+$ conversion.

nucleus in order to produce an excited final state, the emitted positron is of lower energy. Therefore, $\mu^- - e^+$ conversion based on transitions with excited final state nuclei suffers from more serious backgrounds. Past measurements of $\mu^- - e^+$ conversion [233, 378–382], the last one being SINDRUM II [383], have typically assumed that this process is completely mediated through the giant dipole resonance (GDR). SINDRUM II used a Ti target and assumed a Breit-Wigner shape to fit the GDR with 20 MeV excitation energy and 20 MeV width. In the case of Al-27, which is the muon capture target for both future experiments COMET [208] and Mu2e [366], much better data exist and, using the EXFOR database [413], the GDR can be fitted by a Breit-Wigner shape with a mean of 21.1 MeV and a width of 6.7 MeV, which is much more precise than the one used in the past (see Fig. 5.5). Hence, if this process is completely mediated by the GDR, which is an assumption, the positron energy will be 83.9 MeV and thus suffer from a higher background. The major background will be radiative muon and pion captures followed by asymmetric pair production, as broached above, with the first process being dominant. If $\mu^- - e^+$ conversion is proceeding to a certain fraction via the ground state or via states between ground state and the GDR, then the signal will be smeared out over the range between the two values given. However, more recent calculations revealed that a significant fraction (around 40% [6]) are proceeding via the ground state also for this process, which would be good news. Clearly this issue deserves further investigations to clarify how this process is mediated in a nucleus at all and whether the GDR is really playing a key role [6, 414]. For now, however, we will focus on the case of "coherent" conversions, cf. section 5.3.

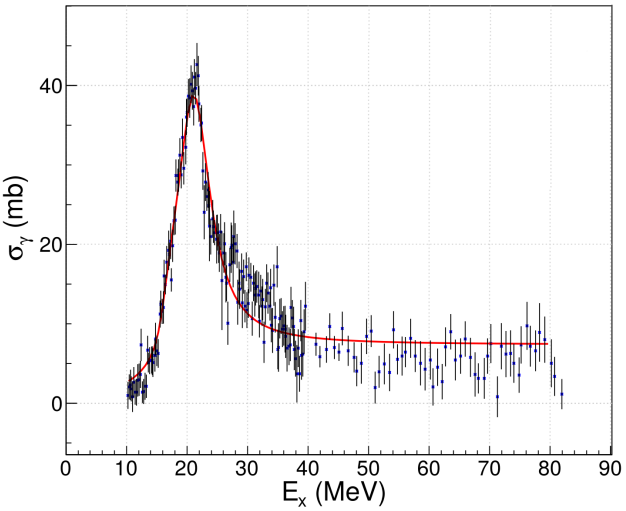

Figure 5.5: Shape of the giant dipole resonance in Al-27 using the EXFOR database. A Breit-Wigner shape is fitted to the data.

5.2 $\mu^- - e^-$ Conversion

This section is dedicated to the conversion of bound muons to electrons, referred to as $\mu^- - e^-$ *conversion*, mediated by doubly charged scalars. On top of a very general computation, we will also present an application of our results to one particular example model, namely the effective theory of a doubly charged scalar introduced in section 3.3. Note that the section at hand is a slightly modified version of Ref. [2], supplemented by the discussion on the complementarity of high- and low-energy physics from Ref. [1]. Consequently, most of this section is adopted from parts of those references.
This section is structured as follows. We first discuss the photonic contributions to $\mu^- - e^-$ conversion in great detail in section 5.2.1, which serves as a first approximation to the detailed result. We then include the non-photonic contributions in section 5.2.2, which will only slightly modify the branching ratios. In section 5.2.4, we turn our attention to the complementarity between indirect searches, such as the $\mu^- - e^-$ conversion, and direct searches performed at the high-energy frontier. We summarise our findings in section 5.2.5. Finally, technical details are subsumed in Appendices A (Feynman rules) and B (details on the scalar three-point function).

Before we start discussing both photonic and non-photonic contributions in the following sections, we want to briefly motivate why these contributions must be addressed separately. For this purpose, we take a look at the length scales involved in the conversion process. We can estimate the nuclear radius of the isotope used with $R = r_0 A^{1/3} \sim \mathcal{O}(10^{-15}\text{ m})$, where $r_0 \sim \mathcal{O}(10^{-15}\text{ m})$ is the proton radius and A the atomic mass number, and the reduced Bohr radius

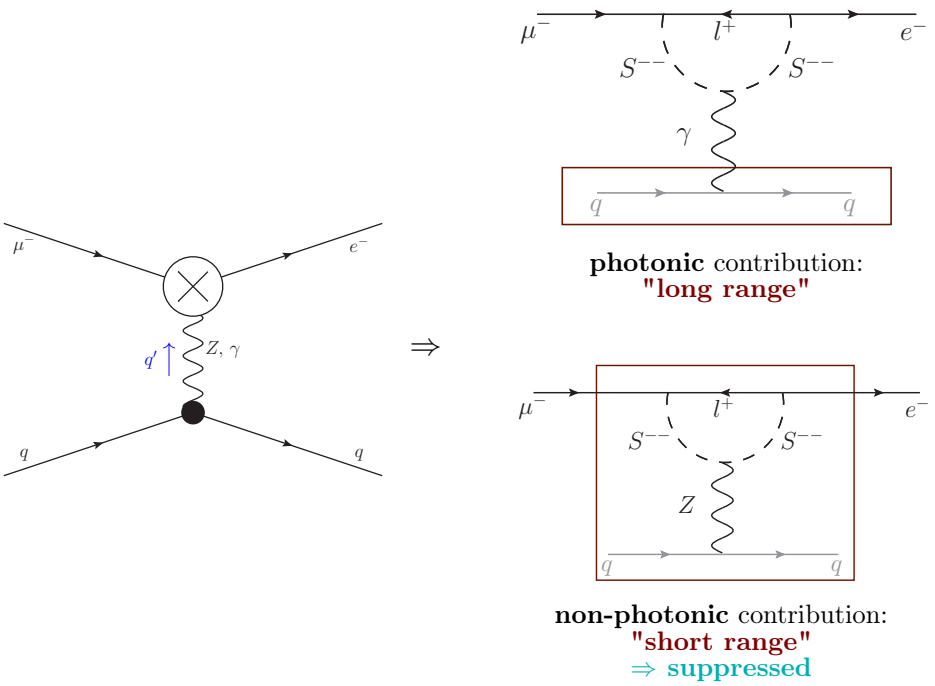

Figure 5.6: Illustration on the substantial difference between the $\mu^- - e^-$ conversion being mediated photonically or non-photonically, which necessitates the qualitative distinction of both contributions. The diagrams on the right are illustrative examples. The parts inside the rectangular frames indicate what happens inside the nucleus.

is given by $a_0 m_e/m_\mu \sim \mathcal{O}(10^{-13}\text{ m})$, with $a_0 \sim \mathcal{O}(10^{-10}\text{ m})$ being the physical Bohr radius. The latter serves as a rough estimate of the most probable distance between the nucleus and the $1s$-state muon. In comparison, we can assess the interaction ranges of both photonic and non-photonic interactions based on the mass of the respective interaction particle(s). We obtain $r_\gamma \to \infty$ and $r_Z \lesssim 10^{-18}$ m. This means that, while the photonic interaction can take place with the muon predominantly located in the area around the reduced Bohr radius, the muon has to be within the nucleus for the non-photonicly mediated conversion process to actually occur. Since the probability for the muon to be located within the nucleus is tiny, however, we expect the non-photonic contributions to be suppressed, unless there is a reason for an enhancement in the particle theory counteracting the suppression. Furthermore, as illustrated in Fig. 5.6, the particle physics interactions which allow for the photon-mediated conversion process happen predominantly outside the nucleus, which is why the photonic contributions are often referred to as *long-range contributions*. This is what makes it possible to factorise the particle from the nuclear physics. As opposed to this, the particle physics interactions generating non-photonic contributions entirely take place inside the nucleus, which requires a treatment based on short-range operators and consequently spoils the factorisation into

nuclear and particle physics parts. As a result, photonic and non-photonic contributions need to be treated qualitatively differently.

5.2.1 Photonic contributions

The goal of this section is to derive the particle physics part of the branching ratio for coherent $\mu^- - e^-$ conversion in a muonic atom, for the moment focusing on the *photonic contributions* only, i.e., those diagrams which basically attach a diagram for $\mu \to e\gamma$ to a nucleus. As we will see, this already comes very close to our final result, because the photonic, predominantly long-range contributions turn out to dominate the non-photonic short-range contributions by far. This is very convenient because, for the case of photonic contributions being dominant, the total amplitude factorises into a particle physics and a nuclear physics part. Thus, the nuclear physics factor (which quantifies all nuclear physics contributions) can be computed separately, and it can easily be updated once improved computations become available – as done for neutrinoless double beta decay.

The physics of $\mu^- - e^-$ conversion

Taking into account gauge invariance,[5] the most general form for the photonic matrix element (i.e., for the $\mu^- - e^- - \gamma$ vertex) can be written as [202, 211, 394, 415, 416]:

$$\begin{aligned} i\mathcal{M} = -i\,e\,A^*_\nu(q)\,\overline{u}_e(p_e)\,\Big[\Big(f_{\mathrm{E0}}(q^2) + \gamma_5\,f_{\mathrm{M0}}(q^2)\Big)\Big(\gamma^\nu - \frac{\not{q}\,q^\nu}{q^2}\Big) \\ + \Big(f_{\mathrm{M1}}(q^2) + \gamma_5\,f_{\mathrm{E1}}(q^2)\Big)\frac{i\,\sigma^{\nu\rho}\,q_\rho}{m_\mu} + 2\frac{q^\nu}{m_\mu}\,f_3(q^2) + 2\frac{q^\nu}{m_\mu}\,\gamma_5\,g_3(q^2)\Big]\,u_\mu(p_\mu)\,, \end{aligned} \tag{5.2.1}$$

where $q = p_\mu - p_e$ is the photon momentum and $\sigma^{\nu\rho} \equiv \frac{i}{2}[\gamma^\nu, \gamma^\rho]$.[6] The functions f are *form factors* that in general depend on the momentum transfer. They are the quantities which ultimately encode the loop structures involved in the diagrams. Note that the amplitude as reported in Eq. (5.2.1) is the same for both $\mu \to e\gamma$ and $\mu^- - e^-$ conversion. However, both processes nevertheless yield qualitatively different information. The reason is that $\mu \to e\gamma$ is strongly simplified by on-shell relations being applicable only for external photons, in particular $q^2 = 0$ (the photon is massless) and $\epsilon_\nu q^\nu = 0$ (the photon is transversal). On the contrary, in $\mu^- - e^-$ conversion, the off-shell part of the amplitude strongly contributes, which is reflected in the resulting bounds on the effective

[5] Note that, due to the (Abelian) Ward identity, it holds that $f_3 = g_3 = 0$ for the photonic case. This is an additional cross check for our computation and was confirmed when determining the form factors explicitly.

[6] In order to prevent any confusion, we do not use the letter "μ" as Lorentz index, but instead we only use it to refer to the muon.

model used as an example here being very different for both processes. We will return to comparing $\mu \to e\gamma$ and $\mu^- - e^-$ conversion towards the end of this section.

The decisive observable is the branching ratio of $\mu^- - e^-$ conversion with respect to ordinary muon capture, which is simple if the photonic contributions dominate [211]:

$$\mathrm{BR}(\mu^- N \to e^- N)\Big|_{\mathrm{photonic}} = \frac{8\alpha^5 m_\mu Z_{\mathrm{eff}}^4 Z F_p^2}{\Gamma_{\mathrm{capt}}} \Xi^2_{\mathrm{particle}} \,, \tag{5.2.2}$$

where α is the fine structure constant and Γ_{capt} is the rate for ordinary muon capture (with emission of a ν_μ) on the nucleus under consideration, which is quasi identical to the total rate. Furthermore, the effective atomic charge

$$Z_{\mathrm{eff}}^4 = \frac{\pi Z}{\alpha^3 m_\mu^3} \cdot 4\pi \int\limits_{r=0}^{\infty} dr\; r^2 |\Phi_{1s,\mu}(r)|^2 \rho_p(r) \,, \tag{5.2.3}$$

with $\Phi_{1s,\mu}(r)$ being the $1s$ wave function of the muon bound to a nucleus of atomic number Z, and the NME,

$$F_p = 4\pi \int\limits_{r=0}^{\infty} dr\; \frac{r}{m_\mu} \sin(r m_\mu) \rho_p(r) \,, \tag{5.2.4}$$

can both be calculated easily if the proton charge density $\rho_p(r)$ inside the nucleus is known.

Let us discuss the physics of $\mu^- - e^-$ conversion before entering the actual computation. In Eq. (5.2.2), all the particle physics is contained in the factor $\Xi^2_{\mathrm{particle}}$, which is our main quantity of interest. It is explicitly given by [211]:

$$\Xi^2_{\mathrm{particle}} = |f_{\mathrm{E0}}(-m_\mu^2) + f_{\mathrm{M1}}(-m_\mu^2)|^2 + |f_{\mathrm{E1}}(-m_\mu^2) + f_{\mathrm{M0}}(-m_\mu^2)|^2 . \tag{5.2.5}$$

Thus, in our computation, we "only" need to extract the form factors $f_{\mathrm{E0,E1,M0,M1}}$ from the amplitude and evaluate them at a four-momentum transfer of $q^2 = -m_\mu^2$. Once we achieve that, we can immediately use Eq. (5.2.2) to obtain the branching ratio for $\mu^- - e^-$ conversion.

However, there are several other aspects to the process which should be discussed before we can start our computation. While the basic principle behind $\mu^- - e^-$ conversion, the capture of a bound muon with subsequent emission of a fast electron, is easy to grasp, several subtleties make this process comparatively difficult to compute in practice. Further (technical) details on this discussion can be found e.g. in Refs. [394, 417–419].

First, let us have a look at the initial state muon. It is not free but in the $1s$ bound state of a muonic atom. The final state electron is not entirely free either, as it does feel the influence of the electric field of the remainder of the

atom present in the final state. Thus, to take into account all resulting effects, it is easiest to perform the computation in real space and use the solutions of the Dirac equation in a Coulomb potential instead of the spinors corresponding to free particles: $\overline{u}_e(p_e) \to \overline{\psi}_e(p_e, r)$ and $u_\mu(p_\mu) \to \psi_\mu(p_\mu, r)$.
Second, a simplification arises from the muon mass being the dominant energy scale compared to the binding energies E_b involved or to the electron mass: $m_\mu \gg m_e > E_b \approx 13.6 \text{ eV} \cdot Z m_\mu/m_e$. Thus, we can set the electron mass to zero, $m_e \approx 0$, and we can treat the muon non-relativistically. This furthermore implies that the kinematics of the process are in essence very similar to those of a t-channel diagram, with both the initial state muon and the initial (and final) state nucleus being nearly at rest; we can thus approximate $q^2 \simeq -m_\mu^2$.
Third, given the nature of the process, it is unavoidable to consider some atomic and nuclear physics aspects. Fortunately, a standard formalism exists to take them into account. For example, the photon couples to electric charges (no matter if it is on- or off-shell), which means that the corresponding part of the matrix element must be proportional to the proton charge density $\rho^{(P)}(r)$ in the nucleus: $\langle N|\overline{q}\,\gamma_\nu\, q|N\rangle \propto Ze\rho^{(P)}(r)\,\delta_{\nu 0}$. Thus, the full amplitude for the process must have the following structure:

$$\mathcal{M} \propto \int \mathrm{d}^3 r\, \overline{\psi^e_{jlm}}(p_e, r)\, \Gamma^\nu\, \psi^\mu_{j_\mu l_\mu m_\mu}(p_\mu, r) Ze\rho^{(P)}(r)\,\delta_{\nu 0}, \tag{5.2.6}$$

where Γ^ν includes the form factors and Lorentz structure displayed explicitly between the two spinors in Eq. (5.2.1). Given that the nucleus is taken to be non-relativistic, its four-current density consists of only the 0-component to a good approximation, which is why effectively only Γ^0 contributes to the amplitude.[7] This implies further simplifications: the pre-factor $q^\nu = p_\mu^\nu - p_e^\nu$ in front of the form factors f_3 and g_3 reduces to $q^0 \simeq m_\mu - m_\mu = 0$ for the case of a non-relativistic muon in the initial state dictating the electron energy in the final state. Thus, even for non-vanishing f_3 and g_3, they would not contribute to the conversion process.
Finally, we need to discuss the forms of the muon and electron wave functions. They depend on the details of the atomic physics configuration. We follow the standard approach taken in textbooks [417], and write the fermionic spinor in terms of "upper" and "lower" radial components f and g. Since we work in the Dirac representation, only the upper component survives in the non-relativistic limit (i.e. for the muon). Encoding the angular part in spherical harmonic spinors Ω_{jlm}, we can thus describe the physics of both the muon and the electron by wave functions of the following form:

$$\psi_{jlm} = \begin{pmatrix} f(r)\,\Omega_{jlm} \\ (-1)^{1/2(1+l-l')}\, g(r)\,\Omega_{jl'm} \end{pmatrix}, \tag{5.2.7}$$

[7] Note that at this point we have in fact broken Lorentz invariance, because we have chosen a particular system – namely the rest frame of the nucleus. However, for a non-relativistic bound system this makes perfect sense, because all relevant quantities can be expressed easily and, after all, we can compute a Lorentz-invariant amplitude in any frame.

with total angular momentum j, orbital angular momenta l and $l' = 2j - l$, and spin projection m on j. In the $1s$ state, the muon has the quantum numbers $(j, l, l', m) = (1/2, 0, 1, \pm 1/2)$. Thus, angular momentum conservation dictates quantum numbers of $(1/2, 0, 1, \pm 1/2)$ or $(1/2, 1, 0, \pm 1/2)$ for the final electron. Depending on the configuration, different parts of the amplitude in Eq. (5.2.1) will contribute (e.g., only structures featuring γ_5 survive for $l = 1$). Exploiting that the initial state muon is nearly at rest, while the final state electron is highly relativistic, we can furthermore set $g_\mu^{l=0} \simeq 0$ as well as $f_e^{l=1} = -g_e^{l=0}$ and $g_e^{l=1} = f_e^{l=0}$. At last, because the two final states with $l = 0$ and $l = 1$ are distinguishable, we have to sum over probabilities rather than amplitudes; hence the form of Eq. (5.2.5).

Determination of the form factors

In our example model, or more generally in any setting featuring a doubly charged scalar coupling to RH charged leptons as in Eq. (3.3.1), $\mu^- - e^-$ conversion is realised at one-loop level only. The decisive diagrams are those in which the initial state muon turns into a virtual anti-lepton/S^{--} combination, which then turns into an electron. A photon can couple to either of these particles, thus implying four different diagrams (see Fig. 5.7, Diagrams I to IV).[8] In principle, one could also have a loop containing a W-boson and a neutrino, with three possibilities to couple a photon to (see Fig. 5.7, Diagrams V to VII). The latter three diagrams are, however, strongly suppressed by the GIM mechanism [44].
Furthermore, one could in either of these diagrams trade the photon for a Z-boson, which yields another seven diagrams. In addition, a Z-boson could also couple to the neutrino line (which the photon could not), see Diagram VIII in Fig. 5.7. Finally, one could also replace all Z-boson lines by Higgs bosons, thus producing another set of eight diagrams. Note that also for Z-bosons and Higgs bosons mediating the process, Diagrams V to VIII are GIM-suppressed in contrast to Diagrams I to IV. In addition, all these diagrams with heavy exchange particles contribute to the non-photonic short-range part of the amplitude, see section 5.2.2, which is by far subdominant. Finally, there could also be box-diagrams with two W-bosons each, see Diagrams IX and X in Fig. 5.7. These could mediate the process but are GIM-suppressed, too [420]. Thus, starting with the photonic (predominantly long-range) part, the only relevant diagrams are I to IV as displayed in Fig. 5.7. We will compute these in the following.

Beginning with momentum assignments, we have chosen the photon momentum to be incoming, i.e., we use $q' = p_e - p_\mu = -q$ in order to adapt a notation consistent with our tool of choice, `Package-X` [416], to reliably com-

[8] In Figs. 5.7a to 5.7j, the greyish parts indicate that the quarks are bound within the nucleus. We will solely need the black part of each diagram to determine the form factors, so that we are displaying the hadronic part only for the sake of illustration.

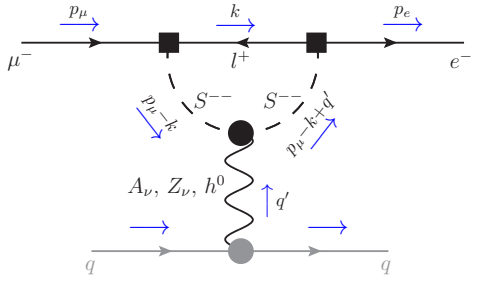

(a) Diagram I

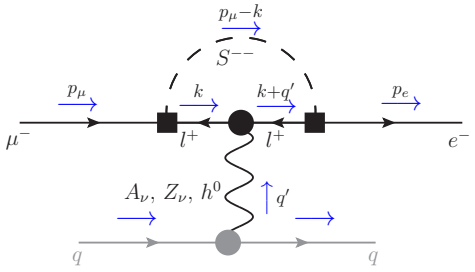

(b) Diagram II

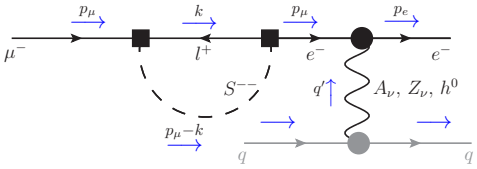

(c) Diagram III

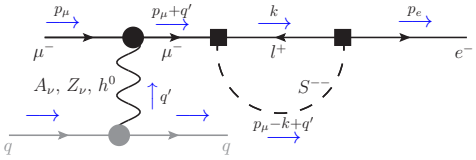

(d) Diagram IV

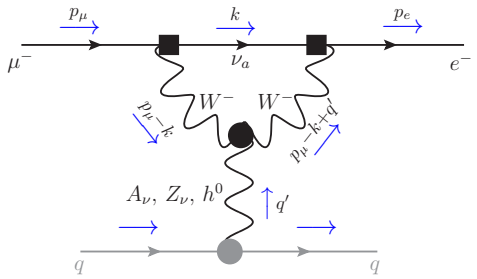

(e) Diagram V

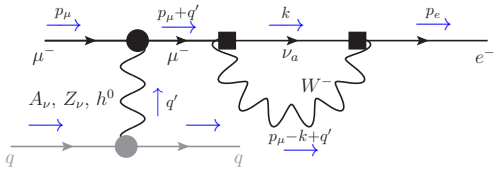

(f) Diagram VI

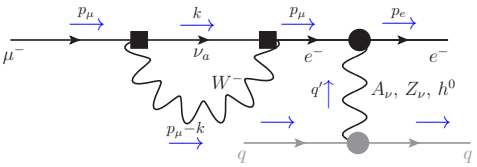

(g) Diagram VII

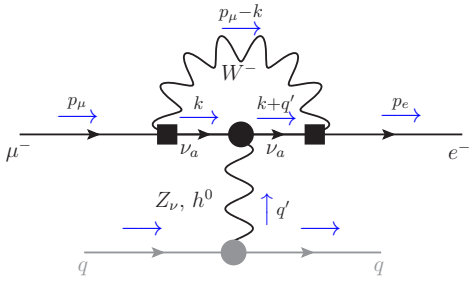

(h) Diagram VIII

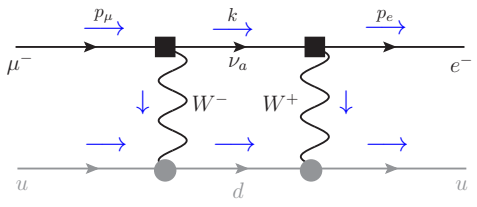

(i) Diagram IX

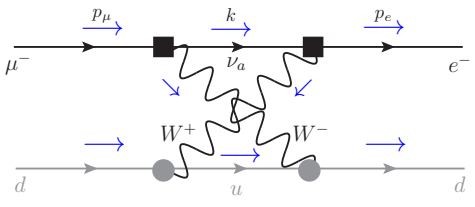

(j) Diagram X

Figure 5.7: One-loop contributions to μ^-– e^- conversion.

pute the loop-integrals. We furthermore use the approximation of a massless electron, which only introduces an error at the sub-% level. We also use the fact that the electron is on-shell and the muon is approximately on-shell (as it is only bound non-relativistically): $p_e^2 = m_e^2 \approx 0$, $p_\mu^2 \simeq m_\mu^2$, and $q'^2 \simeq -m_\mu^2$. In order to obtain the decisive matrix elements, we make use of the Feynman rules given in Appendix A. Let us now go through all contributions in detail. From Diagram I in Fig. 5.7a, we obtain the matrix element:

$$\begin{aligned} i\mathcal{M}_{\mathrm{I}} = &-4Q_S\, e\, f_{ea}^*\, f_{a\mu}\, A_\nu(q')\, \overline{u}_e(p_e) \\ &\int \frac{\mathrm{d}^d k}{(2\pi)^d} \frac{\mathrm{P_L} \not{k} (2p_\mu - 2k + q')^\nu\, u_\mu(p_\mu)}{[k^2 - m_a^2 + i\epsilon][(p_\mu - k + q')^2 - M_S^2 + i\epsilon][(p_\mu - k)^2 - M_S^2 + i\epsilon]}\,, \end{aligned} \tag{5.2.8}$$

where $d = 4 - 2\varepsilon$ is the dimension of the integral, and we have written the matrix element in terms of the charge $Q_S = -2$.[9] We use `Package-X` [416], where the most general form of the matrix element given in Eq. (5.2.1) is put in the form of:

$$\begin{aligned} i\mathcal{M} = i\, e\, A_\nu(q')\, \overline{u}_e(p_e) \Big[&\Big(\gamma^\nu - \frac{\not{q}' q'^\nu}{q'^2}\Big) F_1(q'^2) + \frac{i\,\sigma^{\nu\rho}\, q'_\rho}{m_\mu} F_2(q'^2) + 2\frac{q'^\nu}{m_\mu} F_3(q'^2) \\ &+ \Big(\gamma^\nu - \frac{\not{q}' q'^\nu}{q'^2}\Big) \gamma_5\, G_1(q'^2) + \frac{i\,\sigma^{\nu\rho}\, q'_\rho}{m_\mu} \gamma_5\, G_2(q'^2) + 2\frac{q'^\nu}{m_\mu} \gamma_5\, G_3(q'^2)\Big]\, u_\mu(p_\mu)\,, \end{aligned} \tag{5.2.9}$$

to compute the form factors F_1, F_2, F_3, G_1, G_2, and G_3. The form factors obtained from the `Package-X` computation are related to the ones from Eq. (5.2.1) by:

$$\begin{aligned} f_{\mathrm{E0}}(q^2) &= -F_1(q'^2)\,, \\ f_{\mathrm{M0}}(q^2) &= G_1(q'^2)\,, \\ f_{\mathrm{E1}}(q^2) &= G_2(q'^2)\,, \\ f_{\mathrm{M1}}(q^2) &= F_2(q'^2)\,, \\ f_3(q^2) &= -F_3(q'^2)\,, \\ g_3(q^2) &= -G_3(q'^2)\,. \end{aligned} \tag{5.2.10}$$

Before calculating the factor $\Xi^2_{\mathrm{particle}}$ from the form factors, we will first check our computation by taking a closer look at the UV divergences. Since there is no tree level three-point vertex connecting the muon, the electron, and the photon, and thus no corresponding counterterm in the Lagrangian, the combination of Diagrams I – IV in Fig. 5.7 must be finite. To check this

[9] This seemingly too formal notation serves to display the cancellation of divergences more clearly. Note furthermore that we use the convention $d = 4 - 2\varepsilon$ in contrast to $d = 4 - \epsilon$, which was employed in section 4.1, to ease the comparison with `Package-X`.

explicitly, we extract the divergent part from each matrix element, which for Diagram I is given by:

$$i\mathcal{M}_{\rm I}^{\rm div} = \frac{i}{(4\pi)^2}\,\frac{2}{\varepsilon}\,Q_S\,e\,f_{ea}^*\,f_{a\mu}\,A_\nu(q')\,\overline{u}_e(p_e)\,{\rm P_L}\,\gamma^\nu\,u_\mu(p_\mu)\,. \tag{5.2.11}$$

The matrix element for the second diagram given in Fig. 5.7b yields:

$$\begin{aligned} i\mathcal{M}_{\rm II} = {}& -4Q_{l^+}\,e\,f_{ea}^*\,f_{a\mu}\,A_\nu(q')\,\overline{u}_e(p_e) \\ & \int\frac{{\rm d}^dk}{(2\pi)^d}\,\frac{{\rm P_L}(\not k+\not q'+m_a)\,\gamma^\nu\,(\not k+m_a){\rm P_R}}{[k^2-m_a^2+i\epsilon][(p_\mu-k)^2-M_S^2+i\epsilon][(k+q')^2-m_a^2+i\epsilon]}\,u_\mu(p_\mu)\,, \end{aligned} \tag{5.2.12}$$

where $Q_{l^+}=1$, and it adds

$$i\mathcal{M}_{\rm II}^{\rm div} = -\frac{i}{(4\pi)^2}\,\frac{1}{\varepsilon}\,Q_{l^+}\,e\,f_{ea}^*\,f_{a\mu}\,A_\nu(q')\,\overline{u}_e(p_e)\,{\rm P_L}\,\gamma^\rho\,\gamma^\nu\,\gamma_\rho\,{\rm P_R}\,u_\mu(p_\mu) \tag{5.2.13}$$

to the divergent part.
From Fig. 5.7c, we extract:

$$\begin{aligned} i\mathcal{M}_{\rm III} = {}& -4Q_{e^-}\,e\,f_{ea}^*\,f_{a\mu}\,A_\nu(q') \\ & \overline{u}_e(p_e)\int\frac{{\rm d}^dk}{(2\pi)^d}\,\frac{\gamma^\nu\not p_\mu\,{\rm P_L}\not k}{[p_\mu^2+i\epsilon][(p_\mu-k)^2-M_S^2+i\epsilon][k^2-m_a^2+i\epsilon]}\,u_\mu(p_\mu)\,, \end{aligned} \tag{5.2.14}$$

with $Q_{e^-}=-1$, and obtain

$$i\mathcal{M}_{\rm III}^{\rm div} = -\frac{i}{(4\pi)^2}\,\frac{2}{\varepsilon}\,\frac{Q_{e^-}}{m_\mu^2}\,e\,f_{ea}^*\,f_{a\mu}\,A_\nu(q')\,\overline{u}_e(p_e)\,\gamma^\nu\not p_\mu\,{\rm P_L}\not p_\mu\,u_\mu(p_\mu)\,. \tag{5.2.15}$$

Finally, the matrix element of Fig. 5.7d leads to:

$$\begin{aligned} i\mathcal{M}_{\rm IV} = {}& -4Q_{\mu^-}\,e\,f_{ea}^*\,f_{a\mu}\,A_\nu(q')\,\overline{u}_e(p_e) \\ & \int\frac{{\rm d}^dk}{(2\pi)^d}\,\frac{{\rm P_L}\not k\,(\not p_\mu+\not q'+m_\mu)\,\gamma^\nu\,u_\mu(p_\mu)}{[(p_\mu+q')^2-m_\mu^2+i\epsilon][(p_\mu-k+q')^2-M_S^2+i\epsilon][k^2-m_a^2+i\epsilon]}\,, \end{aligned} \tag{5.2.16}$$

with $Q_{\mu^-}=-1$, and thus a divergent contribution of

$$i\mathcal{M}_{\rm IV}^{\rm div} = \frac{i}{(4\pi)^2}\,\frac{2}{\varepsilon}\,\frac{Q_{\mu^-}}{m_\mu^2}\,e\,f_{ea}^*\,f_{a\mu}\,A_\nu(q')\,\overline{u}_e(p_e)\,{\rm P_L}\,(\not p_\mu+\not q')\,(\not p_\mu+\not q'+m_\mu)\,\gamma^\nu\,u_\mu(p_\mu)\,. \tag{5.2.17}$$

In $d=4$ dimensions, the Lorentz structures simplify due to the relations $\gamma^\rho\,\gamma^\nu\,\gamma_\rho=-2\gamma^\nu$ and $\not p\not p=p^2$, and upon employing the approximate on-shell

conditions. As a consequence, the divergent part of the $\mu^- - e^-$ conversion amplitude takes the form:

$$i\mathcal{M}^{\text{div}} = \frac{i}{(4\pi)^2}\,\frac{1}{\varepsilon}\,e\,f^*_{ea}\,f_{a\mu}\,A_\nu(q')\,\overline{u}_e(p_e)\,[(2Q_S+2Q_{l^+}-Q_{e^-}-Q_{\mu^-})\mathrm{P_L}\,\gamma^\nu]\,u_\mu(p_\mu)\,, \tag{5.2.18}$$

which indeed vanishes as soon as we enter the charges explicitly, as to be expected.

Checking with `Package-X` confirms that, indeed, all form factors are finite. It also shows that, under the assumption of both the muon and the electron being approximately on-shell, in combination with kinematic relations following a vanishingly small momentum of the nucleus, both F_3 and G_3 vanish exactly. This confirms the general structure in Eq. (5.2.1) for the photonic case and agrees with the considerations of the previous segment on the physics of $\mu^- - e^-$ conversion, where the same arguments led to $q^0 = -q'^0 \to 0$ and thereby to the disappearance of these structures from the branching ratio.

We have also extracted the finite parts of the form factors, which are the actual physics contributions. They take the following forms:

$$\begin{aligned}
&F_1(-m_\mu^2) = G_1(-m_\mu^2) = \\
&= -\frac{1}{128\,\pi^2 m_\mu^4}\sum_{a=e,\,\mu,\,\tau} f^*_{ea}\,f_{a\mu}\Big[2\,m_\mu^2(-5m_a^2+6m_\mu^2+5M_S^2) - 2\,S_a\,m_\mu^2 \\
&\quad (m_a^2+3m_\mu^2-M_S^2)\,\ln\Big[\frac{2m_a^2}{2m_a^2+m_\mu^2(1+S_a)}\Big] + 4\,S_S\,m_\mu^2(m_a^2+m_\mu^2-M_S^2) \\
&\quad \ln\Big[\frac{2M_S^2}{2M_S^2+m_\mu^2(1+S_S)}\Big] + \Big(3m_a^2(2m_a^2-m_\mu^2-4M_S^2)+5m_\mu^4-7m_\mu^2\,M_S^2\Big) \\
&\quad + 6M_S^4\Big)\ln\Big[\frac{m_a^2}{M_S^2}+2\,T_a(-6m_a^2+m_\mu^2+6M_S^2)\ln\Big[\frac{2m_a\,M_S}{m_a^2-m_\mu^2+M_S^2-T_a}\Big] \\
&\quad + 2\,m_\mu^2\Big[\Big(m_a^4+8m_a^2\,m_\mu^2+M_S^4-2M_S^2(m_a^2+2m_\mu^2)\Big) \\
&\quad C_0[0,\,-m_\mu^2,\,m_\mu^2;\,m_a,\,M_S,\,m_a] \\
&\quad + 2\Big(m_a^4-2M_S^2(m_a^2-2m_\mu^2)+M_S^4\Big)\,C_0[0,\,-m_\mu^2,\,m_\mu^2;\,M_S,\,m_a,\,M_S]\Big]\Big]\,,
\end{aligned} \tag{5.2.19}$$

as well as

$$\begin{aligned}
&F_2(-m_\mu^2) = -G_2(-m_\mu^2) = \\
&= -\frac{1}{128\,\pi^2 m_\mu^4}\sum_{a=e,\,\mu,\,\tau} f^*_{ea}\,f_{a\mu}\Big[2\,m_\mu^2(-m_a^2+6m_\mu^2+M_S^2) + 2\,S_a\,m_\mu^2(3m_a^2 \\
&\quad + m_\mu^2-3M_S^2)\,\ln\Big[\frac{2m_a^2}{2m_a^2+m_\mu^2(1+S_a)}\Big] + 4\,S_S\,m_\mu^2(-3m_a^2+m_\mu^2+3M_S^2) \\
&\quad \ln\Big[\frac{2M_S^2}{2M_S^2+m_\mu^2(1+S_S)}\Big] + \Big(m_a^2(-2m_a^2-7m_\mu^2+4M_S^2)+m_\mu^4+5m_\mu^2\,M_S^2
\end{aligned}$$

$$
\begin{aligned}
&- 2M_S^4\Big) \ln\Big[\frac{m_a^2}{M_S^2}\Big] + 2\,T_a(2m_a^2 - 3m_\mu^2 - 2M_S^2)\,\ln\Big[\frac{2m_a\,M_S}{m_a^2 - m_\mu^2 + M_S^2 - T_a}\Big] \\
&+ 2\,m_\mu^2\Big[\Big(- 3m_a^4 - 3M_S^4 + 2M_S^2(3m_a^2 + 2m_\mu^2)\Big) \\
&C_0[0,\, -m_\mu^2,\, m_\mu^2;\, m_a,\, M_S,\, m_a] \\
&+ 2\Big(- 3m_a^4 + 2m_a^2(3M_S^2 + 2m_\mu^2) - 3M_S^4\Big)\, C_0[0,\, -m_\mu^2,\, m_\mu^2;\, M_S,\, m_a,\, M_S]\Big]\Big].
\end{aligned}
\tag{5.2.20}
$$

Here, we have used the following abbreviations:

$$
\begin{aligned}
&S_i \equiv \sqrt{1 + 4m_i^2/m_\mu^2}\,, \qquad S_S \equiv \sqrt{1 + 4M_S^2/m_\mu^2}\,, \qquad \text{and} \\
&T_a \equiv \sqrt{(m_a - m_\mu - M_S)(m_a + m_\mu - M_S)(m_a - m_\mu + M_S)(m_a + m_\mu + M_S)}.
\end{aligned}
\tag{5.2.21}
$$

Moreover, the scalar three-point function in four dimensions is given by [416]:

$$
\begin{aligned}
C_0[p_1^2,\, p_2^2,\, Q^2; m_2,\, m_1,\, m_0] = -\int_0^1 \mathrm{d}x \int_0^{1-x} \mathrm{d}y \,\Big[p_1^2\, x^2 + p_2^2\, y^2 \\
+ (p_1^2 + p_2^2 - Q^2)xy + (m_1^2 - m_0^2 - p_1^2)x + (m_2^2 - m_0^2 - p_2^2)y + m_0^2 - i\epsilon\Big]^{-1},
\end{aligned}
\tag{5.2.22}
$$

which corresponds to the assignment given in Fig. B.1 in Appendix B, and which makes use of $Q \equiv p_1 - p_2$.

The scalar three-point function in Eq. (5.2.22) agrees with the original one by Passarino and Veltman [421–423] upon rearranging the mass terms and considering the change of metric,[10] such that

$$
C_0[p_1^2,\, p_2^2,\, Q^2; m_2,\, m_1,\, m_0] = -C_0^{\text{Passarino}-\text{Veltman}}[-p_1^2,\, -p_2^2,\, -Q^2; m_1,\, m_0,\, m_2]\,.
$$

Inserting the form factors listed in Eqs. (5.2.19) and (5.2.20) into Eq. (5.2.5), we eventually obtain:

$$
\begin{aligned}
\Xi^2_{\text{particle}} &= \Big|f_{\text{E0}}(-m_\mu^2) + f_{\text{M1}}(-m_\mu^2)\Big|^2 + \Big|f_{\text{M0}}(-m_\mu^2) + f_{\text{E1}}(-m_\mu^2)\Big|^2 \\
&= \Big| - F_1(-m_\mu^2) + F_2(-m_\mu^2)\Big|^2 + \Big|G_1(-m_\mu^2) + G_2(-m_\mu^2)\Big|^2 \\
&= 2\,\Big|F_1(-m_\mu^2) - F_2(-m_\mu^2)\Big|^2 \\
&= \frac{1}{512\,\pi^4\,m_\mu^8}\,\Bigg|\sum_{a=e,\,\mu,\,\tau} f_{ea}^*\, f_{a\mu}\,\Bigg(2\,m_\mu^2(m_a^2 - M_S^2) + 4\,S_S\,m_\mu^2(M_S^2 - m_a^2)\times
\end{aligned}
$$

[10] In order to compare the scalar three-point function from Passarino and Veltman with the one given in Eq. (5.2.22), one needs to switch the Minkowski metric from $(-1, 1, 1, 1)$ to $(1, -1, -1, -1)$. One also needs to shift the outer Feynman parameter $x = 1 - x'$, such that $\int_0^1 \mathrm{d}x \int_0^x \mathrm{d}y \to \int_0^1 \mathrm{d}x' \int_0^{1-x'} \mathrm{d}y$.

$$\ln\Big[\frac{2M_S^2}{2M_S^2+m_\mu^2(1+S_S)}\Big]+2\,S_a\,m_\mu^2(m_a^2+m_\mu^2-M_S^2)\,\ln\Big[\frac{2m_a^2}{2m_a^2+m_\mu^2(1+S_a)}\Big]$$
$$-(2m_a^4+m_\mu^4-3m_\mu^2\,M_S^2+2M_S^4+m_a^2\,m_\mu^2-4m_a^2\,M_S^2)\ln\Big[\frac{m_a^2}{M_S^2}\Big]$$
$$+2\,T_a(2m_a^2-m_\mu^2-2M_S^2)\,\ln\Big[\frac{2m_a\,M_S}{m_a^2-m_\mu^2+M_S^2-T_a}\Big]$$
$$+2\,m_\mu^2(m_a^2-M_S^2)\Big[(-m_a^2-2m_\mu^2+M_S^2)\,C_0[0,\,-m_\mu^2,\,m_\mu^2;\,m_a,\,M_S,\,m_a]$$
$$+2(-m_a^2+m_\mu^2+M_S^2)\,C_0[0,\,-m_\mu^2,\,m_\mu^2;\,M_S,\,m_a,\,M_S]\Big]\Big)\Big|^2\,. \tag{5.2.23}$$

We can greatly simplify this expression by exploiting the mass hierarchy $M_S \gg m_{e,\mu,\tau}$. Hence, each term in Eq. (5.2.23) is expanded around $M_S \to \infty$ up to $\mathcal{O}(1/M_S^2)$, which has to be done in a careful manner.[11] That way, we observe delicate cancellations at the orders M_S^4, M_S^2, and M_S^0, such that the remaining expression takes the much simpler form

$$\Xi^2_{\text{particle}} = \frac{1}{288\,\pi^4\,m_\mu^2\,M_S^4}\Big|\sum_{a=e,\,\mu,\,\tau} f_{ea}^*\,f_{a\mu}\Big(4m_a^2\,m_\mu-m_\mu^3+2(-2m_a^2+m_\mu^2)$$
$$\sqrt{4m_a^2+m_\mu^2}\;\text{Arctanh}\Big[\frac{m_\mu}{\sqrt{4m_a^2+m_\mu^2}}\Big]+m_\mu^3\,\ln\Big[\frac{m_a^2}{M_S^2}\Big]\Big)\Big|^2\,, \tag{5.2.24}$$

at leading order. Including the next-to-leading contribution would change our result by roughly 4%/at the per mille level for the τ contribution/the μ or e contributions being dominant, as we have checked numerically. Note that the cancellations mentioned may not materialise numerically when employing the full expression in Eq. (5.2.23), in case large numbers are not treated with sufficient accuracy in a numerical computation.

[11] While the expansion of the first few terms does not make a problem, the Passarino-Veltman functions require a cautious treatment. To this end, we rewrite the Passarino-Veltman functions in terms of dilogarithms. Instead of the `Mathematica` function `PolyLog[2,x]`, `Package-X` [416] uses its own function `DiLog[x,A]`. The latter has a branch cut discontinuity in the complex x-plane running from 1 to ∞. For real $x \leq 1$ or complex x the `DiLog[x,A]` is equivalent to `PolyLog[2,x]`. However, for real $x > 1$, the side of the branch cut which `DiLog[x,A]` evaluates is given by the prescription $\lim_{\epsilon\to 0}\text{Li}_2[x+iA\epsilon]$. Thus, the sign of A fixes where `DiLog` evaluates. To expand the `DiLog` functions in the limit $M_S \to \infty$, we need to insert numerical values for A. Since the A's all consist of combinations of m_a, m_μ, and M_S, we fix the scalar mass within A to an arbitrary value (considering $M_S \gg m_a$), and expand the remaining function.

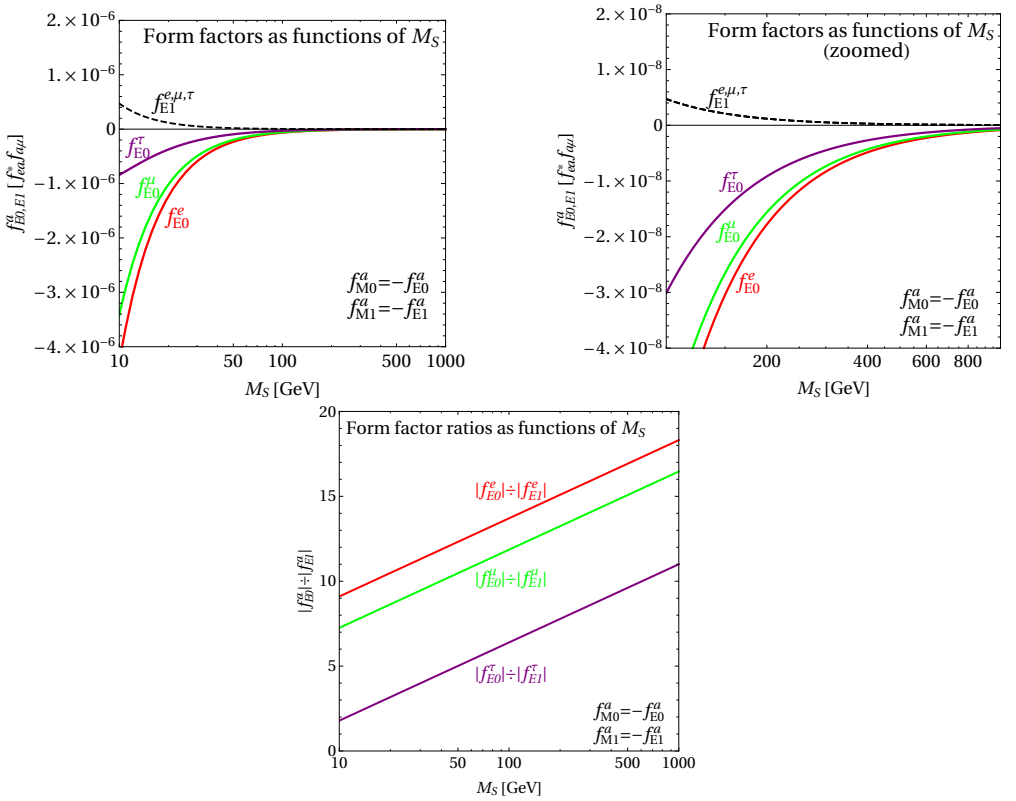

Figure 5.8: Form factors and ratios of form factors as functions of M_S.

Let us take a moment to compare our results to the previous ones obtained in Ref. [375], based on an estimate using EFT. We should in fact recover the results obtained there in the limit of a sufficiently heavy scalar. To perform this consistency check, it is first of all useful to look at the form factors themselves, which are displayed in the upper two panels of Fig. 5.8 (in a zoomed version in the upper right case), in units of $f^*_{ea}f_{a\mu}$. As can be seen, the magnitudes of the form factors $f^a_{\rm E0}$ $(= -f^a_{\rm M0})$ are in all cases $a = e, \mu, \tau$ bigger for smaller scalar masses, however, they later on decrease from $\mathcal{O}(10^{-8})$ – $\mathcal{O}(10^{-7})$ for $M_S \sim 100$ GeV to $\mathcal{O}(10^{-10})$ – $\mathcal{O}(10^{-9})$ for $M_S \sim 1000$ GeV. The form factors $f^a_{\rm E1} = -f^a_{\rm M1}$, in turn, do not depend on the charged lepton masses and decrease from about $\mathcal{O}(10^{-9})$ for $M_S \sim 100$ GeV to $\mathcal{O}(10^{-11})$ for $M_S \sim 1000$ GeV. That already implies that the approximation for the numerical values of the form factors used in Ref. [375] for the case of doubly charged scalars is only accurate to about 10%. This can also be seen from the lower panel of Fig. 5.8, displaying the ratio between the form factors $f^a_{\rm E0}$ and $f^a_{\rm E1}$, and it implies a percent accuracy of the photonic decay rate when computed with $f^a_{\rm E1}$ and $f^a_{\rm M1}$ being neglected. Note that, however, as we will see in section 5.2.2, non-photonic short-range contributions can lead to a modification of the same size.

For completeness, let us display the explicit versions of the purely photonic

form factors in the limit of a very large M_S:

$$\begin{aligned}
\frac{f^a_{\mathrm{E0}}}{f^*_{ea} f_{a\mu}} &= -\frac{f^a_{\mathrm{M0}}}{f^*_{ea} f_{a\mu}} = \frac{2m_a^2 + m_\mu^2 \log\left(\frac{m_a}{M_S}\right)}{12\pi^2 M_S^2} + \frac{\sqrt{m_\mu^2 + 4m_a^2}(m_\mu^2 - 2m_a^2)}{12\pi^2 m_\mu M_S^2} \times \\
&\qquad \mathrm{Arctanh}\left(\frac{m_\mu}{\sqrt{m_\mu^2 + 4m_a^2}}\right), \\
\frac{f^a_{\mathrm{E1}}}{f^*_{ea} f_{a\mu}} &= -\frac{f^a_{\mathrm{M1}}}{f^*_{ea} f_{a\mu}} = \frac{m_\mu^2}{24\pi^2 M_S^2},
\end{aligned} \tag{5.2.25}$$

evaluated at $q^2 = -m_\mu^2$. While our formulae for the form factors are basically identical to those obtained in Ref. [375], note that this reference seems to contain a relative sign difference between f_{E0} and f_{M0} compared to our results, which can alter the resulting numerical predictions. Given that we have automatised our computation to a high degree and that we have explicitly performed several decisive cross-checks, such as showing that the divergent parts of the loop amplitudes contained in Eqs. (5.2.11), (5.2.13), (5.2.15), and (5.2.17) do indeed cancel, we are confident that all our relative signs should be correct.

The expression displayed in Eq. (5.2.24) is our final result for the photonic contribution of the doubly charged scalar to $\mu^- - e^-$ conversion. In combination with Eq. (5.2.2), it can be used to compute the corresponding branching ratio for any choice of Yukawa couplings f_{ab} and scalar mass M_S, as long as the nuclear physics quantities entering the equations are known. However, these quantities suffer from uncertainties which we currently cannot resolve. Thus, when aiming at a bound on the squared particle physics amplitude displayed in Eq. (5.2.24), it is easiest to absorb all uncertainties into the experimental bounds, meaning that an experimental upper bound on the branching ratio translates into a range of upper bounds on $\Xi^2_{\mathrm{particle}}$. This one can do as long as the nuclear physics and particle physics parts factorise, as is the case in Eq. (5.2.2).

Resulting bounds

The main nuclear physics quantities entering the branching ratio in Eq. (5.2.2) are Z, Z_{eff}, and F_p. We have taken into consideration those isotopes for which either existing limits can be found or which are planned to be used in future experiments. A detailed discussion on both the nuclear physics and the experimental aspects is given in section 5.1. Note that, as long as the particle physics and the nuclear physics parts factorise, see Eq. (5.2.2), all nuclear physics dependence can be absorbed into the experimental bounds. Hence, we can conveniently compare bounds from different experiments which constrain

the same particle physics amplitude.

To get a first impression of the limits one can obtain from this process, we ignore relative phases for the time being, i.e., we take $f_{ab}^* = f_{ab}$. To get a feeling for how strong the constraints could get, we choose the following scenarios: as limiting cases we take a rather optimistic scenario with comparatively large couplings, $f_{ab} = 10^{-2}$ ($\forall a, b = e, \mu, \tau$) (in black), and a rather pessimistic scenario with small couplings, $f_{ab} = 10^{-4}$ (in grey). As we will see, these scenarios indeed comprise "envelopes" of the more concrete scenarios, although of course they comprise no strict boundaries. E.g., even more "optimistic" scenarios could be consistent with data if the scalar mass M_S was chosen to be sufficiently large.
On the other hand, three categories of valid benchmark points, referred to as red, purple, and blue scenarios, were introduced in section 3.3 based on Ref. [47]. These categories of points were chosen such that they reproduce all relevant low-energy phenomenology, i.e., all neutrino oscillation parameters as well as all LFV/LNV bounds, with $\mu^- - e^-$ conversion being the only exception. Note that the consistency of these benchmark categories partially arises from correlations, like $f_{e\mu} \simeq -\frac{f_{\mu\tau}^*}{f_{\mu\mu}^*} f_{e\tau}$ for the purple points, which lead to cancellations in the rate for $\mu \to e\gamma$. However, these cancellations do not appear anymore in $\mu^- - e^-$ conversion, as we will illustrate below. In order to not only show a few isolated points as found in Ref. [47], we will for illustrative purposes present idealised scenarios which roughly correspond to the three categories of benchmark points. The explicit parameter choices for these scenarios are displayed in Tab. 5.2, and they approximately correspond to the average of the values reported in Tab. 7 of Ref. [47], which we present as Fig. 3.4 in section 3.3.

We are now ready to present our results for $\mu^- - e^-$ conversion when only taking into account the photonic (predominantly long-range) contributions. Fig. 5.9 summarises all the information we have collected so far, and it also illustrates how strongly the doubly charged scalar mass can be constrained. We have displayed the particle physics parts of the amplitude as functions of the doubly charged scalar mass M_S, i.e., the photonic/long-range contribution Ξ_{particle} from Eq. (5.2.24). The next step is to compare the predictions to the experimental bounds. As already indicated in section 5.1, we have collected several current (SINDRUM II [383, 385, 411]) and future (DeeMe [412], COMET [208], Mu2e [366], PRISM/PRIME [45]) limits on the branching ratio of $\mu^- - e^-$ conversion. However, due to both nuclear physics uncertainties and experiments on different isotopes potentially pushing one and the same particle physics observable, we have decided to display a range of bounds in Fig. 5.9. Thereby, the nominally best limits are represented by the bold horizontal lines, and the variation among the different isotopes and/or experiments is indicated by the lightly coloured rectangles, which absorb all uncertainties as long as the

	red	**purple**	**blue**
f_{ee}	10^{-16}	10^{-15}	10^{-1}
$f_{e\mu}$	10^{-2}	10^{-3}	10^{-4}
$f_{e\tau}$	10^{-19}	10^{-2}	10^{-2}
$f_{\mu\mu}$	10^{-4}	10^{-3}	10^{-3}
$f_{\mu\tau}$	10^{-5}	10^{-4}	10^{-4}
$f^*_{ee}\, f_{e\mu}$	10^{-18}	10^{-18}	$\mathbf{10^{-5}}$
$f^*_{e\mu}\, f_{\mu\mu}$	$\mathbf{10^{-6}}$	$\mathbf{10^{-6}}$	10^{-7}
$f^*_{e\tau}\, f_{\mu\tau}$	10^{-24}	$\mathbf{10^{-6}}$	10^{-6}

Table 5.2: *Upper part*: Couplings for the three scenarios discussed in the text. *Lower part*: Combinations of couplings entering the $\mu^- - e^-$ conversion amplitude. Bold figures indicate the dominant contributions.

particle physics part of the amplitude can be extracted. Moreover, we have included the sensitivity expected to be reached in Phase I of COMET. The corresponding bound of $\Xi^{\rm Al}_{\rm particle} = 3.87 \cdot 10^{-15}$ on the particle physics observable is represented by the dashed green line and stems from the single event sensitivity of $\mathrm{BR}(\mu^- \mathrm{Al} \to e^- \mathrm{Al}) = 3.1 \cdot 10^{-15}$ reported in Ref. [424]. Note that we have *not* indicated the variation with nuclear physics uncertainties, because we have not found any reliable up-to-date information. It is however evident how to include information on this point, so that it will be easy to update our plot once this information becomes available.

Looking at the numbers, it is evident that we can in fact obtain very strong bounds on the doubly charged scalar mass from not having observed $\mu^- - e^-$ conversion. In Tab. 5.3, we have displayed both the current limits and the future sensitivities, as well as the sensitivity that will be reached within COMET's Phase I. The ranges displayed in Tab. 5.3 are obtained by taking both the most optimistic (i.e., the bold horizontal lines in Fig. 5.9) and the most pessimistic (i.e., the upper edges of the lightly coloured rectangles in Fig. 5.9) bounds at face value. This accounts for the possible variations among the different experiments. However, we would like to stress once more that further variations due to nuclear physics uncertainties may well be possible. While these are not expected to dramatically change our results, they may be able to at least change the last few digits in the figures quoted in Tab. 5.3. Nevertheless, it is evident that even the most pessimistic limits are in fact quite impressive, revealing that, for doubly charged scalars, $\mu^- - e^-$ conversion may be able to lead to bounds stronger than those obtained by colliders [1], see also section 5.2.4.

The question to answer is why the bounds from $\mu^- - e^-$ conversion seem to

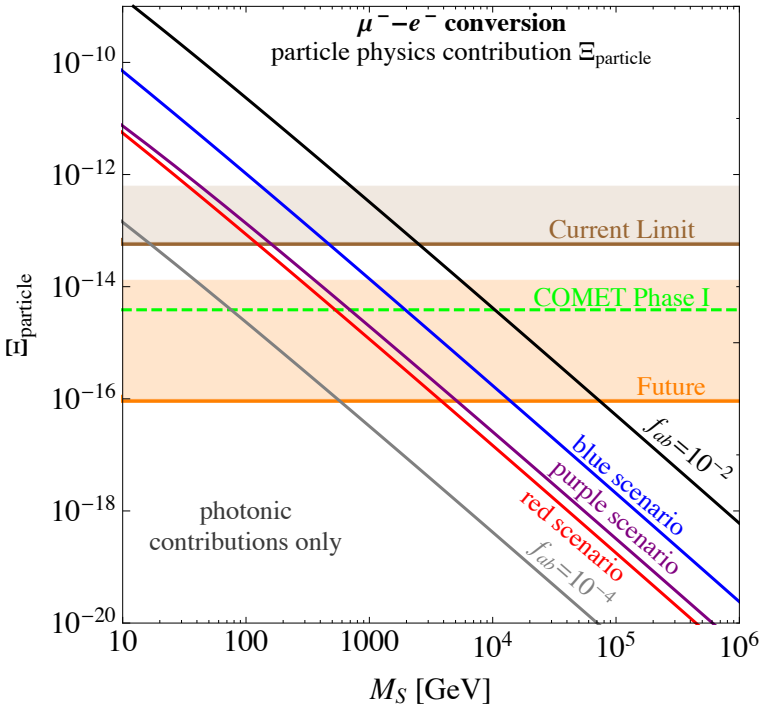

Figure 5.9: Bounds on the particle physics contribution Ξ_{particle} arising from the photonic (mainly long-range) contributions only.

be significantly stronger than those for $\mu \to e\,\gamma$ obtained in Ref. [47]. This is particularly surprising when disregarding the non-photonic short-range contributions, as we have done up to this point, since then at first sight $\mu^- - e^-$ conversion looks just like a $\mu \to e\,\gamma$ diagram attached to a nucleus, see Fig. 5.7. However, the result can be understood by carefully comparing the amplitudes for both processes. The branching ratio of $\mu \to e + \gamma$ depends on an amplitude of the form:

$$\mathcal{A} \propto |f^*_{ee}\, f_{e\mu} + f^*_{e\mu}\, f_{\mu\mu} + f^*_{e\tau}\, f_{\tau\mu}| \cdot C, \tag{5.2.26}$$

where C is a flavour-independent constant incorporating all non-Yukawa couplings (see also Tab. 3.1). As explained in detail in section 3.3, the benchmark points in Ref. [47] had been chosen such that all experimental bounds are fulfilled. In particular for the purple and blue points, cancellations appear in Eq. (5.2.26), which allow to evade the (quite strong) bound from $\mu \to e\,\gamma$. On the other hand, glancing at Eq. (5.2.24), the amplitude for $\mu^- - e^-$ conversion is of the form:

$$\mathcal{A} \propto |C_e\, f^*_{ee}\, f_{e\mu} + C_\mu\, f^*_{e\mu}\, f_{\mu\mu} + C_\tau\, f^*_{e\tau}\, f_{\tau\mu}|, \tag{5.2.27}$$

where now the "constant" C from Eq. (5.2.26) has gained a flavour dependence, $C \to C_{e,\mu,\tau}$. Thus, one cannot simply extract this factor from the amplitude in Eq. (5.2.27) and, in particular, the cancellations at work to evade the $\mu \to e\,\gamma$ bound will not work for $\mu^- - e^-$ conversion anymore. Instead, comparatively

	current limit	future sensitivity	COMET I (^{27}Al)
black	$M_S > 708.6 - 2390.2$	$M_S > 5500.0 - 70369.3$	$M_S > 10401.9$
blue	$M_S > 131.9 - 447.1$	$M_S > 1031.5 - 13271.3$	$M_S > 1954.1$
purple	$M_S > 42.5 - 152.3$	$M_S > 360.7 - 4885.2$	$M_S > 694.5$
red	$M_S > 33.9 - 118.1$	$M_S > 276.3 - 3656.1$	$M_S > 528.0$
grey	$M_S > 4.1 - 15.9$	$M_S > 38.7 - 548.7$	$M_S > 75.7$

Table 5.3: Lower limits on the mass M_S in GeV resulting from $\mu^- - e^-$ conversion, displaying the range from the most pessimistic to the most optimistic values. Figures are deliberately shown with a too good precision, in order to ease the comparison with Tab. 5.4.

large values of the Yukawa couplings are strongly constrained by the experimental limits. This is perfectly consistent with the figures quoted in the lower part of Tab. 5.2, where the sizes of the combinations $(f^*_{ee} f_{e\mu}, f^*_{e\mu} f_{\mu\mu}, f^*_{e\tau} f_{\tau\mu})$ appearing in Eq. (5.2.27) are estimated for the three scenarios. The largest such combination appears for the blue scenario, $|f^*_{ee} f_{e\mu}| \sim 10^{-5}$, while the red and purple scenarios instead seem to yield a very similar size. Indeed this tendency is perfectly visible in both Fig. 5.9 and Tab. 5.3, where the bounds on the blue scenario indeed turn out to be stronger than those on the red and purple scenarios, which look rather similar.

Summing up, we have shown that already the photonic (predominantly long-range) contributions to $\mu^- - e^-$ conversion lead to comparatively strong lower bounds on the scalar mass M_S.

5.2.2 Non-photonic contributions

The next step is to include the non-photonic (short-range) contributions to $\mu^- - e^-$ conversion.

Computing the form factors

The non-photonic contributions to the $\mu^- - e^-$ conversion amplitude are commonly subsumed into four fermion interactions, i.e., we are considering point-like (short-range) operators coupling one μ^- and one e^- to two quarks. It is a priori not clear whether these contributions could modify the $\mu^- - e^-$ conversion rate significantly. Quite generally, including these terms spoils the factorisation of the branching ratio into nuclear physics and particle physics parts, such that Eq. (5.2.2) is not applicable anymore. In general, the effect on the particle physics amplitude will be to now turn into a combined amplitude incorporating both photonic (mainly long-range) and non-photonic (short-range) contributions, the latter being dependent on Z and N:

$$\Xi_{\text{particle}} \to \Xi_{\text{combined}}(Z,N) = \Xi_{\text{photonic}} + \Xi_{\text{non-photonic}}(Z,N).$$

However, as we will see, in our case the non-photonic short-range contributions turn out to be completely *subdominant*. Thus, although Eq. (5.2.2) is in general *not* correct, applying it would introduce only a very small error, and we can thus approximate $\Xi_{\text{particle}} \simeq \Xi_{\text{photonic}}$ to a very good precision. We will in the following illustrate how to explicitly compute the non-photonic short-range contributions to $\mu^- - e^-$ conversion.

Considering effective operators up to dimension-six, a general interaction of an electron and a muon with two quarks is described by [211]:

$$\begin{aligned}\mathcal{L}_{\text{non-photonic}} = -\frac{G_F}{\sqrt{2}} \sum_{q=u,d,s,\cdots} \Big[&\Big(g_{LS(q)} \overline{e_{\text{L}}}\, \mu_{\text{R}} + g_{\text{RS}(q)} \overline{e_{\text{R}}}\, \mu_{\text{L}}\Big) \overline{q}\, q \\ &+ \Big(g_{\text{LP}(q)} \overline{e_{\text{L}}}\, \mu_{\text{R}} + g_{\text{RP}(q)} \overline{e_{\text{R}}}\, \mu_{\text{L}}\Big) \overline{q}\, \gamma_5\, q \\ &+ \Big(g_{\text{LV}(q)} \overline{e_{\text{L}}}\, \gamma^\nu\, \mu_{\text{L}} + g_{\text{RV}(q)} \overline{e_{\text{R}}}\, \gamma^\nu\, \mu_{\text{R}}\Big) \overline{q}\, \gamma_\nu\, q \\ &+ \Big(g_{\text{LA}(q)} \overline{e_{\text{L}}}\, \gamma^\nu\, \mu_{\text{L}} + g_{\text{RA}(q)} \overline{e_{\text{R}}}\, \gamma^\nu\, \mu_{\text{R}}\Big) \overline{q}\, \gamma_\nu\, \gamma_5\, q \\ &+ \frac{1}{2}\Big(g_{\text{LT}(q)} \overline{e_{\text{L}}}\, \sigma^{\nu\rho}\, \mu_{\text{R}} + g_{\text{RT}(q)} \overline{e_{\text{R}}}\, \sigma^{\nu\rho} \mu_{\text{L}}\Big) \overline{q}\, \sigma_{\nu\rho}\, q + \text{h.c.}\Big]\,. \end{aligned} \tag{5.2.28}$$

The effective four-fermion couplings given above originate from integrating out all particles which could possibly be exchanged between two quarks and two charged leptons. In our setup, the dominant non-photonic contribution arises from the Z-boson exchange between two quarks in the nucleus and the particle physics loop, depicted in Diagrams I to IV in Figs. 5.7. The terms involving neutrinos in the loops are again GIM-suppressed [44], which is the case for both categories, penguin diagrams (Diagrams V to VIII) and box-diagrams (Diagrams IX and X). The diagrams based on Higgs exchange are suppressed even further, a back-of-the-envelope estimate resulting in a suppression of $\mathcal{O}(10^{-3})$ compared to the other non-photonic short-range contributions, which are already suppressed themselves. We will thus completely disregard the diagrams based on Higgs-exchange. Note that, in order to consistently obtain the form factors $g_{\text{XK}(q)}$ (X = R, L and K = S, P, V, A, T), we match the relevant set of diagrams to the four fermion operators using a generic μ-e-Z interaction Γ_ν, see Fig. 5.10.

The Feynman rules tell us:

$$\begin{aligned} i\mathcal{M} =& \overline{u}_e(p_e)\, \Gamma_\nu\, u_\mu(p_\mu) \times \frac{-i}{q'^2 - M_Z^2} \left(g^{\nu\rho} - \frac{q'^\nu q'^\rho}{M_Z^2}\right) \\ &\times \overline{q}\, \frac{ig}{4\cos\theta_W}\, \gamma_\rho \Big[1 + k_q \sin^2\theta_W + s_q\, \gamma_5\Big] q\,, \end{aligned} \tag{5.2.29}$$

for the "full theory" diagram on the left. Here, the coefficients k_q and s_q depend on the quark being up- or down-type: $k_{d,s,b} = 4/3$, $s_{d,s,b} = 1$, $k_{u,c,t} = -8/3$,

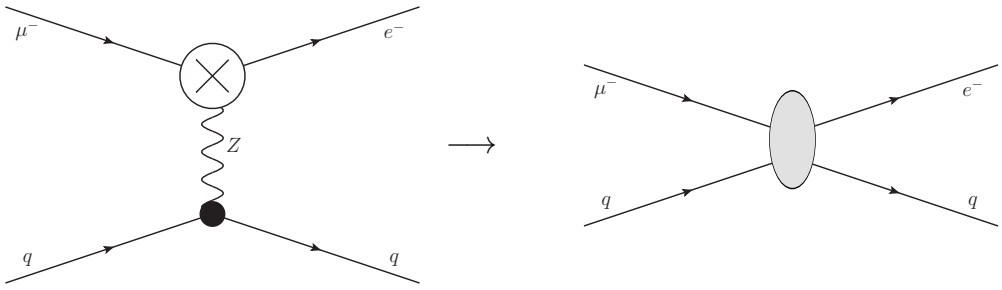

Figure 5.10: Integrating out the Z-boson results into a non-photonic short-range contribution.

and $s_{u,c,t} = -1$. By contracting the bosonic propagator, i.e. taking the limit $M_Z^2 \gg q'^2$, the matrix element takes the form:

$$\begin{aligned} i\mathcal{M} &= \overline{u}_e(p_e)\,\Gamma_\nu\; u_\mu(p_\mu)\,\frac{i}{M_Z^2}\,g^{\nu\rho}\,\overline{q}\,\frac{ig}{4\cos\theta_W}\,\gamma_\rho\left[1 + k_q\,\sin^2\theta_W + s_q\,\gamma_5\right]q \\ &= -\frac{g}{4M_Z^2\,\cos\theta_W}\,\overline{u}_e(p_e)\,\Gamma_\nu\,u_\mu(p_\mu)\left[(1 + k_q\,\sin^2\theta_W)\underbrace{\boxed{\overline{q}\,\gamma^\nu\,q}}_{\text{vector coupling}} + s_q\underbrace{\boxed{\overline{q}\,\gamma^\nu\,\gamma_5\,q}}_{\substack{\text{axial vector}\\ \text{coupling}}}\right]. \end{aligned} \tag{5.2.30}$$

Apparently, only the vector and axial vector structures are realised. Since we consider coherent $\mu^- - e^-$ conversion, however, only the vector coupling will ultimately contribute to the branching ratio. Taking into account gauge invariance, the most general form for the generic coupling Γ_ν in terms of "chiral" form factors can be written as [416]:

$$\begin{aligned} \Gamma_\nu =& \gamma_\nu\,\mathrm{P_L}\,A_\mathrm{L}\,(q'^2) + \frac{i\sigma_{\nu\rho}\,q'^\rho}{m_\mu + m_e}\,\mathrm{P_L}\,B_\mathrm{L}(q'^2) + 2\frac{q'_\nu}{m_\mu + m_e}\,\mathrm{P_L}\,C_\mathrm{L}(q'^2) \\ &+ \gamma_\nu\,\mathrm{P_R}\,A_\mathrm{R}\,(q'^2) + \frac{i\sigma_{\nu\rho}\,q'^\rho}{m_\mu + m_e}\,\mathrm{P_R}\,B_\mathrm{R}(q'^2) + 2\frac{q'_\nu}{m_\mu + m_e}\,\mathrm{P_R}\,C_\mathrm{R}(q'^2)\,. \end{aligned} \tag{5.2.31}$$

However, as mentioned earlier, we only take into account effective operators with mass dimension up to six. Since the combined mass dimension of four spin-1/2 fields and the momentum q' already exceeds dimension six, we can consistently drop such terms. Moreover, the doubly charged scalar solely couples to RH leptons. Since we assume the electron to be massless, all form factors g_LK vanish identically. Thus, the dominant contribution to the non-photonic short-range part of coherent $\mu^- - e^-$ conversion emerges from just one single term. After rewriting the couplings in Eq. (5.2.30) such that they

match those in Eq. (5.2.28), the relevant effective Lagrangian is given by:

$$\mathcal{L}_{\text{non-photonic}} = -\frac{G_F}{\sqrt{2}} \underbrace{\frac{2(1+k_q \sin^2\theta_W)\cos\theta_W}{g} A_{\text{R}}(q'^2)}_{=g_{\text{RV}(q)}} \ \overline{e_{\text{R}}}\,\gamma_\nu\,\mu_{\text{R}}\ \ \overline{q}\,\gamma^\nu\,q\,. \tag{5.2.32}$$

However, this Lagrangian still operates at the quark level, while what we are interested in is the analogous vertex coupling the muon and the electron to nucleons. Converting the Lagrangian in Eq. (5.2.32) to nucleon level, the new coupling constants $g^{(0)}_{\text{XK}}$ and $g^{(1)}_{\text{XK}}$ can be re-expressed in terms of the nucleon form factors $G^{(q,p)}_{\text{K}}$ and $G^{(q,n)}_{\text{K}}$, see Ref. [211] for details:

$$\begin{aligned} g^{(0)}_{\text{XK}} &= \frac{1}{2}\sum_{q=u,d,s} g_{\text{XK}(q)}\Big(G^{(q,p)}_{\text{K}} + G^{(q,n)}_{\text{K}}\Big)\,, \\ g^{(1)}_{\text{XK}} &= \frac{1}{2}\sum_{q=u,d,s} g_{\text{XK}(q)}\Big(G^{(q,p)}_{\text{K}} - G^{(q,n)}_{\text{K}}\Big)\,. \end{aligned} \tag{5.2.33}$$

Taking the limit of isospin invariance, we can relate the proton and neutron form factors [370]: $G^{(u,p)}_{\text{K}} = G^{(d,n)}_{\text{K}}$, $G^{(u,n)}_{\text{K}} = G^{(d,p)}_{\text{K}}$, and $G^{(s,p)}_{\text{K}} = G^{(s,n)}_{\text{K}}$; furthermore, it is $G^{(u,p)}_{\text{V}} = 2$, $G^{(u,n)}_{\text{V}} = 1$, and $G^{(s,p)}_{\text{V}} = 0$ for the vector current. Again employing the non-relativistic approximation for the muon wave function, the branching ratio of coherent $\mu^- - e^-$ conversion takes the general form [211]:

$$\begin{aligned} \text{BR}(\mu^- N \to e^- N) =& \frac{|\vec{p}_e| E_e m_\mu^3 G_F^2 \alpha^3 Z_{\text{eff}}^4 F_p^2}{8\pi^2 Z\,\Gamma_{\text{capt}}} \times \\ & \Bigg[\Big|(Z+N)(g^{(0)}_{LS}+g^{(0)}_{LV}) + (Z-N)(g^{(1)}_{LS}+g^{(1)}_{LV})\Big|^2 \\ & + \Big|(Z+N)(g^{(0)}_{RS}+g^{(0)}_{RV}) + (Z-N)(g^{(1)}_{RS}+g^{(1)}_{RV})\Big|^2\Bigg], \end{aligned} \tag{5.2.34}$$

under the assumptions of equal proton and neutron densities as well as a quasi-constant muon wave function within the nucleus. Here, G_F is Fermi's constant and $\alpha = e^2/(4\pi) = g^2 \sin^2\theta_W/(4\pi)$. All other quantities are defined as in Eq. (5.2.2).

Within our framework there are neither scalar contributions, i.e. $g^{(0,1)}_{\text{LS}} = g^{(0,1)}_{\text{RS}} = 0$, nor contributions that include left-handed (LH) electrons, i.e. $g^{(0,1)}_{\text{LV}} = 0$. Moreover, we take the electron to be massless, which leads to $E_e = |\vec{p}_e| \simeq m_\mu$. In combination with Eqs. (5.2.32) and (5.2.33), the branching

ratio hence simplifies to:

$$\begin{aligned}\mathrm{BR}(\mu^- N \to e^- N) &= \frac{8\alpha^5 m_\mu Z_{\mathrm{eff}}^4 Z F_p^2}{\Gamma_{\mathrm{capt}}} \\ &\times \underbrace{\frac{m_\mu^4 \cos^2\theta_W}{128\,\pi\alpha Z^2 M_W^4 \sin^2\theta_W}\left|\Big(3(Z+N) - 4\,Z\sin^2\theta_W\Big) A_{\mathrm{R}}(-m_\mu^2))\right|^2}_{\equiv \Xi^2_{\mathrm{non-photonic}}}, \end{aligned} \tag{5.2.35}$$

where we have used $G_F = \alpha\pi/(\sqrt{2}M_W^2\sin^2\theta_W)$. Here, we have rewritten the non-photonic branching ratio such that we can extract a $\Xi_{\mathrm{non-photonic}}$ in analogy to the photonic contributions. However, in contrast to the photonic part Ξ_{photonic}, one cannot factorise the particle and nuclear physics contributions, in the sense that $\Xi_{\mathrm{non-photonic}}$ depends on the nuclear characteristics (Z, N): $\Xi_{\mathrm{non-photonic}} \equiv \Xi_{\mathrm{non-photonic}}(Z, N)$. While this looks like as if it made the distinction between particle physics and nuclear physics parts impossible, it will turn out that the dependence on (Z, N) is in reality so weak that it can be dropped without significantly changing the results. This is again a reflection of the short-range contribution being subdominant by far.

In order to determine the chiral form factor $A_{\mathrm{R}}(q'^2)$, we proceed in a way similar to what we did for the photonic form factors, meaning that we consider the process $\mu \to e\,Z$ for an off-shell gauge boson. From Diagram I in Fig. 5.7a, we obtain the matrix element:

$$\begin{aligned} i\mathcal{M}_{\mathrm{I}} = &-8\,f_{ea}^* f_{a\mu}\, g' \sin\theta_W\, Z^\nu(q') \\ &\overline{u}_e(p_e)\int \frac{\mathrm{d}^d k}{(2\pi)^d} \frac{\mathrm{P_L}\,\not{k}(2p_\mu - 2k + q')_\nu}{[k^2 - m_a^2][(p_\mu - k + q')^2 - M_S^2][(p_\mu - k)^2 - M_S^2]}\, u_\mu(p_\mu), \end{aligned} \tag{5.2.36}$$

where we have dropped the "$+i\epsilon$" terms, which define the pole structure, for brevity. For Diagram II, see Fig. 5.7b, the matrix element is given by:

$$\begin{aligned} i\mathcal{M}_{\mathrm{II}} = &-f_{ea}^* f_{a\mu}\frac{g}{\cos\theta_W} Z^\nu(q')\,\overline{u}_e(p_e) \\ &\int \frac{\mathrm{d}^d k}{(2\pi)^d} \frac{\mathrm{P_L}(\not{k} + \not{q}' + m_a)\gamma_\nu(1 - 4\sin^2\theta_W + \gamma_5)(\not{k} + m_a)\mathrm{P_R}}{[k^2 - m_a^2][(p_\mu - k)^2 - M_S^2][(k + q')^2 - m_a^2]}\, u_\mu(p_\mu)\,. \end{aligned} \tag{5.2.37}$$

From Fig. 5.7c, we extract:

$$\begin{aligned} i\mathcal{M}_{\mathrm{III}} = &-f_{ea}^* f_{a\mu}\frac{g}{\cos\theta_W} Z^\nu(q') \\ &\overline{u}_e(p_e)\int \frac{\mathrm{d}^d k}{(2\pi)^d} \frac{\gamma_\nu(-1 + 4\sin^2\theta_W + \gamma_5)\not{p}_\mu \not{k}\,\mathrm{P_R}}{p_\mu^2\,[k^2 - m_a^2][(p_\mu - k)^2 - M_S^2]}\, u_\mu(p_\mu)\,. \end{aligned} \tag{5.2.38}$$

And, finally, from Fig. 5.7d:

$$i\mathcal{M}_{\mathrm{IV}} = -\, f_{ea}^{*} f_{a\mu}\, \frac{g}{\cos\theta_W}\, Z^{\nu}(q') \\ \overline{u}_e(p_e) \int \frac{\mathrm{d}^d k}{(2\pi)^d}\, \frac{\mathrm{P_L}\, \not{k}(\not{p}_e + m_\mu)\gamma_\nu(-1 + 4\sin^2\theta_W + \gamma_5)}{-m_\mu^2\,[k^2 - m_a^2][(p_e - k)^2 - M_S^2]}\, u_\mu(p_\mu)\,. \tag{5.2.39}$$

Again using `Package-X`, we compute each diagram's contribution to A_{R}, and combine them using $g' = g\tan\theta_W$. Due to the absence of a tree-level three-point vertex connecting muon, electron, and Z-boson, the form factor A_{R} has to be UV-finite. Similarly to the photonic case, the UV divergences occurring in the individual diagrams I - IV indeed cancel each other, thus leaving A_{R} finite. As before, we can simplify the form factor by exploiting the mass hierarchy $M_S \gg m_{e,\mu,\tau}$ to obtain:

$$A_{\mathrm{R}}(-m_\mu^2) = \frac{-ig}{24\pi^2\,\cos\theta_W\, M_S^2\, m_\mu} \sum_{a=e,\,\mu,\,\tau} f_{ea}^{*} f_{a\mu} \Bigg(m_\mu\, m_a^2(-3 + 8\sin^2\theta_W) \\ + 2\sqrt{4m_a^2 + m_\mu^2}\Big(2m_\mu^2\sin^2\theta_W + m_a^2(3 - 4\sin^2\theta_W)\Big) \\ \times \mathrm{Arctanh}\left[\frac{m_\mu}{\sqrt{4m_a^2 + m_\mu^2}}\right] + \Big(3m_a^2 m_\mu + 2m_\mu^3\sin^2\theta_W\Big)\ln\left[\frac{m_a^2}{M_S^2}\right]\Bigg)\,. \tag{5.2.40}$$

So, the somewhat artificial (because in reality not dominating) solely non-photonic particle physics factor $\Xi_{\mathrm{non-photonic}}$ can be deduced to be:

$$\Xi^2_{\mathrm{non-photonic}}(Z,\,N) = \frac{m_\mu^2\,|3(Z+N) - 4\,Z\sin^2\theta_W|^2}{18432\,\pi^4 Z^2 M_W^4\, M_S^4 \sin^4\theta_W} \Bigg| \sum_{a=e,\mu,\tau} f_{ea}^{*} f_{a\mu} \\ \times \Bigg(m_\mu\, m_a^2(-3 + 8\sin^2\theta_W) + 2\sqrt{4m_a^2 + m_\mu^2} \\ \times \Big(2m_\mu^2\sin^2\theta_W + m_a^2(3 - 4\sin^2\theta_W)\Big)\,\mathrm{Arctanh}\left[\frac{m_\mu}{\sqrt{4m_a^2 + m_\mu^2}}\right] \\ + \Big(3m_a^2 m_\mu + 2m_\mu^3\sin^2\theta_W\Big)\ln\left[\frac{m_a^2}{M_S^2}\right]\Bigg)\Bigg|^2\,, \tag{5.2.41}$$

at leading order.

5.2.3 The total branching ratio

In general, both the photonic and non-photonic processes contribute to μ^-–e^- conversion. Kinematics dictate that $q'^2 \simeq -m_\mu^2$, which in combination with

the non-relativistic approximation of the muon wave function implies that the photonic (predominantly long-range) contribution can effectively be treated as an addition $\Delta g_{\rm RV}^{(0,1)}$ to the vectorial coupling constants $g_{\rm RV}^{(0,1)}$, see Eq. (141) of Ref. [211]. We thus obtain:

$$g_{\rm RV}^{(0,1)} \to g_{\rm RV}^{(0,1)} + \Delta g_{\rm RV}^{(0,1)}\,, \quad \text{where} \quad \Delta g_{\rm RV}^{(0,1)} = \frac{4\sqrt{2}\,\alpha\,\pi}{G_F\,m_\mu^2}\Big(F_2(-m_\mu^2) - F_1(-m_\mu^2)\Big), \tag{5.2.42}$$

with the form factors F_1 and F_2 explicitly given in Eqs. (5.2.19) and (5.2.20), respectively. We can now understand why the non-photonic short-range contributions are subdominant: while both $|F_2(-m_\mu^2) - F_1(-m_\mu^2)|$ and $|A_{\rm R}(-m_\mu^2)|$ are of $\mathcal{O}(m_a^2/M_S^2)$, we can see from Eq. (5.2.42) that the photonic contributions are considerably *less suppressed*, receiving a relative enhancement factor that should naively be of the order of $\alpha/(G_F\,m_\mu^2) \sim M_W^2/m_\mu^2 \sim 10^5$.
Replacing the purely non-photonic couplings in favour of the ones given above in Eq. (5.2.42), we can derive the general branching ratio in analogy to the derivation of Eq. (5.2.35). The combined branching ratio, incorporating both photonic (long-range) and non-photonic (short-range) contributions, takes the form:

$$\begin{aligned}
&{\rm BR}(\mu^- N \to e^- N) = \frac{8\alpha^5 m_\mu Z_{\rm eff}^4 Z F_p^2}{\Gamma_{\rm capt}}\,\Xi^2_{\rm combined}(Z,N)\,,\\
&\text{with}\quad \Xi^2_{\rm combined} = \frac{m_\mu^4}{8192\,\pi^4\,Z^2\,M_W^4\sin^4\theta_W}\left|\sum_{a=e,\mu,\tau} f_{ea}^* f_{a\mu} \times \right.\\
&\Bigg(-\frac{2(3(Z+N) - 4\,Z\sin^2\theta_W)}{3\,m_\mu\,M_S^2}\Big(m_\mu\,m_a^2(-3 + 8\sin^2\theta_W)\\
&+ 2\sqrt{4m_a^2+m_\mu^2}\Big(2m_\mu^2\sin^2\theta_W + m_a^2(3 - 4\sin^2\theta_W)\Big)\,{\rm Arctanh}\left[\frac{m_\mu}{\sqrt{4m_a^2+m_\mu^2}}\right]\\
&+ \Big(3m_a^2 m_\mu + 2m_\mu^3\sin^2\theta_W\Big)\ln\left[\frac{m_a^2}{M_S^2}\right]\Big) + \frac{16}{3}\,\frac{M_W^2\,Z\sin^2\theta_W}{m_\mu^3\,M_S^2}\Big(4m_a^2\,m_\mu - m_\mu^3\\
&\left. + 2(-2m_a^2 + m_\mu^2)\sqrt{4m_a^2+m_\mu^2}\,{\rm Arctanh}\left[\frac{m_\mu}{\sqrt{4m_a^2+m_\mu^2}}\right] + m_\mu^3\,\ln\left[\frac{m_a^2}{M_S^2}\right]\Big)\Bigg)\right|^2,
\end{aligned} \tag{5.2.43}$$

at leading order in the small ratios m_a^2/M_S^2.
As already pointed out and as is now clearly visible from Eq. (5.2.43), $\Xi_{\rm combined}$ is not pure particle physics quantity, in the sense that it also depends on the nuclear characteristics Z and N. However, we can nevertheless use it to compare the impact of a certain bound on the New Physics parameters, as long as we take into account the variation with Z and N. Thus, when plotting $\Xi_{\rm combined}$ as a function of the scalar mass M_S, one would not only obtain a

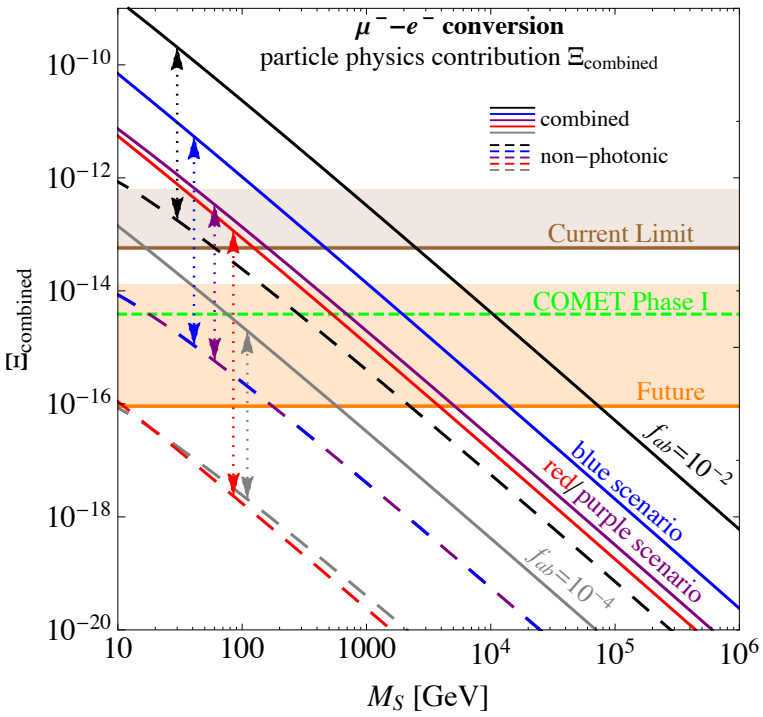

Figure 5.11: Bounds on the full particle physics contribution Ξ_{combined}.

simple line but a band, the width arising from varying Z and N. However, as we will see, numerically this variation is very mild, since it only affects the subdominant contribution to the decay – in a logarithmic plot, the width of the band would not even be visible. Thus, in practice, we can disregard the variation with Z and N whenever presenting a bound just for illustrative purposes.

We are now ready to present our final results for $\mu^- - e^-$ conversion, which are displayed in Fig. 5.11. In contrast to Fig. 5.9, we now present both the total contribution [Ξ_{combined}, see Eq. (5.2.43)] and the non-photonic short-range contribution [$\Xi_{\text{non-photonic}}$, see Eq. (5.2.35)]. Note that the latter quantity is in fact not physical, as explained, in the sense that in reality it does not occur in isolation, i.e. without the photonic contributions. However, artificially separating them makes it evident that the non-photonic contributions are indeed very subdominant, by several orders of magnitude for each of the benchmark scenarios displayed. Thus, it is an excellent approximation to take $\Xi_{\text{combined}} \simeq \Xi_{\text{photonic}}$, and to completely disregard the non-photonic short-range part, effectively going back to our intermediate result from Eqs. (5.2.24) and (5.2.2). Furthermore, as explained above, the lines representing the non-photonic contributions for the different scenarios are in fact bands with finite widths, due to their dependence on the isotope under consideration. However, the widths are so small that they would hardly be visible in the logarithmic plot presented in Fig. 5.11.

Furthermore, we extract the bounds on the scalar mass M_S obtained from the combination of photonic and non-photonic contributions in analogy to section

	current limit	future sensitivity	COMET I (^{27}Al)
black	$M_S > 708.1 - 2388.6$	$M_S > 5497.1 - 70326.3$	$M_S > 10396.1$
blue	$M_S > 131.9 - 447.1$	$M_S > 1031.4 - 13269.4$	$M_S > 1953.9$
purple	$M_S > 42.5 - 152.2$	$M_S > 360.6 - 4880.6$	$M_S > 693.9$
red	$M_S > 33.9 - 118.1$	$M_S > 276.3 - 3656.1$	$M_S > 528.0$
grey	$M_S > 4.1 - 15.9$	$M_S > 38.7 - 548.4$	$M_S > 75.7$

Table 5.4: Lower limits on the mass M_S in GeV resulting from the total branching ratio for $\mu^- - e^-$ conversion, displaying the range from the most pessimistic to the most optimistic values. Figures are deliberately shown with a too-good precision, in order to ease the comparison with Tab. 5.3. Indeed, the figures are nearly identical to those obtained when only taking into account the photonic contribution, just as to be expected from Fig. 5.11.

5.2.1. The resulting ranges of lower limits displayed in Tab. 5.4 differ from the values for the purely photonic contributions only at the per mille level, cf. Tab. 5.3. While this confirms that we can render the non-photonic contributions negligible, however, it is also visible that – depending on the combinations of couplings – the naive estimate of the effect of the non-photonic contributions may underestimate them by several orders of magnitude. Thus, it is in fact not a priori clear that the non-photonic short-range diagrams are always negligible, contrary to what had been claimed earlier in Ref. [375].

Although we can neglect the non-photonic contributions due to their smallness, there are two interesting observations related to them, which we want to briefly discuss. First, we cannot distinguish the blue from the purple non-photonic contributions, while they differ by about an order of magnitude in the photonic case. This can again be understood by having a close look at the amplitudes for both processes. The amplitude that enters the non-photonic $\Xi_{\text{non-photonic}}$ takes the form:

$$\mathcal{A} \propto \left| f^*_{ee}\, f_{e\mu}\, D(m_e) + f^*_{e\mu}\, f_{\mu\mu}\, D(m_\mu) + f^*_{e\tau}\, f_{\tau\mu}\, D(m_\tau) \right| ,$$

where the function $D(m_a)$, which is proportional to the form factor A_{R} for a fixed m_a, strongly varies with m_a. The dominant term (without including the couplings $f^*_{ea} f_{a\mu}$) stems from the τ propagating in the loop, i.e. $D(m_\tau)$. It exceeds the μ and e contributions by about three to four orders of magnitude. Furthermore, neither the combination $f^*_{ee} f_{e\mu}$ nor $f^*_{e\mu} f_{\mu\mu}$, see Tab. 5.2, can bypass this difference in the blue and purple scenarios. Thus, the equality of the non-photonic contribution of blue and purple scenarios is traced back to the identical combination of $f^*_{e\tau} f_{\tau\mu}$ in both scenarios.
The second observation is that – in contrast to the photonic case where the red scenario consistently attains values more than an order of magnitude higher – the red and grey scenarios are comparable in the non-photonic case. Following the argument given above, the grey scenario should dominate, due to

$f^*_{e\tau} f_{\tau\mu} = 10^{-8}$ (grey) in comparison to $f^*_{e\tau} f_{\tau\mu} = 10^{-24}$ (red), which seems to contradict the observations from the plot. However, for the red scenario, $f^*_{e\tau} f_{\tau\mu}$ is smaller than the combinations $f^*_{ee} f_{e\mu}$ and $f^*_{e\mu} f_{\mu\mu}$ by at least six orders of magnitude, see Tab. 5.2. It hence overcompensates the dominance of $D(m_\tau)$, such that $f^*_{e\mu}\, f_{\mu\mu}\, D(m_\mu)$ is the relevant contribution in the red scenario. The latter yields the same order of magnitude results as the $f^*_{e\tau}\, f_{\tau\mu}\, D(m_\tau)$ contribution of the grey scenario.

Summing up, we have presented a detailed computation of μ^-– e^- conversion mediated by a doubly charged $\mathrm{SU(2)_L}$ singlet scalar coupling to pairs of RH charged leptons. The formulae obtained are general, however, for illustration the numerical results focus on the scenarios obtained in Ref. [47]. In all cases, the current/future lower bounds on the doubly charged scalar mass M_S resulting from the non-observation of μ^-– e^- conversion turn out to be very strong, which illustrates the benefit of new measurements of μ^-– e^- conversion.

5.2.4 Complementarity between low- and high-energy data

Thus far, we have explored the benefits of exploiting the complementarity between bounds from low-energy LFV/LNV experiments and the data from neutrino oscillations. Following the discussion on the importance of complementarity for testing neutrino mass models in section 3.3, we now extend the complementarity analysis by direct searches performed at the high-energy frontier. It will turn out that our particle physics setting is a prime example of how high- and low-energy physics can cross-fertilise each other. Whilst COMET is expected to drastically improve the limits at the intensity frontier, the Large Hadron Collider (LHC) will probe the TeV region for new particles like S^{++} during Run II. Hence, it is these two probes that we concentrate on here, assessing their respective reach. While the μ^-– e^- conversion is discussed in detail throughout this chapter, we refer to section 3.3 or Refs. [1, 47] for more information on the high-energy probes.

Focussing on the complementarity between LHC searches and low-energy probes, the resulting bounds on the scenarios found in Ref. [47] are displayed in Fig. 5.12. The model predictions are illustrated in two ways, for actual benchmark points (displayed as red, purple, and blue dots) taken from Ref. [47], and for the representative sets of couplings in Tab. 5.2 (displayed as red, purple, and blue lines), which comprise "averaged" versions of the points with low M_S and illustrate how the bounds vary with the scalar mass M_S for fixed couplings. Note that, for large M_S, the spread of the points around the line becomes bigger, which is expected due to LFV/LNV bounds generally becoming weaker for large M_S. As visible from Fig. 5.12, μ^-– e^- conversion bounds push from top to bottom. As indicated in both sections 3.3 and 5.1, we em-

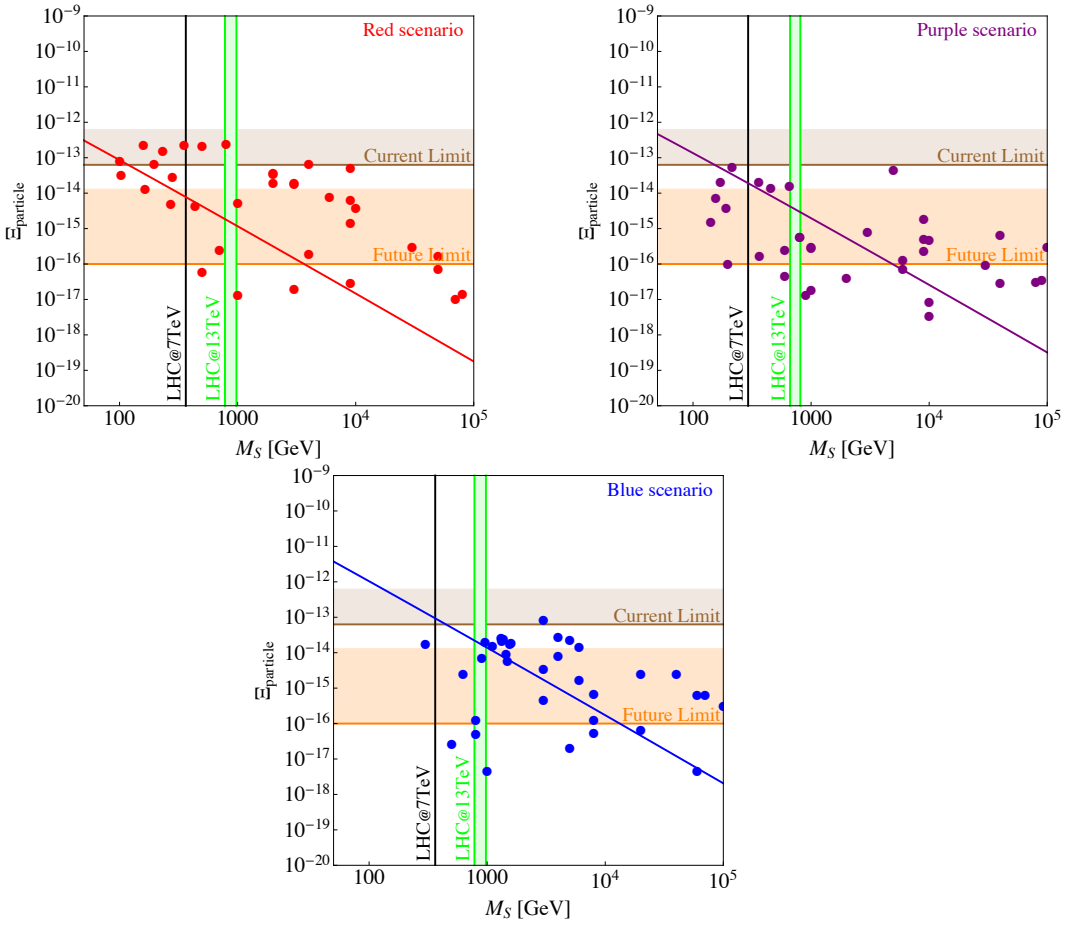

Figure 5.12: Particle physics parts Ξ_{particle} as functions of the scalar mass M_S for the red/purple/blue scenarios. Different limits from $\mu^- - e^-$ conversion and from LHC searches are indicated, see sections 3.3 and 5.1 for details.

ploy the bounds from current and future experiments [45, 366, 385, 411, 425]. The different scenarios can be constrained depending on the exact values of the model parameters. For example, the blue line is easier to constrain than the red/purple lines. The reason is that the flavour-dependent coefficients in Eq. (5.2.24), while being sufficiently different to spoil cancellations between the three contributions to the total amplitude, are nevertheless all of the same order. Thus, the benchmark lines with the largest value of $|f^*_{ee} f_{e\mu}|$, $|f^*_{e\mu} f_{\mu\mu}|$, or $|f^*_{e\tau} f_{\tau\mu}|$ will be the easiest to constrain.

The complementary nature of these approaches is very clear from Fig. 5.12, with the LHC able to exclude scalar masses approaching 1 TeV, while $\mu^- - e^-$ conversion holds the promise of orders of magnitude improvement in constraining the particle physics amplitude in Eq. (5.2.24), albeit with uncertainties due to nuclear physics. From a general perspective, the framework considered provides a minimal and clear example of complementarity between two of the

most important experimental particle physics strategies presently being pursued, towards uncovering the physics beyond the SM, which must necessarily be present to account for neutrino mass and mixing.

5.2.5 Summary

In this section, we have presented a detailed computation of $\mu^- - e^-$ conversion, i.e., a reaction turning a muon bound to an atomic nucleus into an electron, for the case of the process being mediated by a doubly charged singlet scalar particle. After having identified the decisive Feynman diagrams, we have computed the resulting amplitude for the conversion and we have mapped it to the known most general amplitude for the process. We have taken into account both the photonic (predominantly long-range) and the non-photonic (short-range) contributions, the latter of which are however subdominant and can be neglected in practice. Our results are fully general and hold for any doubly charged singlet scalar coupling to pairs of RH charged leptons, thereby closing a big gap in the contemporary knowledge on $\mu^- - e^-$ conversion. Even for doubly charged scalars which are no singlets under SU(2), such as the doubly charged component of a Higgs triplet field, most of the computation presented practically remains the same – a generalisation of our results is both possible and doable with moderate effort.

In addition, we have investigated how strongly the parameters related to the doubly charged scalar can be constrained by future experimental limits on the conversion process, which are expected to dramatically improve within the coming years. For illustrative purposes, we have also included the explicit example of one particular model, namely the effective theory of the doubly charged scalar, which generates a valid light neutrino mass at two-loop level and which contains our general setting as a subset. As we have seen, despite intrinsic nuclear physics uncertainties, the limits to be expected from the conversion process strongly constrain the mass of the doubly charged scalar. Furthermore, we have shown how the intensity and the energy frontiers provide complementary constraints. Depending on the benchmark scenario, future indirect limits from $\mu^- - e^-$ conversion might even be more stringent than the direct limits which will be obtained by the LHC. Thus, realistically, experiments on LFV can serve as a valuable addition to collider studies in the hunt for New Physics beyond the SM.

5.3 $\mu^- - e^+$ Conversion

This section is devoted to the lepton flavour and lepton number violating conversion of bound muons into positrons, referred to as $\mu^- - e^+$ *conversion*. On a level accessible to particle physicists, we will in great detail present the computation of the conversion process based on one explicit type of short-range operator, $J_x^\nu J_{y,\nu} j_z$, which is the single one for which the corresponding nuclear

matrix element is presently known. We will furthermore relate this short-range operator to concrete realisations of New Physics scenarios at high scales. By doing so, we add several decisive bits to the few results already available on the process mediated by Majorana neutrinos in Ref. [6]. The main goal of our discussion is to make the respective computation accessible to the particle physics community, so that promising models can be investigated while the nuclear physics community can simultaneously advance the computation of nuclear matrix elements. In addition to the technical aspects of the computation, we will present an illustrative discussion of the physics potential of $\mu^- - e^+$ conversion based on a number of particle physics settings generating the said short-range operator. This makes it clear that this process is in fact a promising alternative possibility to detect lepton number violation in the $e\mu$-sector instead of the ee-sector, where this is usually attempted by means of the related but much more popular process of neutrinoless double beta decay $0\nu\beta\beta$. Nevertheless, a combined effort of experiments and theory, both in nuclear and particle physics, will be necessary to fully assess the potential of $\mu^- - e^+$ conversion.

Note furthermore that this section is a slightly modified version of merging Refs. [3, 4]. Hence, most of the section at hand is adopted from parts of those references.

The remainder of this section is structured as follows. In section 5.3.1 we introduce the effective operator language for $\mu^- - e^+$ conversion, which forms the basis for our discussion. The main computation is laid out in section 5.3.2, where we derive the decay rate for $\mu^- - e^+$ induced by ϵ_3^{xyz} in sufficient detail to enable the reader to reproduce our results. In section 5.3.3 we show how to map particle physics models to the operator ϵ_3^{xyz}, which is the key to understanding how experimental bounds constrain the possibilities for physics beyond the SM. Subsequently, in section 5.3.4, we illustrate the reach and possible physics impact of future experiments based on several particle physics models generating ϵ_3^{xyz}. Finally, we point out three directions in which advances are necessary in order to gain physics insights from $\mu^- - e^+$ conversion in section 5.3.5. We resume our discussion in section 5.3.6. To make the text as accessible as possible, we have postponed technical aspects to the appendices. Therefore, Appendix C is dedicated to explaining the differences in our notation compared to that of Ref. [6], Appendix D is devoted to detail on how to handle the many spins appearing in the computation, and Appendix A lists all Feynman rules used.

A general parametrisation of the $\mu^- - e^+$ conversion using an effective field theory approach comprises two different regimes, namely short-range and long-range contributions, which need to be treated qualitatively differently. Within both regimes, the effective field theory treatment allows for a (particle-) model-independent treatment, respectively, and thus to simultaneously discuss different settings. When contemplating lepton number violating processes, both

heavy and light Majorana neutrinos automatically offer exchange mechanisms. In case of a heavy neutrino exchange, one has to employ the short-range formalism whereas the light neutrino exchange is described by the long-range formalism. Without making use of an effective field theory treatment, both Majorana neutrino cases were studied in Ref. [6], revealing that their rates are too small even for distant-future experiments to detect. Given that no detailed treatment on either short- or long-range contributions currently exists from the particle physics side, we want to initiate the discussion by focusing on the most informative case. Although there are promising settings leading to long-range operators, for example the R-parity violating SUSY diagrams reported in Ref. [426] (realising the long-range $\epsilon_{1,2}$, cf. Eq. (5.3.1)[12]), the candidates we have found do not realise the long-range operator ϵ_3 which, at the moment, is the only case for which nuclear matrix elements have been computed (see Ref. [6]). On the contrary, there are several settings known that realise the short-range operator ϵ_3. Consequently, we will take a closer look at these short-range realisations and the corresponding models in this thesis.

5.3.1 Possible short-range operators

We start by discussing the possible short-range contributions to the LNV *and* LFV $\mu^- - e^+$ conversion. We will emphasise the technical aspects, in particular when performing the matching of concrete models to the effective operator coefficients.

In order to consider the short-range contributions to $\mu^- - e^+$ conversion within a general framework, we turn to an effective field theory (EFT) treatment. Hence, the bound muon and the positron interact with the quarks inside the nucleus via point-like vertices. Due to the charge flow, we can thus imagine the process as having one muon μ^- and two up-quarks u as ingoing particles and one positron e^+ and two down-quarks d outgoing, all of which are connected via a "big" effective vertex.

We restrict ourselves to the lowest dimensional short-range operators which have dimension 9. Thus, our effective Lagrangian will consist of combinations of two hadronic currents J and one leptonic current j, with a prefactor G_F^2/m_p of mass dimension (-5) to balance out the mass dimensions. Note that the factor G_F^2 is motivated by the W-bosons that are often present in such a transition. The strength of these vertices will be parametrised by dimensionless coefficients ϵ_a^{xyz}, which are labeled by the index a and whose superscript xyz indicates the currents' chiralities involved in the operators.

Let us now write down the most general short-range Lagrangian, which can be done analogously to $0\nu\beta\beta$ [252]. Taking into account Lorentz invariance,

[12]The long-range contributions can be parametrised in a manner similar to the short-range contributions, see [251] for a thorough discussion for the analogous case of $0\nu\beta\beta$.

it is given by:

$$\begin{aligned}\mathcal{L}^{\mu e}_{\text{short-range}} = \frac{G_F^2}{2m_p} \sum_{x,y,z=\text{L,R}} [&\epsilon_1^{xyz} J_x J_y j_z + \epsilon_2^{xyz} J_x^{\nu\rho} J_{y,\nu\rho} j_z + \epsilon_3^{xyz} J_x^{\nu} J_{y,\nu} j_z \\ &+ \epsilon_4^{xyz} J_x^{\nu} J_{y,\nu\rho} j_z^{\rho} + \epsilon_5^{xyz} J_x^{\nu} J_y j_{z,\nu} + \epsilon_6^{xyz} J_x^{\nu} J_y^{\rho} j_{z,\nu\rho} + \epsilon_7^{xyz} J_x J_y^{\nu\rho} j_{z,\nu\rho} \\ &+ \epsilon_8^{xyz} J_{x,\nu\alpha} J_y^{\rho\alpha} j_{z,\rho}^{\nu}] \,,\end{aligned} \tag{5.3.1}$$

where $G_F = \sqrt{2} g^2/(8M_W^2)$ is the Fermi constant and m_p is the proton mass. The hadronic currents are defined similarly as done in Ref. [253]:

$$J_{\text{R,L}} = \overline{d}(1 \pm \gamma_5)u, \quad J^{\nu}_{\text{R,L}} = \overline{d}\,\gamma^{\nu}(1 \pm \gamma_5)u, \quad J^{\nu\rho}_{\text{R,L}} = \overline{d}\,\sigma^{\nu\rho}(1 \pm \gamma_5)u \,. \tag{5.3.2}$$

The leptonic currents are defined analogously, however, for $\mu^- - e^+$ conversion they must connect μ-e instead of e-e:

$$\begin{aligned}&j_{\text{R,L}} = \overline{e^c}(1 \pm \gamma_5)\mu = 2\overline{(e_{\text{R,L}})^c}\,\mu_{\text{R,L}}, \quad j^{\nu}_{\text{R,L}} = \overline{e^c}\,\gamma^{\nu}(1 \pm \gamma_5)\mu = 2\overline{(e_{\text{L,R}})^c}\,\gamma^{\nu}\mu_{\text{R,L}} \,, \\ &\text{and} \quad j^{\nu\rho}_{\text{R,L}} = \overline{e^c}\,\sigma^{\nu\rho}(1 \pm \gamma_5)\mu = 2\overline{(e_{\text{R,L}})^c}\,\sigma^{\nu\rho}\mu_{\text{R,L}} \,.\end{aligned} \tag{5.3.3}$$

Depending on the nature of the LNV physics, one or the other operator may be realised, and a bound on the very same operator can have different implications depending on which model generates it. According to Ref. [252], the terms proportional to $\epsilon_{6,7,8}$ can be neglected for neutrinoless double beta decay. In fact, when exploiting the identity of the two electrons, they can even be shown to vanish exactly [427] and are thus strictly irrelevant for $0\nu\beta\beta$. The same line of reasoning is not valid for $\mu^- - e^+$ conversion, though, since obviously μ and e are not identical. If we restrict the discussion to the part of the process which is mediated between the ground states of the nuclei, i.e., transitions from ground-state to ground state ($\sim 40\%$ of all transitions [6, 414]), the outgoing positron carries away an energy of roughly m_μ, while the transfer to the final state nucleus is small. In addition, one can assume that the initial and final state nuclei are non-relativistic to a good approximation. Therefore, the hadronic currents can be approximated by their non-relativistic versions, $J^-_\nu(t, \vec{x}) \simeq J^-_\nu(\vec{x})\mathrm{e}^{iEt}$, where E is the energy of the corresponding state. By doing so, Eq. (5.3.20) shows that:

$$\mathrm{e}^{i(E_f - E_i)t}\, J^{\sigma}(\vec{x}_1) J^{\rho}(\vec{x}_2) = \mathrm{e}^{i(E_f - E_i)t}\, J^{\sigma}(\vec{x}_2) J^{\rho}(\vec{x}_1) \,, \tag{5.3.4}$$

which means that the expression is symmetric under the exchange of $\vec{x}_1 \leftrightarrow \vec{x}_2$. Given that $j^{\nu\rho}_{\text{R,L}}$ is anti-symmetric under $\rho \leftrightarrow \sigma$, the expressions related to the effective couplings $\epsilon_{6,7,8}$ will thus not contribute to the decay rate. Note that switching to an incoherent process leads to a final state nucleus with different J^π and an outgoing positron with reduced kinetic energy. However, as long as both initial and final state nuclei are non-relativistic and one can use a

point-like vertex, the above arguments remain valid.
Note further that, although the operators in Eq. (5.3.1) can appear in very different chirality structures, in most cases the experimental limit depends much more on the index a of ϵ_a rather than on which chiral structure is realised [4, 252, 253, 428]. In many realistic settings, however, only one or a few of the short-range operators from Eq. (5.3.1) are realised.

Treating the short-range contributions via an EFT allows for a clean separation of the nuclear physics part from the respective particle physics part, valid for a rather large class of models (namely all that realise the short-range operators under consideration). It thereby allows for a (particle-) model-independent computation of the NMEs and, thus, a wide range of particle physics models can be attacked by a single strike. Consequently, it is concurrently essential to determine the relevant $\mu^- - e^+$ conversion NMEs, such that limits from this LNV process can be derived, cf. section 5.3.4.

5.3.2 Computing the decay rate: a very explicit example

The aim of this section is to perform the computation for the decay rate for one particular short-range operator, which we choose to be $\epsilon_3^{\mathrm{LLR}}$. This choice is motivated by several arguments:

1. First of all, ϵ_3^{xxz} (with $x, z = \mathrm{L}, \mathrm{R}$) is the only choice for which the NMEs have already been computed (in fact for both short- and long-range contributions [6]). Ref. [6] actually aimed at comparing the two cases of light and heavy neutrino exchange, with the latter realising $\epsilon_3^{\mathrm{LLL}}$. However, once the identification with the operator coefficients has been performed (see our section 5.3.3), the results in fact carry over to our case, which in particular holds for the NME.

2. Second, while the explicit computation has been performed to some extend in Ref. [6], the computation presented mostly focuses on nuclear physics aspects and is not easily accessible for the average particle physicist. We would like to remedy this issue by presenting all relevant steps in detail, so that the pervious results are easier to use for the particle physics community.

3. After all, many aspects of the computation would not change if another operator was chosen from Eq. (5.3.1). Given that all these operators are point-like, it is mainly the external projections that change, as well as the connection of the hadronic currents to the nucleus, but the more involved aspects of the computation basically remain the same.

4. We will discuss the physics potential of future experiments in constraining the operator ϵ_3 in section 5.3.4. Some of the results there will be much easier to grasp with the background of the explicit computation at hand. We will consider several example models in this section which

could potentially be constrained by a future measurement of $\mu^- - e^+$ conversion.

5. Finally, we will in the following also include a particular example to show how the operator ϵ_3 can be obtained from a concrete underlying model. While this may sound like a slightly ambiguous strategy, it serves the additional purpose to show how the operator matching can be performed in passing when doing the full computation. The alternative, but of course equivalent, strategy would be to match on the level of Lagrangians and simply use the Feynman rules for the effective model. Since the latter option is implicitly contained in the following derivation, from Eq. (5.3.13) onwards, we have however decided to show an example as explicit as possible.

Having justified our procedure, we start by quickly addressing the explicit example.

The example chosen

While the few earlier references available [6,429–432] focused on $\mu^- - e^+$ conversion mediated by heavy Majorana neutrinos, we will present the computation by means of the effective theory of a doubly charged scalar introduced in section 3.3. In this scenario, $\mu^- - e^+$ conversion is realised via the diagram in Fig. 5.13, and the following interactions are required for its description:

$$\begin{aligned}\mathcal{L}_{\text{int}} = f_{ab}\, S^{++}\, \overline{(E_{\text{R}a})^c}\, E_{\text{R}b} - \frac{g^2 v^4\, \xi}{4\Lambda^3}\, W_\nu^+\, W^{+\nu}\, S^{--} \\ + \frac{g}{2\sqrt{2}} V_{ud}\, W_\nu^-\, \overline{d}\, \gamma^\nu\, (1-\gamma_5)\, u \,+ \text{h.c.}\end{aligned} \tag{5.3.5}$$

The former two are chosen in agreement with Eqs. (3.3.1) and (3.3.3),[13] and the corresponding Feynman rules are displayed in Appendix A. Given the weak interaction contained in Eq. (5.3.5), it can already be anticipated that the only operators possibly realised from Eq. (5.3.1) are $\epsilon_{3,6}^{\text{LL}x}$, with $x = \text{L}, \text{R}$ (where we sloppily but conventionally refer to the operator coefficient as "operator"). Since Fig. 5.13 is realised by the effective coupling in Eq. (5.3.5), there is no operator featuring ϵ_6. Furthermore, the doubly charged scalar S^{--} coupling to the two RH leptons, cf. Eq. (5.3.5), implies that $x = \text{R}$. Thus we expect our computation to yield a term ϵ_3^{LLR} at some point.

[13] Note that we use a different convention for f_{ab} with respect to Refs. [3,4], on which this section is based, in order to be consistent with section 5.2.

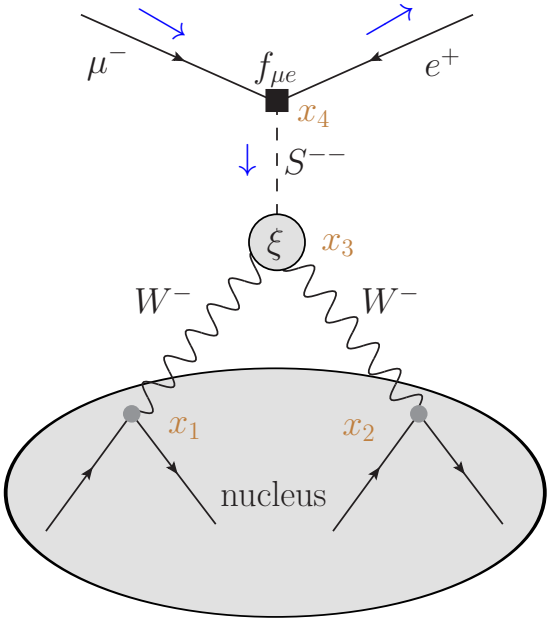

Figure 5.13: Realisation of $\mu^- - e^+$ conversion via a doubly charged scalar. The x_i denote the space-time points as used in Eq. (5.3.7).

How to obtain the amplitude

To generate the diagram in Fig. 5.13, we need to go to fourth order in perturbation theory. Hence, the resulting leading order amplitude reads

$$\begin{aligned}&\langle N', f|S^{(4)}|N, i\rangle \\ &= \frac{1}{4!}\,\langle N', f|\int \mathrm{d}^4x_1\,\mathrm{d}^4x_2\,\mathrm{d}^4x_3\,\mathrm{d}^4x_4\,\widehat{T}\Big\{\mathcal{L}_{\text{int}}(x_1)\mathcal{L}_{\text{int}}(x_2)\mathcal{L}_{\text{int}}(x_3)\mathcal{L}_{\text{int}}(x_4)\Big\}|N, i\rangle\,,\end{aligned} \tag{5.3.6}$$

where $\widehat{T}$ indicates time-ordering. The external (real) states are denoted by $\langle N'|$ and $|N\rangle$ for the final and initial state nucleus as well as $\langle f|$ and $|i\rangle$ for the final state positron and the initial bound muon. Upon assigning the space-time four-vectors x_i to fixed vertices, we obtain a combinatorial factor of 4!. Furthermore, we need to take into account that there is an additional factor of 2 due to the symmetric property of f_{ab}, i.e., $[f_{e\mu}\overline{(E_{\mathrm{R}e})^c}\,E_{\mathrm{R}\mu} + f_{\mu e}\overline{(E_{\mathrm{R}\mu})^c}\,E_{\mathrm{R}e}]S^{++} = 2\,f_{e\mu}\overline{(E_{\mathrm{R}e})^c}\,E_{\mathrm{R}\mu}\,S^{++}$. This way, the amplitude takes the form

$$\begin{aligned}&\langle N', f|S^{(4)}|N, i\rangle \\ &= -\frac{f_{e\mu}\,g^4v^4\,\xi V_{ud}^2}{16\Lambda^3}\langle N', f|\int \mathrm{d}^4x_1\,\mathrm{d}^4x_2\,\mathrm{d}^4x_3\,\mathrm{d}^4x_4\,\widehat{T}\Big\{J_{\mathrm{L},\nu}(x_1)W^{-\nu}(x_1)\,J_{\mathrm{L},\rho}(x_2) \\ &\quad W^{-\rho}(x_2)\,W^+_\sigma(x_3)W^{+\sigma}(x_3)S^{--}(x_3)\,S^{++}(x_4)\overline{(E_{\mathrm{R}e})^c}(x_4)E_{\mathrm{R}\mu}(x_4)\Big\}|N, i\rangle\,.\end{aligned} \tag{5.3.7}$$

The next step is to contract the boson fields. There are two indistinguishable options to contract the W-bosons, which leads to an additional factor 2:

$$\begin{aligned}
&\widehat{T}\Big\{W^{-\nu}(x_1)\,W^{-\rho}(x_2)\,W^{+}_{\sigma}(x_3)W^{+\sigma}(x_3)\,S^{--}(x_3)\,S^{++}(x_4)\Big\}\\
&=\widehat{N}\Big\{\overbrace{W^{-\nu}(x_1)\,\overbrace{W^{-\rho}(x_2)\,W^{+}_{\sigma}(x_3)}W^{+\sigma}(x_3)}\,S^{--}(x_3)\,S^{++}(x_4)\\
&+\overbrace{W^{-\nu}(x_1)\,\overbrace{W^{-\rho}(x_2)\,W^{+}_{\sigma}(x_3)}W^{+\sigma}(x_3)}\,S^{--}(x_3)\,S^{++}(x_4)\Big\}\\
&=2\,\Delta_W^{\nu\sigma}(x_1-x_3)\Delta^{\rho}_{W\,\sigma}(x_2-x_3)\,\Delta_S(x_3-x_4)\,,
\end{aligned}\tag{5.3.8}$$

when phrased in terms of propagators in coordinate space. The propagators in coordinate space can be written as Fourier transforms of their momentum space representations,

$$\begin{aligned}
\Delta_S(x-y)&=\int\frac{\mathrm{d}^dq}{(2\pi)^d}\,\mathrm{e}^{-iq\cdot(x-y)}\,\frac{i}{q^2-M_S^2+i\varepsilon}\,,\\
\Delta_W^{\nu\sigma}(x-y)&=\int\frac{\mathrm{d}^dq}{(2\pi)^d}\,\mathrm{e}^{-iq\cdot(x-y)}\,\frac{-i}{q^2-M_W^2+i\varepsilon}\left(g^{\nu\sigma}-\frac{q^\nu q^\sigma}{M_W^2}\right),
\end{aligned}\tag{5.3.9}$$

where the momenta q propagate from space-time point y to x, respectively. That way, we introduce the momenta q (propagating from x_4 to x_3), l (propagating from x_3 to x_2), and k (propagating from x_3 to x_1).

At this point, instead of obstinately pursuing the computation, it is useful to take a closer look at the energy scales of the conversion process, see e.g. Refs. [6, 433]. We only consider the $g.s.\to g.s.$ process, which means that both the initial and final nucleus are in the ground state ($g.s.$). Although the $g.s.\to g.s.$ process is estimated to constitute only about $\sim 40\%$ of the total amount of nuclear transitions [414], it is experimentally favoured due to its minimal background for the outgoing positron, as it carries away the maximal energy. The basic concept of the $\mu^- - e^+$ conversion is that a muon is trapped by an atom, cascades down in energy levels until it is bound in the $1s$ state, and gets then captured by the nucleus, thereby emitting a positron. The total energy of the muon in the $1s$ bound state is given by $E_\mu = m_\mu - \varepsilon_b$, where m_μ is the muon mass and ε_b is its binding enery. Since the binding energy is roughly $\varepsilon_b \simeq m_\mu/m_e \cdot 13.6\ \mathrm{eV}\cdot Z \ll m_\mu$, the muon can in any case be considered as non-relativistic. The energy of the positron hence results into:

$$E_e = \underbrace{m_\mu-\varepsilon_b}_{\sim\mathcal{O}(100\ \mathrm{MeV})} - \underbrace{(E_f-E_i)}_{\sim\mathcal{O}(\mathrm{MeV})} \sim \mathcal{O}(100\ \mathrm{MeV})\,,\tag{5.3.10}$$

where $E_{i,f}$ are the energies of the initial and final nuclear ground states, respectively. Both nuclei are – to a good approximation – at rest, which in combination with the nuclei not being excited leads to $E_f - E_i \sim \mathcal{O}(\mathrm{MeV})$ [430]. Two things can therefore be concluded:

1. The positron energy peaks around m_μ, which allows for a separation from most of the background positrons stemming from, e.g., β^+ decay stemming from potential impurities. To also suppress the background positrons from radiative muon capture there are certain requirements on the target nucleus mass, see Ref. [46]. This will hold as long as the experiment is able to distinguish positrons from electrons (which is non-trivial if they are fast). For more information, see section 5.1.

2. The energy transfer from the bound muon to the nucleus is small, $\mathcal{O}(\text{MeV})$, which implies that $l^2, k^2, q^2 \ll M_S^2, M_W^2$. The latter amounts to effectively integrating out both the W-bosons and the doubly charged scalar.

Upon contracting the bosonic propagators, the matrix element takes the form

$$\begin{aligned} -i\,\frac{f_{e\mu}\,g^4 v^4\,\xi V_{ud}^2}{8\Lambda^3\,M_S^2\,M_W^4}\int \mathrm{d}^4x_1\,\mathrm{d}^4x_2\,\mathrm{d}^4x_3\,\mathrm{d}^4x_4\int\frac{\mathrm{d}^4q\,\mathrm{d}^4k\,\mathrm{d}^4l}{(2\pi)^{12}}\,\langle N', f|\,\mathrm{e}^{-iq\cdot(x_3-x_4)} \\ \mathrm{e}^{-ik\cdot(x_1-x_3)}\mathrm{e}^{-il\cdot(x_2-x_3)}\,\widehat{T}\Big\{J_{\mathrm{L},\nu}(x_1)J_{\mathrm{L}}^{\nu}(x_2)\underbrace{\overline{(E_{\mathrm{R}e})^c}(x_4)E_{\mathrm{R}\mu}(x_4)}_{=j_{\mathrm{R}}(x_4)/2}\Big\}|N,i\rangle\,. \end{aligned} \tag{5.3.11}$$

Since we contracted the gauge boson propagators, it is reasonable to also switch to a notation using Fermi's constant, i.e., $G_F/\sqrt{2} = g^2/(8M_W^2)$. At this point, we can also identify the short-range operator coefficient. For brevity, we introduce the operator coefficient that is realised in this scenario, as derived in more detail in section 5.3.3:

$$\epsilon_3^{\mathrm{LLR}} \equiv 4V_{ud}^2\,m_p\,\frac{f_{e\mu}v^4\,\xi}{\Lambda^3 M_S^2}. \tag{5.3.12}$$

We furthermore note that x_3-dependences solely remain in the exponential functions. Hence, we obtain a four-dimensional delta-function, $(2\pi)^4\,\delta^{(4)}(l - q + k)$, upon performing the x_3-integration. We can dispose of the l-integration subsequently. That way, we obtain:

$$\begin{aligned} &-i\,\frac{G_F^2}{2m_p}\,\epsilon_3^{\mathrm{LLR}}\int \mathrm{d}^4x_1\,\mathrm{d}^4x_2\,\mathrm{d}^4x_4\int\frac{\mathrm{d}^4q\,\mathrm{d}^4k}{(2\pi)^8} \\ &\langle N', f|\,\mathrm{e}^{iq\cdot x_4}\mathrm{e}^{-ik\cdot x_1}\mathrm{e}^{-i(q-k)\cdot x_2}\widehat{T}\Big\{J_{\mathrm{L},\nu}(x_1)J_{\mathrm{L}}^{\nu}(x_2)j_{\mathrm{R}}(x_4)\Big\}|N,i\rangle\,. \end{aligned} \tag{5.3.13}$$

Next, we consider the remaining structures,

$$\begin{aligned} &\langle N', f|\widehat{T}\Big\{J_{\mathrm{L},\nu}(x_1)J_{\mathrm{L}}^{\nu}(x_2)j_{\mathrm{R}}(x_4)\Big\}|N,i\rangle \\ =&\langle N'|\widehat{T}\Big\{J_{\mathrm{L},\nu}(x_1)J_{\mathrm{L}}^{\nu}(x_2)\Big\}|N\rangle\langle f\,|j_{\mathrm{R}}(x_4)|\,i\rangle\,, \end{aligned} \tag{5.3.14}$$

which allows to split the structure into hadronic and leptonic parts.

Starting with the leptonic part, we need to take into account that neither the muon nor the positron are freely propagating. The muon is bound in the $1s$ state, whereas the positron is a free particle which propagates under the influence of the Coulomb potential of the nucleus. Consequently, we need to modify the spinors u and v of the muon and the positron, respectively, to describe a bound state and a continuum state subject to a potential, instead of freely propagating particles and antiparticles. This can be done by using [6, 430]:[14]

$$\begin{aligned} u_\mu^{\text{free}} &\to \phi_\mu(\vec{x}_4)\, u_\mu^{\text{free}} \\ \text{and} \quad v_e^{\text{free}} &\to \sqrt{F(Z-2, E_e)}\, v_e^{\text{free}}\,, \end{aligned} \tag{5.3.15}$$

where the bound muon wave function ϕ_μ and the Fermi function $F(Z, E)$ are given by[15]

$$\begin{aligned} \phi_\mu(\vec{x}) &= \frac{Z^{3/2}}{(\pi a_\mu^3)^{1/2}}\, \mathrm{e}^{-\frac{Z}{a_\mu}|\vec{x}|} \\ \text{and} \quad F(Z,E) &= \left[\frac{2}{\Gamma[2\gamma_1+1]}\right]^2 (2|\vec{p}_e|R)^{2(\gamma_1-1)} |\Gamma[\gamma_1 - iy]|^2 \mathrm{e}^{-\pi y}\,. \end{aligned}$$

Here, $a_\mu = 4\pi/(m_\mu e^2)$ is the muon's Bohr radius, $\gamma_1 = \sqrt{1-(\alpha Z)^2}$, $y = \alpha Z E/|\vec{p}_e|$, and $\alpha \simeq 1/137$ is the fine structure constant. Furthermore, Z denotes the atomic number and $R = 1.1\, A^{1/3}$ fm the nuclear radius for an atom with mass number A. We will abbreviate $u_\mu \equiv u_\mu^{\text{free}}$ and $v_e \equiv v_e^{\text{free}}$ in the following. That way, the leptonic part of the amplitude can be rewritten such that

$$\langle f|j_{\mathrm{R}}(x_4)|i\rangle = 2\,\mathrm{e}^{ik_e\cdot x_4}\, \underbrace{\mathrm{e}^{-ik_\mu\cdot x_4}}_{\approx \mathrm{e}^{-iE_\mu\cdot x_4^0}} \sqrt{F(Z-2,E_e)}\, \phi_\mu(\vec{x}_4)\, \overline{v_e}(k_e)\, \mathrm{P_R}\, u_\mu(k_\mu)\,, \tag{5.3.16}$$

with $\mathrm{P_R} \equiv (1+\gamma_5)/2$ and the muon (positron) momentum denoted by k_μ (k_e). Given that we assume the muon to be non-relativistic, we can thus simplify Eq. (5.3.13) using

$$\begin{aligned} &\int \mathrm{d}^4x_{1,2,4} \int \frac{\mathrm{d}^4q\, \mathrm{d}^4k}{(2\pi)^8}\, \mathrm{e}^{iq\cdot x_4} \mathrm{e}^{-ik\cdot x_1} \mathrm{e}^{-i(q-k)\cdot x_2} \mathrm{e}^{ik_e\cdot x_4} \mathrm{e}^{-iE_\mu\cdot x_4^0} \\ &= \int \mathrm{d}^4x_{1,2}\, \mathrm{d}^3x_4 \int \frac{\mathrm{d}^3q\, \mathrm{d}^4k}{(2\pi)^7}\, \mathrm{e}^{-ik\cdot(x_1-x_2)} \mathrm{e}^{-i\vec{q}\cdot(\vec{x}_4-\vec{x}_2)} \mathrm{e}^{-i\vec{k}_e\cdot\vec{x}_4} \mathrm{e}^{-i(E_\mu-E_e)x_2^0}\,. \end{aligned} \tag{5.3.17}$$

[14] Note that Ref. [6] uses another normalisation for the spinors than we do, which also reflects in different relations for the spin sums. The translation will be discussed in Appendix C.

[15] Note that we consistently use the non-relativistic approximation for the bound muon wave function. Note also that the sign of y is opposite to the the usual one quoted in Fermi functions, due to the emitted particle being a positron rather than an electron, cf. Appendix F.3 in Ref. [226].

Moving on to the hadronic part, we need to incorporate the information that the quarks are not locally fixed, but instead distributed within the nucleons. This can be done by introducing so-called *nucleon form factors*, which model the charge distribution. We use the dipole parametrisation such that

$$\tilde{F}(\vec{p}^{\,2},\,\Lambda_i) = \frac{1}{(1+\vec{p}^{\,2}/\Lambda_i^2)^2}\,, \tag{5.3.18}$$

where the scale $\Lambda_i \sim \mathcal{O}(\mathrm{GeV})$ depends on how the quarks interact. As there are two nucleon interactions taking place, we thus include an additional factor of $\tilde{F}(\vec{k}^{\,2},\,\Lambda_i)\,\tilde{F}((\vec{k}-\vec{q})^2,\,\Lambda_i)$. We can neglect the $\vec{q}$-dependence due to the momentum transfer being of the order $m_\mu \ll \Lambda_i$. As a result, not only the k^0- but also the $\vec{q}$-dependence restricts itself to the exponential functions, allowing for

$$\begin{aligned}
&\int \mathrm{d}^4x_{1,2}\,\mathrm{d}^3x_4 \int \frac{\mathrm{d}^3q\,\mathrm{d}^4k}{(2\pi)^7}\,\mathrm{e}^{-ik\cdot(x_1-x_2)}\mathrm{e}^{-i\vec{q}\cdot(\vec{x}_4-\vec{x}_2)}\mathrm{e}^{-i\vec{k}_e\cdot\vec{x}_4}\mathrm{e}^{-i(E_\mu-E_e)x_2^0}\\
&\quad\times \tilde{F}^2(\vec{k}^{\,2},\,\Lambda_i)\,\phi_\mu(\vec{x}_4) =\\
&\int \mathrm{d}^4x_{1,2} \int \frac{\mathrm{d}^3k}{(2\pi)^3}\,\mathrm{e}^{i\vec{k}\cdot(\vec{x}_1-\vec{x}_2)}\mathrm{e}^{-i\vec{k}_e\cdot\vec{x}_2}\mathrm{e}^{-i(E_\mu-E_e)x_2^0}\,\delta(x_1^0-x_2^0)\,\tilde{F}^2(\vec{k}^{\,2},\,\Lambda_i)\,\phi_\mu(\vec{x}_2)\,.
\end{aligned} \tag{5.3.19}$$

Moreover, we can re-express the hadronic part using a non-relativistic approximation, which leads to

$$\begin{aligned}
&\langle N'|\widehat{T}\Big\{J_{\mathrm{L},\nu}(x_1)J_{\mathrm{L}}^{\nu}(x_2)\Big\}|N\rangle\\
=&\sum_n \Big\{\Theta(x_1^0-x_2^0)\,\mathrm{e}^{i(E_f-E_n)x_1^0}\,\mathrm{e}^{i(E_n-E_i)x_2^0}\langle N'|J_{\mathrm{L},\nu}(\vec{x}_1)|n\rangle\langle n|J_{\mathrm{L}}^{\nu}(\vec{x}_2)|N\rangle\\
&+\Theta(x_2^0-x_1^0)\,\mathrm{e}^{i(E_f-E_n)x_2^0}\,\mathrm{e}^{i(E_n-E_i)x_1^0}\langle N'|J_{\mathrm{L},\nu}(\vec{x}_2)|n\rangle\langle n|J_{\mathrm{L}}^{\nu}(\vec{x}_1)|N\rangle\Big\}\,,
\end{aligned} \tag{5.3.20}$$

where $\Theta(x)$ denotes the Heaviside function. Here, we take the sum over the virtual intermediate nuclear states labeled by n and make use of $J_{\mathrm{L},\nu}(\vec{x}) \equiv J_{\mathrm{L},\nu}(0,\vec{x})$. Further simplifications arise from the aforementioned considerations that implied $x_1^0 = x_2^0$. The latter results into n-independent factors which allow us to carry out the sum explicitly and make use of the completeness of the set of states introduced: $\sum_n |n\rangle\langle n| = 1$. In combination with $\Theta(0) = 1/2$, the hadronic part, Eq. (5.3.20), takes the following form after performing the x_1^0-integration:

$$\mathrm{e}^{i(E_f-E_i)x_2^0}\langle N'|J_{\mathrm{L},\nu}(\vec{x}_1)J_{\mathrm{L}}^{\nu}(\vec{x}_2)|N\rangle\,. \tag{5.3.21}$$

Checking for x_2^0-dependences we note that, at this point, x_2^0 only appears in exponents. Upon carrying out this integration, we finally obtain the conservation of external energies, $2\pi\,\delta(E_f - E_i + E_e - E_\mu)$, as to be expected.

Combining these modifications that enter due to the physical properties of the process, we can rewrite Eq. (5.3.13) into

$$-i\,\frac{G_F^2\epsilon_3^{\mathrm{LLR}}}{m_p}\,(2\pi)\,\delta(E_f-E_i+E_e-E_\mu)\,\overline{v_e}(k_e)\,\mathrm{P_R}\,u_\mu(k_\mu)\int \mathrm{d}^3x_{1,2}\int\frac{\mathrm{d}^3k}{(2\pi)^3}$$
$$\langle N'|\,\mathrm{e}^{i\vec{k}\cdot(\vec{x}_1-\vec{x}_2)}\mathrm{e}^{-i\vec{k}_e\cdot\vec{x}_2}\,\tilde{F}^2(\vec{k}^{\,2},\,\Lambda_i)\,\sqrt{F(Z-2,E_e)}\,\phi_\mu(\vec{x}_2)\,J_{\mathrm{L},\nu}(\vec{x}_1)J_{\mathrm{L}}^{\nu}(\vec{x}_2)|N\rangle\,. \tag{5.3.22}$$

Within the non-relativistic approximation, the hadronic currents can be written in terms of effective transition operators. These consist of the basic spin and isospin structures. In principle, there are five spin structures and only one isospin structure [414]. As explained in Refs. [6, 414, 429, 433], however, two spin structures are expected to be most important: the Fermi ($\propto g_V$) and Gamow-Teller ($\propto g_A$) parts. Hence, the hadronic current can be rephrased as

$$\begin{aligned}&\tilde{F}(\vec{k}^{\,2},\,\Lambda_i)\,J_{\mathrm{L},\nu}(\vec{x}\,)\\&\to\sum_m\tau_m^-\,\Big(g_V\,\tilde{F}(\vec{k}^{\,2},\,\Lambda_V)\,g_{\nu 0}+g_A\,\tilde{F}(\vec{k}^{\,2},\,\Lambda_A)\,g_{\nu j}\,\sigma_m^j\Big)\,\delta^{(3)}(\vec{x}-\vec{r}_m\,)\,,\end{aligned} \tag{5.3.23}$$

where we sum over all nucleons, with $\vec{r}_m$ being the position of the m-th nucleon. Here, τ_m^- is the nuclear isospin raising operator, which means that it can change protons into neutrons (as needed for $\mu^- - e^+$ conversion):

$$\tau_m^-\,|\mathrm{proton}\rangle_m=|\mathrm{neutron}\rangle_m\quad\text{and}\quad\tau_m^-\,|\mathrm{neutron}\rangle_m=0\,. \tag{5.3.24}$$

The Gamow-Teller operator flips the spin of the m-th nucleon into the j-th direction. Note that we have employed different scales Λ_i, with $i=V,A$, depending on the type of interaction. Generic values are $\Lambda_V=0.71$ GeV and $\Lambda_A=1.09$ GeV [6].

Now we have collected all ingredients to obtain the final version of the amplitude. Using Eq. (5.3.22) together with

$$\begin{aligned}&\tilde{F}(\vec{k}^{\,2},\,\Lambda_{i_1})\,J_{\mathrm{L},\nu}(\vec{x}_1)\,\tilde{F}(\vec{k}^{\,2},\,\Lambda_{i_2})\,J_{\mathrm{L}}^{\nu}(\vec{x}_2)\to\\&\sum_{m,l}\tau_m^-\tau_l^-\,\Big(g_V^2\,\tilde{F}^2(\vec{k}^{\,2},\,\Lambda_V)-g_A^2\,\tilde{F}^2(\vec{k}^{\,2},\,\Lambda_A)\,\vec{\sigma}_m\cdot\vec{\sigma}_l\Big)\,\delta^{(3)}(\vec{x}_1-\vec{r}_m\,)\,\delta^{(3)}(\vec{x}_2-\vec{r}_l\,),\end{aligned} \tag{5.3.25}$$

we obtain the final version of the amplitude:

$$\begin{aligned}\mathcal{M}=&\frac{G_F^2\epsilon_3^{\mathrm{LLR}}g_A^2m_e}{2R}\,\sqrt{F(Z-2,E_e)}\,\delta(E_f-E_i+E_e-E_\mu)\\&\overline{v_e}(k_e)\,\mathrm{P_R}\,u_\mu(k_\mu)\,\mathcal{M}^{(\mu^-,e^+)\,\phi}\,.\end{aligned} \tag{5.3.26}$$

In accordance with Ref. [6], cf. Appendix D in order to understand the equivalence in detail, we define the *nuclear matrix element* to be[16]

$$\mathcal{M}^{(\mu^-,e^+)\,\phi} \equiv \frac{4\pi}{(2\pi)^3}\,\frac{R}{m_p m_e}\int \mathrm{d}^3k\,\langle N'|\sum_{m,l}\tau_m^-\tau_l^- \left[\tilde{F}^2(\vec{k}^{\,2},\,\Lambda_A)\,\vec{\sigma}_m\cdot\vec{\sigma}_l - \frac{g_V^2}{g_A^2}\,\tilde{F}^2(\vec{k}^{\,2},\,\Lambda_V)\right] \mathrm{e}^{i\vec{k}\cdot(\vec{r}_m-\vec{r}_l)}\mathrm{e}^{-i\vec{k}_e\cdot\vec{r}_l}\,\phi_\mu(\vec{r}_l)\,|N\rangle\,. \tag{5.3.27}$$

We have now reached an important point: once the reader's favourite nuclear physics expert has computed a numerical values for the NME $\mathcal{M}^{(\mu^-,e^+)\,\phi}$, this can be directly inserted into Eq. (5.3.26) and used to constrain any particle physics model leading to the operator $\epsilon_3^{\mathrm{LLR}}$. The same could in principle be done for all other short-range operators in Eq. (5.3.1), provided that the corresponding NMEs are known.

Let us end this subsection by a remark that enables the reader to understand how to derive and use the decay rate in case ϵ_3^{xyz} is realised. It is important to note that, in case the conversion is realised by means of a RH hadronic current, one has to rephrase this hadronic current as

$$\begin{aligned}&\tilde{F}(\vec{k}^{\,2},\,\Lambda_i)\,J_{\mathrm{R},\nu}(\vec{x}\,)\\ &\to\sum_m\tau_m^-\,\left(g_V\,\tilde{F}(\vec{k}^{\,2},\,\Lambda_V)\,g_{\nu 0}-g_A\,\tilde{F}(\vec{k}^{\,2},\,\Lambda_A)\,g_{\nu j}\,\sigma_m^j\right)\,\delta^{(3)}(\vec{x}-\vec{r}_m\,)\,,\end{aligned} \tag{5.3.28}$$

in contrast to the LH hadronic current in Eq. (5.3.23). This means that, in case of $x = y$, the NME in Eq. (5.3.27) is valid for both $x = \mathrm{L},\mathrm{R}$, leading to the more general decay rate in Eq. (5.3.37). On the other hand, in case $x \neq y$, the sign in front of the Gamow-Teller part in Eq. (5.3.27) is changed. Naturally, this change translates to the NME given in Eq. (5.3.36).

From the amplitude to the decay rate

In order to derive the decay rate from the matrix element obtained above, we need to employ Fermi's Golden Rule,

$$\Gamma = 2\pi\,\frac{V/T}{(2\pi)^3}\int \mathrm{d}^3k_e\,|\mathcal{M}|^2\,, \tag{5.3.29}$$

where an integral over the positron's momentum k_e is performed. Here, T is some time interval covering the process, and V is some volume that we set to

[16] Note that Eqs. (37) and (49) in Ref. [6], which both are supposed to contain expressions for the NME in case of a realisation via heavy Majorana neutrinos, differ by a factor of 2. After carefully checking an analogous discussion for $0\nu\beta\beta$ [434], we reckon that Eq. (49) of [434] is the correct normalisation, while the additional factor of 2 in Eq. (37) of [434] is a typo. Our matrix element in Eq. (5.3.27) is defined to be consistent with Eq. (49) in Ref. [6].

be unity, i.e., $V = 1$. The latter was already done silently when introducing the electron wave function in Eq. (5.3.16).[17]

Next, we take the spin average over the initial and the spin sum over the final states. With respect to the free spinors and to the Lorentz structure, we deal with the expression

$$\frac{1}{2}\sum_{r,s} |\overline{v_e^r}(k_e)\,\mathrm{P_R}\,u_\mu^s(k_\mu)|^2 = \frac{1}{4}\,. \tag{5.3.30}$$

Note that we obtain this result independently of the normalisation that was used for the free spinors, because the normalisation of the spinors and the according spin sums ultimately cancel in the squared amplitude (as they should in order to yield a consistent result). In doing so, we get

$$\begin{aligned}&\frac{1}{2}\sum_{\text{spins}} |i\mathcal{M}|^2 \\ &= \frac{g_A^4 m_e^2 G_F^4 |\epsilon_3^{\text{LLR}}|^2}{16R^2}\,|F(Z-2,E_e)|\text{“}\delta(E_f - E_i + E_e - E_\mu)^2\text{”}\,|\mathcal{M}^{(\mu^-,e^+)\,\phi}|^2\,,\end{aligned} \tag{5.3.31}$$

where we encounter two issues that we need to discuss briefly.
First of all, we can assume to good approximation that the muon wave function only varies slowly within the nucleus, which is justified both by the muon being non-relativistic and by the size of the nucleus being tiny compared to the muon's Bohr radius. Thus, the following standard approximation is valid [435]:

$$|\mathcal{M}^{(\mu^-,e^+)\,\phi}|^2 = \langle\phi_\mu\rangle^2\,|\mathcal{M}^{(\mu^-,e^+)}|^2 \quad \text{with} \quad |\mathcal{M}^{(\mu^-,e^+)}| = |\mathcal{M}^{(\mu^-,e^+)\,\phi}|_{\phi=1}\,. \tag{5.3.32}$$

We can use $\langle\phi_\mu\rangle^2 = \frac{\alpha^3 m_\mu^3}{\pi}\frac{Z_{\text{eff}}}{Z}$ as an approximation for the muon average probability density [435], where Z_{eff} denotes the effective atomic charge that accounts for the deviation from the wave function at the origin [433], as defined in Eq. (5.2.3). It can be obtained conveniently by taking the average of the muon wave function over the nuclear density [211, 418].
Second, we also encounter the standard "issue" of squaring the delta-function. How to treat this square is discussed thoroughly in many textbooks, see e.g. Ref. [436], and it results in

$$\text{“}\delta(E_f - E_i + E_e - E_\mu)^2\text{”} = \frac{T}{2\pi}\,\delta(E_f - E_i + E_e - E_\mu)\,. \tag{5.3.33}$$

[17] In our normalisation with respect to free spinors, the wave function is given by $\overline{\psi}_e = \mathrm{e}^{ik_e\cdot x}\overline{v}_e$, where $V \equiv 1$ has already been employed. So, the electron wave function is 'normalised to one particle in the volume $V = 1$' [417].

Putting everything together, the decay rate takes the form

$$\Gamma = \frac{g_A^4 m_e^2 G_F^4 |\epsilon_3^{\text{LLR}}|^2}{16R^2} \left|F(Z-2,E_e)\right| \langle\phi_\mu\rangle^2 \int \frac{\mathrm{d}^3 k_e}{(2\pi)^3} \delta(E_f - E_i + E_e - E_\mu) \left|\mathcal{M}^{(\mu^-,e^+)}\right|^2 . \tag{5.3.34}$$

For a $g.s. \to g.s.$ transition, we can assume that $E_i \simeq E_f$. In addition, we take the positron to be highly relativistic, i.e. $E_e \simeq |\vec{k}_e|$, while the muon is perfectly non-relativistic, i.e. $E_\mu \simeq m_\mu$. As a consequence, the delta-function reduces considerably, $\delta(E_f - E_i + E_e - E_\mu) \to \delta(|\vec{k}_e| - m_\mu)$. Furthermore, as shown in Appendix D, the NME only depends on the absolute value of $\vec{k}_e$ but not on its direction. Hence, the angular integration simply provides a factor of 4π, and the remaining $|\vec{k}_e|$ integration only enforces $|\vec{k}_e| = m_\mu$. So, the decay rate – after performing the phase space integration of the NME – takes its final form:

$$\Gamma = \frac{g_A^4\, G_F^4\, m_e^2\, m_\mu^2\, |\epsilon_3^{\text{LLR}}|^2}{32\pi^2 R^2} \left|F(Z-2,E_e)\right| \langle\phi_\mu\rangle^2 \left|\mathcal{M}^{(\mu^-,e^+)}\right|^2 . \tag{5.3.35}$$

The NME used here is obtained from combining Eqs. (5.3.27) and (D.0.14):

$$\begin{aligned}\mathcal{M}^{(\mu^-,e^+)} =& \frac{8R}{m_p m_e} \int \mathrm{d}k\, k^2 \langle N'| \sum_{m,l} \tau_m^- \tau_l^- \\ & \left[\tilde{F}^2(\vec{k}^{\,2},\, \Lambda_A)\, \vec{\sigma}_m \cdot \vec{\sigma}_l - \frac{g_V^2}{g_A^2}\, \tilde{F}^2(\vec{k}^{\,2},\, \Lambda_V)\right] j_0(k r_{lm}) \\ & \sum_\lambda \sqrt{2\lambda+1}\, j_\lambda(k_e R_{lm}) j_\lambda(k_e r_{lm}/2) \left\{ Y_\lambda(\Omega_{r_{lm}}) \otimes Y_\lambda(\Omega_{R_{lm}}) \right\}_{00} |N\rangle .\end{aligned} \tag{5.3.36}$$

Note that our decay rate, Eq. (5.3.35), differs from the one obtained in Ref. [6] by a factor of π, even upon using the translations discussed in Appendix C. The tension between the results only appears at the level of decay rates. As shown in Appendix C, the results agree on the level of amplitudes.
More generally, in case only a short-range operator of type ϵ_3^{xxz} is realised,[18] the decay rate is given by:

$$\Gamma = \frac{g_A^4\, G_F^4\, m_e^2\, m_\mu^2\, |\epsilon_3^{xxz}|^2}{32\pi^2 R^2} \left|F(Z-2,E_e)\right| \langle\phi_\mu\rangle^2 \left|\mathcal{M}^{(\mu^-,e^+)}\right|^2 . \tag{5.3.37}$$

So far, the NME for the short-range operator ϵ_3^{xxz} for ^{48}Ti is accessible, taking the value $|\mathcal{M}^{(\mu^-,e^+)}| = 5.2$ [6]. Using this value, one can compute the

[18] Recall that, in case ϵ_3^{xyz} with $x \neq y$ is realised, the NME takes a slightly different form, i.e., there is a relative sign change in between the Gamow-Teller and the Fermi contributions in comparison to $x = y$ in Eqs. (5.3.27) and (5.3.36) from employing Eq. (5.3.28).

decay rate by means of Eq. (5.3.37), in case the particle physics model of choice realises ϵ_3^{xxz}. Thereby, particle physics models realising some form of this short-range operator coefficient can be constrained by a non-observation of the process. Since it is not clear how much LNV is present in which corner of flavour space, it is useful to estimate the muon conversion rates for different settings and compare the discovery potential for future $\mu^- - e^+$ conversion and $0\nu\beta\beta$ experiments, which we will do in section 5.3.4.

Eq. (5.3.37) is the desired result: given a concrete particle physics model that reproduces ϵ_3, one can match this operator coefficient to fundamental model parameters. As soon as the NME $\mathcal{M}^{(\mu^-,e^+)}$ is known, all other quantities contained in the decay rate are either known constants of Nature[19] or they can be computed easily. Apart from the obvious dependence on the NME, nuclear characteristics are contained in the radius R (i.e., the atomic number A) and in the Fermi function $F(Z-2, E_e)$. However, at least for the set of isotopes discussed in the literature on muon conversion, the main variation with Z and/or A lies within the NME itself, whereas all other isotope-dependent quantities vary comparatively mildly.

5.3.3 Matching concrete particle physics models onto effective operator coefficients

In this section, we will discuss how to map certain particle physics models onto the effective operator coefficients contained in Eq. (5.3.1). Given that in our computation performed in the previous section we have drawn the explicit comparison to Ref. [6] at several places, we will start this section by a simplified discussion focusing on drawing the parallels between the heavy neutrino exchange discussed in that reference and our example model featuring the doubly charged scalar. We will then present a more detailed discussion on how to obtain ϵ-coefficients from several concrete models. Feynman rules which may be necessary to reproduce our results are listed in Appendix A.

Heavy neutrino exchange vs. doubly charged scalar exchange

In order to use the NMEs as derived for the exchange of heavy Majorana neutrinos [6], we calculated the conversion amplitude, factorised it into particle and nuclear physics contributions, and determined the factorised decay rate, see section 5.3.2. To further check if we performed every step of the computation consistently, we now match the amputated diagram for the realisation of $\mu^- - e^+$ conversion via the doubly charged scalar to the version with the heavy Majorana neutrino. With this procedure we can compare our

[19] Note that, however, the value of the axial vector coupling g_A may be affected by *quenching* [408], just as for $0\nu\beta\beta$. On the other hand, at present there is no agreement on whether this is an actual issue, or not [437].

decay rate, Eq. (5.3.35) where the short-range operator was explicitly given by Eq. (5.3.12), with Eq. (50) from Ref. [6].

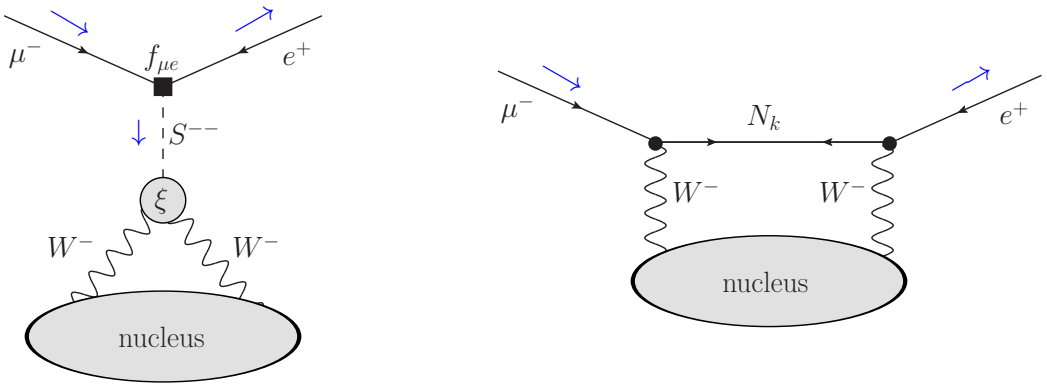

Figure 5.14: Realisation of μ^-– e^+ conversion via (*left*): a doubly charged scalar or (*right*): a heavy Majorana neutrino.

From the Feynman diagrams in Fig. 5.14, we obtain two amplitudes from which we amputate the nuclear parts. This is a reasonable procedure since for both realisations of the μ^-– e^+ conversion the nuclear part of the process – depicted by the greyish circle – is identical. Starting with the left-hand side of Fig. 5.14, we extract

$$\begin{aligned} &\overline{v}_e \, \mathrm{P_R} \, u_\mu \, \frac{-i g^2 \, f_{e\mu} \, v^4 \, \xi \, g_{\sigma' \rho'}}{\Lambda^3} \, \frac{i}{q^2 - M_S^2} \, \frac{-i g^{\sigma\sigma'}}{k_1^2 - M_W^2} \, \frac{-i g^{\rho\rho'}}{k_2^2 - M_W^2} \\ &\xrightarrow{M_{S,W}^2 \gg k_{1,2}^2, q^2} \quad \overline{v}_e \, \mathrm{P_R} \, u_\mu \, \frac{i g^2 \, f_{e\mu} \, v^4 \, \xi \, g^{\sigma\rho}}{M_W^4 \, \Lambda^3 \, M_S^2} \, . \end{aligned} \tag{5.3.38}$$

Analogously, we obtain

$$\begin{aligned} &\sum_k \overline{v_e} \, \gamma_{\rho'} \, \mathrm{P_R} \, \gamma_{\sigma'} \, u_\mu \, U_{ek} U_{\mu k} \, \frac{g^2}{2} \, \frac{i M_k}{l^2 - M_k^2} \, \frac{-i g^{\sigma\sigma'}}{k_1^2 - M_W^2} \, \frac{-i g^{\rho\rho'}}{k_2^2 - M_W^2} \\ &\xrightarrow{M_{k,W}^2 \gg k_{1,2}^2, l^2} \quad \overline{v_e} \, \gamma_\rho \, \mathrm{P_R} \, \gamma_\sigma \, u_\mu \, \frac{i g^2}{2 \, M_W^4} \underbrace{\sum_{k=4,5,\ldots} \frac{U_{ek} U_{\mu k}}{M_k^2}}_{\equiv \langle M_N^{-1} \rangle_{\mu e}} \end{aligned} \tag{5.3.39}$$

from the heavy Majorana neutrino exchange, where the sum extends over all heavy mass eigenstates N_k with admixtures U_{ak} to the active flavours a.

At first sight something seems to be wrong, given that the Lorentz structures of Eqs. (5.3.38) and (5.3.39) differ. However, taking into account that the hadronic part is symmetric under exchange of the indices, i.e. $J^\sigma(\vec{x}_1) J^\rho(\vec{x}_2) = J^\sigma(\vec{x}_2) J^\rho(\vec{x}_1)$, it becomes clear that only the symmetric part of

$$\gamma_\rho \, \mathrm{P_R} \, \gamma_\sigma = \gamma_\rho \, \gamma_\sigma \, \mathrm{P_L} = \left(g_{\rho\sigma} + \frac{1}{2} [\gamma_\rho, \, \gamma_\sigma] \right) \mathrm{P_L}$$

contributes to the decay rate. Consequently, the relevant part of Eq. (5.3.39) is given by

$$\overline{v}_e \, \mathrm{P_L} u_\mu \, \frac{i g^2 \, g_{\sigma\rho}}{2 \, M_W^4} \, \langle M_N^{-1} \rangle_{\mu e} \, . \tag{5.3.40}$$

In contrast to the doubly charged scalar, which only couples to RH charged leptons, the heavy Majorana neutrino interacts weakly which leads to LH "external" leptons. Upon calculating the decay rate, both amplitudes are spin-summed and spin-averaged. As a result, only

$$\frac{1}{2} \sum_{\text{spins}} |\overline{v}_e \, \mathrm{P_R} \, u_\mu|^2 \qquad \text{and} \qquad \frac{1}{2} \sum_{\text{spins}} |\overline{v}_e \, \mathrm{P_L} \, u_\mu|^2 \tag{5.3.41}$$

are of importance to the final result. Since both expressions equally lead to the factor 1/4, the chirality of the external leptons does not play a role and can be neglected for the matching. We thus obtain the following correspondence between the two models:

$$\frac{2 \, f_{e\mu} \, v^4 \, \xi}{\Lambda^3 \, M_S^2} \qquad \Longleftrightarrow \qquad \langle M_N^{-1} \rangle_{\mu e}, \tag{5.3.42}$$

which can be understood when comparing Eqs. (5.3.38) and (5.3.40).

Matching particle physics models onto the corresponding operator coefficients

Now that we have compared two concrete settings to each other, we will show that this is not a mere coincidence and demonstrate on a general ground how to match a model onto the general effective vertex coefficients presented in Eq. (5.3.1), and thus justify the section above.

We start with the model already used in the previous section, in which the SM particle content is extended by a number n of SM singlet, RH Majorana neutrinos N_k, as used in Ref. [6]. When rotating the full neutrino mass matrix to a diagonal shape, we end up with $k = 3+n$ Majorana neutrinos with masses m_k. Choosing the specific setting of a Seesaw model [32, 36, 124, 438–440], one obtains three very light (active) neutrinos $\nu_{1,2,3}$ and n heavy (sterile) neutrinos $N_{4,5,...}$. Vice versa, the SM's neutrino flavour eigenstates ν_a can be expressed in terms of light and heavy Majorana mass eigenstates,

$$\nu_a = \sum_{l=1,2,3 \ \text{(light)}} U_{al}^* \nu_l + \sum_{l=4,5,... \ \text{(heavy)}} U_{al}^* N_l \, ,$$

which allows for the suppressed coupling of charged leptons to heavy Majorana neutrinos, see Fig. A.5, whose strength is parametrised by the active-sterile mixing element U_{al} (where $l = 4, 5, ...$). This coupling results in the realisation of the $\mu^- - e^+$ conversion, as depicted on the left-hand side of Fig. 5.15. Note

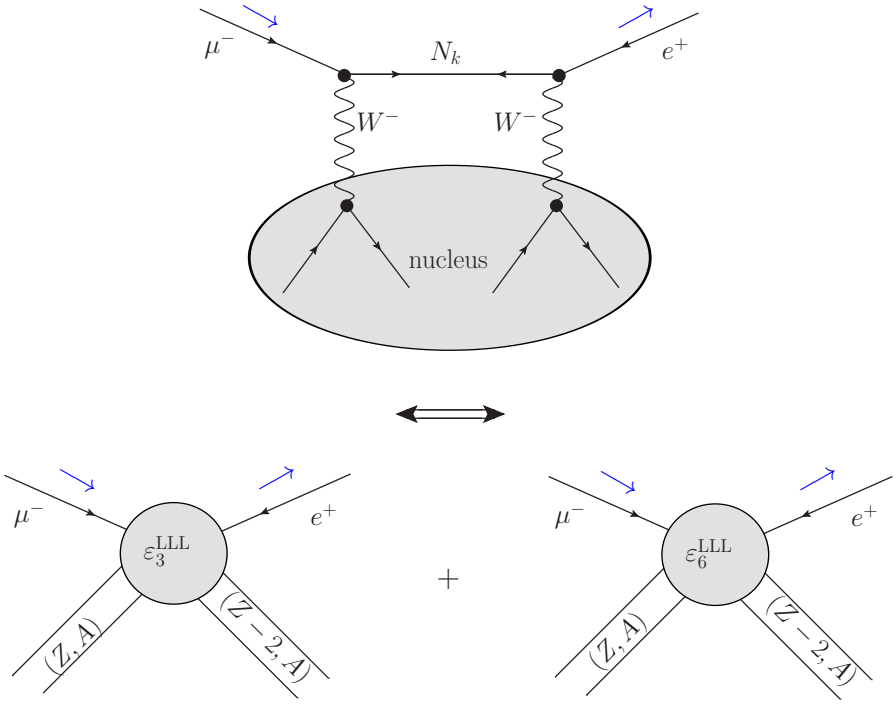

Figure 5.15: Model with heavy Majoranas N_k mapped onto short-range operators.

that, within this model, the analogous process with light instead of heavy neutrinos leads to a contribution to the long-range part of ϵ_3, which we disregard for the time being.
From the left-hand side of Fig. 5.15, we obtain

$$\begin{aligned} i\mathcal{M}_k = &\,\overline{d}\,\frac{ig}{2\sqrt{2}}\,V_{ud}\,\gamma^\nu\,(1-\gamma_5)\,u\,\overline{d}\,\frac{ig}{2\sqrt{2}}\,V_{ud}\,\gamma^\rho\,(1-\gamma_5)\,u\,\frac{-ig_{\nu\nu'}}{l_1^2-M_W^2}\,\frac{-ig_{\rho\rho'}}{l_2^2-M_W^2} \\ &\cdot\,\overline{e^c}\,\frac{-ig}{2\sqrt{2}}\,U_{ek}\,\gamma^{\nu'}\,(1+\gamma_5)\,\frac{i(\not{q}+M_k)}{q^2-M_k^2}\,\frac{ig}{2\sqrt{2}}\,U_{\mu k}\,\gamma^{\rho'}\,(1-\gamma_5)\,\mu\,, \end{aligned} \tag{5.3.43}$$

with a sum over the different k in case more than one heavy neutrino exist. In the short-range limit (i.e., $l_{1,2}^2,\, q^2 \ll M_k^2,\, M_W^2$), and by summing over all heavy mass eigenstates, this turns into

$$i\mathcal{M} = i\frac{g^4}{64\,M_W^4}\,V_{ud}^2\,\langle M_N^{-1}\rangle_{\mu e}\,\overline{d}\,\gamma^\nu\,(1-\gamma_5)\,u\,\overline{d}\,\gamma^\rho\,(1-\gamma_5)\,u\,\overline{e^c}\,\gamma_\nu\,(1+\gamma_5)\,\gamma_\rho\,(1-\gamma_5)\,\mu. \tag{5.3.44}$$

The leptonic current is expressed in terms of the bilinear covariants to match Eq. (5.3.1),

$$\overline{e^c}\,\gamma_\nu\,(1+\gamma_5)\,\gamma_\rho\,(1-\gamma_5)\,\mu = 2g_{\nu\rho}\,\underbrace{\overline{e^c}\,(1-\gamma_5)\,\mu}_{=j_{\mathrm{L}}} + 2i\,\underbrace{\overline{e^c}\,\sigma_{\nu\rho}\,(1-\gamma_5)\,\mu}_{=j_{\mathrm{L},\nu\rho}}\,. \tag{5.3.45}$$

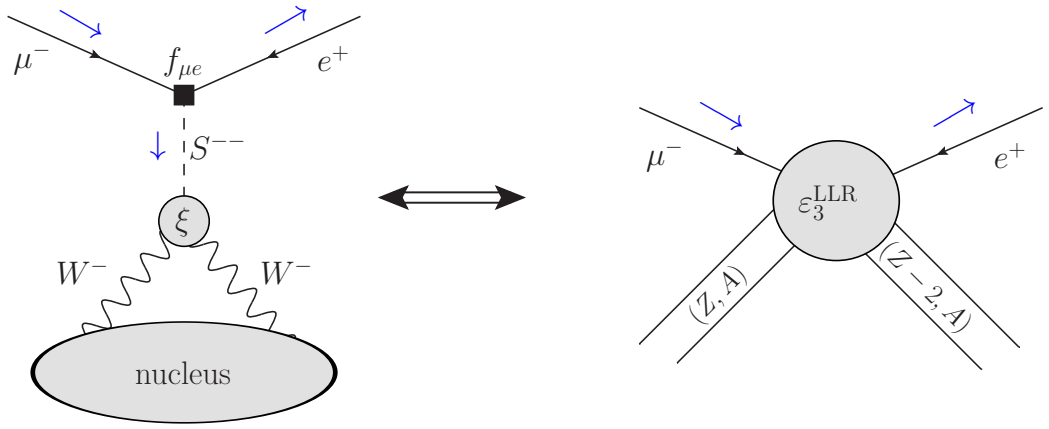

Figure 5.16: Model with doubly charged scalar S^{--} mapped onto a short-range operator.

In terms of Fermi's constant and using hadronic and leptonic currents, this amplitude then takes the form

$$i\mathcal{M} = i\,\frac{G_F^2}{2m_p}\Big[\underbrace{2V_{ud}^2\,m_p\,\langle M_N^{-1}\rangle_{\mu e}}_{=\epsilon_3^{\mathrm{LLL}}}\,J_{\mathrm{L}}^{\nu}\,J_{\mathrm{L},\nu}\,j_{\mathrm{L}} + \underbrace{2iV_{ud}^2\,m_p\,\langle M_N^{-1}\rangle_{\mu e}}_{=\epsilon_6^{\mathrm{LLL}}}\,J_{\mathrm{L}}^{\nu}\,J_{\mathrm{L}}^{\rho}\,j_{\mathrm{L},\nu\rho}\Big]\,. \tag{5.3.46}$$

As already indicated on the right-hand side of Fig. 5.15, the structures $\epsilon_{3,6}^{\mathrm{LLL}}$ are realised in this model. Due to the symmetry of the non-relativistic hadronic currents, however, we can simply omit ϵ_6. Thus, in the end, the Seesaw model only admits the single operator

$$\frac{G_F^2}{2m_p}\,\epsilon_3^{\mathrm{LLL}}\,J_{\mathrm{L}}^{\nu}\,J_{\mathrm{L},\nu}\,j_{\mathrm{L}}\,. \tag{5.3.47}$$

Another model that includes LNV is the SM extended by a doubly charged scalar. This model was introduced in section 3.3 and employed to derive the decay rate in section 5.3.2. Within this setting, the LNV $\mu^- - e^+$ conversion is realised by the left-hand side of Fig. 5.16.
The corresponding amplitude is given by

$$\begin{aligned} i\mathcal{M} = {}& \overline{d}\,\frac{ig}{2\sqrt{2}}\,V_{ud}\,\gamma^{\nu}\,(1-\gamma_5)\,u\,\overline{d}\,\frac{ig}{2\sqrt{2}}\,V_{ud}\,\gamma^{\rho}\,(1-\gamma_5)\,u\,\frac{-ig_{\nu\nu'}}{l_1^2-M_W^2}\,\frac{-ig_{\rho\rho'}}{l_2^2-M_W^2} \\ & \overline{e^c}\,2if_{e\mu}\,\frac{1}{2}\,(1+\gamma_5)\,\mu\frac{-ig^2v^4\,\xi}{2\Lambda^3}\,g^{\rho'\nu'}\,\frac{i}{q^2-M_S^2}\,. \end{aligned} \tag{5.3.48}$$

Taking the short-range limit ($l_{1,2}^2,\ q^2 \ll M_S^2,\ M_W^2$), we obtain

$$i\mathcal{M} = -i\,\frac{G_F^2}{2m_p}\Big[\underbrace{4V_{ud}^2\,m_p\,\frac{f_{e\mu}v^4\,\xi}{\Lambda^3 M_S^2}}_{=\epsilon_3^{\mathrm{LLR}}}\,J_{\mathrm{L}}^{\nu}\,J_{\mathrm{L},\nu}\,j_{\mathrm{R}}\Big]\,, \tag{5.3.49}$$

which is precisely the result used in Eq. (5.3.12). Note that we have used the hadronic/leptonic currents from Eqs. (5.3.2) and (5.3.3), as well as some standard identifications such as Fermi's constant.

Another model realising only ϵ_3 is a Left-Right symmetric model supplemented by additional Higgs bosons and singlet fermions as put forward in Ref. [441] and displayed in Fig. 5.17. The resulting effective short-range oper-

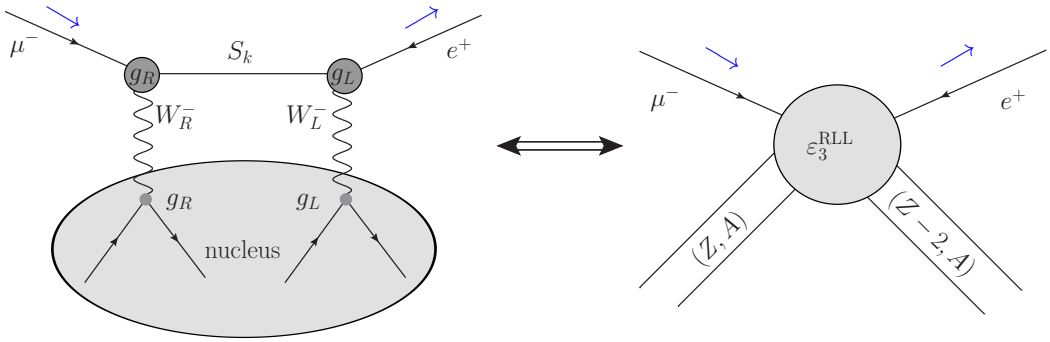

Figure 5.17: Left-Right symmetric model mapped onto short-range operators.

ator and coupling are:

$$J_{\mathrm{R}}^{\mu} J_{\mathrm{L},\mu} j_{\mathrm{L}} \quad \Rightarrow \quad \epsilon_3^{\mathrm{RLL}} = V_{ud}^2 \frac{\langle p \rangle^3}{m_e} \left(\frac{g_{\mathrm{R}}}{g_{\mathrm{L}}} \right) \sum_{j=1}^{3} \frac{V_{ej}^{\nu S} V_{\mu j}^{SS}}{M_{S_j}^2} \tan \zeta_{\mathrm{LR}} \,, \tag{5.3.50}$$

where ζ_{LR} is the W-boson mixing angle, $g_{\mathrm{R}} \sim g_{\mathrm{L}}$ are the $\mathrm{SU}(2)_{\mathrm{R,L}}$ gauge couplings, and M_{S_j} denotes the mass of the respective singlet fermion S_j contained in the model; furthermore, $\langle p \rangle \simeq 100$ MeV is the average nucleon momentum scale whose definition includes the factor of m_p that would otherwise appear in $\epsilon_3^{\mathrm{RLL}}$, see Ref. [441] for details. Although this example does not fulfil the requirements of using Eq. (5.3.37) in combination with the NME derived in Ref. [6] and displayed in Eq. (5.3.36), we will include it in the following discussion and estimate its NME to be of the same order of magnitude. This approach is justified by considering the NMEs of $0\nu\beta\beta$ for which this estimate holds [252]. Furthermore, we only aim at ballpark estimates on the discovery potential for ϵ_3 anyway because the NME values are uncertain, see section 5.1.

Our second-to-last example is taken from the two-loop neutrino mass model of Ref. [242], where the SM is extended by an SU(2) triplet and a doubly charged scalar. Within this setting, μ^-– e^+ conversion is realised by the diagram on the left-hand side of Fig. 5.18. The doubly charged component of the triplet and the singlet scalar mix to physical mass eigenstates $P_{1,2}^{\pm\pm}$ which realise the conversion via:

$$J_{\mathrm{L}}^{\mu} J_{\mathrm{L},\mu} j_{\mathrm{R}} \quad \Rightarrow \quad \epsilon_3^{\mathrm{LLR}} = \frac{4 m_p V_{ud}^2}{\sqrt{2}} Y_{e\mu} |\sin(2\omega)| \left| \frac{1}{M_1^2} - \frac{1}{M_2^2} \right| \,, \tag{5.3.51}$$

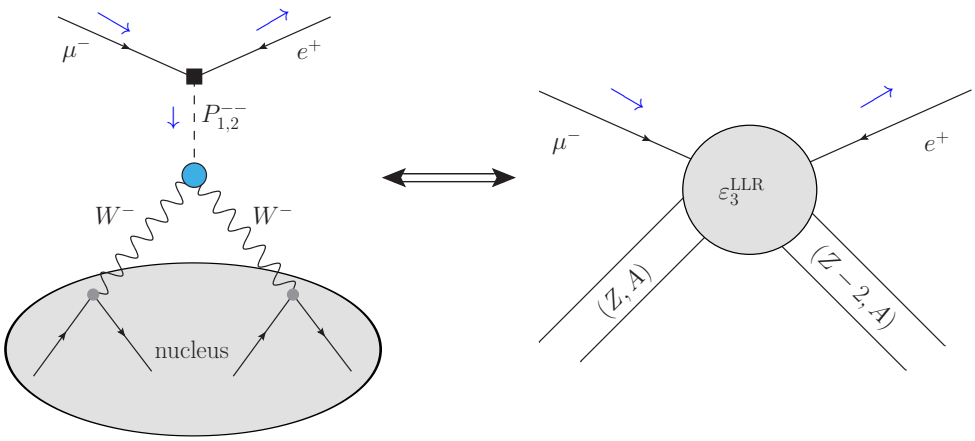

Figure 5.18: Cheng-Geng-Ng model mapped onto short-range operators.

where ω is the mixing angle of the doubly charged scalar mass eigenstates of masses $M_{1,2}$, v_T is the vacuum expectation value of the triplet Higgs, and $Y_{e\mu}$ denotes the singlet Yukawa coupling to two charged RH leptons.

Finally, we want to briefly discuss another class of models that generate LNV, which we have not yet mentioned, to show that it is by far not only the few examples mentioned that are covered by our formalism. Our final example are the so-called R-parity violating (RPV) supersymmetric (SUSY) theories. Within the framework of RPV SUSY, there are several mechanisms that provide LNV which are discussed broadly in the literature, see e.g. Refs. [161, 253, 442] for the case of $0\nu\beta\beta$. While we focus on short-range operators here, there are also interesting long-range contributions that can lead to sizeable contributions (see e.g. Ref. [426], where the cases of sbottom/stau exchanges avoid stringent bounds on the SUSY parameter space). When contemplating RPV SUSY, there are several mechanisms that provide $\mu^- - e^+$ conversion. For models with neutralino exchange being dominant [161], the contribution is similar to that from heavy RH neutrinos, cf. Eq. (5.3.46). Although in this case ϵ_3 is realised, such that limits from experiment can be translated, we do not consider it in the following due to its smallness. To demonstrate the potential that lies in $\mu^- - e^+$ conversion when contemplating RPV-SUSY, we consider the illustrative case of a gluino exchange being the dominating conversion mechanism. Although there is a number of Feynman diagrams contributing to the $\mu^- - e^+$ conversion due to gluino exchange [442], we will focus on the diagram given on the left-hand side of Fig. 5.19 for demonstration purposes. The couplings necessary to realise Fig. 5.19 can be taken from Ref. [167], Eq. (B.8), and [161], Eq. (18), amongst others. They read:

$$\mathcal{L} = \lambda'_{ijk}\, \tilde{d}^*_{k\mathrm{R}}\, \overline{l^c_{i\mathrm{R}}}\, u_{j\mathrm{L}} + g_3\, \frac{\lambda^{(a)}_{\alpha\beta}}{\sqrt{2}}\, \overline{q^\alpha}\, \mathrm{P_L}\, \tilde{g}^{(a)}\, \tilde{q}^\beta_{\mathrm{R}}\,. \tag{5.3.52}$$

Here, α, β denote the colour indices, and $\lambda^{(a)}$ are the Gell-Mann matrices with

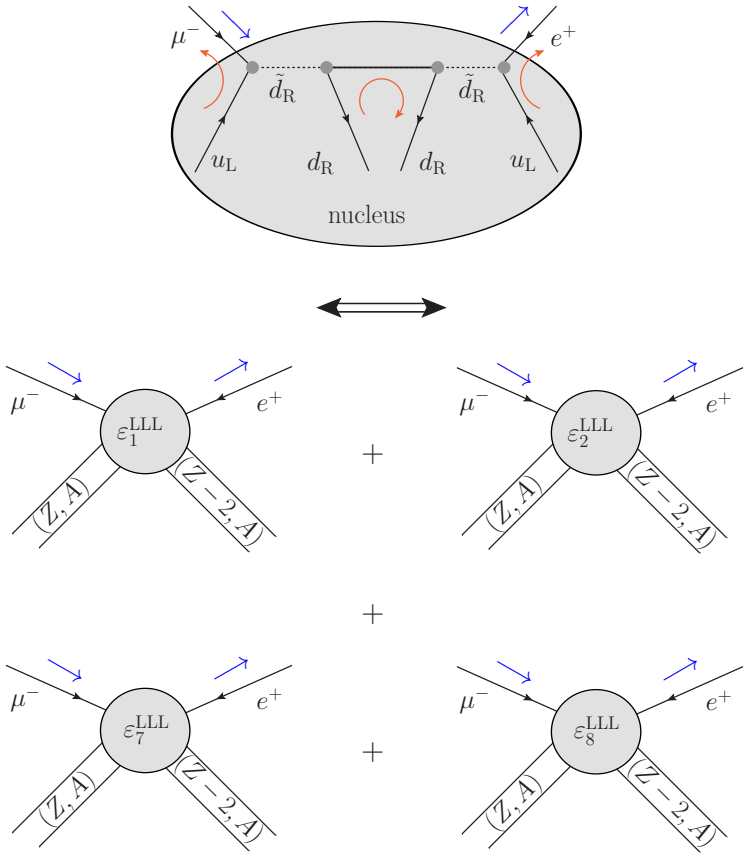

Figure 5.19: Model with R-parity violation: realisation via gluino exchange, mapped onto short-range operators. The red arrows indicate the fermion flow, i.e. the order in which each fermionic chain is written down.

$a = 1, \cdots, 8$. Upon employing the orientation of fermion flow as given on the left-hand side of Fig. 5.19, we obtain the amplitude

$$\begin{aligned} i\mathcal{M} \propto \left(\frac{i\,g_3}{\sqrt{2}}\right)^2 \lambda'_{211}\,\lambda'_{111}\,\frac{i}{p_1^2 - m_{\tilde{d}R}^2}\,\frac{i}{p_2^2 - m_{\tilde{d}R}^2}\,\overline{(\mu_L)^c}\,u_L\,\overline{(e^c)_R}\,u_L \\ \overline{d_R}\,\frac{i(\not{p}_1 - \not{p}_2 + M_{\tilde{g}})}{(p_1 - p_2)^2 - M_{\tilde{g}}^2}\,(d_R)^c\,. \end{aligned} \tag{5.3.53}$$

Taking the short-range limit, where $p_1^2,\ p_2^2,\ (p_1 - p_2)^2 \ll m_{\tilde{d}_R}^2,\ M_{\tilde{g}}^2$, the amplitude takes the form

$$i\mathcal{M} \propto \frac{i g_3^2}{2 m_{\tilde{d}R}^4\,M_{\tilde{g}}}\,\lambda'_{211}\,\lambda'_{111}\Big(\overline{(\mu_L)^c}\,u_L\Big)\Big(\overline{(e^c)_R}\,u_L\Big)\Big(\overline{d_R}\,(d_R)^c\Big)\,. \tag{5.3.54}$$

To match this expression onto the operators in Eq. (5.3.1), we need to rearrange the fermionic fields which can be done by employing Fierz transformations and some algebraic acrobatics. From rearranging the fermionic fields, we obtain

that the following four effective operators:

$$\begin{aligned}
&\left(\overline{(\mu_{\mathrm{L}})^c}\, u_{\mathrm{L}}\right)\left(\overline{(e^c)_{\mathrm{R}}}\, u_{\mathrm{L}}\right)\left(\overline{d_{\mathrm{R}}}\,(d_{\mathrm{R}})^c\right) \\
&= -\frac{1}{2}\underbrace{\left(\overline{d}\,\mathrm{P_L} u\right)\left(\overline{d}\,\mathrm{P_L} u\right)\left(\overline{e^c}\,\mathrm{P_L}\mu\right)}_{\to \epsilon_1^{\mathrm{LLL}}} - \underbrace{\left(\overline{d}\,\sigma_{\nu\rho}\,\mathrm{P_L} u\right)\left(\overline{d}\,\sigma^{\nu\rho}\,\mathrm{P_L} u\right)\left(\overline{e^c}\,\mathrm{P_L}\mu\right)}_{\to \epsilon_2^{\mathrm{LLL}}} \\
&\quad -\frac{1}{2}\underbrace{\left(\overline{d}\,\sigma_{\nu\rho}\,\mathrm{P_L} u\right)\left(\overline{d}\,\mathrm{P_L} u\right)\left(\overline{e^c}\,\sigma^{\nu\rho}\,\mathrm{P_L}\mu\right)}_{\to \epsilon_7^{\mathrm{LLL}}} \\
&\quad - i\underbrace{\left(\overline{d}\,\sigma_{\nu\rho}\,\mathrm{P_L} u\right)\left(\overline{d}\,\sigma^{\nu\kappa}\,\mathrm{P_L} u\right)\left(\overline{e^c}\,\sigma^{\rho}{}_{\kappa}\,\mathrm{P_L}\mu\right)}_{\to \epsilon_8^{\mathrm{LLL}}} .
\end{aligned} \tag{5.3.55}$$

Note that, due to the non-relativistic treatment of the hadronic currents, the operators corresponding to $\epsilon_{7,8}^{\mathrm{LLL}}$ will not contribute to the decay rate at this level of approximation. A general problem with these RPV models is that, although potentially promising, they cannot be properly assessed at the moment – which is why we could not include them in our analysis in section 5.3.4. For example, the short-range contributions discussed in [442] only realise the operators ϵ_1 and/or ϵ_2, and the same is true for the particularly promising long-range operators proposed in Ref. [426]. Thus, even though we can evaluate the effective operator coefficients in these settings and they seem to be rather large (possibly even larger than the ones we have included in Fig. 5.20), at the moment no computation of the corresponding NMEs is available for these cases. Therefore, we are unable to give a reliable prediction on how strongly these promising contributions could be constrained in the future. This is one particular example of advances being necessary on the nuclear physics side, and it may possibly motivate nuclear physics theorists to spread out their techniques of computing NMEs to cases involving $\mu^- - e^+$ conversion.

The strength of this formalism lies in its factorisation of the nuclear physics from the specifics of the particle physics model realising the conversion process. Consequently, by computing only a small number of NMEs, a wide range of particle physics models can be investigated. However, at this moment, only the NME for ϵ_3^{xxz} is available and we are in need of further NME computations for future analysis of e.g. RPV SUSY models in order to fully exploit the discovery potential that lies within the next generation of groundbreaking bound muon experiments like COMET [208], DeeMe [412], or Mu2e [366].

5.3.4 Physics reach of COMET and similar experiments

The goal of this section is to illustrate how experiments like COMET [208] could make a countable physics impact when aiming to measure $\mu^- - e^+$ con-

version. Note that, however, this section is only illustrative because currently several key pieces of information have not become available yet: while for the known case of the operator ϵ_3^{xxz} upcoming experiments can by an inch *not* scratch the surface of the relevant parameters, we will see that they are still close enough for investigations of the other possible operators to be interesting.

To illustrate the potential of future experiments to detect LNV in the $e\mu$-sector, we display the limits on and sensitivities to the two effective parameters $\epsilon_{3,ee}^{\mathrm{LLL}}$ and $\epsilon_{3,e\mu}^{xyz}$ [20] in Fig. 5.20, both for ongoing and future experiments on $0\nu\beta\beta$ and on $\mu^- - e^+$ conversion. In the former case, we illustrate the current limits for GERDA phase I (light green region, from Ref. [255]) and for the first data of phase II (light grey slice, from Ref. [443]), as well as a future projection of what could possibly be reached by experiments with Ge-76 (light red region, from Ref. [444]). In the case of $\mu^- - e^+$ conversion, however, the information is much more scarce, as already mentioned. For example, up to now no experiment has used Al-27 to study ordinary $\mu^- - e^-$ conversion, which is why there is no actual upper limit from that isotope. Other limits do exist, and for illustration we show how the bound on Au-197 from SINDRUM II (light blue region, from Ref. [383]; see Ref. [2] and/or section 5.1 for a collection of further limits) would translate into a limit on $\epsilon_{3,e\mu}$, provided that the sensitivity for $\mu^- - e^-$ conversion is identical to that for $\mu^- - e^+$ conversion (which is a good approximation up to a factor of $\mathcal{O}(1)$ [46, 378, 381]). It is, however, important to keep in mind that the values of the NMEs are uncertain as stated in section 5.1. While we would expect somewhat similar numbers for all isotopes, which is roughly the case for $0\nu\beta\beta$-NMEs [445], the only explicit value for $\mu^- - e^+$ conversion mediated by heavy particles was 5.2, computed in Ref. [6] for Ti-48, as to be investigated by PRISM/PRIME (light orange region, from Ref. [45]). However, for Al-27 as used in COMET, we have not found a tabulated value, so that we had to rely on the value of 5.2 at least serving as a ballpark estimate (light yellow region, from Ref. [208]). Clearly, the message is that further investigations from the nuclear physics side are needed.

In any case, the values used should serve as an illustration. What is clearly visible from the plot, though, is that the possible upper bounds from $0\nu\beta\beta$ on $\epsilon_{3,ee}$ are superior compared to those from $\mu^- - e^+$ conversion on $\epsilon_{3,e\mu}$, by about eight to nine orders of magnitude at least. This is to be expected, since experiments on $0\nu\beta\beta$ can usually operate with a solid target while muon conversion experiments have to rely on high intensity muon beams, such that there is a massive enhancement of the former type of experiments by the Avogadro number. However, this is not the full picture, since there could be particle physics models in which much more LNV is contained in the $e\mu$- than in the ee-sector, i.e., their predictions would be situated in the upper left half of the plot. Although this information has not always been worked out, we have already in a first investigation been able to identify several models in

[20] Note that we allow for $x \neq y$ when illustrating the reach of future experiments, as argued for in section 5.3.2, although relying on the NMEs determined for $x = y$.

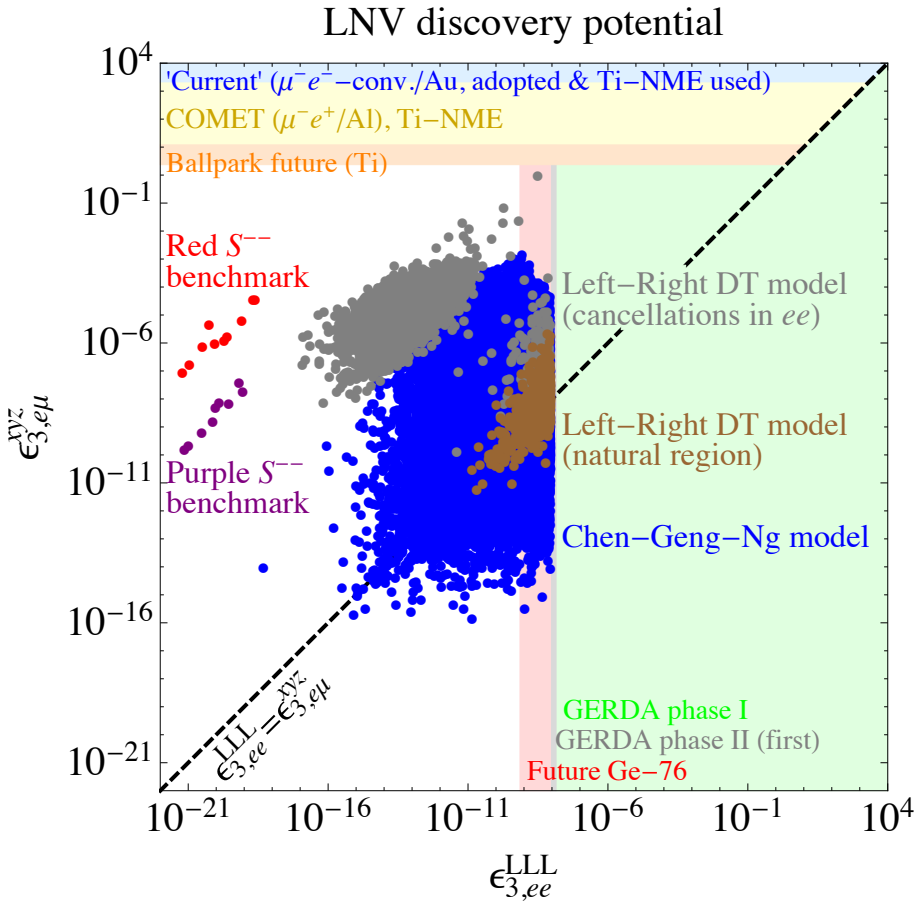

Figure 5.20: Illustration of the reach of future experiments for ϵ_3.

which LNV is much more prominent in the $e\mu$-sector, depicted by the scattered points in Fig. 5.20, many of which are located in the upper left half of the plot. The examples displayed are the red and purple allowed benchmark points from a two-loop neutrino mass model containing a doubly charged scalar [47], two regions from a Left-Right symmetric model supplemented by additional Higgs bosons and singlet fermions [441] (with the natural points depicted in brown and those which feature a cancellation in the ee-sector by the grey points), and an explicit example of $\mu^- - e^+$ conversion mediated by a superposition of doubly charged singlet and triplet scalar components [242] (blue points in the plot).[21] While these models still cannot be probed by the upcoming conversion experiments, at least the grey points nearly peak into the region accessible by future experiments, thereby illustrating that valuable new information is likely to be reached for more suitable settings and/or other operators. In particular, some of the potential long-range contributions look promising [426].

Recall further that there are hardly any detailed investigations available

[21] Note that we have already imposed the current bounds, which is why some sets of points seem to feature a sharp edge on the right.

at the moment, and we have only presented a few example models so that, in fact, there is potential to reveal further particle physics settings that can be probed by $\mu^- - e^+$ conversion.

5.3.5 Optimising the search for $\mu^+ - e^-$ conversion

Having discussed several aspects of the process of $\mu^- - e^+$ conversion, we can conclude that, in order to optimise our chances, improvements in the following three areas are needed:

1. **Experimentally**, not many very detailed sensitivity studies exist at this stage for $\mu^- - e^+$ conversion. Although new backgrounds such as protons [379] and pions [380] may appear, we can nevertheless expect sensitivity levels to be at least similar to those on $\mu^- - e^-$ conversion [378, 380, 382], with some previous limits being nearly identical for both processes [378, 381]. Only for COMET, a detailed sensitivity study has been conducted recently [46], but further studies can and should be done with existing resources.

2. **Nuclear matrix elements** have hardly been computed for $\mu^- - e^+$ conversion, which is particularly true for Al-27. The only two available are those for ϵ_3^{xxz} with light ($\mathcal{M}_\nu = 0.025$) and heavy ($\mathcal{M}_N = 5.2$) neutrino mediation [6, 433], both for Ti-48, with the latter being equivalent to the NME needed for the short-range ϵ_3-operator from Eq. (5.3.1). However, no further up-to-date computations seem to exist, *neither* for isotopes other than Ti-48 *nor* for short-range operators other than ϵ_3^{xxz}.[22] Furthermore, there seem to exist no theoretical works investigating which percentage of $\mu^- - e^+$ conversion takes place via the $g.s. \to g.s.$ transition and how this influences the discovery potential. This makes it currently *impossible* to present the full picture. Indeed, glancing at Fig. 5.20, it seems realistic that some models may be promising, and further investigations could reveal settings in reach of experiments. In section 5.3.3, we have identified other contributions realising operators ϵ_1 and ϵ_2. These contributions do look rather promising, and they may in fact have a greater potential to be detected in the near future. However, without any computations of NMEs, this cannot be judged. We would therefore like to transmit this message to the nuclear theory community since, in fact, LNV could possibly be found in $\mu^- - e^+$ conversion more easily than in $0\nu\beta\beta$. *Getting a better understanding of the nuclear physics part is the most important ingredient to make progress on $\mu^- - e^+$ conversion.*

[22] There is in fact one computation of the NME available for the case of Al-27 [414], however, that reference only treated the possibly unobservable [258] case of light neutrino mediation, but no short-range operators – and at least for Ti-48, this result did not carry over to heavy mediators [6, 433].

3. On the **particle physics** side there are, for many models, no detailed studies on how much LNV could be present in the $e\mu$-sector, and there is no information on which operators are realised. There exist detailed studies on $0\nu\beta\beta$ though, see e.g. Refs. [254, 446], which has been the focus for years. But, as we have illustrated in section 5.3.4, LNV in the ee-sector may be suppressed. However, most cases are only studied superficially, while new options like $\mu^- - e^+$ conversion can be available but are not discussed in detail. Sections 5.3.1, 5.3.2, and 5.3.3 make a step towards remedying the situation by providing a comprehensive study on $\mu^- - e^+$ conversion from a technical point of view and by investigating several LNV models.

Summing up, we are in a position in which experiments have a great potential to advance our knowledge on charged LFV and LNV in the $e\mu$-sector. However, the theory side has to gain momentum, both for particle and nuclear physics, since beneficial steps are obvious but not made. Only if all three communities pull together, advances will be achieved.

5.3.6 Summary

In this section, we have presented the complete computation of the rate for the LFV *and* LNV $\mu^- - e^+$ conversion, mediated by the effective operator $J_x^\nu J_{y,\nu} j_z$. After introducing the effective operator language in the way appropriate for this process, we have detailed the whole pathway from the amplitude to the decay rate. Our main target group are particle physicists, which is why we had a particular focus on displaying the steps related to the nuclear physics part involved as explicitly as possible. We have furthermore pointed out several concrete New Physics realisations of the effective operator used, all of which can in principle be experimentally probed by $\mu^- - e^+$ conversion. We augmented the discussion by an illustration of which physics impact upcoming experiments like COMET could make. We have also presented three areas which, if advanced further, could greatly help gaining fundamental physics insights using $\mu^- - e^+$ conversion: the more detailed investigation of particle physics models in what regards LNV in the $e\mu$ sector (to understand the possible gain), more involved experimental sensitivity studies (to determine the physics potential of upcoming experimental setups), and the up-to-now missing computation of the NMEs for the process (to sharpen the resulting limits on promising theories).

At the moment, with hardly any NME values being available, this is about as far as one could possibly go when aiming to obtain concrete numbers. However, given that we have now detailed how to perform the computation for the operator ϵ_3, it should at least in principle be clear how to approach the computation for other effective operators. Furthermore, several nuclear physics theory groups have already shown interest in the process, and if they succeed in obtaining further NMEs, the results from both sides could readily be put

together, to see which types of New Physics are the most promising in what concerns this $\mu^- - e^+$ conversion.

We want to end this text by stressing that the investigation of the $\mu^- - e^+$ conversion process has got quite some potential to it. It is a rare occasion in physics that we can expect near-future experiments to realistically improve a limit by four to five orders of magnitude. This is an opportunity we should not ignore, which is why we hope to have provided one of the initial sparks for further and more detailed investigations.

Chapter 6

Renormalisation Group Analysis of the Littlest Seesaw Model

In this chapter, we present a comprehensive renormalisation group analysis of the Littlest Seesaw model, which was introduced in section 3.4. We perform the first χ^2 analysis of the low-energy masses and mixing angles, in the presence of renormalisation group corrections, for various right-handed neutrino masses and mass orderings, both with and without supersymmetry. Note that this chapter is a slightly modified version of Ref. [5], ergo the two of them overlap for the most part.

Despite the impressive experimental progress in neutrino oscillation experiments [447], the dynamical origin of neutrino mass generation and lepton flavour mixing remains unknown [53, 448].[1] Furthermore, the octant of the atmospheric angle has not been determined yet, and its precise value is uncertain. While T2K prefers a close-to-maximal atmospheric mixing angle [24], NOνA excludes maximal mixing at 2.6σ [26]. The forthcoming results from T2K and NOνA will hopefully clarify the situation. An accurate determination of the atmospheric angle is important in order to test predictive neutrino mass and mixing models.

A highly interesting candidate for the origin of both naturally small neutrino masses and predictive lepton flavour mixing patterns is the Littlest Seesaw (LS) model, as reviewed in section 3.4. It combines the Seesaw mechanism based on two right-handed (RH) heavy neutrinos with constrained sequential dominance (CSD), giving rise to a very constrained neutrino Yukawa coupling matrix. As a result, the LS is highly predictive for both neutrino masses and PMNS mixing parameters. Note that there are four different cases for the LS, Cases A, B, C, and D, depending on the mass ordering of the RH neutrinos and on the particular structure of the neutrino Yukawa coupling matrix. Taking a closer look at the UV scenarios motivating the LS, we realise that the LS

[1] For more information on the subject of the origin of neutrino mass, see the overview in section 3.1.

model is reasonably defined at the scale of some grand unified theory (GUT). Since we are interested in the phenomenological viability of the four cases of the LS model, we, however, need to take into account that experiments are performed at the electroweak (EW) scale. Given that the GUT and EW scales are multiple orders of magnitude apart, we must incorporate that physical parameters change with the energy scale, following the notion of renormalisation group (RG) effects in section 4.1.

A first study of the RG corrections to the LS model was performed in Ref. [310]. The purpose of Ref. [5] (and this chapter) is to improve on that analysis and to debate the cases where the RG corrections are the most important. We therefore briefly review the progress and limitations of the approach and results in Ref. [310]. In Ref. [310] the authors focussed on analytically understanding the RG effects on the neutrino mixing angles for Cases A and B in great detail, while threshold effects were discussed based on two fixed RH neutrino masses, taken as 10^{12} GeV and 10^{15} GeV, close to the scale of GUTs, $\Lambda_{\rm GUT} = 2 \times 10^{16}$ GeV [310]. These analytical results were verified numerically. Furthermore, Cases C and D were investigated only numerically. However, the RG running of neutrino masses and lepton flavour mixing parameters were calculated at low energies, always assuming phenomenological best-fit values at high energies, which was justified a posteriori by the fact that *in most cases* the RG corrections to the neutrino mass ratio,[2] as well as the mixing angles were observed to be rather small [310]. Such cases with small RG corrections lead to an atmospheric mixing angle close to its maximal value, which is in some tension with the latest global fits. To account for the running of the neutrino masses, Ref. [310] modified the Dirac neutrino Yukawa matrix Y_ν by an overall factor of 1.25 with respect to the best-fit values obtained from tree-level analyses. This factor was chosen based on scaling the neutrino masses for Case A to obtain appropriate values at the EW scale, and subsequently used for all four LS cases. In other words, the numerical analysis of Ref. [310] chose input parameters that were extracted from a tree-level best fit, and adjusted them by an overall correction factor based on one specific case to include some corrections for the significant running in the neutrino masses.
There are several problems with this approach, though, as follows:

- The overall factor of 1.25 to the Dirac neutrino Yukawa matrix implies that only the running of the neutrino masses themselves is significantly affected by the choice of input parameters, while the neutrino mixing angles are still stable. Furthermore, it assumes that keeping the ratio of the input parameters unchanged when incorporating RG effects is reasonable. Both assumptions turn out to be incorrect.

- Having modified the Dirac neutrino Yukawa matrix based on Case A, Ref. [310] employs the same factor for all other Cases B, C, and D,

[2] This is in fact not true for the neutrino masses m_2 and m_3. Their running can be significant, as demonstrated in Figs. 1-4 in Ref. [310].

although the running behaviour can change fundamentally with the LS case.

- Most importantly, as mentioned above, the RG running of neutrino masses and lepton flavour mixing parameters were calculated at low energies, assuming phenomenological best-fit values at high energies. Clearly the correct approach would be to implement a complete scan of model input parameters in order to determine the optimum set of high energy input values from a global fit of the low energy parameters. This is what we will do in this chapter. As a consequence, the approximate measure of the goodness-of-fit[3] yields less than mediocre results for the input parameters used in Ref. [310]: $\chi^2_{\mathrm{A,B}}(\Lambda_{\mathrm{EW}}) \approx 50$ and $\chi^2_{\mathrm{C,D}}(\Lambda_{\mathrm{EW}}) \approx 175$. In comparison, our complete scan here will reveal much improved best-fit scenarios with $\chi^2_{\mathrm{A}}(\Lambda_{\mathrm{EW}}) = 7.1$, $\chi^2_{\mathrm{B}}(\Lambda_{\mathrm{EW}}) = 4.2$, $\chi^2_{\mathrm{C}}(\Lambda_{\mathrm{EW}}) = 3.2$, and $\chi^2_{\mathrm{D}}(\Lambda_{\mathrm{EW}}) = 1.5$.

On these grounds, we will carry out a detailed RG analysis of the LS model. As such it is no longer sufficient to fix the input parameters by fitting to the high-energy masses and mixing angles. Consequently, we implement a complete scan of model parameters for each case individually, to determine the optimum set of high-energy input values from a global fit of the low-energy parameters (which include the effects of RG running), and to re-assess whether RG corrections might still be sufficient to obtain a realistic atmospheric mixing angle. For that purpose, we employ the method of least squares based on two different estimators, as reviewed in section 4.3. We shall find that the largest corrections occur in the Standard Model (SM), although we shall also perform a detailed analysis of the Minimal Supersymmetric Standard Model (MSSM)[4] for various values of $\tan\beta$ for completeness. Since the RG corrections for the latter are relatively small, we relegate some of those results to Appendix F.

Based on the introduction of the LS in section 3.4, the conspectus of RG effects in section 4.1, and the overview on the χ^2 function as means of identifying best possible input parameters as well as an estimate of the goodness-of-fit in section 4.3, we have organised the remainder of this chapter as follows. In section 6.1 we qualitatively discuss the effects expected from RG corrections in the LS models. We focus on some key features that will help understand the findings in later sections, instead of aiming at a complete discussion of the RG effects. In section 6.2 we discuss the SM results in some detail, since this is where the RG corrections can be the largest, serving to reduce the atmospheric angle from a near maximal value at high energies to one close to the best-fit value at low energies in some cases. Subsequently, section 6.3 broaches the results for the RG analysis of the LS model in the MSSM, after which we com-

[3]Note that the goal is to minimise the value for χ^2, as defined in e.g. Ref. [43] and discussed in detail in section 4.3.

[4]When we refer to the MSSM or SM we really mean the LS models with or without supersymmetry. We shall use this rather imprecise terminology throughout this chapter.

pare the MSSM results to those obtained for the SM in section 6.4. Finally, we summarise our findings in section 6.5. Furthermore, there are two appendices being pertinent to this chapter. First, there is Appendix E, which introduces the notation needed to discuss benchmark scenarios for the LS model in the MSSM. And second, Appendix F displays tables with the results of the MSSM scenarios investigated but not included in section 6.3.

6.1 RGE Running in Littlest Seesaw Scenarios

Although the best-fit input parameters in this chapter were determined by means of numerically solving the renormalisation group equations (RGEs), we will briefly recapitulate some features of the LS's RG running to facilitate comprehending the distinctive behaviour of the different cases. This qualitative discussion is based on the more thorough analytical approaches in Refs. [310, 331]. We furthermore refer to sections 4.1 and 4.2 for a conspectus of RG effects and effective field theories.
We switch from denoting the heavy RH neutrino masses by M_{atm}, M_{sol} to labeling them by M_1, M_2 – to avoid mixing up the different cases and their opposite ordering of heavy neutrino masses. That is to say that, irrespective of the case discussed, M_2 always denotes the higher scale and M_1 the lower one.

For the LS, there are three different energy regimes of interest. Starting at the GUT scale, we can use the full theory's parameters and RGEs to describe the evolution down to $\mu = M_2$. At $\mu = M_2$, the heavier N_{R} is integrated out, and the light neutrino mass matrix as well as the RGEs have to be adapted. It is important to carefully match the full theory on the effective field theory (EFT) below the Seesaw scale, denoted by EFT 2. Using the modified RGEs, the parameters are further evolved down to $\mu = M_1$, where the remaining N_{R} is integrated out, and the parameters of this intermediate EFT 2 are matched to the EFT below M_1, denoted by EFT 1. Once again, the light neutrino mass matrix along with the RGEs have to be adjusted. As we assume a strong mass hierarchy, $M_2 \gg M_1$, it is important to decouple the heavy neutrinos subsequently and describe the intermediate RG behaviour accordingly.

Taking a closer look at the highest regime, we specify the LS input parameters at the GUT scale and additionally choose the flavour basis, i.e. both $Y_l(\mu = \Lambda_{\text{GUT}})$ and $M_{\text{R}}(\mu = \Lambda_{\text{GUT}})$ are diagonal. For now we are interested in the evolution of the neutrino mixing parameters, which implies narrowly watching how the mismatch between the basis where the charged-lepton Yukawa matrix Y_l is diagonal and the one where the light neutrino mass matrix m_ν is diagonal unfolds. Consequently, we track the RG running of both Y_l and m_ν. Above the upper Seesaw threshold, $\mu = M_2$, the evolution of the flavour structure of m_ν is mainly driven by $Y_\nu Y_\nu^\dagger$. Consequently, the varying flavour structures of the Dirac neutrino Yukawa matrix need to be examined more

thoroughly:

- Case A:
  Whether we take the benchmark input parameters as stated in section 3.4 or the global-fit parameters determined in sections 6.2 and 6.3, there is a hierarchy $a \sim \mathcal{O}(0.04) \ll b \sim \mathcal{O}(0.4)$, which allows for a further simplification:

$$\begin{aligned} Y_\nu Y_\nu^\dagger &= \begin{pmatrix} b^2 & nb^2 & (n-2)b^2 \\ nb^2 & a^2+n^2b^2 & a^2+n(n-2)b^2 \\ (n-2)b^2 & a^2+n(n-2)b^2 & a^2+(n-2)^2b^2 \end{pmatrix} \\ &\xrightarrow{n=3, a \ll b} \begin{pmatrix} b^2 & 3b^2 & b^2 \\ 3b^2 & \boxed{9b^2} & 3b^2 \\ b^2 & 3b^2 & b^2 \end{pmatrix} . \end{aligned} \tag{6.1.1}$$

  Consequently, Ref. [310] only considers the dominant $9b^2$ term and thereby solves the simplified RGE for m_ν analytically.

- Case B:
  In analogy to Case A, there is a hierarchy with respect to the input parameters $a \sim \mathcal{O}(0.04) \ll b \sim \mathcal{O}(0.4)$:

$$\begin{aligned} Y_\nu Y_\nu^\dagger &= \begin{pmatrix} b^2 & (n-2)b^2 & nb^2 \\ (n-2)b^2 & a^2+(n-2)^2b^2 & a^2+n(n-2)b^2 \\ nb^2 & a^2+n(n-2)b^2 & a^2+n^2b^2 \end{pmatrix} \\ &\xrightarrow{n=3, a \ll b} \begin{pmatrix} b^2 & b^2 & 3b^2 \\ b^2 & b^2 & 3b^2 \\ 3b^2 & 3b^2 & \boxed{9b^2} \end{pmatrix} . \end{aligned} \tag{6.1.2}$$

  Therefore, the simplified RGE of m_ν, which only takes into account the dominant (33)-entry, can be solved analytically.

- Case C:
  Due to the opposite ordering of heavy neutrino masses, the hierarchy arising from either the benchmark or the global-fit input parameters is also reversed, namely $a \sim \mathcal{O}(1.2) \gg b \sim \mathcal{O}(0.01)$:

$$\begin{aligned} Y_\nu Y_\nu^\dagger &= \begin{pmatrix} b^2 & nb^2 & (n-2)b^2 \\ nb^2 & a^2+n^2b^2 & a^2+n(n-2)b^2 \\ (n-2)b^2 & a^2+n(n-2)b^2 & a^2+(n-2)^2b^2 \end{pmatrix} \\ &\xrightarrow{n=3, b \ll a} \begin{pmatrix} b^2 & 3b^2 & b^2 \\ 3b^2 & \boxed{a^2} & \boxed{a^2} \\ b^2 & \boxed{a^2} & \boxed{a^2} \end{pmatrix} . \end{aligned} \tag{6.1.3}$$

Even when considering only the dominant contributions arising from a^2, the resulting simplified RGE of m_ν cannot be solved analytically anymore, due to the non-diagonal elements strongly affecting the flavour structure of m_ν.

- Case D:
  In analogy to Case C, there is a hierarchy to the input parameters $a \sim \mathcal{O}(1.2) \gg b \sim \mathcal{O}(0.01)$:

$$Y_\nu Y_\nu^\dagger = \begin{pmatrix} b^2 & (n-2)b^2 & nb^2 \\ (n-2)b^2 & a^2+(n-2)^2b^2 & a^2+n(n-2)b^2 \\ nb^2 & a^2+n(n-2)b^2 & a^2+n^2b^2 \end{pmatrix} \xrightarrow{n=3, b \ll a} \begin{pmatrix} b^2 & b^2 & 3b^2 \\ b^2 & a^2 & a^2 \\ 3b^2 & a^2 & a^2 \end{pmatrix} . \tag{6.1.4}$$

  Thus, even the simplified RGE of m_ν turns out to be too involved to be solved analytically. Consequently, Cases C and D are both investigated via a numerical approach in Ref. [310].

Note that, as apparent from the discussion in section 3.4 below Eqs. (3.4.17) and (3.4.18), it is $Y_\nu^{\mathrm{A}} Y_\nu^{\mathrm{A}\dagger} = Y_\nu^{\mathrm{C}} Y_\nu^{\mathrm{C}\dagger}$ and $Y_\nu^{\mathrm{B}} Y_\nu^{\mathrm{B}\dagger} = Y_\nu^{\mathrm{D}} Y_\nu^{\mathrm{D}\dagger}$. However, due to the inverted hierarchy with respect to a, b (stemming from the inverted heavy neutrino mass ordering), different entries dominate the RG evolution of m_ν, leading to different RG running behaviours. Thus, the degeneracy of the cases is resolved. This means that, although (in case of starting from the same set of benchmark input parameters) the neutrino masses and mixing angles of Case A, C and Case B, D at the GUT scale are identical,[5] the running behaviour of the mixing angles, which is mainly governed by $Y_\nu Y_\nu^\dagger$, can be rather different. Moreover, the discussion above uncovers a deeper connection among Cases A↔B and Cases C↔D, manifest in the shared respective input parameter as well as in the similar/same structure of $Y_\nu Y_\nu^\dagger$ dominating the running of m_ν. Having determined $m_\nu(M_2)$ from either the analytical or numerical RG evolution, we need to diagonalise the light neutrino mass matrix. That way, we obtain not only the neutrino masses $m_{2,3}(M_2)$ but also the transformation matrix $U_{\nu_{\mathrm{L}}}$. The latter, in combination with the unitary matrix $U_{e_{\mathrm{L}}}$ taking part in diagonalising Y_l, yields the PMNS matrix – and thereby the neutrino mixing parameters at the high scale $\mu = M_2$. Thus, still within the high-energy regime, we focus on the charged-lepton Yukawa matrix. Since we are interested in the flavour mixing caused by the running of Y_l, flavour-independent terms are neglected. But besides that, the RGE for Y_l can be solved analytically without further simplifications, meaning that once again $Y_\nu Y_\nu^\dagger$ drives the

[5] See sections 3.4 and 6.2.

flavour mixing. Finally, at $\mu = M_2$, Y_l is diagonalised by means of a bi-unitary transformation involving both $U_{e_{\rm L}}$ and $U_{E_{\rm R}}$. Consequently, one would have all necessary parameters at hand to extract approximations for the mixing angles, see Ref. [310]. For more information concerning the diagonalisation of Yukawa and mass matrices as well as the mismatch of mass eigenbases, see section 3.1.

Taking a closer look at the intermediate energy regime, $M_2 > \mu > M_1$, we need to employ EFT 2 to describe the parameters and RG running. At the threshold $\mu = M_2$, the effective light neutrino mass matrix can be written as

$$m_\nu^{(2)} = v^2 \left(\kappa^{(2)} + \tilde{Y}_\nu M_1^{-1} \tilde{Y}_\nu^T \right) , \tag{6.1.5}$$

where $\kappa^{(2)} \propto \hat{Y}_\nu M_2^{-1} \hat{Y}_\nu^T$ stems from decoupling the heavier RH neutrino with mass M_2. The expression $\tilde{Y}_\nu$ ($\hat{Y}_\nu$) is obtained from Y_ν by removing the column corresponding to the decoupled heavy neutrino of mass M_2 (the RH neutrino of mass M_1). Please note that the two terms on the right-hand side of Eq. (6.1.5) are governed by different RGEs, leading to so-called "threshold effects". The RGEs of $\kappa^{(2)}$ and $\tilde{Y}_\nu M_1^{-1} \tilde{Y}_\nu^T$ have different coefficients for the terms proportional to the Higgs self-coupling and gauge coupling contributions within the framework of the SM [331]. In combination with the strong mass hierarchy of the heavy RH neutrinos, which enforces a subsequent decoupling, the threshold effects become significant and thereby enhance the running effects on the neutrino mixing parameters.[6] From the discussion in Ref. [310], we learn that the threshold-effect-related corrections to the neutrino mixing angles between M_2 and M_1 are dominated by an expression proportional to $\kappa^{(2)}$. Hence, we examine the combination $\hat{Y}_\nu M_2^{-1} \hat{Y}_\nu^T$ for the four cases:

- Case A:

$$\hat{Y}_\nu M_2^{-1} \hat{Y}_\nu^T = M_{\rm sol}^{-1} \begin{pmatrix} b^2 & 3b^2 & b^2 \\ 3b^2 & 9b^2 & 3b^2 \\ b^2 & 3b^2 & b^2 \end{pmatrix} . \tag{6.1.6}$$

- Case B:

$$\hat{Y}_\nu M_2^{-1} \hat{Y}_\nu^T = M_{\rm sol}^{-1} \begin{pmatrix} b^2 & b^2 & 3b^2 \\ b^2 & b^2 & 3b^2 \\ 3b^2 & 3b^2 & 9b^2 \end{pmatrix} . \tag{6.1.7}$$

- Case C and Case D:

$$\hat{Y}_\nu M_2^{-1} \hat{Y}_\nu^T = M_{\rm atm}^{-1} \begin{pmatrix} 0 & 0 & 0 \\ 0 & a^2 & a^2 \\ 0 & a^2 & a^2 \end{pmatrix} . \tag{6.1.8}$$

[6] This can be understood by assuming that, if the expression $U^T(\kappa^{(2)} + \tilde{Y}_\nu M_1^{-1} \tilde{Y}_\nu^T)U$ is diagonal, then $U^T(x\kappa^{(2)} + \tilde{x}\tilde{Y}_\nu M_1^{-1} \tilde{Y}_\nu^T)U$ is only diagonal for $x = \tilde{x}$. Since this is not the case here, meaning the two terms scale differently, there is an additional "off-diagonalness".

It is evident that the different order of the heavy neutrino decoupling once again evokes distinct flavour structures. Thus, this demonstrates that the connection between Cases A,B and Cases C,D carries on to lower energy regimes as well. Note that, although the flavour structure of $\kappa^{(2)}$ drives the mixing parameters' running from threshold effects, its contribution comes with a suppression factor. Moreover, bare in mind that we only considered the threshold effects arising in EFT 2, but no further contributions from both the neutrino and charged-lepton sectors. These additional contributions may compete with the threshold effects in some cases, and lead to deviations from the similar features of Cases A,B and Cases C,D.

Going below the lower threshold, $\mu < M_1$, the running effects of the mixing angles become insignificant. This is not the case for the running of the light neutrino masses, which is too complicated to describe analytically in all regimes, and therefore was not discussed above. Nevertheless, there are a few details of the neutrino matrix running that we want to briefly mention: depending on the size of the Y_ν entries, the sign of the flavour-independent contribution to the RGE of m_ν can switch; and the coefficients of the flavour-dependent contributions for the SM and MSSM differ as well, including a sign switch in some of them. As a consequence, a parameter can run in the opposite direction for the framework of the SM with respect to the MSSM. This feature is most apparent for the light neutrino masses, which exhibit strong overall running in opposite directions when comparing the LS in the contexts of the SM and of the MSSM. In order to access all parameters – neutrino masses, mixing angles, and phases – at all scales, we turn to a numerical treatment using the *Mathematica* package `REAP` [331]. Therefore, it is important to mention that the conventions used in `REAP` slightly differ from the ones discussed in sections 3.1 and 3.4. First of all, with the help of Ref. [331], we can relate the two neutrino Yukawa matrices, which leads to $Y_\nu^{\texttt{REAP}} = Y_\nu^\dagger$. This needs to be taken into account when entering explicit LS scenarios into `REAP`. Secondly, note that `REAP` also uses the Particle Data Group (PDG) standard parametrisation, which means that, while the mixing angles are identical to ours, the Majorana phase is given by $-\varphi_2/2 = \sigma$. `REAP` uses $\delta_{\texttt{REAP}} \in [0, 2\pi[$, whereas we use $\delta \in [-\pi, \pi[$. Consequently, it is $\delta = \delta_{\texttt{REAP}} - 2\pi$ for $\delta_{\texttt{REAP}} \in [\pi, 2\pi[$.

There are two conclusions to be emphasised from the discussion above:

- Despite yielding identical neutrino masses and mixing parameters at the GUT scale, for identical input parameters (a, b), Cases A,C and Cases B,D exhibit a fundamentally different running behaviour.

- There is an intrinsic connection between the evolution of Cases A$\leftrightarrow$B (Cases C$\leftrightarrow$D), which is reflected in the parameter b (a) dominating the running as well as $Y_\nu Y_\nu^\dagger$ being mainly diagonal (being driven by the same block matrix). This distinction between Cases A,B versus Cases

C,D properties becomes even more evident when taking a closer look at the energy regime $M_2 > \mu > M_1$.

6.2 SM Results

We investigate the running effects on the neutrino parameters m_2, m_3, θ_{12}, θ_{13}, θ_{23}, δ, and σ numerically by means of `REAP` [331]. Our analysis involves not only the four different Cases A, B, C, and D, but also four settings for the heavy RH neutrino masses: $(M_2,\, M_1) = (10^{12}, 10^{10})$, $(10^{15}, 10^{10})$, $(10^{15}, 10^{12})$, $(10^{14}, 10^{13})$ [in GeV]. Recall that for Cases A and B, it is $M_2 = M_{\rm sol}$ and $M_1 = M_{\rm atm}$, whereas it is $M_2 = M_{\rm atm}$ and $M_1 = M_{\rm sol}$ for Cases C and D. For each case and RH mass setting, we have furthermore performed vacuum stability checks which validated all scenarios under consideration. To determine the optimum set of input parameters, we employ the method of least squares and make use of two distinct χ^2 functions introduced before as estimators. Subsequently, we also utilise these χ^2's as measures to preliminarily assess the goodness-of-fit. A more thorough discussion on the method of least squares as well as all the necessary definitions have been presented in section 4.3. As we fixed two of the four input parameters of the LS, namely $(n,\, \eta)$, depending on the case, we minimise $\chi^2_{(\delta)}$ with respect to the free input parameters $(m_a,\, m_b)$. After scanning over the grid of free input parameters, we obtain the optimum set of $(m_a,\, m_b)$ at the GUT scale, which are presented in Tab. 6.1 together with their corresponding $\chi^2_{(\delta)}$ values (obtained at the EW scale). As explained in section 4.3, one should not compare the absolute values for χ^2_δ and χ^2 when assessing the goodness-of-it.[7] Nonetheless, both estimators should point towards the same input parameters for consistency and indeed they do. Thus, we will only refer to results of the estimator χ^2 in the following discussion. Furthermore, we can use the number of degrees of freedom as an approximate measure for the goodness-of-fit, which means that a good fit yields $\chi^2 \sim \mathcal{O}(1)$.

When comparing the different RH neutrino mass settings for each case, respectively, there are several observations to reflect about:

- The first and foremost observation is that the RH mass setting $(10^{15}, 10^{12})$ makes for the best fit to the global fit values given in Tab. 4.1, for each of the LS cases individually; closely followed by the mass setting $(10^{15}, 10^{10})$. The scenario $(10^{14}, 10^{13})$ is already significantly poorer, and the goodness-of-fit further deteriorates for $(10^{12}, 10^{10})$. This shows that it is beneficial for the running effects to have M_2 closer to the GUT scale. In addition, the mass of M_1 barely – as long as it is still viable for a see-saw scenario – changes the outcome, which is to say that the heavier

[7] It will turn out that, despite using two distinct estimators with different benchmarks for a good fit (see section 4.3), their minimum values are nearly identical. This is due to the comparably large uncertainty on the Dirac phase. So, for the SM, χ^2 and χ^2_δ differ a few percent by at most, see Tabs. 6.1 and 6.2.

	M_{atm} [GeV]	M_{sol} [GeV]	m_a [meV]	m_b [meV]	χ^2	χ^2_δ
Case A	10^{10}	10^{12}	35.670	3.6221	11.78	11.83
	10^{10}	10^{15}	37.968	4.1578	7.168	7.186
	10^{12}	10^{15}	39.505	4.1592	7.140	7.159
	10^{13}	10^{14}	38.011	3.7985	10.70	10.75
Case B	10^{10}	10^{12}	35.636	3.6600	6.419	6.434
	10^{10}	10^{15}	37.958	4.2020	4.405	4.459
	10^{12}	10^{15}	39.498	4.2031	4.386	4.440
	10^{13}	10^{14}	37.978	3.8377	5.856	5.877
Case C	10^{12}	10^{10}	36.950	3.4974	11.76	11.81
	10^{15}	10^{10}	47.215	3.9735	3.246	3.311
	10^{15}	10^{12}	47.226	4.1757	3.236	3.302
	10^{14}	10^{13}	39.029	3.7492	9.888	9.939
Case D	10^{12}	10^{10}	36.915	3.5340	6.404	6.419
	10^{15}	10^{10}	47.188	3.9885	1.498	1.527
	10^{15}	10^{12}	47.198	4.1913	1.494	1.523
	10^{14}	10^{13}	38.994	3.7843	5.215	5.233

Table 6.1: Best-fit values for SM Cases A, B, C, and D, with varying RH neutrino masses. When needed, the values of $\chi^2_{(\delta)}$ with further digits can be found in the corresponding table in Ref. [5].

of the RH neutrinos plays the dominant role regarding the RG running behaviour and the goodness-of-fit. The detailed results for the RH mass setting $(10^{15}, 10^{12})$ will be shown in Figs. 6.1 to 6.4. The results for the remaining three mass settings are displayed in Tabs. 6.4 and 6.5.

- For Case A, the best-fit values for m_b for mass settings $(10^{15}, 10^{12})$ and $(10^{15}, 10^{10})$ – which yield nearly identical χ^2's – are almost the same, while the m_a differ notably. Furthermore, m_b decreases with M_2. The same is true for Case B. For Cases C and D, respectively, it is the best-fit values for m_a that are almost identical for the comparatively good RH mass settings $(10^{15}, 10^{12})$ and $(10^{15}, 10^{10})$, while m_b does vary. Moreover, m_a lowers with M_2. Recalling the qualitative discussion in section 6.1, these observations can most likely be traced back to the deeper connection between Cases A↔B as well Cases C↔D. For A↔B, the parameter $b \propto \sqrt{M_2 m_b}$ dominates the RG effects of the mixing angles, whereas for C↔D the parameter $a \propto \sqrt{M_2 m_a}$ does so. This already hints towards the overall importance of the running of the mixing angles in order to predict feasible neutrino parameters at the EW scale, which we will come back to when investigating the different LS cases. This line of reasoning

Case	$\chi^2_{\text{old}}(\Lambda_{\text{EW}})$	$\chi^2_{\delta\,\text{old}}(\Lambda_{\text{EW}})$	$\chi^2(\Lambda_{\text{EW}})$	$\chi^2_{\delta}(\Lambda_{\text{EW}})$
A	50.3072	50.318	7.14042	7.15869
B	50.3012	50.3739	4.38607	4.44012
C	179.711	179.824	3.23646	3.30174
D	172.773	172.781	1.49388	1.52265

Table 6.2: χ^2 values for the four cases, where the subscript "old" denotes the input parameters used in Ref. [310], namely $m_a = 41.5156$ meV and $m_b = 4.19375$ meV. In order to compare these to the results from our analysis, we also include their χ^2 values in the two right-handed columns of this table. Please bare in mind that the latter are based on varying input parameters $m_{a,b}$, which are specified in Tab. 6.1.

also explains the first observation, namely that the mass of the heavier RH neutrino impacts the goodness-of-fit predominantly.

- Cases A and B yield a nearly identical input parameter m_a for each RH neutrino mass setting individually, which hints towards yet another correlation between Cases A and B. The same holds true for Cases C and D with a slightly larger deviation in m_a in comparison to Cases A↔B. For the input parameter m_b, there does not seem to be a correlation between the different LS cases. While the discussion above did feature equivalent RG behaviour of two LS cases, respectively, this observation shows a correlation with respect to the absolute value of m_a. The reason behind this connection, however, proves more elusive, because m_a is related to the lighter RH neutrino scale for Cases A,B but to the heavier scale for Cases C,D. Nevertheless, we will return to addressing this feature towards the end of this section.

To emphasise the importance of performing global fits to the experimental data at the EW scale for each LS case separately, we compare the χ^2 values of the modified benchmark scenarios from Ref. [310] with the best-fit scenarios obtained from our analysis. As already mentioned at the beginning of chapter 6, the input values (m_a, m_b) in Ref. [310] are taken from a tree-level best fit and adjusted by an overall factor of 1.25, which was obtained from Case A and aims at including the significant running of the neutrino masses.[8] In contrast, our analysis scans over the model input parameters in order to determine the optimum set of high-energy input values from a global fit of the low-energy parameters. The χ^2 values for the input parameters used in Ref. [310] are listed in Tab. 6.2. Comparing these to the χ^2 values presented in Tab. 6.1,

[8] Please note that the overall factor of 1.25 is applied to Y_ν, which translates to a factor of 1.25^2 on the input parameters $m_{a,b}$. Furthermore, there is a typo in Ref. [310] when quoting the parameter m_a. The tree-level values used are, in fac,t $m_a = 26.57$ meV and $m_b = 2.684$ meV.

Neutrino Parameter	best-fit-value
θ_{12}	33.58°
θ_{13}	8.46°
θ_{23}	41.61°
m_2	8.66 meV
m_3	50.24 meV
δ	-99°

Table 6.3: Mixing angles, Dirac phase, and neutrino masses in the LS as extracted from Tab. 4.1.

there are two striking characteristics. First of all, the overall values for the goodness-of-fit improve drastically, moving the χ^2 values from "in tension with experimental data" to "predict experimental data nicely". Secondly, the χ^2_{old} values listed in Tab. 6.2 suggest that Case A is the one most compatible with experimental data, followed closely by Case B and, after a significant gap, by Cases D and C. It turns out that quite the opposite is true when implementing global fits for each case individually, resulting in the following order: Case D yields best fit, followed by Case C, Case B, and Case A. Both these features can be traced back to Ref. [310] superficially modifying the input parameters to fit Case A. As we have already seen in the discussion above, Cases A and B are connected intrinsically, while displaying detached behaviour from the equally connected Cases C and D, which does not only concern the running effects but also the absolute value of a suitable input parameter m_a. Consequently, the input parameters from Ref. [310] work significantly better for Cases A and B but are, nevertheless, not even close to the best-fit choices due to the simplistic way of selecting them.

We choose the RH neutrino mass setting $(10^{15}, 10^{12})$ to further investigate the different LS cases. We are interested in understanding the features that decide how well compatible with experimental data a certain case is and how this relates to the RG effects. From Tab. 6.1, we learn that Case D is the most compatible with experimental data. Moreover, Case D does not only more or less reproduce the neutrino parameters at the EW scale but it does so impressively – leading to $\chi^2 = 1.49$. The next best scenario is Case C with a still impressive $\chi^2 = 3.24$, followed closely by Case B with $\chi^2 = 4.39$ and, with some deterioration, Case A with $\chi^2 = 7.14$. In order to understand the underlying characteristics that make Case D most suitable and Case A least, we start by investigating the behaviour of the neutrino parameters. From the tables displayed in the upper left corner of Figs. 6.1 to 6.4, respectively, there are several observations to consider:

	Λ_{GUT}	M_{sol}	M_{atm}	Λ_{EW}
θ_{13}(deg)	9.02263	8.90546	8.42392	8.42372
θ_{12}(deg)	34.2361	33.9648	34.0685	34.0683
θ_{23}(deg)	46.1399	45.2711	44.7222	44.7215
m_2(meV)	13.2556	12.4937	11.8151	8.63167
m_3(meV)	74.3711	69.3002	68.7768	50.2462
δ_{CP}(deg)	−85.3086	−89.73	−92.1065	−92.1067
σ_{CP}(deg)	−145.074	−145.752	−144.249	−144.249

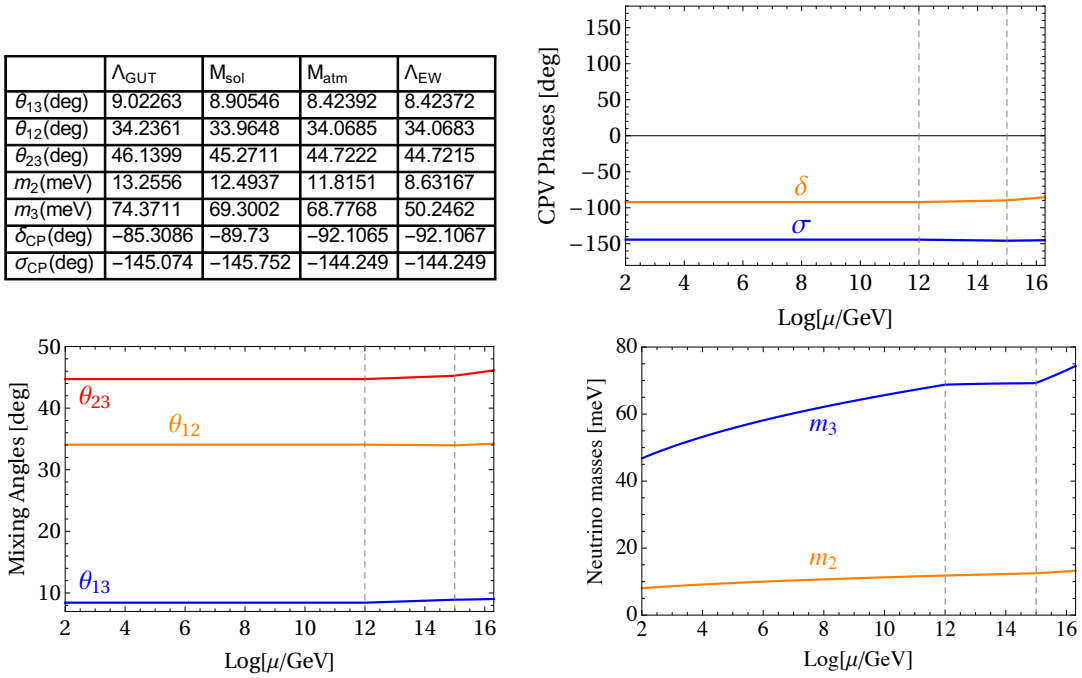

Figure 6.1: Case A – SM with $M_{\rm atm} = 10^{12}$ GeV and $M_{\rm sol} = 10^{15}$ GeV.

	Λ_{GUT}	M_{sol}	M_{atm}	Λ_{EW}
θ_{13}(deg)	9.11673	8.99248	8.50595	8.50593
θ_{12}(deg)	34.214	33.9416	34.0475	34.0472
θ_{23}(deg)	43.7587	43.4787	44.0007	44.0001
m_2(meV)	13.3793	12.6031	11.9202	8.70744
m_3(meV)	74.4495	69.3218	68.7791	50.2421
δ_{CP}(deg)	−95.0473	−89.5046	−87.1443	−87.1442
σ_{CP}(deg)	−34.6563	−35.1008	−36.5847	−36.5848

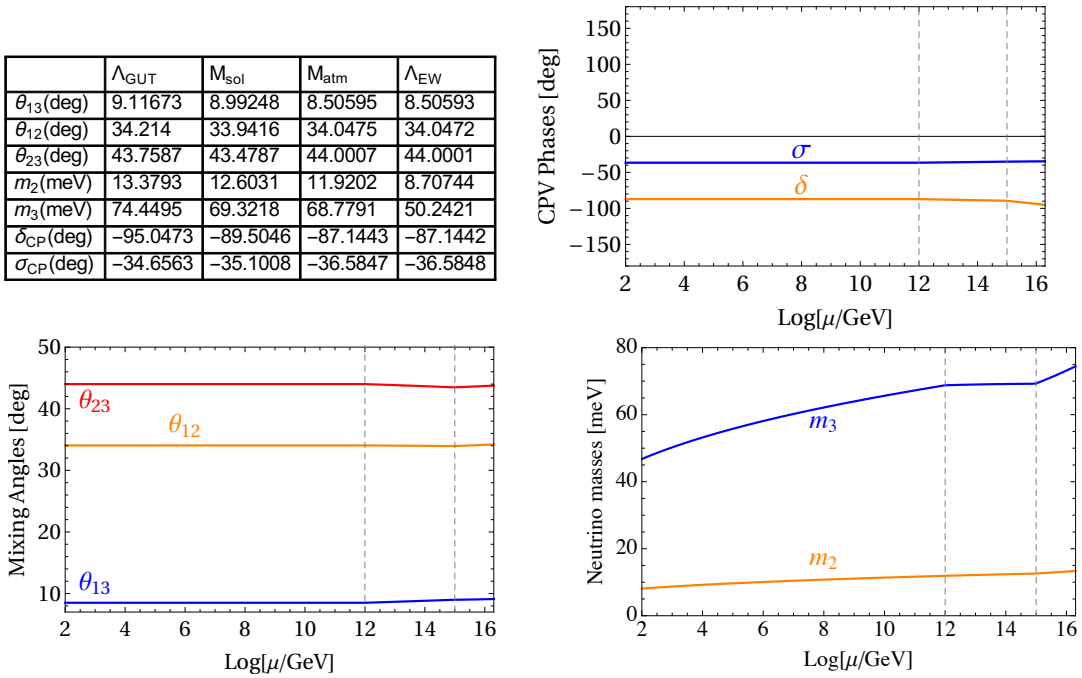

Figure 6.2: Case B – SM with $M_{\rm atm} = 10^{12}$ GeV and $M_{\rm sol} = 10^{15}$ GeV.

	Λ_{GUT}	M_{atm}	M_{sol}	Λ_{EW}
θ_{13}(deg)	7.59277	7.77844	8.44382	8.44364
θ_{12}(deg)	34.5412	34.5044	34.3653	34.3651
θ_{23}(deg)	44.8323	42.839	43.3682	43.3674
m_2(meV)	13.4894	12.1601	12.0902	8.70107
m_3(meV)	87.7143	75.4873	69.8207	50.249
δ_{CP}(deg)	−90.8415	−88.7048	−85.969	−85.969
σ_{CP}(deg)	−140.949	−142.673	−144.724	−144.724

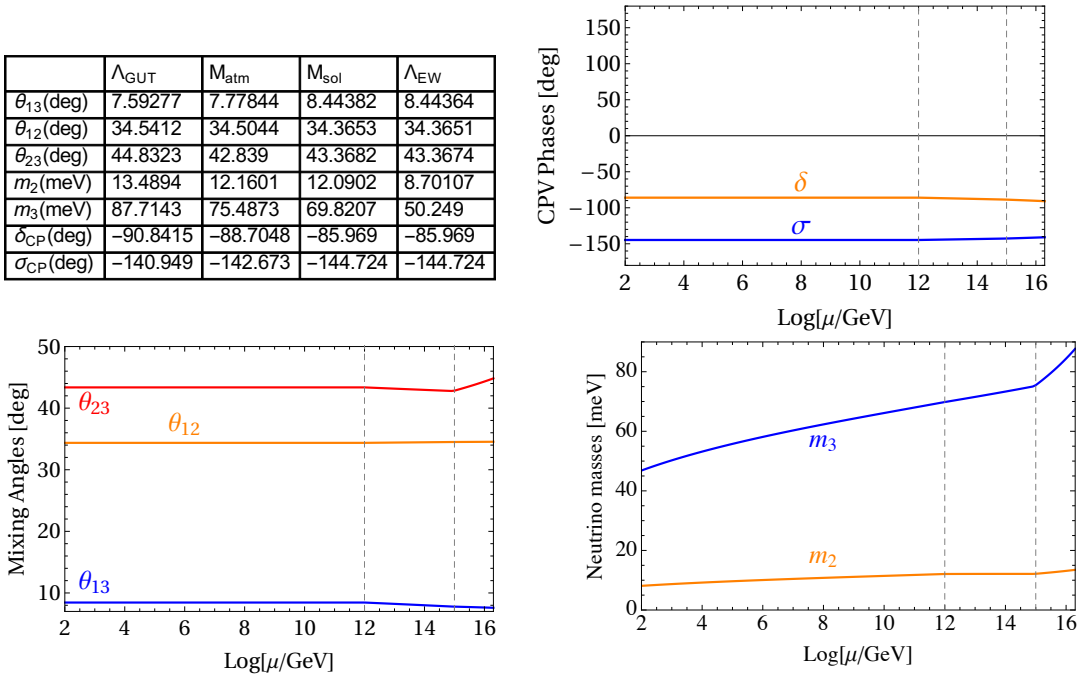

Figure 6.3: Case C – SM with $M_{\rm atm} = 10^{15}$ GeV and $M_{\rm sol} = 10^{12}$ GeV.

	Λ_{GUT}	M_{atm}	M_{sol}	Λ_{EW}
θ_{13}(deg)	7.62574	7.81215	8.47979	8.4798
θ_{12}(deg)	34.5348	34.4977	34.3575	34.3572
θ_{23}(deg)	45.1425	42.9816	42.3751	42.3744
m_2(meV)	13.537	12.2035	12.1317	8.73113
m_3(meV)	87.6802	75.4657	69.8112	50.2431
δ_{CP}(deg)	−89.2885	−88.0086	−90.3508	−90.3507
σ_{CP}(deg)	−38.9558	−40.649	−38.9917	−38.9917

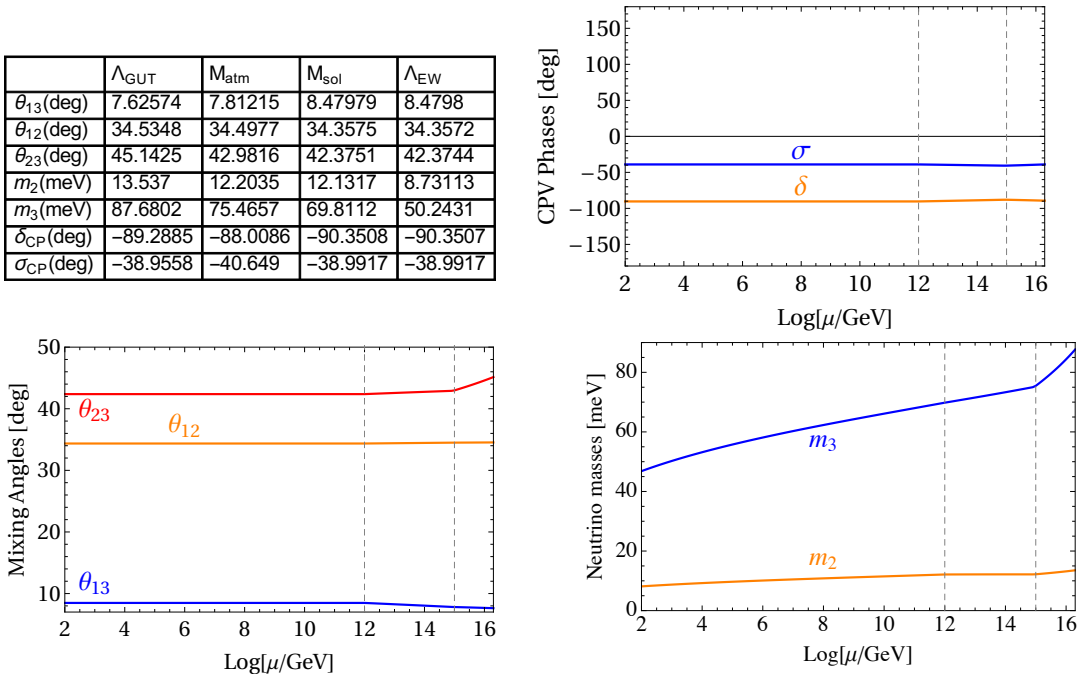

Figure 6.4: Case D – SM with $M_{\rm atm} = 10^{15}$ GeV and $M_{\rm sol} = 10^{12}$ GeV.

- Starting with the mixing angle $\boldsymbol{\theta_{12}}$, we compare its experimental value to the predictions of the four different LS cases at the EW scale. Case A's best-fit scenario predicts $\theta_{12}^{\mathrm{A}} = 34.07^\circ$, Case B's $\theta_{12}^{\mathrm{B}} = 34.05^\circ$, Case C's $\theta_{12}^{\mathrm{C}} = 34.37^\circ$, and Case D predicts $\theta_{12}^{\mathrm{D}} = 34.36^\circ$. First of all, we once again observe the nearly identical predictions for Cases A,B and Cases C,D. Secondly, the measured solar angle of $\theta_{12}^{\mathrm{exp}} = 33.58^\circ$ – see Tab. 6.3 – lies below the range of predicted values, with Cases A and B getting closest. However, the variation among the predicted values is small. That is to say, that the 1σ deviation from the measured value gives a range of $[32.83^\circ, 34.33^\circ]$, which encompassed Cases A and B, and it is fairly close to the values predicted for Cases C and D. Taking a closer look at the influence of the RG running effects, on display in the lower left panels of Figs. 6.1 to 6.4, it turns out that the overall alteration of θ_{12} due to the running in between the GUT and the EW scale is almost identical four all four cases. Following a decline by roughly 0.27 meV with the energy scale from GUT to EW scale, the observed connection between Cases A,B as well as Cases C,D already occurs at the GUT scale and translates to the EW scale.

- Next, we analyse the mixing angle $\boldsymbol{\theta_{13}}$. From Case A, we obtain $\theta_{13}^{\mathrm{A}} = 8.42^\circ$. For Case B, the reactor angle is predicted to be $\theta_{13}^{\mathrm{B}} = 8.51^\circ$, while we obtain $\theta_{13}^{\mathrm{C}} = 8.44^\circ$ for Case C and $\theta_{13}^{\mathrm{D}} = 8.48^\circ$ for Case D. The first and somewhat unexpected observation is that, for θ_{13}, there seems to be no clear correlation between the cases from the predicted angle at the EW scale. Second of all, the measured value $\theta_{13}^{\mathrm{exp}} = 8.46^\circ$, see Tab. 6.3, is right in the middle of the range of predicted angles. Including the 1σ deviations from the measured best-fit angle, one obtains a region of $[8.31^\circ, 8.61^\circ]$, which covers the predicted angles for all four LS cases. The running effects for θ_{13} are highly case-dependent, see the lower left panels of Figs. 6.1 to 6.4, respectively. While the reactor angle decreases with the energy scale by roughly 0.6° from the GUT to the EW scale for Cases A and B, it increases by about 0.85° over the same area for Cases C and D. This obscures the fact that Cases A and B are indeed generating quite similar θ_{13} values at the GUT scale, as do Cases C and D. At the EW scale, all four scenarios have converged, and the predicted angles do not reveal the original connection anymore.

- For the atmospheric mixing angle $\boldsymbol{\theta_{23}}$, we obtain $\theta_{23}^{\mathrm{A}} = 44.72^\circ$ for Case A, $\theta_{23}^{\mathrm{B}} = 44.00^\circ$ for Case B, $\theta_{23}^{\mathrm{C}} = 43.37^\circ$ for Case C, and $\theta_{23}^{\mathrm{D}} = 42.37^\circ$ for Case D. Firstly, as with the reactor angle, there is no apparent correlation among the four LS cases with respect to the atmospheric angle at the EW scale. Secondly, the measured value of $\theta_{23}^{\mathrm{exp}} = 41.61^\circ$ is below the range of predicted values. Here, however, it is Case D that is closest to the experimental best-fit value. Considering the 1σ uncertainties of the measurement, the atmospheric angle lies within $[40.40^\circ, 43.17^\circ]$, which

only covers the prediction of Case D. Note that, in contrast to the other two mixing angles, where either all cases were within the 1σ region or at least at close proximity, only Case C is somewhat close to the 1σ region for the atmospheric angle, whereas Cases A and B are well beyond the upper margin. Furthermore, θ_{23} also differs from the other mixing angles in terms of its connections between the LS cases. Not only do the best-fit scenarios for the different LS cases predict rather distinct values at the EW scale, but they also exhibit no connection with respect to the values at the GUT scale and RG running behaviour. The latter manifests in Case A displaying a decrease by 0.33° in between the GUT and the EW scales, whereas Case B has an increase by 0.24°. It is striking that Case A does not only differ from Case B in running strength but in direction. Case C, moreover, displays a decrease by 1.46°, while Case D shows an even stronger decrease of 2.77°. In combination with the already dissimilar GUT scale values, we obtain a strong preference towards Case D based on its predicted θ_{23}. Thus, the atmospheric angle plays the decisive role with regard to the compatibility of the LS cases with experimental data.

- When including the CP violating Dirac phase $\boldsymbol{\delta}$ in the estimator and thereby in the goodness-of-fit analysis, we also need to discuss its predicted values with respect to the measured value and the 1σ region. Since the 1σ region encompasses values within $[-158^\circ, -48^\circ]$ around a best-fit experimental value of $\delta = -99^\circ$, all Dirac phases derived from the LS cases lie within this range. Moreover, they are also within a – relative to the 1σ region – narrow band above the best-fit value, namely $\delta^{\mathrm{A}} = -92.11^\circ$, $\delta^{\mathrm{B}} = -87.14^\circ$, $\delta^{\mathrm{C}} = -85.97^\circ$, and $\delta^{\mathrm{D}} = -90.35^\circ$. The running behaviour with respect to δ differs among the four LS cases. While Cases B and C have δ increasing with decreasing energy scale, Cases A and D display a decreasing δ. Nonetheless, the strength of the running differs with running effects in between 1° and 7°. So, overall, there is no hint towards a relation between any of the four LS cases in δ – neither in the starting values at the GUT scale or the values obtained at the EW scale, nor in the total running behaviour. Since involving the Dirac phase in the global fit does not alter the results, we will focus on the other five neutrino parameters in the discussion that is to follow.

- Turning to the neutrino masses, we start by comparing the measured value of $\boldsymbol{m_2}$ to the LS predictions. Case A predicts a lighter neutrino mass of $m_2^{\mathrm{A}} = 8.63$ meV. For Case B, we obtain $m_2^{\mathrm{B}} = 8.71$ meV, for Case C $m_2^{\mathrm{C}} = 8.70$ meV, and $m_2^{\mathrm{D}} = 8.73$ meV for Case D. The experimental best-fit value is given by $m_2^{\mathrm{exp}} = 8.66$ meV with a 1σ region of $[8.56\ \mathrm{meV}, 8.77\ \mathrm{meV}]$. Consequently, all four LS cases predict similarly good values well within the 1σ region. Taking a closer look at the RG running behaviour of m_2, see the lower right panel in Figs. 6.1 to 6.4, we

note that the running effects are similarly strong for all four cases. In addition, all four cases display a decrease of roughly 4.7 meV for m_2 in between the GUT and the EW scale. At the GUT scale, the m_2 values show no clear relation between different cases and all lie in close range to each other, which leads to the four predicted EW scale masses being equally good.

- For the heavier of the light neutrino masses, $\boldsymbol{m_3}$, we obtain the following predictions from the four LS cases: $m_3^{\mathrm{A}} = 50.25$ meV, $m_3^{\mathrm{B}} = 50.24$ meV, $m_3^{\mathrm{C}} = 50.25$ meV, and $m_3^{\mathrm{D}} = 50.24$ meV. These nearly identical predictions are consistent with the experimentally measured value of $m_3^{\mathrm{exp}} = 50.24$ meV that lies within the 1σ region given by $[49.84\,\mathrm{meV}, 50.63\mathrm{meV}]$. The running of m_3 between the GUT and the EW scales is extreme for all four LS cases, see the lower right plot in Figs. 6.1 to 6.4, respectively. There are, furthermore, interesting features that we want to briefly address. First of all, the m_3 values for Cases A and B at the GUT scale are nearly identical, which is also true for Cases C and D. Thus, once again revealing a deeper connection among the cases that gets diluted by the running. Second of all, the GUT scale values of Cases C,D are significantly higher than those of Cases A,B. Consequently, as the RG effects decrease the value of m_3 with the energy scale, the RG running in Cases C and D is notably stronger.

From the discussion of the neutrino parameters, we can summarise the following. First of all, the absolute values predicted for the parameters θ_{12}, θ_{13}, and m_3 at the GUT scale are nearly identical for Cases A,B as well as for Cases C,D. As opposed to this, the predictions for θ_{23} and m_2 at the GUT scale are without case-induced pattern. Second of all, the RG running of m_3 and θ_{13} are similar for Cases A,B and Cases C,D, respectively. On top of that, m_2 and θ_{12} exhibit the same RG running behaviour for all four LS cases. The only parameter not showing any case-dependent pattern is θ_{23}.
What can we learn from these observations and where do they come from? As we have already realised when investigating the different RH neutrino mass settings above, there are two additional connections between Cases A and B as well as Cases C and D, namely the absolute value of the input parameter m_a for the best-fit scenario and the predominant dependence on either m_b or m_a of the RG running of the mixing angles. In order to understand the reasoning behind the above observations, we need to briefly recapitulate some basic features of the LS and its RG running:

- From Ref. [310], we can extract the following estimates for the neutrino parameters at the GUT scale derived for Case A:

$$m_2 \approx 3m_b\,, \qquad m_3 \approx 2m_a \tag{6.2.1}$$

$$\sin\theta_{13} \approx \frac{\tan(2\theta)}{2\sqrt{3}}\,, \quad \tan\theta_{12} \approx \frac{1}{\sqrt{2}}\Big[1 - \frac{1}{4}\tan^2(2\theta)\Big]^{1/2}\,, \\ \text{and} \quad \tan\theta_{23} \approx 1 + \frac{2\tan(2\theta)}{\sqrt{6}}\cos\omega\,, \tag{6.2.2}$$

with $\tan(2\theta) \approx \sqrt{6}m_b(n-1)/|m_a + m_b e^{i\eta}(n-1)^2|$ and $\omega = \arg[m_a + m_b e^{i\eta}(n-1)^2] - \eta$. Without running effects, these estimations also hold true for Case C. The mixing parameters for Case B, and since we do not need to consider running effects at the GUT scale also for Case D, are $m^{\rm B}_{2,3} = m^{\rm A}_{2,3}$, $\theta^{\rm B}_{12} = \theta^{\rm A}_{12}$, $\theta^{\rm B}_{13} = \theta^{\rm A}_{13}$, and $\theta^{\rm B}_{23} = \pi/2 - \theta^{A}_{23}$, see section 3.4.
Although we have only drawn connections between Cases A,B and Cases C,D with respect to the input parameter m_a, one has to bare in mind that the input values m_b are all within a close range, namely within [4.16 meV, 4.20 meV]. A variation of only 0.04 meV does not alter $\tan(2\theta)$ or ω significantly. Consequently, Cases A and B yield similar $\tan(2\theta)$ or ω, as do Cases C and D.
These estimates already answer why for similar m_a, as given for Cases A,B and Cases C,D, the neutrino parameters m_3, θ_{12}, and θ_{13} are almost identical at the GUT scale. It also explains why the GUT scale values for parameter m_2 – predominantly depending on input parameter m_b – are within a close range without exhibiting a clear case-dependent structure. And at last, it unveils why the θ_{23} values at the GUT scale do not show any indication of the connection between the different cases. The connection between the cases appears in the choice of m_a, and it would suggest similar atmospheric angles for Cases A and B (or analogously for Cases C and D). However, due to the relation between the atmospheric angle for A and B, as given above, there is an offset of a few degrees. The same is true for Cases C and D.

- Furthermore, from the derivation of the mixing angles' RGE running for Cases A and B in Ref. [310], we know that for $\mu > M_2$ *only the running of* θ_{23} differs for Cases A and B. The latter is significant, as for the atmospheric angle most of the running occurs within that region. Moreover, the corrections to the GUT scale value of θ_{23} come with opposite signs for Case A and B, which explains why one decreases and the other increases its atmospheric angle. The running behaviour of the mixing angles in EFT 2 differs for Cases A and B, but is still quite similar since only the coefficients in front of a few terms are different. As the same structure is responsible for the running above M_2 for Cases C and D, there is no sign change, which agrees with our numerical observations. On the other hand, our numerical results indicate that, for the regime $M_2 > \mu > M_1$, θ_{23} increases for Case C but further decreases for Case D, which gives an edge to Case D regarding the global fit to the data. A more in-depth investigation of this feature, however, is beyond the scope of this work.

Case A	$\Lambda_{\rm GUT}$	$M_{\rm sol}$	$M_{\rm atm}$	$\Lambda_{\rm EW}$
θ_{13}(deg)	9.37234	9.23195	8.4238	8.42366
θ_{12}(deg)	34.1528	33.8874	34.0685	34.0683
θ_{23}(deg)	46.5262	45.6647	44.7283	44.7277
m_2(meV)	13.188	12.4328	11.2768	8.63111
m_3(meV)	71.8213	66.9262	65.6484	50.2468
$\delta_{\rm CP}$(deg)	−83.9919	−88.2031	−92.1116	−92.1117
$\sigma_{\rm CP}$(deg)	−146.076	−146.776	−144.245	−144.245

Case B	$\Lambda_{\rm GUT}$	$M_{\rm sol}$	$M_{\rm atm}$	$\Lambda_{\rm EW}$
θ_{13}(deg)	9.47026	9.32237	8.50624	8.50625
θ_{12}(deg)	34.1288	33.8625	34.0475	34.0472
θ_{23}(deg)	43.361	43.0872	44.006	44.0055
m_2(meV)	13.3088	12.5396	11.3769	8.70725
m_3(meV)	71.9068	66.9555	65.6468	50.2428
$\delta_{\rm CP}$(deg)	−96.3739	−91.0063	−87.1518	−87.1518
$\sigma_{\rm CP}$(deg)	−33.6431	−34.1026	−36.5768	−36.5768

Case A	$\Lambda_{\rm GUT}$	$M_{\rm sol}$	$M_{\rm atm}$	$\Lambda_{\rm EW}$
θ_{13}(deg)	8.71028	8.70979	8.41446	8.41431
θ_{12}(deg)	34.3076	34.3066	34.3717	34.3715
θ_{23}(deg)	45.8168	45.8138	45.5273	45.5268
m_2(meV)	11.5878	11.5589	11.0847	8.45521
m_3(meV)	66.8983	66.7295	65.8627	50.2394
$\delta_{\rm CP}$(deg)	−86.4977	−86.5119	−87.6476	−87.6477
$\sigma_{\rm CP}$(deg)	−144.176	−144.178	−143.327	−143.327

Case B	$\Lambda_{\rm GUT}$	$M_{\rm sol}$	$M_{\rm atm}$	$\Lambda_{\rm EW}$
θ_{13}(deg)	8.80762	8.8072	8.50932	8.50932
θ_{12}(deg)	34.2856	34.2846	34.351	34.3508
θ_{23}(deg)	44.0847	44.0834	44.3782	44.3777
m_2(meV)	11.6958	11.6667	11.1898	8.53546
m_3(meV)	66.9099	66.7408	65.8631	50.2397
$\delta_{\rm CP}$(deg)	−93.8742	−93.8565	−92.7142	−92.7142
$\sigma_{\rm CP}$(deg)	−35.5442	−35.5456	−36.4031	−36.4031

Case A	$\Lambda_{\rm GUT}$	$M_{\rm sol}$	$M_{\rm atm}$	$\Lambda_{\rm EW}$
θ_{13}(deg)	8.57452	8.55772	8.41639	8.41604
θ_{12}(deg)	34.3378	34.2893	34.3201	34.3199
θ_{23}(deg)	45.6829	45.5049	45.3528	45.3519
m_2(meV)	12.1703	12.0439	11.8348	8.49291
m_3(meV)	71.1824	70.2577	70.0093	50.2414
$\delta_{\rm CP}$(deg)	−87.0182	−87.7866	−88.344	−88.3446
$\sigma_{\rm CP}$(deg)	−143.785	−143.924	−143.52	−143.52

Case B	$\Lambda_{\rm GUT}$	$M_{\rm sol}$	$M_{\rm atm}$	$\Lambda_{\rm EW}$
θ_{13}(deg)	8.66875	8.6508	8.50827	8.50813
θ_{12}(deg)	34.3169	34.2682	34.2996	34.2993
θ_{23}(deg)	44.2245	44.1398	44.2663	44.2656
m_2(meV)	12.2832	12.1545	11.9444	8.5718
m_3(meV)	71.1937	70.2601	70.0065	50.2408
$\delta_{\rm CP}$(deg)	−93.3433	−92.3337	−91.751	−91.7503
$\sigma_{\rm CP}$(deg)	−35.9437	−36.0461	−36.4756	−36.476

Table 6.4: SM Cases (*left*) A and (*right*) B with (*top*) $M_{\rm atm} = 10^{10}$ GeV and $M_{\rm sol} = 10^{15}$ GeV, (*middle*) $M_{\rm atm} = 10^{10}$ GeV and $M_{\rm sol} = 10^{12}$ GeV, (*bottom*) $M_{\rm atm} = 10^{13}$ GeV and $M_{\rm sol} = 10^{14}$ GeV.

In summary, the connection between Cases A, B and C, D stems from a combination of two features. Due to the similar running in *most* of the five neutrino parameters, the parameters at the GUT scale have to be similar. On top of that, we know from the estimates in Eqs. (6.2.1) and (6.2.2) that similar GUT scale neutrino parameters enforce similar input parameters. Take for example the neutrino masses: from our numerical analysis, we learn that m_2 and m_3 exhibit nearly identical running for Cases A and B. Since each of the neutrino masses is directly linked to an input parameter, this already sets a suitable range of the said input parameters, which is refined by including the mixing angles to the fit. The same can be done for Cases C and D. As the running of m_3 is stronger in comparison to the one in Cases A,B, the input parameter m_a has to be larger for Cases C, D which can be observed in our results.
Due to the intrinsic features of the LS cases and their connections among each other, it is possible to obtain comparatively good values for m_2, m_3, θ_{12}, and θ_{13} at the EW scale. For θ_{23}, however, both the running behaviour and the relation between GUT scale value and input parameters does not follow the other neutrino parameters' connection between cases. As a consequence, the atmospheric angles at the EW scale show the widest spread depending on the case, and thus are most important with respect to the compatibility with ex-

Case C	$\Lambda_{\rm GUT}$	$M_{\rm atm}$	$M_{\rm sol}$	$\Lambda_{\rm EW}$
θ_{13}(deg)	7.22473	7.40132	8.44361	8.44345
θ_{12}(deg)	34.6106	34.5777	34.3663	34.3661
θ_{23}(deg)	44.5671	42.544	43.3705	43.3699
m_2(meV)	12.8612	11.5978	11.4511	8.70016
m_3(meV)	87.5232	75.31	66.1357	50.2482
$\delta_{\rm CP}$(deg)	−92.2976	−90.2501	−85.9572	−85.9573
$\sigma_{\rm CP}$(deg)	−139.882	−141.528	−144.721	−144.721

Case D	$\Lambda_{\rm GUT}$	$M_{\rm atm}$	$M_{\rm sol}$	$\Lambda_{\rm EW}$
θ_{13}(deg)	7.25642	7.43372	8.47969	8.47969
θ_{12}(deg)	34.6048	34.5716	34.3584	34.3582
θ_{23}(deg)	45.4112	43.2493	42.3764	42.3759
m_2(meV)	12.9079	11.6403	11.4908	8.73044
m_3(meV)	87.4857	75.2851	66.1285	50.2432
$\delta_{\rm CP}$(deg)	−87.8282	−86.6234	−90.3667	−90.3666
$\sigma_{\rm CP}$(deg)	−40.0263	−41.6336	−38.9915	−38.9915

Case C	$\Lambda_{\rm GUT}$	$M_{\rm atm}$	$M_{\rm sol}$	$\Lambda_{\rm EW}$
θ_{13}(deg)	8.12687	8.12736	8.41453	8.41438
θ_{12}(deg)	34.4339	34.4336	34.3726	34.3724
θ_{23}(deg)	45.2693	45.2632	45.5235	45.5229
m_2(meV)	11.2539	11.2246	11.0842	8.45521
m_3(meV)	68.8981	68.7092	65.8593	50.2388
$\delta_{\rm CP}$(deg)	−88.7493	−88.7429	−87.6296	−87.6297
$\sigma_{\rm CP}$(deg)	−142.494	−142.499	−143.328	−143.328

Case D	$\Lambda_{\rm GUT}$	$M_{\rm atm}$	$M_{\rm sol}$	$\Lambda_{\rm EW}$
θ_{13}(deg)	8.21894	8.21952	8.50936	8.50937
θ_{12}(deg)	34.4146	34.4143	34.3519	34.3517
θ_{23}(deg)	44.6491	44.6424	44.3737	44.3731
m_2(meV)	11.3625	11.3329	11.1894	8.53548
m_3(meV)	68.8885	68.6998	65.8602	50.2395
$\delta_{\rm CP}$(deg)	−91.6086	−91.6044	−92.7245	−92.7244
$\sigma_{\rm CP}$(deg)	−37.2403	−37.2456	−36.4099	−36.4099

Case C	$\Lambda_{\rm GUT}$	$M_{\rm atm}$	$M_{\rm sol}$	$\Lambda_{\rm EW}$
θ_{13}(deg)	8.24687	8.27765	8.41906	8.41893
θ_{12}(deg)	34.4087	34.3969	34.3643	34.364
θ_{23}(deg)	45.376	45.0433	45.1684	45.1677
m_2(meV)	12.0514	11.8534	11.8214	8.4979
m_3(meV)	72.852	71.1124	69.8924	50.2424
$\delta_{\rm CP}$(deg)	−88.2831	−87.9969	−87.4735	−87.4733
$\sigma_{\rm CP}$(deg)	−142.84	−143.148	−143.567	−143.567

Case D	$\Lambda_{\rm GUT}$	$M_{\rm atm}$	$M_{\rm sol}$	$\Lambda_{\rm EW}$
θ_{13}(deg)	8.33064	8.36166	8.50421	8.5043
θ_{12}(deg)	34.3908	34.3789	34.3457	34.3453
θ_{23}(deg)	44.5477	44.1896	44.0525	44.0516
m_2(meV)	12.1547	11.955	11.9219	8.57009
m_3(meV)	72.8436	71.1056	69.8902	50.2409
$\delta_{\rm CP}$(deg)	−92.0414	−91.7175	−92.2248	−92.225
$\sigma_{\rm CP}$(deg)	−36.918	−37.221	−36.818	−36.8178

Table 6.5: SM Cases (*left*) C and (*right*) D with (*top*) $M_{\rm atm} = 10^{15}$ GeV and $M_{\rm sol} = 10^{10}$ GeV, (*middle*) $M_{\rm atm} = 10^{12}$ GeV and $M_{\rm sol} = 10^{10}$ GeV, (*bottom*) $M_{\rm atm} = 10^{14}$ GeV and $M_{\rm sol} = 10^{13}$ GeV.

perimental data. It is therefore not surprising that the hierarchy with respect to how well a scenario predicts θ_{23} is reflected in the goodness-of-fit values χ^2, thereby favouring Case D with a remarkable $\chi^2 = 1.49$ over also excellent goodness-of-fit results between 3.24 and 7.14 for Cases A, B, and C.

6.3 MSSM Results

In this section we examine the LS within the framework of the MSSM. We vary the supersymmetric (SUSY) breaking scale, considering $M_{\rm SUSY} = 1$, 3, 10 TeV. For each MSSM setting with fixed $M_{\rm SUSY}$, we furthermore investigate how $\tan\beta$ as well as the threshold effects, comprised in the parameter $\overline{\eta}_b$ and explained in Appendix E, affect the goodness-of-fit. To this end, we consider $\tan\beta = 5$, 30, 50 and $\overline{\eta}_b = -0.6$, 0, 0.6. The results are collected in Tabs. 6.6 and 6.7 with the corresponding predictions for neutrino masses and PMNS parameters in Figs. 6.5 to 6.8 and in Appendix F, Tabs. F.1 to F.4. Note that we display detailed results for the setting with $M_{\rm SUSY} = 1$ TeV, $\tan\beta = 5$, and $\overline{\eta}_b = 0.6$ in Figs. 6.5 to 6.8. We choose this MSSM setting for a more detailed representation of the parameters' running behaviour, because it yields the most compatible results with experimental data for Cases B, C, and D.

The MSSM results indicate the following:

- Independently of the SUSY breaking scale and/or $\tan\beta$, Case B yields the best fit to experimental data. The next best scenario with respect to the goodness-of-fit is Case D which, depending on the specific setting, can follow Case B closely. The compatibility with experimental data deteriorates for Case A and further for Case C. How strongly the four cases vary in terms of $\chi^2_{(\delta)}$ depends on the choice of M_{SUSY} and $\tan\beta$.

- Looking at the influence of M_{SUSY} on the overall performance of a scenario, we keep $\tan\beta$ fixed and compare the approximate goodness-of-fit measure $\chi^2_{(\delta)}$ for the three SUSY breaking scales. Performing this task for each LS case individually, we find that changing M_{SUSY} barely affects the compatibility with data. There are only slight changes in $\chi^2_{(\delta)}$. We observe an increase in the absolute value of $\chi^2_{(\delta)}$ with higher M_{SUSY} for $\tan\beta = 5$. For $\tan\beta = 30$, Case A prefers higher M_{SUSY} while Cases B, C, and D prefer lower values. And for $\tan\beta = 50$, the goodness-of-fit increases with the SUSY breaking scale – meaning $\chi^2_{(\delta)}$ declines.

- Moreover, we find that – for each M_{SUSY} and LS case – the higher $\tan\beta$ the higher $\chi^2_{(\delta)}$, which means the poorer the overall agreement with experimental data.

- Just as we have ascertained for the SM, both estimators employed yield the same set of input parameters for each MSSM setting in question. We observe again that the variation between the estimator's minima is tiny (below 1 %), which is the result of the comparably large uncertainty on the Dirac phase. On these grounds, we will refer to the χ^2 values when further discussing the fundamental behaviour with respect to the different MSSM settings.

- By including observations from Tabs. 6.6 and 6.7, we learn that for each LS case and setting, i.e. fixed SUSY breaking scale and $\tan\beta$, it is always the highest value of $\overline{\eta}_b$ under consideration that yields the best fit. How strongly the goodness-of-fit, and thereby its measure χ^2, vary with $\overline{\eta}_b$ depends predominantly on $\tan\beta$. The higher $\tan\beta$, the more variation with $\overline{\eta}_b$ one observes in χ^2.

- When taking a closer look at the varying threshold effects for $\tan\beta = 30$ in Tabs. 6.6 and 6.7, we observe unusually large values for χ^2 for the threshold effects $\overline{\eta}_b = -0.6$. The latter can be explained by considering that this setting is at the border to the region where we run into trouble regarding non-perturbativity, which means that at least one of the Yukawa couplings becomes non-perturbative.

As discussed later in section 6.4, we know that *most* neutrino parameters do not only exhibit connections between Cases A↔B and C↔D for the SM, but

also for the benchmark MSSM scenario with $M_{\rm SUSY} = 1$ TeV, $\tan\beta = 5$, and $\overline{\eta}_b = 0.6$. The analogous behaviour observed among the cases is connected to their similar input parameter m_a, which we examine in section 6.2 for the SM. In section 6.2, we learn that the connection for Cases A↔B and C↔D originates from a combination of the similar running behaviour in most neutrino parameters, see also section 6.1, which enforces similar starting values at the GUT scale, and the way the GUT scale parameters are linked to the two input parameters m_a and m_b. The line of reasoning employed for the SM caries over to the MSSM – with minor modifications, see Ref. [310]. We, thus, expect similar m_a for Cases A, B and C, D, respectively, within a fixed MSSM setting, as well as an overall narrow range for m_b. This can indeed be observed in Tabs. 6.6 and 6.7, where we display the input parameters m_a and m_b (in meV). In the following, we briefly broach how varying $M_{\rm SUSY}$ and $\tan\beta$ influences these connections:

- As already discussed above, we expect the input parameter m_a to reflect the connections between Cases A↔B and C↔D. In addition, we expect that the input parameter m_b does not display any such connections but lies in a narrow region for all cases. Both projections prove to be correct. How close the input parameter m_a for Case A is to the one for Case B, however, depends on $\tan\beta$. The same is true for Cases C and D. In other words, the higher $\tan\beta$ the further apart are the m_a of the connected cases. This can be traced back to the RG running, which depends on $\tan\beta$.[9] That is to say that there is – in general – more running for higher $\tan\beta$ and, consequently, more deviation in GUT scale values depending on the case, which translates most directly to m_a.

- Fixing $\tan\beta$ to either of the three settings, one can observe an increase in both m_a and m_b with $M_{\rm SUSY}$.

- Fixing $M_{\rm SUSY}$, on the other hand, does not yield any such clear tendency for neither m_a nor m_b.

- The overall range of values obtained by varying the SUSY breaking scale and $\tan\beta$ is similar for all four LS cases, namely about 1 meV for m_a and roughly 0.11 meV for m_b. This means that a variation in the MSSM setting has a nearly identical impact on all four LS cases, which is further supported when taking a closer look at the relative changes in m_a in between the settings studied.

One could in principle elaborate further on the discussion above, and also study the correlations of the LS cases on the level of neutrino parameters. That way, one could confirm the key role of the atmospheric angle for the goodness-of-fit for all MSSM settings. This is, however, beyond the scope of this work.

[9] When switching from SM to MSSM, the vacuum expectation value v^2 is replaced by $v^2 \sin^2\beta$. That way, the effective neutrino mass depends on $\tan\beta$.

		Case A				Case B			
$\tan\beta$	$\overline{\eta}_b$	m_a	m_b	χ^2	χ^2_δ	m_a	m_b	χ^2	χ^2_δ
	-0.6	16.115	1.5791	11.59	11.64	16.104	1.5970	8.556	8.571
5	0	16.110	1.5787	11.59	11.64	16.100	1.5966	8.555	8.570
	0.6	16.110	1.5786	11.59	11.64	16.099	1.5965	8.555	8.569
	-0.6	17.478	1.5123	47.11	47.13	17.355	1.7502	47.62	47.63
30	0	15.672	1.5129	14.28	14.33	15.651	1.5543	11.19	11.20
	0.6	15.662	1.5128	14.16	14.21	15.641	1.5532	11.06	11.07
50	0	16.331	1.5116	23.89	23.92	16.276	1.6243	21.60	21.61
	0.6	16.180	1.5116	21.47	21.51	16.133	1.6081	18.95	18.96

(a) $M_{\text{SUSY}} = 1$ TeV

		Case A				Case B			
$\tan\beta$	$\overline{\eta}_b$	m_a	m_b	χ^2	χ^2_δ	m_a	m_b	χ^2	χ^2_δ
	-0.6	16.325	1.5997	11.59	11.63	16.314	1.6178	8.585	8.599
5	0	16.321	1.5993	11.59	11.63	16.310	1.6174	8.583	8.597
	0.6	16.320	1.5993	11.59	11.63	16.310	1.6174	8.583	8.597
	-0.6	16.358	1.5358	20.26	20.30	16.314	1.6252	17.67	17.69
30	0	15.895	1.5346	14.259	14.30	15.873	1.5763	11.19	11.20
	0.6	15.886	1.5345	14.15	14.19	15.865	1.5754	11.08	11.09
50	0	16.527	1.5333	23.25	23.29	16.473	1.6434	20.95	20.97
	0.6	16.402	1.5333	21.30	21.34	16.355	1.6300	18.80	18.82

(b) $M_{\text{SUSY}} = 3$ TeV

		Case A				Case B			
$\tan\beta$	$\overline{\eta}_b$	m_a	m_b	χ^2	χ^2_δ	m_a	m_b	χ^2	χ^2_δ
	-0.6	16.563	1.6231	11.58	11.63	16.553	1.6415	8.615	8.630
5	0	16.559	1.6227	11.58	11.63	16.548	1.6411	8.614	8.629
	0.6	16.558	1.6226	11.58	11.63	16.548	1.6410	8.614	8.628
	-0.6	16.383	1.5592	17.14	17.18	16.349	1.6260	14.32	14.33
30	0	16.138	1.5585	14.20	14.25	16.117	1.6005	11.17	11.19
	0.6	16.130	1.5584	14.11	14.16	16.109	1.5997	11.08	11.10
50	0	16.744	1.5572	22.62	22.66	16.692	1.6647	20.31	20.32
	0.6	16.641	1.5572	21.06	21.10	16.594	1.6537	18.59	18.60

(c) $M_{\text{SUSY}} = 10$ TeV

Table 6.6: Best-fit values for Cases A and B with $M_{\text{atm}} = 10^{12}$ GeV and $M_{\text{sol}} = 10^{15}$ GeV: (*top*) $M_{\text{SUSY}} = 1$ TeV, (*middle*) $M_{\text{SUSY}} = 3$ TeV, (*bottom*) $M_{\text{SUSY}} = 10$ TeV, as well as varying $\tan\beta$ and threshold effects denoted by $\overline{\eta}_b$. The input parameters m_a and m_b are given in meV. When needed, the values of $\chi^2_{(\delta)}$ with more digits can be found in the corresponding table in Ref. [5].

		Case C				Case D			
$\tan\beta$	$\overline{\eta}_b$	m_a	m_b	χ^2	χ^2_δ	m_a	m_b	χ^2	χ^2_δ
	-0.6	16.854	1.6177	14.76	14.81	16.834	1.6377	9.154	9.168
5	0	16.849	1.6173	14.76	14.80	16.830	1.6372	9.153	9.167
	0.6	16.849	1.6172	14.76	14.80	16.829	1.6371	9.153	9.166
	-0.6	18.324	1.5559	52.07	52.09	18.153	1.7971	48.46	48.47
30	0	16.357	1.5491	17.42	17.46	16.324	1.5924	11.77	11.79
	0.6	16.346	1.5490	17.29	17.33	16.313	1.5913	11.65	11.66
50	0	17.074	1.5507	27.67	27.70	16.994	1.6656	22.30	22.31
	0.6	16.910	1.5501	25.11	25.14	16.841	1.6486	19.62	19.64

(a) $M_{\rm SUSY} = 1$ TeV

		Case C				Case D			
$\tan\beta$	$\overline{\eta}_b$	m_a	m_b	χ^2	χ^2_δ	m_a	m_b	χ^2	χ^2_δ
	-0.6	17.084	1.6394	14.80	14.85	17.064	1.6596	9.192	9.205
5	0	17.080	1.6389	14.80	14.84	17.060	1.6592	9.190	9.204
	0.6	17.079	1.6389	14.80	14.84	17.059	1.6591	9.190	9.204
	-0.6	17.103	1.5751	23.88	23.91	17.039	1.6665	18.34	18.36
30	0	16.599	1.5718	17.44	17.48	16.565	1.6155	11.78	11.80
	0.6	16.589	1.5717	17.32	17.36	16.556	1.6145	11.67	11.69
50	0	17.288	1.5734	27.06	27.09	17.209	1.6857	21.66	21.67
	0.6	17.151	1.5729	24.98	25.01	17.082	1.6717	19.49	19.50

(b) $M_{\rm SUSY} = 3$ TeV

		Case C				Case D			
$\tan\beta$	$\overline{\eta}_b$	m_a	m_b	χ^2	χ^2_δ	m_a	m_b	χ^2	χ^2_δ
	-0.6	17.346	1.6639	14.85	14.89	17.325	1.6845	9.234	9.247
5	0	17.341	1.6635	14.85	14.89	17.321	1.6841	9.232	9.246
	0.6	17.341	1.6635	14.85	14.89	17.320	1.6840	9.232	9.246
	-0.6	17.130	1.5988	20.60	20.63	17.080	1.6677	14.97	14.98
30	0	16.865	1.5969	17.43	17.47	16.830	1.6409	11.78	11.80
	0.6	16.856	1.5968	17.34	17.38	16.822	1.6400	11.69	11.70
50	0	17.525	1.5984	26.45	26.48	17.449	1.7082	21.02	21.03
	0.6	17.413	1.5979	24.78	24.81	17.343	1.6966	19.28	19.29

(c) $M_{\rm SUSY} = 10$ TeV

Table 6.7: Best-fit values for Cases C and D with $M_{\rm atm} = 10^{15}$ GeV and $M_{\rm sol} = 10^{12}$ GeV: (*top*) $M_{\rm SUSY} = 1$ TeV, (*middle*) $M_{\rm SUSY} = 3$ TeV, (*bottom*) $M_{\rm SUSY} = 10$ TeV, as well as varying $\tan\beta$ and threshold effects denoted by $\overline{\eta}_b$. The input parameters m_a and m_b are given in meV. When needed, the values of $\chi^2_{(\delta)}$ with more digits can be found in the corresponding table in Ref. [5].

Case A, M_{SUSY}= 1 TeV, tanβ=5, $\bar{\eta}_b$=0.6

	Λ_{GUT}	M_{sol}	M_{atm}	Λ_{EW}
θ_{13}(deg)	8.41036	8.41346	8.41449	8.41694
θ_{12}(deg)	34.3737	34.4593	34.4613	34.4648
θ_{23}(deg)	45.5262	45.4286	45.4309	45.4401
m_2(meV)	5.06633	5.24637	6.02352	8.53262
m_3(meV)	30.1179	30.9015	35.4702	50.2415
δ_{CP}(deg)	−87.6504	−87.8008	−87.8032	−87.8023
σ_{CP}(deg)	−143.312	−143.071	−143.067	−143.067

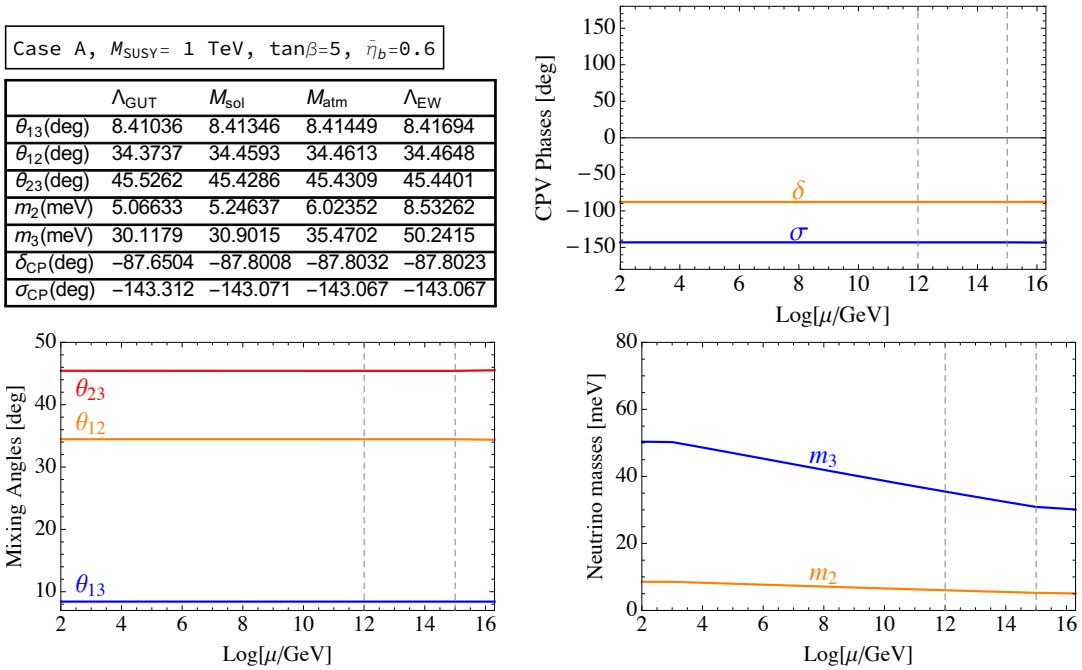

Figure 6.5: Case A – MSSM with $M_{\rm SUSY} = 1$ TeV, $M_{\rm atm} = 10^{12}$ GeV, and $M_{\rm sol} = 10^{15}$ GeV.

Case B, M_{SUSY}= 1 TeV, tanβ=5, $\bar{\eta}_b$=0.6

	Λ_{GUT}	M_{sol}	M_{atm}	Λ_{EW}
θ_{13}(deg)	8.51005	8.51324	8.51367	8.51358
θ_{12}(deg)	34.352	34.4385	34.4407	34.4447
θ_{23}(deg)	44.3793	44.8056	44.8152	44.824
m_2(meV)	5.1186	5.29897	6.08388	8.61828
m_3(meV)	30.1278	30.8981	35.4659	50.2358
δ_{CP}(deg)	−92.7339	−92.8746	−92.8791	−92.8798
σ_{CP}(deg)	−36.4007	−36.3526	−36.3507	−36.3508

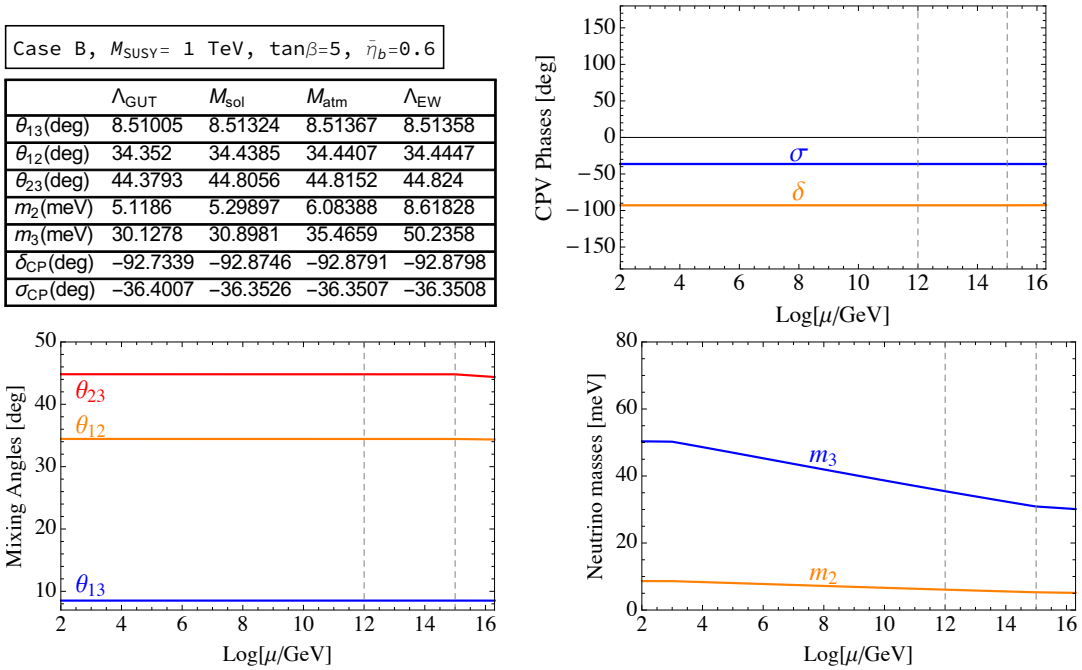

Figure 6.6: Case B – MSSM with $M_{\rm SUSY} = 1$ TeV, $M_{\rm atm} = 10^{12}$ GeV, and $M_{\rm sol} = 10^{15}$ GeV.

Case C, M_{SUSY}= 1 TeV, tanβ=5, $\bar{\eta}_b$=0.6

	Λ_{GUT}	M_{atm}	M_{sol}	Λ_{EW}
θ_{13}(deg)	8.24007	8.4019	8.40691	8.40931
θ_{12}(deg)	34.4101	34.376	34.3761	34.3796
θ_{23}(deg)	45.3698	46.0094	46.0286	46.0376
m_2(meV)	5.19862	5.30131	6.08268	8.62214
m_3(meV)	31.4486	30.921	35.4421	50.2356
δ_{CP}(deg)	−88.3094	−88.4373	−88.441	−88.4404
σ_{CP}(deg)	−142.821	−142.338	−142.325	−142.325

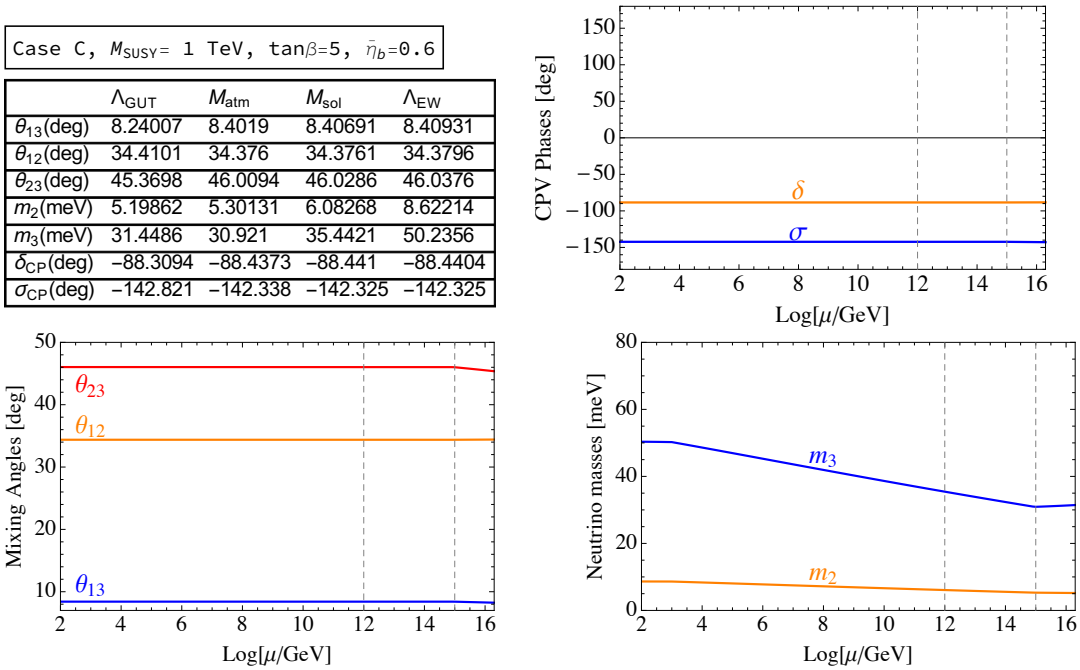

Figure 6.7: Case C – MSSM with $M_{\rm SUSY} = 1$ TeV, $M_{\rm atm} = 10^{15}$ GeV, and $M_{\rm sol} = 10^{12}$ GeV.

Case D, M_{SUSY}= 1 TeV, tanβ=5, $\bar{\eta}_b$=0.6

	Λ_{GUT}	M_{atm}	M_{sol}	Λ_{EW}
θ_{13}(deg)	8.35016	8.51379	8.51826	8.51814
θ_{12}(deg)	34.3867	34.3516	34.3518	34.3559
θ_{23}(deg)	44.5297	44.9844	44.9997	45.0084
m_2(meV)	5.25717	5.36091	6.15107	8.71916
m_3(meV)	31.4436	30.921	35.4422	50.2352
δ_{CP}(deg)	−92.117	−92.9792	−93.0036	−93.0043
σ_{CP}(deg)	−36.8616	−36.3566	−36.3425	−36.3427

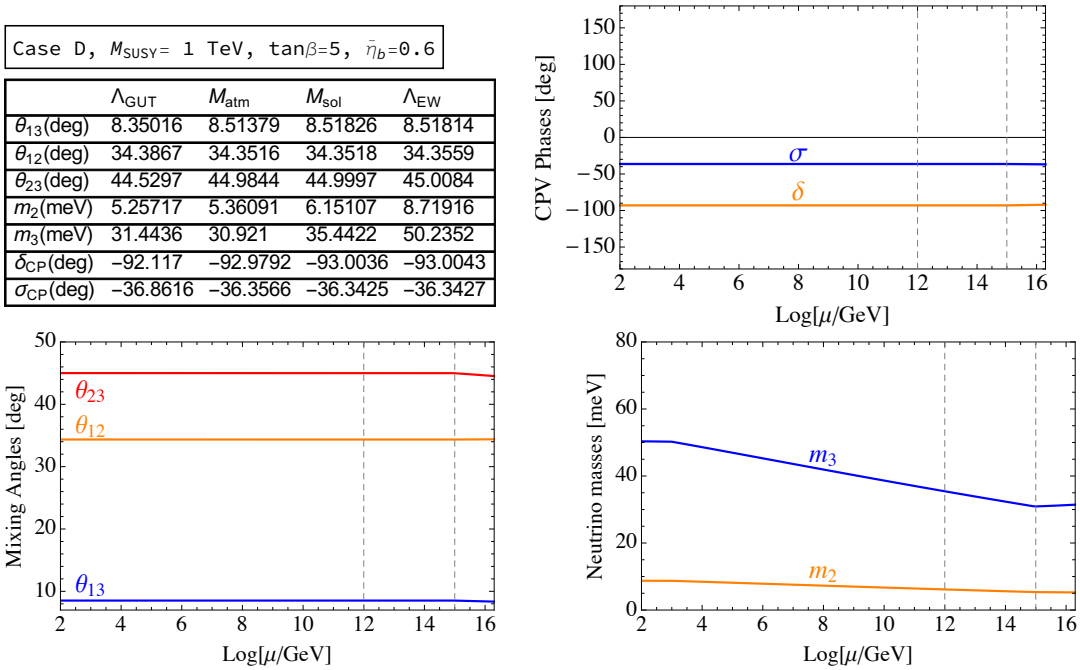

Figure 6.8: Case D – MSSM with $M_{\rm SUSY} = 1$ TeV, $M_{\rm atm} = 10^{15}$ GeV, and $M_{\rm sol} = 10^{12}$ GeV.

6.4 Comparing SM and MSSM Results

The purpose of this section is to compare the SM and MSSM behaviours. To this end, we choose one benchmark MSSM scenario with the SUSY breaking scale at $M_{\text{SUSY}} = 1$ TeV and a threshold effect parameter of $\overline{\eta}_b = 0.6$. The meaning of the latter is explained in Appendix E. A more thorough discussion of the MSSM behaviour including different SUSY breaking scales and varying threshold effects can be found in the previous section 6.3. Note that we employ the RH neutrino mass setting $(10^{15}, 10^{12})$ GeV throughout the following analysis.
In Tab. 6.8, we collect the goodness-of-fit values for the SM and the benchmark MSSM scenario with varying $\tan\beta$. There are several observations worth mentioning:

- First and foremost, we note that the SM scenarios make for significantly better fits to the experimental data for each LS case individually. In fact, the poorest fit from the SM, namely Case A at $\chi^2 = 7.14$, still outperforms the best for the MSSM, namely Case B with $\tan\beta = 5$ at $\chi^2 = 8.56$.
- While for the SM, the goodness-of-fit deteriorates from Case D via C and B to Case A, the order changes for the MSSM benchmark scenario, leading to Case B being most compatible with experimental data – followed somewhat closely by Case D, and then by Cases A and C.

To understand why the SM does yield better agreement with experimental data than the MSSM scenario as well as to understand the distinct characteristics with respect to the relative suitability of the different LS cases, we investigate and compare the behaviour of the neutrino parameters. As we

Case	χ^2_{MSSM}			$\chi^2_{\delta\ \text{MSSM}}$			χ^2_{SM}	$\chi^2_{\delta\ \text{SM}}$
	$t_\beta = 5$	$t_\beta = 30$	$t_\beta = 50$	$t_\beta = 5$	$t_\beta = 30$	$t_\beta = 50$		
A	11.5885	14.1634	21.4783	11.6367	14.2082	21.5109	7.14042	7.15869
B	8.55503	11.0593	18.9483	8.56943	11.0734	18.9616	4.38607	4.44012
C	14.7613	17.2949	25.1095	14.8042	17.3349	25.1423	3.23646	3.30174
D	9.15257	11.6451	19.6235	9.16639	11.6586	19.6361	1.49388	1.52265

Table 6.8: Best-fit χ^2 values at Λ_{EW} for the four cases for the SM as well as the MSSM with $M_{\text{SUSY}} = 1$ TeV, $\overline{\eta}_b = 0.6$, and varying $t_\beta \equiv \tan\beta$. The corresponding m_a and m_b are displayed in Tabs. 6.1, 6.6, and 6.7.

strive to compare the SM with the MSSM, we focus the discussion on generic differences in the initial values (meaning at the GUT scale) and the RG running behaviour of the neutrino parameters, without delving into the specifics of the MSSM. Since $\tan\beta = 5$ makes for the most suitable predictions from the MSSM benchmark scenario, we use its predicted neutrino parameters when

comparing to the SM. From the upper left panels of Figs. 6.1 to 6.4 for the SM in combination with Figs. 6.5 to 6.8 for the MSSM benchmark scenario, we can condense the following characteristics with respect to the neutrino parameters:

- The mixing angle $\boldsymbol{\theta_{12}}$ is predicted to be in between [34.36°, 34.46°] for the $\tan\beta = 5$ MSSM benchmark scenario, whereas it yields values in the range of [34.05°, 34.37°] for the SM, both at the EW scale and depending on the LS case. The measured solar angle is $\theta_{12}^{\text{exp}} = 33.58°$ with a 1σ range of [32.83°, 34.33°]. Consequently, the SM predictions for Cases A, B are encompassed in and those for Cases C, D close to the standard deviation, whereas the MSSM predictions for Cases C, D lie about as close as the SM's Cases C, D and the MSSM's Cases A, B are further above. Thereby, the solar angle has a bias towards the SM for Cases A and B, while there is no preference when considering Cases C and D. As observed in the previous section, there is an intrinsic connection between Cases A↔B and Cases C↔D for the SM, which also appears for the MSSM benchmark scenario. That is to say that – in case of this MSSM scenario – Cases A and B generate quite similar values at the GUT scale, they display an overall identical but minor increase based on the RG running between the GUT and the EW scale, and thus predict similar θ_{12} at the EW scale. For the MSSM benchmark scenario, Cases C and D behave analogously, apart from a decline in the solar angle with the decrease of the energy scale and deviating absolute values at the GUT scale.

- Analysing the predictions for the mixing angle $\boldsymbol{\theta_{13}}$, we obtain a LS-case-dependent range of [8.41°, 8.52°] for the $\tan\beta = 5$ MSSM benchmark scenario at the EW scale, while the SM yields values in between [8.42°, 8.51°]. With an experimental value of $\theta_{13}^{\text{exp}} = 8.46°$ within a 1σ range of [8.31°, 8.61°], both predicted ranges are centred around the measured value and fully encompassed within the 1σ region. Thus, there is no general bias towards either the SM or the MSSM scenario from the reactor angle. From the SM discussion in section 6.2, we recall that Cases A and B generate similar initial values at the GUT scale, they undergo the same overall decline with the energy scale, and thereby predict similar values at the EW scale. The same holds true for Cases C and D, but with an increase in θ_{13} from the GUT to the EW scale, and absolute values that differ from Cases A, B at the GUT scale. Nevertheless, all four cases converge to a narrow region and predict similar reactor angles within the framework of the SM. Since the MSSM scenario displays a nearly identical range of predicted θ_{13}, one might assume that the underlying behaviour is equivalent. This, however, does not stand up to scrutiny. From Figs. 6.5 to 6.8, we learn that the starting values at the GUT scale are spread. The RG running, on the other hand, does yet again display the connection between the cases, leading to hardly any

alteration of θ_{13} due to running effects for Cases A and B, and an increase by 0.17° from the GUT to the EW scale for Cases C and D. This allows for the EW scale values of Cases A and C to be close. The same is observed for the EW scale reactor angles of Cases B and D. Since the measured mixing angle lies centred in between the different LS cases, there is no strong preference for any case to be discerned within the framework of the MSSM – which is also true for the SM.

- For the atmospheric mixing angle $\boldsymbol{\theta_{23}}$, the MSSM benchmark scenario with $\tan\beta = 5$ predicts values within the range of $[44.82^\circ, 46.04^\circ]$ at the EW scale, depending on the LS case. The atmospheric angles predicted by the LS cases within the framework of the SM are within the range of $[42.37^\circ, 44.72^\circ]$. The measured value of $\theta_{23}^{\text{exp}} = 41.61^\circ$ within the 1σ region of $[40.40^\circ, 43.17^\circ]$ is below the range of predicted values in either case. Note that all atmospheric angles predicted within the framework of the SM are below the range of θ_{23}'s derived from the MSSM scenario. Furthermore, the spread of the predicted values depending on the LS case is large in comparison to the other two mixing angles, which is true for both frameworks, the SM and the MSSM. The atmospheric angle also differs from the other mixing angles in terms of connections between the different LS cases. For neither the SM nor the MSSM framework, there are connections for the prediction at the GUT scale or the RG running behaviour. Consequently, the atmospheric angle plays the decisive role with respect to the compatibility of a scenario with experimental data – and it favours the SM over the MSSM as a framework for the respective LS cases. It is, therefore, not surprising that the goodness-of-fit, estimated by χ^2, reflects the order of how well a case and/or scenario predicts θ_{23}. As an example of this feature take the atmospheric angles predicted by the SM's Case A, $\theta_{23}^{\text{SM,A}} = 44.72^\circ$, and the MSSM's Case B, $\theta_{23}^{\text{MSSM,B}} = 44.82^\circ$. The former is least suitable within the framework of the SM, whereas the latter is most compatible for the MSSM. Although they stem from different frameworks and LS cases, their overall performance with respect to compatibility with experimental data is similar – $\chi^2_{\text{SM,A}} = 7.14$ and $\chi^2_{\text{MSSM,B}} = 8.56$ – and mirrors the ordering of their atmospheric angles.

- Turning to the neutrino masses, we compare the $\boldsymbol{m_2}$ predictions from the SM to the ones from the MSSM benchmark scenario. From the SM, we obtain a range of [8.63 meV, 8.73 meV]. The MSSM benchmark scenario with $\tan\beta = 5$ predicts lighter neutrino masses in the region of [8.53 meV, 8.72 meV]. The measured neutrino mass of $m_2^{\text{exp}} = 8.66$ meV is embedded in the 1σ region of [8.56 meV, 8.77 meV]. Consequently, all cases but the MSSM's Case A predict values well within the 1σ region. Nevertheless, the MSSM's Case A generates a lighter neutrino mass that is in close proximity to the 1σ region. Another feature worth mention-

ing is the MSSM's RG running effects in distinction from the SM's RG behaviour. Within the framework of the SM, the four LS cases show no obvious connection at the GUT scale, where their absolute values are in close proximity to one another – at roughly $m_2(\mu = \Lambda_{\rm GUT}) = 13.4$ meV. Due to the RG running effects, the light neutrino mass decreases for each LS case by about the same amount, leading to equally good predictions at the EW scale. The picture is somewhat different within the framework of the MSSM. Starting from absolute values at about $m_2(\mu = \Lambda_{\rm GUT}) = 5.15$ meV, the RG effects increase the light neutrino mass in between the GUT and the EW scales. Since the magnitude of the increase varies slightly, we obtain a marginally wider region of m_2 values at the EW scale than we do for the SM. The opposite direction of the RG running can be traced back to the coefficients in the RGEs that differ for the SM and the MSSM, including a relative sign [331, 449]. Despite the fundamental differences in terms of RG behaviour, the prediction of m_2 only gives a narrow edge to the SM over the MSSM for Case A. For the remaining three LS cases, there is no preference for either the SM or the MSSM from the light neutrino mass.

- For the neutrino mass $\boldsymbol{m_3}$, the predicted values are nearly identical for any case within either the SM or the MSSM framework – $m_3^{\rm SM} \in$ [50.24 meV, 50.25 meV] and $m_3^{\rm MSSM} = 50.24$ meV. They are also consistent with the measured value $m_3^{\rm exp} = 50.24$ meV, which lies in the 1σ region of [49.84 meV, 50.63 meV]. Although there is no bias towards any scenario or case from the heavier of the light neutrino masses, the features leading to the EW scale value differ. As already observed for the lighter neutrino mass m_2, m_3 undergoes different alterations due to the RG effects. Recall that the SM Cases A and B start from roughly the same value at the GUT scale, as do Cases C and D. The initial GUT scale values are significantly higher for the latter. All four LS cases exhibit a decrease of m_3 with the energy scale – with stronger effects for Cases C, D. Taking a closer look at the MSSM, we note that both Cases A, B and Cases C, D start from nearly identical values at the GUT scale – with the latter being a bit higher. The RG running effects are opposite to those of the SM, meaning that m_3 increases from the GUT to the EW scale, which in analogy to m_2 is attributed to the coefficients of the RGEs [331, 449]. Nevertheless, both frameworks and all four scenarios within predict the measured value perfectly, and thus give no bias regarding the goodness-of-fit.

Intriguingly, both the SM as well as the MSSM framework can generate comparably good values for the neutrino parameters θ_{13}, m_2, and m_3, which are the parameters that have the lowest spread with respect to the LS case. Note that, for θ_{13} and m_3, all four LS cases in both frameworks are within the 1σ region, and for m_2 there is only one outlier, namely the MSSM's Case A. The

latter allows for a slight preference of the SM over the MSSM but only when considering Case A. A more important distinction stems from the mixing angle θ_{12}. First of all, θ_{12} has a bias towards the SM for the Cases A and B, while it does not display a bias for Cases C and D – giving an overall edge to the SM. Secondly, the reshuffled order with respect to how well the different LS cases do hints towards the observation that the hierarchy among the LS cases changes depending on the framework. The most decisive role with respect to compatibility with data, however, falls to the atmospheric angle θ_{23} once again. For θ_{23}, there is not only the widest spread regarding the different LS cases but also the most explicit gap between the values predicted by the SM and those derived from the MSSM. In addition, the ordering of LS cases by means of how well they predict the atmospheric angle directly translates into their overall performance. It is therefore, once again, the atmospheric angle that is most significant and makes for the substantially better fits of the SM scenarios to the experimental data.

6.5 Summary

In this chapter, we have performed a detailed RG analysis of the LS models, focussing on those cases where the RG corrections can become significant. Unlike a previous analysis [310], where the input parameters were fixed independently of RG corrections, we have implemented a complete scan of model parameters for each case individually. That way, we determined the optimum set of high-energy input values from a global fit of the low-energy parameters which include the effects of RG running. In all cases we have employed a χ^2 analysis of the low-energy masses and mixing angles for various RH neutrino masses and mass orderings. The scan for each LS case individually was executed both within the framework of the SM and the MSSM, pinpointing the optimum set of input values (m_a, m_b) at the GUT scale from global fits to experimental data at the EW scale. Perhaps not surprisingly, the values of χ^2 that we obtain here are significantly lower than those obtained in the previous analysis, where the input parameters were determined independently of RG corrections.

We have found that the most favourable RG corrections occur in the SM, rather than in the MSSM. Amongst the three mixing angles, we ascertained that the atmospheric angle is often the most sensitive to RG corrections in both the SM and the MSSM, although in the latter the corrections are relatively small. Without including RG corrections, the LS predictions are in some tension with the latest global fits, mainly because of the atmospheric angle being predicted to be close to maximal. The sensitivity of the atmospheric angle to RG corrections in the SM thus allows for a better fit at low energies, corresponding to an atmospheric angle in the first octant close to the current best-fit value for normal mass ordering.

For the SM, we have performed the analysis with various RH neutrino

masses, and for the MSSM we have investigated different SUSY breaking scales, $\tan\beta$, and threshold effects. In the case of the SM, it turns out that its beneficial for the running effects if the heavier of the RH neutrinos is closer to the GUT scale, with masses $(10^{15}, 10^{12})$ GeV yielding the best results. In this case, the SM resulted in: $\chi^2_{\rm A} = 7.1$, $\chi^2_{\rm B} = 4.4$, $\chi^2_{\rm C} = 3.2$, and $\chi^2_{\rm D} = 1.5$, corresponding to exceptionally good agreement with experimental data, especially for Case D.

We emphasise that the atmospheric angle plays a key role in our analysis, and is the crucial factor in obtaining low χ^2 values for a given setup. While it is possible to obtain comparably good results for m_2, m_3, θ_{12}, and θ_{13} at the EW scale for all LS cases, it is θ_{23} that varies most among the different cases within the SM or the MSSM. While the SM and MSSM can generate comparably good m_2, m_3, and θ_{13}, and there is some preference of θ_{12} in favour of Cases A and B of the SM, the most decisive parameter is θ_{23}, for which the SM predictions are significantly better. This is partly a result of the fact that RG corrections in the MSSM are relatively small, compared to the SM, and so the prediction of near maximal atmospheric mixing is maintained at low energies in the MSSM.

Forthcoming results from T2K and NOνA on the atmospheric mixing angle will test the predictions of the LS models. The inclusion of RG corrections in a consistent way, as done in this chapter, will be crucial in confronting such theoretical models with data.

Chapter 7

Summary and Conclusions

In this thesis, we have presented three main research pillars, the realisation of which form the foundation of this dissertation. On the one hand, we have studied the promising charged lepton flavour/number violating (LFV/LNV) conversion of bound muons, and made vital contributions towards a more complete theoretical treatment for both types of conversion processes. On the other hand, we have presented a comprehensive renormalisation group (RG) analysis of the Littlest Seesaw model, demonstrating the need to include running effects when confronting New Physics models with oscillation data.

In chapters 2 to 4, we have provided a number of reviews dedicated to the introduction of basic findings, notions, and methods relevant to neutrino physics and to the search for New Physics beyond the Standard Model (SM). In addition, we have introduced the New Physics models predominantly employed later on. Apart from laying the foundation for later chapters, the goal of these chapters was to illustrate opportunities to increase the testability of New Physics models, especially those with additional LFV and/or LNV in order to unravel novel physics. In particular, we have motivated exploiting complementary searches, highlighting the importance of the research conducted as part of this thesis. Chapters 5 and 6 are the scientific centrepiece of this thesis. Therefore, we present their findings in detail below.

Chapter 5 is devoted to both $\mu^- - e^-$ and $\mu^- - e^+$ conversion, i.e., the reactions turning a muon bound to an atomic nucleus into an electron or a positron, respectively. We started by reviewing the key experimental aspects of both types of bound muon conversion, including backgrounds, sensitivities, and nuclear physics aspects, in section 5.1. We have also pointed out different areas which need further advances in order to fully exploit or even boost the discovery potential of bound muon conversions.
In section 5.2, we have presented a detailed computation of $\mu^- - e^-$ conversion for the case of the process being mediated by a doubly charged singlet scalar particle. After having identified the decisive Feynman diagrams, we have com-

puted the resulting amplitude for the conversion and mapped it to the known most general amplitude for the process. We took into account both the photonic (predominantly long-range) and the non-photonic (short-range) contributions, the latter of which are however subdominant and can be neglected in practice. Our results are fully general and hold for any doubly charged singlet scalar coupling to pairs of right-handed (RH) charged leptons, thereby closing a big gap in the contemporary knowledge on $\mu^- - e^-$ conversion. Even for doubly charged scalars which are no singlets under SU(2), such as the doubly charged component of a Higgs triplet field, most of the computation presented would practically remain the same – a generalisation of our results is both possible and doable with moderate effort. In addition, we have investigated how strongly the parameters related to the doubly charged scalar can be constrained by future experimental limits on this conversion process, which are expected to dramatically improve within the coming years. For illustrative purposes, we have also included the explicit example of one particular model, namely the effective theory of the doubly charged scalar, which generates a valid light neutrino mass at two-loop level and which contains our general setting as a subset. As we have seen, despite intrinsic nuclear physics uncertainties, the limits to be expected from the conversion process strongly constrain the mass of the doubly charged scalar. Furthermore, we have shown how the intensity and the energy frontiers provide complementary constraints. Depending on the benchmark scenario, future indirect limits from $\mu^- - e^-$ conversion might even be more stringent than the direct limits which will be obtained by the Large Hadron Collider.

In section 5.3, we have presented the complete computation of the rate for the LFV *and* LNV $\mu^- - e^+$ conversion, mediated by the effective operator $J_x^\nu J_{y,\nu} j_z$. After introducing the effective operator language in the way appropriate for this process, we have detailed the whole pathway from the amplitude to the decay rate. Our main target group are particle physicists, which is why we had a particular focus on displaying the steps related to the nuclear physics part involved as explicitly as possible. We furthermore pointed out several concrete New Physics realisations of the effective operator used, all of which can in principle be experimentally probed by $\mu^- - e^+$ conversion. We augmented the discussion by an illustration of which physics impact upcoming experiments like COMET could make. We have also identified three branches which, if advanced further, could greatly help gaining fundamental physics insights using $\mu^- - e^+$ conversion: the more detailed investigation of particle physics models in what regards LNV in the $e\mu$ sector (to understand the possible gain), more involved experimental sensitivity studies (to determine the physics potential of upcoming experimental setups), and the up-to-now missing computation of the nuclear matrix elements (NMEs) for the process (to sharpen the resulting limits on promising theories). At the moment, with hardly any NME values being available, this is about as far as one could possibly go when aiming to obtain concrete numbers. However, given that we have detailed how to per-

form the computation for the operator ϵ_3, it should at least in principle be clear how to approach the computation for other effective operators.
In conclusion, near-future experiments have a great potential to advance our knowledge on charged-lepton LFV and LNV. They can serve as a valuable addition to collider studies in the hunt for New Physics beyond the SM. Nevertheless, there remain several gaps in our theoretical knowledge, which is why we hope that our research was able to provide a starting point for further detailed investigations.

In chapter 6, we have performed a detailed RG analysis of the Littlest Seesaw (LS) model, focussing on those cases where the RG corrections can become significant. Unlike a previous analysis [310], where the input parameters were fixed independently of RG corrections, we have implemented a complete scan of model parameters for each case individually. That way, we could determine the optimum set of high-energy input values from a global fit of the low-energy parameters which include the effects of RG running. In all cases we have employed a χ^2 analysis of the low-energy masses and mixing angles for various RH neutrino masses and mass orderings. The scan for each LS case individually has been executed both within the framework of the SM and the Minimal Supersymmetric Standard Model (MSSM), pinpointing the optimum set of input values at the grand unified theory (GUT) scale from global fits to experimental data at the electroweak (EW) scale. Perhaps not too surprisingly, the values of χ^2 that we obtained here are significantly lower than those obtained in the previous analysis, where the input parameters were determined independently of RG corrections.
We have found that the most favourable RG corrections occur in the SM, rather than in the MSSM. Amongst the three mixing angles, we ascertained that the atmospheric angle is often the most sensitive to RG corrections in both the SM and the MSSM, although in the latter the corrections are relatively small. Without including RG corrections, the LS predictions are in some tension with the latest global fits, mainly because of the atmospheric angle being predicted to be close to maximal. The sensitivity of the atmospheric angle to RG corrections in the SM thus allows for a better fit at low energies, corresponding to an atmospheric angle in the first octant close to the current best-fit value for normal mass ordering. For the SM, we have performed the analysis with various RH neutrino masses, and for the MSSM we have investigated different supersymmetric (SUSY) breaking scales, $\tan\beta$, and threshold effects. In the case of the SM, it turns out that its beneficial for the running effects if the heavier of the RH neutrinos is closer to the GUT scale, with masses $(10^{15}, 10^{12})$ GeV yielding the best results.
We emphasise that the atmospheric angle plays a key role in our analysis and is the crucial factor in obtaining low χ^2 values for a given setup. While it is possible to obtain comparably good results for m_2, m_3, θ_{12}, and θ_{13} at the EW scale for all LS cases, it is θ_{23} that varies most among the different cases

within the SM or the MSSM. While the SM and MSSM both can generate comparably good m_2, m_3, and θ_{13}, and there are some differences with respect to θ_{12} depending on the case, the most decisive parameter is θ_{23}, for which the SM predictions are significantly better. This is partly a result of the fact that RG corrections in the MSSM are relatively small, compared to the SM, and so the prediction of near maximal atmospheric mixing is maintained at low energies in the MSSM.

Forthcoming results from T2K and NOνA on the atmospheric mixing angle will test the predictions of the LS models. The inclusion of RG corrections in a consistent way, as done in chapter 6 will be crucial in confronting such theoretical models with data.

Acknowledgements

This thesis would not have been possible without the support of so many people within and outside the Max Planck Institute for Physics, and neither would my time as a doctoral researcher have been as pleasant and joyful. I am grateful to have had the privilege of working with and being amidst such remarkable people whom I would like to thank here. As it is almost Christmas, and I have to hand in tomorrow, I might have forgotten to mention some people by name. If so, please forgive me! I'm happy to thank you in person and/or by means of inviting you for an ice-cream :) .

First and foremost, I would like to express my gratitude to my supervisors, Alexander Merle and Georg Raffelt. They have managed to keep the balance between guiding me through my research projects and challenging me to take steps on my own. It is safe to say that I have learnt a lot from them: not only from their impressive knowledge on physics but also from the way they work and how they supervise. I am grateful that I was given the opportunity to explore own scientific ideas while having their day-to-day support. Moreover, I would like to thank them for actively supporting me to attend many schools and conferences including a research stay in Southampton. I also would like to express my special gratitude to Alexander Merle. Alex, you have been more of a mentor than a supervisor. Thank you for helping me expand my strengths and challenging me in areas where I still needed to grow. I would also like to thank you for the freedom and support to invest parts of my time and energy in being PhD representative. Although, I could probably go on thanking you, I would like to just mention one more thing: thank you for introducing me to the Harry Potter audiobooks by Stephen Fry. They are pretty amazing!
I would also like to thank my collaborators, Stephen King, Alexander Merle, Jose Miguel No, Luca Panizzi, and Kai Zuber, for many fruitful and insightful discussions. In particular, I owe my gratitude to Stephen King for hosting me in Southampton, and his whole group for a wonderful time. Likewise, I am grateful to have had the opportunity to spend the Erice workshop with Stephen King, Alexander Merle, and Kai Zuber. I will always gladly remember playing music together and enjoying a glass of Marsala wine.
For proof-reading parts of this thesis, I would like to acknowledge the help of Lena Funcke, Alexander Merle, Alexander Millar, and Tobias Stirner. Thank you for your valuable input!
Drawing up my thesis has been demanding, but I could always count on the moral support and the encouragement of many friends, colleagues and my family. Your support has carried me through. Thank you! There are a few people I

would like to mention in particular: Annette Moessinger, Monika Goldammer, Lena Funcke, Viktor Papara, Alex Millar, Alex Merle, Florian Wolf, Miroslav Gabriel, Katharina Ecker, Cyril Pietsch, Sara Pedron, Katrin Geib, and Simon Weidinger.

This thesis is the result of three years of research conducted at the Max Planck Institute for Physics. For making this time exceptional, I would like to express my deepest gratitude to all my fellow "MPPler". Not only did I receive the necessary support for my research, I also got to know many of you on a personal level. It is the many encounters, the opportunity to laugh, to talk nonsense, and having the "occasional" cup of coffee (or ice-cream) that have mattered a lot to me. The support you so freely give and your openness provide this precious atmosphere to work in and make being a member of the MPP a pleasure. There are a few groups and people I would like to mention specifically.
I would like to start by thanking our administration for the work they do everyday. On countless occasions, it was their commitment that made things possible for me. In particular, I am grateful to our secretaries Monika Goldammer, Annette Moessinger, Sarah Fischer, and Rosita Jurgeleit for always taking the time and going more than the extra mile. I'm pretty sure you keep the theory group running. I also would like to thank Karin Gebhardt for helping arrange all my travels and thereby taking additional organisational duties off my shoulders. A special "thank you" goes to Jana Pietsch, our wonderful librarian, for welcoming me to this institute, and for her tireless search and her impressive ability to chase down all the weird books I needed throughout the last three years. Finally, my time at the MPP would not have been the same without the social activities, i.e., the parties and outings, organised by members of the administration. Many thanks!
For a most pleasant work environment and, in particular, all the conversations not related to physics, I would like to thank the current and former members of the Theoretical Astrophysics group. I also want to extend this thank-you to the String-Theory and the Phenomenology groups. Spending time with you during (coffee, tea, or ice-cream) breaks has not only been a lot of fun but also often provided me with fresh ideas and a clear head. In particular, I would like to thank Ignacio Izaguirre and Maximilian Totzauer for sharing more than just our office. It has been an intense and great time, and I enjoyed our conversations about anything and everything. I also thank Tobias, who had the dubious honour to share the office with me while I was writing this thesis. Thank you for distracting me when necessary and for breaking it to me that I apparently have been misspelling "des Weiteren" for years.
During my time at the MPP, I had the honour to serve as one of seven PhD representatives. For me, this was an incredible experience. I enjoyed being part of this awesome team, and getting to realise many ideas we had. Many thanks to my fellow representatives, Miroslav Gabriel, Florian Wolf, Lena Funcke, Viktor Papara, Nicolas Köhler, and Kazuma Ishio! In connection with our

work as representatives, I would also like to express my gratitude to our directors, as well as to Martin Jäcklein, Anneliese Fleischer, Petra Lindemann, Corina Brunnlechner, Thomas Hahn, Frank Steffen, Sarah Fischer, and Annette Moessinger. I greatly appreciate all the support!
There are a few more people that cannot go unnamed because they maintained a constant supply of sweets and coffein. Firstly, thanks to the ice-cream office, i.e. Henning Bahl, Stefan Hessenberger, and Cyril Pietsch, for providing the ice-cream. Secondly, thanks Alexander Millar, Edoardo Vitagliano, and Tobias Stirner for keeping the coffee kitchen loaded. And thirdly, thanks to Thomas Hahn, Stefan Stonjek, and Stefan Kluth for not only sharing countless bars of chocolate but also for allowing me to steal the last piece.

Last but not least, I would like to express my deepest gratitude to my family and friends. Without you, none of this would have been possible, and I cannot express how blessed I feel to have you in my life. Mama, thank you for sending me a "Nikolauspäckchen" although I hadn't cleaned my shoes :). Papa, thank you for the encouraging messages you send while I was writing. Katrin, thank you for always being there for me and for making me laugh even when I don't feel like it. And Simon, thank you for being there through thick and thin and for not letting me starve while I was writing up.

Appendix A

Feynman Rules for the Effective Theory of a Doubly Charged Scalar Singlet

To perform the matching of model-dependent coefficients as well as to obtain the amplitudes needed for the computation of both the μ^-– e^- and μ^-– e^+ conversion process in sections 5.2 and 5.3, we employ the Feynman rules given in Figs. A.1 to A.8. Here, $\mathrm{P_{L,R}} = (1 \mp \gamma_5)/2$ are the left-/right-handed projectors, the indices a, $b = e$, μ, τ denote the lepton flavour, the indices α, β are Dirac spinor indices, and $k = 1, 2, 3, \cdots$ refer to the mass eigenstates of neutrinos. Note that, unlike in chapters 3 and 5 where we phrase fermionic fields in terms of their left- and right-handed component, we use the full fermionic fields in the Feynman rules below. Both notations are easily related via:

$$l_a = \underbrace{\mathrm{P_R} l_a}_{\equiv E_{a\mathrm{R}}} + \underbrace{\mathrm{P_L} l_a}_{\equiv e_{a\mathrm{L}}}, \tag{A.0.1}$$

where l_a can be a charged lepton or a neutrino. Furthermore, we employ the PMNS matrix, denoted by U, and the CKM matrix, denoted by V, to describe the mixing due to differing mass eigenbases. The former is discussed in detail in section 3.1.

As we aim at demonstrating how to approach both muon conversion processes from a particle physics point of view, we use an effective field theory model for which the Standard Model is extended by a doubly charged scalar $S^{\pm\pm}$ which couples to the right-handed charged leptons via a lepton number violating (LNV) vertex [47], see section 3.3 for more details. The doubly charged scalar interacts with the neutral gauge bosons as described by means of the covariant derivative $D_\mu = \partial_\mu + ig'YB_\mu$. The hypercharge is given by $Y = Q - I_3$ ($= \pm 2$ for $S^{\pm\pm}$), such that the covariant derivative takes the form $D_\mu = \partial_\mu \pm 2ieA_\mu \mp 2ig' \sin\theta_W Z_\mu$. The coupling to the charged W bosons takes place through an effective vertex. Within the context of μ^-– e^+ conversions, we compare the results for mediating the process by this effective theory model to a model where the conversion is mediated by a heavy Majorana neutrino $N_k \leftrightarrow \nu_k$. Thus, the Feynman rules for the latter are also displayed here. Note

that, because there are LNV vertices in the effective theory as well as when extending the Standard Model by heavy Majorana neutrinos, we naturally encounter vertices or Majorana propagators with clashing or parting arrows. For a consistent treatment using the Feynman rule language, we adopt a fixed orientation of the "fermion flow" for each diagram, i.e. the order in which each fermionic chain is written down, and adjust the Feynman rules [450–452]. For example, when reversing the "fermion flow" from Fig. A.6a to A.6b, we instead work with the antifield $l_a^c = C\,\overline{l}_a^T$ and alter the Feynman rules accordingly. In Figs. A.1, A.2b and A.4 to A.8, the red arrow indicates the orientation of the "fermion flow", i.e., of lepton number. The blue arrows denote propagation of the four-momentum.

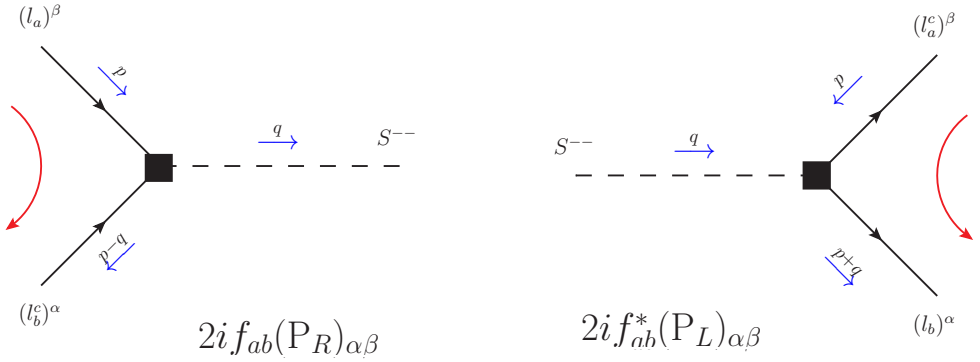

(a) Outgoing S^{--} (b) Incoming S^{--}

Figure A.1: Two-lepton and S^{--} interactions with $f_{ab}^{(*)} = f_{ba}^{(*)}$.

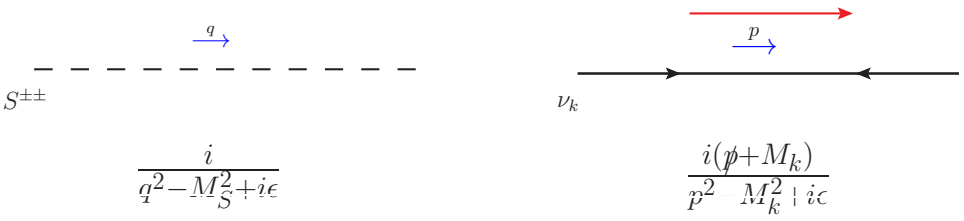

(a) Doubly charged scalar (b) Majorana neutrino

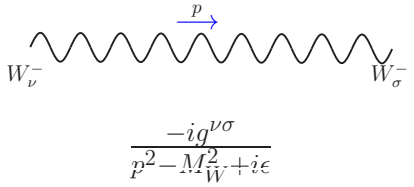

(c) W-boson

Figure A.2: Propagators

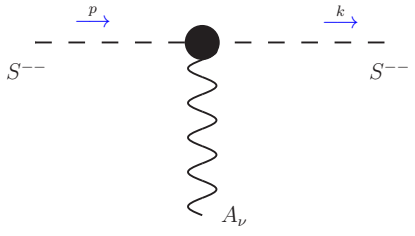

$$-2ie(p+k)^\nu$$

(a) 3-point vertex: two doubly charged scalars and photon

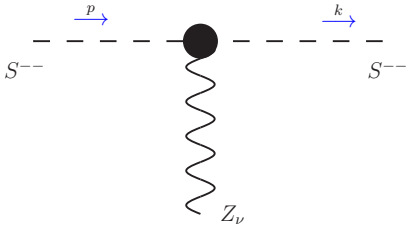

$$2ig' \sin\theta_W (p+k)^\nu$$

(b) 3-point vertex: two doubly charged scalars and Z-boson

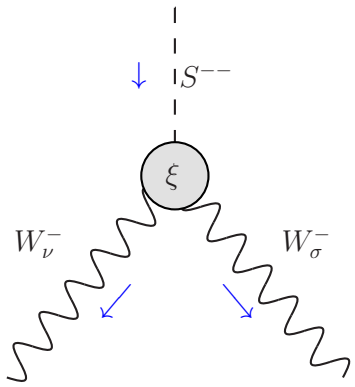

$$-\frac{ig^2v^4\xi}{2\Lambda^3}\, g^{\nu\sigma}$$

(c) Effective vertex coupling S^{--} to two gauge bosons

Figure A.3: S^{--} and its interaction with gauge bosons.

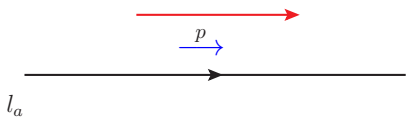

$$\frac{i(\not{p}+m_a)}{p^2-m_a^2+i\epsilon}$$

(a) Usual orientation of 'fermion flow' for a propagating particle

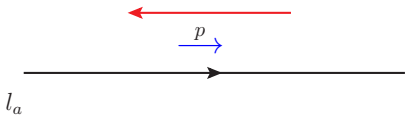

$$\frac{i(-\not{p}+m_a)}{p^2-m_a^2+i\epsilon}$$

(b) Reversed 'fermion flow' for a particle

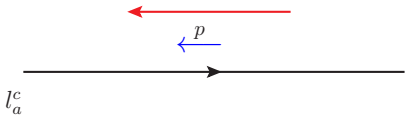

$$\frac{i(\not{p}+m_a)}{p^2-m_a^2+i\epsilon}$$

(c) Reversed 'fermion flow' for an antiparticle

Figure A.4: (Anti-) leptonic propagator and its alteration with the 'fermion flow'.

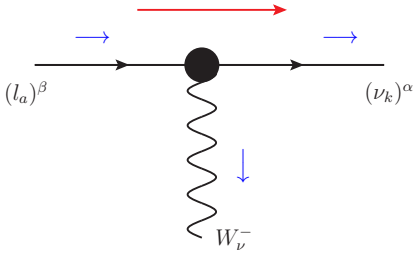

$$\frac{ig}{\sqrt{2}}\,U_{ak}\,(\gamma^\nu \mathrm{P_L})_{\alpha\beta}$$

(a) Usual orientation of 'fermion flow'

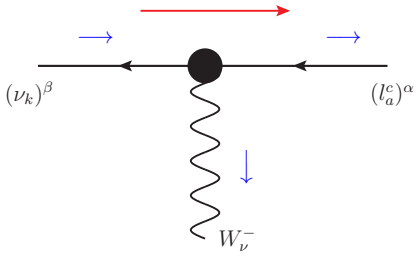

$$-\frac{ig}{\sqrt{2}}\,U_{ak}\,(\gamma^\nu \mathrm{P_R})_{\alpha\beta}$$

(b) Reversed 'fermion flow'

Figure A.5: Charged current interaction with a massive neutrino.

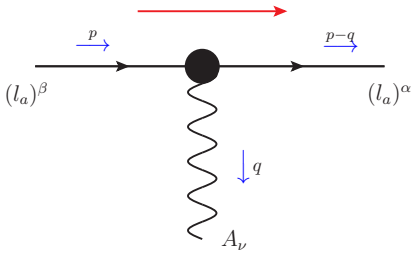

$$-ie(\gamma^\nu)_{\alpha\beta}$$

(a) Usual orientation of 'fermion flow'

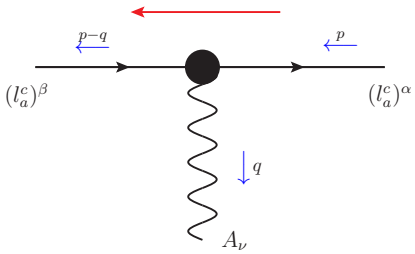

$$ie(\gamma^\nu)_{\beta\alpha}$$

(b) Reversed 'fermion flow'

Figure A.6: Electromagnetic vertex.

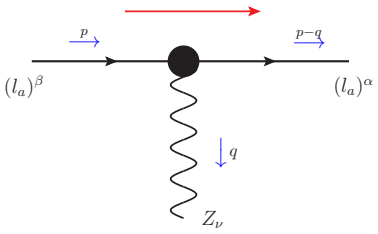

$$\frac{ig'}{4\cos\theta_W}\left(\gamma^\nu[-1+4\sin^2\theta_W+\gamma_5]\right)_{\alpha\beta}$$

(a) Usual orientation of 'fermion flow'

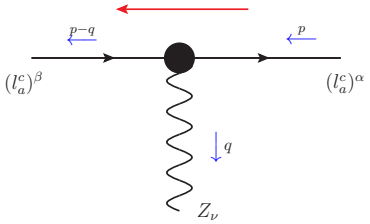

$$\frac{ig'}{4\cos\theta_W}\left(\gamma^\nu[1-4\sin^2\theta_W+\gamma_5]\right)_{\beta\alpha}$$

(b) Reversed 'fermion flow'

Figure A.7: Neutral current interactions – the Z-boson vertex.

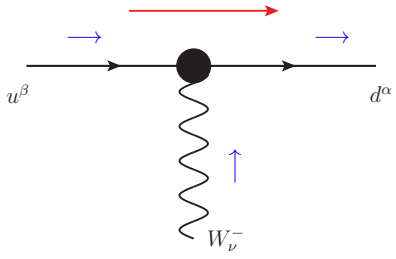

$$\frac{ig}{\sqrt{2}}V_{ud}\left(\gamma^\nu \mathrm{P_L}\right)_{\alpha\beta}$$

Figure A.8: Charged current interaction – Coupling the W-boson to two quarks.

Appendix B

The Scalar Three-point Function

The kinematical configuration corresponding to the scalar three-point function given in Eq. (5.2.22) of section 5.2.1 is displayed in Fig. B.1 below.

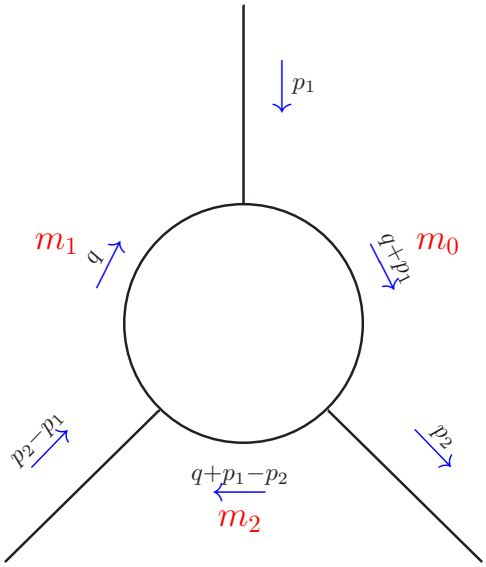

Figure B.1: Kinematic set-up corresponding to the scalar three-point function Eq. (5.2.22).

Appendix C

Differences between our notation and that from Ref. [6]

To compare our results for the amplitude and subsequently the decay rate for μ^+-e conversion in section 5.3 with those from Ref. [6], further remarks are in order:

1. First, note that the normalisation of free spinors in Ref. [6] differs from the one used in the derivation above. The normalisation of spinors as used in Ref. [6] is stated in their Appendix A, and it corresponds to the following spin sums:

$$\sum_r |u^r(p)\overline{u^r}(p)|^2 = \not{p} + m\mathbb{1} \qquad \text{and} \qquad \sum_r |v^r(p)\overline{v^r}(p)|^2 = \not{p} - m\mathbb{1}\,. \tag{C.0.1}$$

   We, on the other hand, use a normalisation that leads to:

$$\sum_r |u^r(p)\overline{u^r}(p)|^2 = \frac{1}{4E}(\not{p}+m\mathbb{1}) \quad \text{and} \quad \sum_r |v^r(p)\overline{v^r}(p)|^2 = \frac{1}{4E}(\not{p}-m\mathbb{1})\,. \tag{C.0.2}$$

   Although the resulting decay rate will not differ, we must translate $u_\mu \to 1/\sqrt{2E_\mu}\, u_\mu$ and $\overline{v}_e \to 1/\sqrt{2E_e}\,\overline{v}_e$ in order to compare on the matrix-element level. Note that the spinor expression in Eq. (A3) of Ref. [6] uses the non-relativistic limit in the Dirac representation.

2. Second, it is important to take into account that one will encounter an additional factor of of $1/(2\pi)^{3/2}$ in the matrix element of Ref. [6], which arises from preponing the phase space integral factor of $1/(2\pi)^3$ to the matrix element, which we do not.

3. Third, Ref. [6] only introduces the relativistic Coulomb factor $F(Z-2, E_e)$ that accounts for the positron propagating under the influence of the nuclear field when stating the decay rate. We, however, already introduce it when deriving the amplitude.

4. Fourth, we have to recall that Ref. [6] realises $\mu^- - e^+$ conversion by means of a heavy Majorana neutrino mediator, whereas we depend on a doubly charged scalar. Thus, we need to perform some sort of matching in order to replace the model-dependent doubly charged scalar contribution by the respective heavy Majorana part, as discussed in detail in section 5.3.3. From there, we obtain the relation:

$$\frac{2\, f_{e\mu}\, V_{ud}^2\, v^4\, \xi}{\Lambda^3\, M_S^2} \quad \Longleftrightarrow \quad \frac{\epsilon_3^{\mathrm{LL}x}}{2m_p} \quad \Longleftrightarrow \quad \langle M_N^{-1} \rangle_{\mu e}\,, \tag{C.0.3}$$

with $x = \mathrm{L}, \mathrm{R}$ and $\langle M_N^{-1} \rangle_{\mu e} = \sum_{k=4,5,\ldots} U_{ek} U_{\mu k} / M_k^2$, where U_{ak} denotes the admixture of the heavy neutrino mass eigenstate N_k to the active flavour a.

5. Last but not least, the chiralities of the external charged leptons have to be considered. While in our scenario both muon and positron are right-handed, the charged leptons are left-handed when coupling to the heavy Majorana neutrinos. Furthermore, note that Ref. [6] uses another convention for the γ-matrices which is based on employing the Pauli metric [106][1] instead of the Minkowski metric. This results into the left-/right-handed projectors having a reversed sign in front of γ_5 with reference to their definition in the basis we use, namely $g^{\nu\rho} = \{+,-,-,-\}$. Since the spin sums lead to the same factor independent of the charged leptons being left- or right-handed, we can consistently replace

$$\begin{aligned} &\overline{v}_e(k_e)\, \mathrm{P_R}\, u_\mu(k_\mu) \xrightarrow{S^{++} \to N_k} \overline{v}_e(k_e)\, \mathrm{P_L}\, u_\mu(k_\mu) \\ &\xrightarrow{\text{adapt notation}} \frac{1}{\sqrt{4E_e E_\mu}}\, \frac{1}{2}\, \overline{v}_e(k_e)\, (1+\gamma_5)\, u_\mu(k_\mu)\,, \end{aligned} \tag{C.0.4}$$

for the sake of comparing our computation to the amplitude in Ref. [6].[2]

Combining the above comments, our matrix element from Eq. (5.3.26) translates into

$$\begin{aligned} \mathcal{M} = &\left(\frac{G_F}{\sqrt{2}}\right)^2 \langle M_N^{-1} \rangle_{\mu e}\, \frac{g_A^2 m_p m_e}{R}\, \delta(E_f - E_i + E_e - E_\mu)\, \mathcal{M}^{(\mu^-, e^+)\,\phi} \\ &\frac{1}{(2\pi)^{3/2}}\, \frac{1}{\sqrt{4E_e E_\mu}}\, \overline{v}_e(k_e)\, (1+\gamma_5)\, u_\mu(k_\mu)\,, \end{aligned} \tag{C.0.5}$$

which agrees with Eq. (32) of Ref. [6].

[1] It is useful to check footnote 3 on page 676.

[2] Here, in the very last step, we switched to [6]'s normalisation of free spinors and to the Pauli metric notation.

Appendix **D**

Understanding Eq. (49) from Ref. [6]

In section 5.3, we employ the nuclear matrix element in the form of Eq. (5.3.36), which coincides with Eq. (49) of Ref. [6], when inserting values for a specific isotope. To understand the notation in Eq. (5.3.36), we use this appendix to demonstrate in detail how to rewrite the exponential functions starting from Eq. (5.3.27):

$$\int \mathrm{d}k\, k^2\, \mathrm{d}\Omega_k\, \langle N'|\, \mathrm{e}^{i\vec{k}\cdot(\vec{r}_m-\vec{r}_l)} \mathrm{e}^{-i\vec{k}_e\cdot\vec{r}_l}\, |N\rangle\,, \tag{D.0.1}$$

with $k = |\vec{k}|$. Since we only take care of the angular integration in the following, we dropped some $\vec{k}^2$-dependent parts of Eq. (5.3.27). Introducing new coordinates,

$$\vec{r}_{lm} = \vec{r}_l - \vec{r}_m \quad \text{with} \quad r_{lm} = |\vec{r}_{lm}|, \quad \text{and} \quad \vec{R}_{lm} = \frac{\vec{r}_l + \vec{r}_m}{2} \quad \text{with } R_{lm} = |\vec{R}_{lm}|\,, \tag{D.0.2}$$

we perform the angular integration,

$$\int \mathrm{d}\Omega_k\, \mathrm{e}^{i\vec{k}\cdot(\vec{r}_m-\vec{r}_l)} = 4\pi j_0(kr_{lm})\,, \tag{D.0.3}$$

and replace the remaining exponential function by its plane wave decomposition:

$$\mathrm{e}^{-i\vec{k}\cdot\vec{x}} = (\mathrm{e}^{i\vec{k}\cdot\vec{x}})^* = 4\pi \sum_{\lambda=0}^{\infty} (-i)^\lambda j_\lambda(kx) \sum_{m_\lambda=-\lambda}^{\lambda} Y_\lambda^{m_\lambda}(\vartheta_k, \varphi_k)\, Y_\lambda^{m_\lambda\,*}(\vartheta_x, \varphi_x)\,, \tag{D.0.4}$$

where $k = |\vec{k}\,|$ and $x = |\vec{x}\,|$. Here, $\vartheta_{k,x}$ and $\varphi_{k,x}$ are the azimuthal and polar angles which fix the directions of $\vec{k}$ and $\vec{x}$, respectively. Furthermore, j_λ denotes the spherical Bessel function and $Y_\lambda^{m_\lambda}$ the spherical harmonic. Thus,

Eq. (D.0.1) takes the form

$$(4\pi)^3 \int \mathrm{d}k\, k^2 \,\langle N'|\, j_0(kr_{lm}) \sum_{\lambda,\lambda'} (-i)^{\lambda+\lambda'} j_\lambda(k_e R_{lm}) j_{\lambda'}(k_e r_{lm}/2) \sum_{m_\lambda, m_{\lambda'}} Y_\lambda^{m_\lambda}(\vartheta_{k_e}, \varphi_{k_e})\, Y_\lambda^{m_\lambda *}(\vartheta_{R_{lm}}, \varphi_{R_{lm}})\, Y_{\lambda'}^{m_{\lambda'}}(\vartheta_{k_e}, \varphi_{k_e})\, Y_{\lambda'}^{m_{\lambda'} *}(\vartheta_{r_{lm}}, \varphi_{r_{lm}})\, |N\rangle\,. \tag{D.0.5}$$

Next, we employ the well-known addition theorem for Legendre polynomials,

$$P_\lambda(\cos\vartheta_{nn'}) = \frac{4\pi}{2\lambda+1} \sum_{m_\lambda=-\lambda}^{\lambda} Y_\lambda^{m_\lambda}(\vartheta_n, \varphi_n)\, Y_\lambda^{m_\lambda *}(\vartheta_{n'}, \varphi_{n'})\,, \tag{D.0.6}$$

where $\cos\vartheta_{nn'} = \vec{n}\cdot\vec{n}' = \cos\vartheta_n \cos\vartheta_{n'} + \sin\vartheta_n \sin\vartheta_{n'} \cos(\varphi_n - \varphi_{n'})$. Note that $\vec{n}$ and $\vec{n}'$ are unit vectors. The resulting Legendre polynomials P_λ can themselves be phrased in terms of spherical harmonics

$$P_\lambda(\cos\vartheta_{nn'}) = \sqrt{\frac{4\pi}{2\lambda+1}}\, Y_\lambda^0(\vartheta_{nn'}, \varphi_{nn'})\,, \tag{D.0.7}$$

and we hence obtain:

$$(4\pi)^2 \int \mathrm{d}k\, k^2 \,\langle N'|\, j_0(kr_{lm}) \sum_{\lambda,\lambda'} (-i)^{\lambda+\lambda'} \sqrt{(2\lambda+1)(2\lambda'+1)}\, j_\lambda(k_e R_{lm}) \, j_{\lambda'}(k_e r_{lm}/2) Y_\lambda^0(\Omega_{k_e R_{lm}})\, Y_\lambda^0(\Omega_{k_e r_{lm}})\, |N\rangle\,, \tag{D.0.8}$$

with $\Omega_{k_e R_{lm}} \equiv (\vartheta_{k_e R_{lm}}, \varphi_{k_e R_{lm}})$ and $\Omega_{k_e r_{lm}} \equiv (\vartheta_{k_e r_{lm}}, \varphi_{k_e r_{lm}})$.

We can further rephrase the spherical harmonics by using the inverse Clebsch-Gordan relation, see Eq. (4-b) in complement C_X of Ref. [453]:

$$Y_\lambda^m(\Omega_1)\, Y_{\lambda'}^{m'}(\Omega_2) = \sum_{LM} (\lambda m_1 \lambda' m_2 | LM) \underbrace{\Phi_{LM}(\Omega_1, \Omega_2)}_{\equiv \left\{ Y_\lambda(\Omega_1) \otimes Y_{\lambda'}(\Omega_2) \right\}_{LM}}\,, \tag{D.0.9}$$

where the connection to the irreducible tensors is established with help of Eq. (1) in Chapter 5.16 of Ref. [454].

One can connect the Clebsch-Gordan coefficients to the *3j* symbols by means of

$$(\lambda_1 m_1 \lambda_2 m_2 | LM) = (-1)^{\lambda_2 - \lambda_1 - M} \sqrt{2L+1} \begin{pmatrix} \lambda_1 & \lambda_2 & L \\ m_1 & m_2 & M \end{pmatrix}, \tag{D.0.10}$$

as stated in Eq. (1.44) of Ref. [455].

In the case of a $g.s. \to g.s.$ transition, which means that both the initial and final nucleus are in the ground state ($g.s.$), the operator has to be a scalar, which enforces $L = 0$ (see also Ref. [454], Chapter 3.2.1). Furthermore, the *3j* symbols satisfy the following properties:

$$\begin{aligned} m_1 + m_2 =& M \,, \\ \begin{pmatrix} \lambda_1 & \lambda_2 & 0 \\ m_1 & m_2 & 0 \end{pmatrix} =& (-1)^{\lambda_1 - m_1} \frac{1}{\sqrt{2\lambda_1 + 1}} \, \delta_{\lambda_1 \lambda_2} \, \delta_{m_1, -m_2} \,, \end{aligned} \tag{D.0.11}$$

which can be found in Ref. [455] under Eqs. (1.41) and (1.42). Since we have $m_\lambda = m_{\lambda'} = 0$, the quantum numbers of the coupled system are fixed to $L = M = 0$. That way, the initial expression in Eq. (D.0.1) can be rearranged to

$$\begin{aligned} (4\pi)^2 \int \mathrm{d}k \, k^2 \, \langle N' | \, j_0(kr_{lm}) \sum_\lambda \sqrt{2\lambda + 1} \, j_\lambda(k_e R_{lm}) j_\lambda(k_e r_{lm}/2) \\ \Big\{ Y_\lambda(\Omega_{k_e r_{lm}}) \otimes Y_\lambda(\Omega_{k_e R_{lm}}) \Big\}_{00} | N \rangle, \end{aligned} \tag{D.0.12}$$

valid for the case of a $g.s. \to g.s.$ nuclear transition.

This can be simplified further when taking into account that according to Ref. [456]'s Eq. (4),

$$\begin{aligned} P_\lambda(\vec{n} \cdot \vec{n}') &= (-1)^\lambda \, 4\pi \Big\{ Y_\lambda(\vec{n}) \otimes Y_\lambda(\vec{n'}) \Big\}_{00} \\ &= (-1)^\lambda \, 4\pi \Big\{ Y_\lambda(\vartheta_n, \varphi_n) \otimes Y_\lambda(\vartheta_{n'}, \varphi_{n'}) \Big\}_{00} \,. \end{aligned} \tag{D.0.13}$$

Applying this relation to $\{\cdots\}_{00}$ in Eq. (D.0.12), it becomes obvious that this expression does indeed not depend on $\vec{k}_e$ anymore. We can, consequently, discard the dependence on the positron's momentum and state the final form of the angular part for $g.s. \to g.s.$ transitions:

$$\begin{aligned} & \int \mathrm{d}k \, k^2 \, \mathrm{d}\Omega_k \, \langle N' | \, \mathrm{e}^{i\vec{k} \cdot (\vec{r}_m - \vec{r}_l)} \mathrm{e}^{-i\vec{k}_e \cdot \vec{r}_l} \, | N \rangle \\ \xrightarrow{g.s. \to g.s.} & (4\pi)^2 \int \mathrm{d}k \, k^2 \, \langle N' | \, j_0(kr_{lm}) \sum_\lambda \sqrt{2\lambda + 1} \, j_\lambda(k_e R_{lm}) j_\lambda(k_e r_{lm}/2) \\ & \Big\{ Y_\lambda(\Omega_{r_{lm}}) \otimes Y_\lambda(\Omega_{R_{lm}}) \Big\}_{00} | N \rangle \,, \end{aligned} \tag{D.0.14}$$

where $\Omega_{R_{lm}}$ and $\Omega_{r_{lm}}$ fix the directions of $\vec{R}_{lm}$ and $\vec{r}_{lm}$ independently of $\vec{k}_e$.

Appendix E

Littlest Seesaw within the framework of the MSSM: Yukawa Couplings for $M_{\rm SUSY} = 1,\, 3,\, 10$ TeV

Throughout chapter 6, we have used the *Mathematica* package `REAP` [331] to solve the RGEs numerically. It is important to employ the appropriate parameters at the grand unified theory (GUT) scale, so that experimental values at low energies (e.g. the scale M_Z of the Z-boson) are reproduced correctly. To simplify matters, we stick to the common approximation that assumes only one single supersymmetric (SUSY) threshold, namely $M_{\rm SUSY}$, at which all supersymmetric particles are integrated out. To extract the proper GUT scale values for the charged-lepton and the quark Yukawa matrices, we make use of the results derived in Ref. [457].[1] In the following, we will present how to calculate these values along the lines of Ref. [457].
The first step is to derive the Yukawa couplings at M_Z from the experimental data. The latter are handed over to `REAP`, which calculates their renormalisation group (RG) running to $M_{\rm SUSY}$. At the SUSY breaking scale, the Standard Model (SM) has to be matched to the Minimal Supersymmetric Standard Model (MSSM). As the radiative corrections can be $\tan\beta$-enhanced, and therefore even exceed the one-loop running contributions, we must include them at the matching scale. This leads to a correction to the down-type quark as well as the charged-lepton Yukawa matrix, which can be simplified to [458]:

$$\begin{aligned} Y_u^{\rm SM} &\simeq \sin\beta\, Y_u^{\rm MSSM}\,, \\ Y_d^{\rm SM} &\simeq \Big(\mathbb{1} + {\rm diag}\Big(\eta_q,\, \eta_q,\, \eta_q' + \eta_A\Big)\Big)\, Y_d^{\rm MSSM}\, \cos\beta\,, \\ Y_l^{\rm SM} &\simeq \Big(\mathbb{1} + {\rm diag}\Big(\eta_\ell,\, \eta_\ell,\, \eta_\ell'\Big)\Big)\, Y_l^{\rm MSSM}\, \cos\beta\,. \end{aligned} \tag{E.0.1}$$

[1] For more information, on the framework used, the explicit low energy input values and more, please consult the reference mentioned. Note that Ref. [457] also assumes the neutrino masses to be generated via the Seesaw mechanism at high energies.

Here, one chooses a basis where the up-type Yukawa matrix is diagonal. Note that only contributions enhanced by $\tan\beta$ are included, which is accurate up to the per cent level. Furthermore, the threshold corrections to the first two generations of down-type quarks and charged leptons are assumed to be of the same size, respectively. This is a good approximation in many SUSY scenarios, provided that the down and strange squark as well as the selectron and smuon are of nearly the same mass. The corrections in Eq. (E.0.1) depend on the specific SUSY scenario under consideration, and they need to be computed accordingly. The parameters η_q and η_q' originate predominantly from gluino contributions in combination with some Wino and Bino loop corrections, whereas η_ℓ and η_ℓ' are caused by electroweak gauginos. The correction from η_A is related to the trilinear soft SUSY breaking term A_u [458]. Note that all parameters η contain the factor $\tan\beta$.
The six parameters used in Eq. (E.0.1) can be combined into four, namely

$$\begin{aligned} &\overline{\eta}_b \equiv \eta_q' + \eta_A - \eta_\ell' \,, \quad \overline{\eta}_q \equiv \eta_q - \eta_\ell' \,, \\ &\overline{\eta}_\ell \equiv \eta_\ell - \eta_\ell' \,, \quad \text{and} \quad \cos\overline{\beta} \equiv (1+\eta_\ell')\cos\beta \,. \end{aligned} \tag{E.0.2}$$

Starting from the basis where the SM Yukawa matrices Y_u and Y_l are diagonal at $M_{\rm SUSY}$, the expressions for the MSSM Yukawa matrices at the SUSY breaking scale are given by [457]:

$$\begin{aligned} Y_u^{\rm MSSM} &\simeq \frac{1}{\sin\overline{\beta}}\, Y_u^{\rm SM} \,, \\ Y_d^{\rm MSSM} &\simeq \text{diag}\left(\frac{1}{1+\overline{\eta}_q}, \frac{1}{1+\overline{\eta}_q}, \frac{1}{1+\overline{\eta}_b}\right) Y_d^{\rm SM}\, \frac{1}{\cos\overline{\beta}} \,, \\ Y_l^{\rm MSSM} &\simeq \text{diag}\left(\frac{1}{1+\overline{\eta}_\ell}, \frac{1}{1+\overline{\eta}_\ell}, 1\right) Y_l^{\rm SM}\, \frac{1}{\cos\overline{\beta}} \,, \end{aligned} \tag{E.0.3}$$

with the CKM parameters fully included in the down-type quark matching condition. As the parameters $\overline{\eta}_\ell$ and $\overline{\eta}_q$ only affect the first two generations of Y_d and Y_l, which are small in comparison, their effect on the RG running can be neglected to good approximation. In other words, there are four parameters needed for the matching procedure at the SUSY breaking scale, but only two out of these, namely $\overline{\eta}_b$ and $\tan\overline{\beta}$, in order to perform the RG evolution to the GUT scale.
The authors of Ref. [457] derived the GUT scale MSSM quantities for three different SUSY breaking scales, namely $M_{\rm SUSY} = 1$, 3, 10 TeV, and provided them in form of data tables at `http:/particlesandcosmology.unibas.ch/RunningParameters.tar.gz`. From these tables, one can extract the GUT scale values depending on the choice of the parameters $\overline{\eta}_\ell$, $\overline{\eta}_q$, $\overline{\eta}_b$, and $\tan\overline{\beta}$. The proper translation between the data made available and the Yukawa couplings as well as CKM parameters we employ as input at the GUT scale is

given in the captions of Figs. 1 to 3 and 5 of Ref. [457]. In order to further reduce the number of possible MSSM settings, we assume that the leptonic corrections η_ℓ and η'_ℓ can be neglected. As a consequence, $\overline{\eta}_\ell = 0$. For $\tan\beta \geq 5$, this yields $\tan\overline{\beta} = (1+\eta'_\ell)^{-1}\tan\beta \xrightarrow{\eta'_\ell=0} \tan\beta$. By these approximations only, we can extract the charged-lepton Yukawa couplings, the up-type Yukawa couplings, as well as the coupling of the bottom quark. In order to also extract the strange and down Yukawa couplings, we further need to specify $\overline{\eta}_q$. Since the RG running of the neutrino parameters, which is the ultimate goal of chapter 6, depends mostly on the bottom quark's coupling, and not on the down and strange quark, we can neglect $\overline{\eta}_q$. We could have used a similar argument when setting $\overline{\eta}_\ell$ to zero as we mostly care for the effect of the τ-lepton on the RG running of the neutrino parameters. As a consequence of these simplifications, we are left with the parameter $\overline{\eta}_b$ comprising the threshold effects and $\tan\beta$ when fixing the MSSM setting. Note that, in addition, the CKM mixing angle θ_{12} and the CP violating phase δ are barely affected by threshold effects and RG running. Consequently, we use their `REAP` default values. The CKM mixing angles θ_{13} and θ_{23}, on the other hand, do depend on $\overline{\eta}_q$ and $\overline{\eta}_b$. With the simplifications discussed above, we also extract their GUT scale values from the data tables in `http://particlesandcosmology.unibas.ch/RunningParameters.tar.gz`. Based on the data provided by the authors of Ref. [457], we investigate MSSM scenarios with the SUSY breaking scales $M_{\text{SUSY}} = 1, 3, 10$ TeV. Furthermore, we choose $\tan\beta = 5, 30, 50$ and threshold effects within the range of $\overline{\eta}_b = -0.6 \to 0.6$. For the latter, the range needs to be adapted depending on $\tan\beta$ to avoid non-perturbative Yukawa couplings. The MSSM settings investigated throughout this work are supposed to be benchmark settings that give an overview on the Littlest Seesaw's RG behaviour within the framework of the MSSM. The corresponding initial values extracted as discussed above and handed over to `REAP` are given in Tab. E.1. In case one has a more specific MSSM scenario in mind and aims at a more precise analysis of its SUSY threshold corrections, there is a software extension to `REAP` called `SusyTc` that generates the appropriate input values from the SUSY breaking terms [459].

$\overline{\eta}_b$	y_e	y_μ	y_τ	y_u	y_c	y_t	y_d	y_s	y_b	θ_{13}	θ_{23}
−0.6	0.0000100945	0.00213102	0.0362684	5.9693×10^{-7}	0.000291996	0.109253	0.0000246664	0.000488532	0.061666	0.00134837	0.0155845
0.	0.0000100285	0.00211708	0.0360309	5.96264×10^{-7}	0.000291671	0.108783	0.000024504	0.00048503	0.024504	0.00337798	0.0390515
0.6	0.000010021	0.00211549	0.0360038	5.96188×10^{-7}	0.000291634	0.10873	0.0000244842	0.00048411	0.0153027	0.00540236	0.0624798

$\overline{\eta}_b$	y_e	y_μ	y_τ	y_u	y_c	y_t	y_d	y_s	y_b	θ_{13}	θ_{23}
−0.6	0.000363675	0.0767986	1.44563	1.06152×10^{-7}	0.0000519282	0.0251939	0.000890915	0.0176456	2.22729	0.00109461	0.012652
0.	0.0000626992	0.0132381	0.235238	9.62619×10^{-8}	0.0000470892	0.017601	0.000153216	0.00303277	0.153216	0.00334198	0.0386363
0.6	0.0000608388	0.0128453	0.227908	9.5837×10^{-8}	0.0000468813	0.0172832	0.000148651	0.00293916	0.0929071	0.00540237	0.0624817

$\overline{\eta}_b$	y_e	y_μ	y_τ	y_u	y_c	y_t	y_d	y_s	y_b	θ_{13}	θ_{23}
0.	0.000122406	0.0258531	0.516257	5.86883×10^{-8}	0.0000287111	0.0113246	0.000299218	0.00592294	0.299218	0.00319911	0.0369864
0.6	0.000108487	0.0229118	0.447801	5.77686×10^{-8}	0.0000282607	0.0105862	0.000265107	0.00524188	0.165692	0.00533248	0.0616758

(a) $M_{\rm SUSY} = 1$ TeV

$\overline{\eta}_b$	y_e	y_μ	y_τ	y_u	y_c	y_t	y_d	y_s	y_b	θ_{13}	θ_{23}
−0.6	0.0000103435	0.00218359	0.0371626	5.99052×10^{-7}	0.000293035	0.107502	0.0000254592	0.000504232	0.063648	0.00137174	0.0158548
0.	0.000010282	0.00217059	0.0369411	5.98534×10^{-7}	0.000292781	0.107112	0.0000253066	0.000500904	0.0253066	0.00343558	0.0397178
0.6	0.0000102749	0.0021691	0.0369158	5.98474×10^{-7}	0.000292752	0.107068	0.0000252878	0.000499968	0.0158049	0.00549417	0.0635431

$\overline{\eta}_b$	y_e	y_μ	y_τ	y_u	y_c	y_t	y_d	y_s	y_b	θ_{13}	θ_{23}
−0.6	0.000134065	0.0283091	0.520298	1.03051×10^{-7}	0.0000504118	0.0247611	0.000330378	0.00654343	0.825945	0.00105734	0.0122213
0.	0.0000639861	0.0135098	0.239886	9.67631×10^{-8}	0.0000473343	0.0173541	0.000157499	0.00311748	0.157499	0.00340223	0.039333
0.6	0.0000622737	0.0131482	0.233154	9.64312×10^{-8}	0.0000471719	0.0170895	0.000153267	0.00303023	0.0957918	0.00549279	0.0635287

$\overline{\eta}_b$	y_e	y_μ	y_τ	y_u	y_c	y_t	y_d	y_s	y_b	θ_{13}	θ_{23}
0.	0.000122775	0.0259306	0.514492	5.87559×10^{-8}	0.0000287439	0.0110242	0.000302287	0.00598353	0.302287	0.00327695	0.0378864
0.6	0.000110569	0.0233515	0.455112	5.80616×10^{-8}	0.0000284039	0.0104332	0.00027216	0.00538102	0.1701	0.00542971	0.0628015

(b) $M_{\rm SUSY} = 3$ TeV

$\overline{\eta}_b$	y_e	y_μ	y_τ	y_u	y_c	y_t	y_d	y_s	y_b	θ_{13}	θ_{23}
−0.6	0.000010599	0.00223751	0.0380796	6.01223×10^{-7}	0.000294096	0.105954	0.0000262324	0.000519544	0.0655811	0.00139466	0.0161197
0.	0.0000105418	0.00222545	0.0378741	6.00821×10^{-7}	0.0002939	0.10563	0.00002609	0.000516398	0.02609	0.00349209	0.0403714
0.6	0.0000105353	0.00222407	0.0378506	6.00775×10^{-7}	0.000293877	0.105592	0.0000260723	0.000515446	0.0162952	0.00558424	0.0645862

$\overline{\eta}_b$	y_e	y_μ	y_τ	y_u	y_c	y_t	y_d	y_s	y_b	θ_{13}	θ_{23}
−0.6	0.000105604	0.0222983	0.404608	1.01321×10^{-7}	0.000049565	0.0216181	0.000261585	0.00518089	0.653963	0.00117363	0.0135653
0.	0.0000653096	0.0137892	0.244604	9.72569×10^{-8}	0.0000475757	0.0171343	0.000161646	0.00319947	0.161646	0.00346139	0.0400172
0.6	0.0000637412	0.013458	0.238454	9.69993×10^{-8}	0.0000474497	0.0169137	0.000157748	0.00311863	0.0985922	0.00558185	0.0645601

$\overline{\eta}_b$	y_e	y_μ	y_τ	y_u	y_c	y_t	y_d	y_s	y_b	θ_{13}	θ_{23}
0.	0.000123385	0.0260589	0.513551	5.88748×10^{-8}	0.0000288018	0.0107731	0.000305452	0.006046	0.305452	0.00335166	0.0387502
0.6	0.000112691	0.0237993	0.462154	5.83517×10^{-8}	0.0000285456	0.0102972	0.000278914	0.0055142	0.174321	0.00552516	0.0639066

(c) $M_{\rm SUSY} = 10$ TeV

Table E.1: Yukawa couplings and CKM mixing angles at the GUT scale depending on $\tan\beta$: (*top*) $\tan\beta = 5$, (*middle*) $\tan\beta = 30$, (*bottom*) $\tan\beta = 50$, respectively, and the threshold effects represented by $\overline{\eta}_b$.

Appendix F

Littlest Seesaw within the framework of the MSSM: Results

In section 6.3 of chapter 6, we have investigated the Littlest Seesaw (LS) model within the framework of the Minimal Supersymmetric Standard Model (MSSM). To that end, we have examined different supersymmetric (SUSY) breaking scales, $M_{\rm SUSY} = 1$, 3, 10 TeV. In addition, we have explored how $\tan\beta$ and the threshold effects, comprised in the parameter $\overline{\eta}_b$ and detailed in Appendix E, affect the goodness-of-fit for the different breaking scales $M_{\rm SUSY}$. For that, we chose $\tan\beta = 5$, 30, 50 and $\overline{\eta}_b = -0.6$, 0, 0.6. The overall results are collected in Tabs. 6.6 and 6.7 of section 6.3, where we also display more details on the best possible MSSM scenario with $M_{\rm SUSY} = 1$ TeV, $\tan\beta = 5$ and $\overline{\eta}_b = 0.6$ (see Figs. 6.5 to 6.8). In turn, this Appendix is dedicated to the remaining MSSM scenarios, and it details their predictions for neutrino masses and PMNS parameters.

Case A, $M_{\rm SUSY}$= 1 TeV, tanβ=30, $\bar{\eta}_b$=0.6

	$\Lambda_{\rm GUT}$	$M_{\rm sol}$	$M_{\rm atm}$	$\Lambda_{\rm EW}$
θ_{13}(deg)	8.29178	8.30287	8.32587	8.41528
θ_{12}(deg)	34.3991	34.4905	34.524	34.6537
θ_{23}(deg)	45.4167	45.3595	45.4453	45.7833
m_2(meV)	4.8607	5.0477	5.8102	8.4537
m_3(meV)	29.247	30.1066	34.6228	50.2399
$\delta_{\rm CP}$(deg)	−88.109	−88.2439	−88.2379	−88.2076
$\sigma_{\rm CP}$(deg)	−142.97	−142.751	−142.748	−142.752

Case A, $M_{\rm SUSY}$= 1 TeV, tanβ=50, $\bar{\eta}_b$=0.6

	$\Lambda_{\rm GUT}$	$M_{\rm sol}$	$M_{\rm atm}$	$\Lambda_{\rm EW}$
θ_{13}(deg)	8.02206	8.05602	8.13662	8.41183
θ_{12}(deg)	34.4555	34.5822	34.7035	35.1262
θ_{23}(deg)	45.1787	45.2155	45.5245	46.5801
m_2(meV)	4.86827	5.04562	5.77991	8.28033
m_3(meV)	30.1434	30.946	35.3479	50.2393
$\delta_{\rm CP}$(deg)	−89.1577	−89.2799	−89.2526	−89.1719
$\sigma_{\rm CP}$(deg)	−142.191	−141.98	−141.98	−141.986

Case A, $M_{\rm SUSY}$= 3 TeV, tanβ=5, $\bar{\eta}_b$=0.6

	$\Lambda_{\rm GUT}$	$M_{\rm sol}$	$M_{\rm atm}$	$\Lambda_{\rm EW}$
θ_{13}(deg)	8.41099	8.41413	8.4152	8.4176
θ_{12}(deg)	34.3736	34.4602	34.4623	34.4657
θ_{23}(deg)	45.5268	45.4279	45.4304	45.4394
m_2(meV)	5.13273	5.31343	6.10123	8.53395
m_3(meV)	30.5107	31.2908	35.9212	50.2401
$\delta_{\rm CP}$(deg)	−87.648	−87.8002	−87.8026	−87.8018
$\sigma_{\rm CP}$(deg)	−143.314	−143.07	−143.065	−143.065

Case A, $M_{\rm SUSY}$= 3 TeV, tanβ=30, $\bar{\eta}_b$=0.6

	$\Lambda_{\rm GUT}$	$M_{\rm sol}$	$M_{\rm atm}$	$\Lambda_{\rm EW}$
θ_{13}(deg)	8.29212	8.30364	8.32767	8.41512
θ_{12}(deg)	34.3991	34.4921	34.5271	34.654
θ_{23}(deg)	45.417	45.3601	45.4497	45.7803
m_2(meV)	4.93041	5.11803	5.8906	8.45511
m_3(meV)	29.6654	30.5211	35.0949	50.2412
$\delta_{\rm CP}$(deg)	−88.1077	−88.2443	−88.238	−88.2084
$\sigma_{\rm CP}$(deg)	−142.971	−142.748	−142.746	−142.75

Case A, $M_{\rm SUSY}$= 3 TeV, tanβ=50, $\bar{\eta}_b$=0.6

	$\Lambda_{\rm GUT}$	$M_{\rm sol}$	$M_{\rm atm}$	$\Lambda_{\rm EW}$
θ_{13}(deg)	8.02706	8.06211	8.14518	8.41153
θ_{12}(deg)	34.4545	34.5838	34.7088	35.1175
θ_{23}(deg)	45.183	45.2225	45.5409	46.562
m_2(meV)	4.93796	5.11551	5.8587	8.28495
m_3(meV)	30.5582	31.3528	35.802	50.2416
$\delta_{\rm CP}$(deg)	−89.1382	−89.2619	−89.2339	−89.1557
$\sigma_{\rm CP}$(deg)	−142.205	−141.992	−141.992	−141.998

Case A, $M_{\rm SUSY}$= 10 TeV, tanβ=5, $\bar{\eta}_b$=0.6

	$\Lambda_{\rm GUT}$	$M_{\rm sol}$	$M_{\rm atm}$	$\Lambda_{\rm EW}$
θ_{13}(deg)	8.41087	8.41406	8.41516	8.41749
θ_{12}(deg)	34.3736	34.4615	34.4637	34.4669
θ_{23}(deg)	45.5267	45.4265	45.429	45.4377
m_2(meV)	5.20752	5.38884	6.18845	8.53483
m_3(meV)	30.9556	31.7312	36.4302	50.2392
$\delta_{\rm CP}$(deg)	−87.6484	−87.8028	−87.8053	−87.8044
$\sigma_{\rm CP}$(deg)	−143.313	−143.066	−143.061	−143.062

Case A, $M_{\rm SUSY}$= 10 TeV, tanβ=30, $\bar{\eta}_b$=0.6

	$\Lambda_{\rm GUT}$	$M_{\rm sol}$	$M_{\rm atm}$	$\Lambda_{\rm EW}$
θ_{13}(deg)	8.29386	8.30583	8.33094	8.41561
θ_{12}(deg)	34.3987	34.4935	34.5301	34.6529
θ_{23}(deg)	45.4186	45.3619	45.4555	45.7755
m_2(meV)	5.00712	5.19537	5.97903	8.45709
m_3(meV)	30.1215	30.9724	35.6089	50.2392
$\delta_{\rm CP}$(deg)	−88.1009	−88.2395	−88.2329	−88.2042
$\sigma_{\rm CP}$(deg)	−142.976	−142.75	−142.747	−142.751

Case A, $M_{\rm SUSY}$= 10 TeV, tanβ=50, $\bar{\eta}_b$=0.6

	$\Lambda_{\rm GUT}$	$M_{\rm sol}$	$M_{\rm atm}$	$\Lambda_{\rm EW}$
θ_{13}(deg)	8.03506	8.07119	8.15671	8.41193
θ_{12}(deg)	34.4529	34.5849	34.7134	35.1045
θ_{23}(deg)	45.1898	45.2319	45.5594	46.5372
m_2(meV)	5.0146	5.19235	5.94544	8.29124
m_3(meV)	31.0055	31.791	36.2919	50.2405
$\delta_{\rm CP}$(deg)	−89.107	−89.2325	−89.2038	−89.1288
$\sigma_{\rm CP}$(deg)	−142.229	−142.011	−142.012	−142.017

Table F.1: Case A – MSSM with $M_{\rm atm} = 10^{12}$ GeV and $M_{\rm sol} = 10^{15}$ GeV.

Case B, $M_{\rm SUSY}$= 1 TeV, tanβ=30, $\bar{\eta}_b$=0.6

	$\Lambda_{\rm GUT}$	$M_{\rm sol}$	$M_{\rm atm}$	$\Lambda_{\rm EW}$
θ_{13}(deg)	8.52149	8.52425	8.5238	8.51986
θ_{12}(deg)	34.3495	34.4448	34.4835	34.6334
θ_{23}(deg)	44.3683	44.7994	44.8876	45.2102
m_2(meV)	4.97919	5.16771	5.94876	8.65838
m_3(meV)	29.2742	30.1062	34.6213	50.2354
$\delta_{\rm CP}$(deg)	−92.7779	−92.9131	−92.924	−92.9499
$\sigma_{\rm CP}$(deg)	−36.3678	−36.3229	−36.322	−36.3269

Case B, $M_{\rm SUSY}$= 1 TeV, tanβ=50, $\bar{\eta}_b$=0.6

	$\Lambda_{\rm GUT}$	$M_{\rm sol}$	$M_{\rm atm}$	$\Lambda_{\rm EW}$
θ_{13}(deg)	8.5531	8.55508	8.55187	8.53458
θ_{12}(deg)	34.3426	34.4812	34.6204	35.1064
θ_{23}(deg)	44.3378	44.8704	45.1752	46.1958
m_2(meV)	5.15347	5.33391	6.11139	8.76263
m_3(meV)	30.2051	30.9417	35.3429	50.2341
$\delta_{\rm CP}$(deg)	−92.8995	−93.0472	−93.0755	−93.138
$\sigma_{\rm CP}$(deg)	−36.2767	−36.2313	−36.2339	−36.2593

Case B, $M_{\rm SUSY}$= 3 TeV, tanβ=5, $\bar{\eta}_b$=0.6

	$\Lambda_{\rm GUT}$	$M_{\rm sol}$	$M_{\rm atm}$	$\Lambda_{\rm EW}$
θ_{13}(deg)	8.50992	8.51314	8.51358	8.51349
θ_{12}(deg)	34.352	34.4397	34.4419	34.4459
θ_{23}(deg)	44.3794	44.8111	44.821	44.8296
m_2(meV)	5.18562	5.36661	6.16227	8.61948
m_3(meV)	30.5226	31.2892	35.9189	50.2374
$\delta_{\rm CP}$(deg)	−92.7334	−92.8758	−92.8804	−92.8812
$\sigma_{\rm CP}$(deg)	−36.4011	−36.3524	−36.3504	−36.3505

Case B, $M_{\rm SUSY}$= 3 TeV, tanβ=30, $\bar{\eta}_b$=0.6

	$\Lambda_{\rm GUT}$	$M_{\rm sol}$	$M_{\rm atm}$	$\Lambda_{\rm EW}$
θ_{13}(deg)	8.52125	8.52403	8.52354	8.51967
θ_{12}(deg)	34.3496	34.4467	34.4871	34.6337
θ_{23}(deg)	44.3685	44.8065	44.8987	45.2141
m_2(meV)	5.05037	5.23945	6.0308	8.65935
m_3(meV)	29.6934	30.5208	35.0935	50.2372
$\delta_{\rm CP}$(deg)	−92.777	−92.9141	−92.9254	−92.9507
$\sigma_{\rm CP}$(deg)	−36.3684	−36.323	−36.3221	−36.3269

Case B, $M_{\rm SUSY}$= 3 TeV, tanβ=50, $\bar{\eta}_b$=0.6

	$\Lambda_{\rm GUT}$	$M_{\rm sol}$	$M_{\rm atm}$	$\Lambda_{\rm EW}$
θ_{13}(deg)	8.55192	8.55388	8.55053	8.5338
θ_{12}(deg)	34.3428	34.4843	34.6278	35.0978
θ_{23}(deg)	44.339	44.8807	45.1946	46.1815
m_2(meV)	5.22372	5.40417	6.19061	8.76152
m_3(meV)	30.6203	31.3481	35.7967	50.2364
$\delta_{\rm CP}$(deg)	−92.895	−93.0448	−93.0736	−93.134
$\sigma_{\rm CP}$(deg)	−36.2801	−36.2342	−36.2369	−36.2615

Case B, $M_{\rm SUSY}$= 10 TeV, tanβ=5, $\bar{\eta}_b$=0.6

	$\Lambda_{\rm GUT}$	$M_{\rm sol}$	$M_{\rm atm}$	$\Lambda_{\rm EW}$
θ_{13}(deg)	8.50991	8.51317	8.51361	8.51352
θ_{12}(deg)	34.352	34.4409	34.4433	34.4471
θ_{23}(deg)	44.3794	44.8171	44.8274	44.8357
m_2(meV)	5.26129	5.44286	6.25046	8.6205
m_3(meV)	30.968	31.7297	36.428	50.2366
$\delta_{\rm CP}$(deg)	−92.7334	−92.8778	−92.8825	−92.8832
$\sigma_{\rm CP}$(deg)	−36.4011	−36.3518	−36.3497	−36.3498

Case B, $M_{\rm SUSY}$= 10 TeV, tanβ=30, $\bar{\eta}_b$=0.6

	$\Lambda_{\rm GUT}$	$M_{\rm sol}$	$M_{\rm atm}$	$\Lambda_{\rm EW}$
θ_{13}(deg)	8.52163	8.52442	8.52389	8.52013
θ_{12}(deg)	34.3495	34.4485	34.4907	34.6326
θ_{23}(deg)	44.3682	44.8137	44.9098	45.215
m_2(meV)	5.12825	5.31789	6.12051	8.66012
m_3(meV)	30.1501	30.9721	35.6075	50.2355
$\delta_{\rm CP}$(deg)	−92.7785	−92.9176	−92.9293	−92.9537
$\sigma_{\rm CP}$(deg)	−36.3674	−36.3212	−36.3204	−36.3251

Case B, $M_{\rm SUSY}$= 10 TeV, tanβ=50, $\bar{\eta}_b$=0.6

	$\Lambda_{\rm GUT}$	$M_{\rm sol}$	$M_{\rm atm}$	$\Lambda_{\rm EW}$
θ_{13}(deg)	8.55132	8.55326	8.54977	8.53377
θ_{12}(deg)	34.343	34.4874	34.6351	35.0848
θ_{23}(deg)	44.3396	44.8909	45.2137	46.1582
m_2(meV)	5.29971	5.48016	6.27636	8.75969
m_3(meV)	31.0676	31.7856	36.2859	50.2348
$\delta_{\rm CP}$(deg)	−92.8927	−93.0446	−93.0742	−93.132
$\sigma_{\rm CP}$(deg)	−36.2818	−36.2353	−36.2382	−36.2618

Table F.2: Case B – MSSM with $M_{\rm atm} = 10^{12}$ GeV and $M_{\rm sol} = 10^{15}$ GeV.

Case C, $M_{\rm SUSY}$= 1 TeV, tanβ=30, $\bar{\eta}_b$=0.6

	$\Lambda_{\rm GUT}$	$M_{\rm atm}$	$M_{\rm sol}$	$\Lambda_{\rm EW}$
θ_{13}(deg)	8.13633	8.29459	8.32058	8.40816
θ_{12}(deg)	34.4319	34.413	34.4451	34.5757
θ_{23}(deg)	45.2776	45.9071	46.0059	46.3369
m_2(meV)	4.98396	5.10008	5.86666	8.53591
m_3(meV)	30.4817	30.1301	34.6065	50.2354
$\delta_{\rm CP}$(deg)	−88.7124	−88.8259	−88.8227	−88.7987
$\sigma_{\rm CP}$(deg)	−142.521	−142.076	−142.064	−142.065

Case C, $M_{\rm SUSY}$= 1 TeV, tanβ=50, $\bar{\eta}_b$=0.6

	$\Lambda_{\rm GUT}$	$M_{\rm atm}$	$M_{\rm sol}$	$\Lambda_{\rm EW}$
θ_{13}(deg)	7.87179	8.05268	8.13519	8.40524
θ_{12}(deg)	34.4861	34.504	34.6244	35.0508
θ_{23}(deg)	45.0529	45.784	46.1019	47.1373
m_2(meV)	4.99807	5.09896	5.8368	8.36121
m_3(meV)	31.4668	30.9436	35.306	50.235
$\delta_{\rm CP}$(deg)	−89.7451	−89.845	−89.8248	−89.7634
$\sigma_{\rm CP}$(deg)	−141.756	−141.315	−141.304	−141.301

Case C, $M_{\rm SUSY}$= 3 TeV, tanβ=5, $\bar{\eta}_b$=0.6

	$\Lambda_{\rm GUT}$	$M_{\rm atm}$	$M_{\rm sol}$	$\Lambda_{\rm EW}$
θ_{13}(deg)	8.2382	8.40206	8.40721	8.40956
θ_{12}(deg)	34.4105	34.376	34.3761	34.3795
θ_{23}(deg)	45.3682	46.0157	46.0355	46.0443
m_2(meV)	5.26846	5.36978	6.16184	8.62435
m_3(meV)	31.8773	31.312	35.893	50.234
$\delta_{\rm CP}$(deg)	−88.3167	−88.4461	−88.45	−88.4493
$\sigma_{\rm CP}$(deg)	−142.815	−142.327	−142.313	−142.313

Case C, $M_{\rm SUSY}$= 3 TeV, tanβ=30, $\bar{\eta}_b$=0.6

	$\Lambda_{\rm GUT}$	$M_{\rm atm}$	$M_{\rm sol}$	$\Lambda_{\rm EW}$
θ_{13}(deg)	8.13465	8.29535	8.32244	8.40808
θ_{12}(deg)	34.4322	34.4135	34.4471	34.5748
θ_{23}(deg)	45.2761	45.9153	46.0182	46.3418
m_2(meV)	5.05707	5.17178	5.94847	8.53823
m_3(meV)	30.9344	30.5444	35.0766	50.2341
$\delta_{\rm CP}$(deg)	−88.719	−88.8339	−88.8306	−88.8071
$\sigma_{\rm CP}$(deg)	−142.516	−142.065	−142.053	−142.054

Case C, $M_{\rm SUSY}$= 3 TeV, tanβ=50, $\bar{\eta}_b$=0.6

	$\Lambda_{\rm GUT}$	$M_{\rm atm}$	$M_{\rm sol}$	$\Lambda_{\rm EW}$
θ_{13}(deg)	7.87533	8.0593	8.14433	8.40562
θ_{12}(deg)	34.4854	34.5044	34.6285	35.0408
θ_{23}(deg)	45.0558	45.7989	46.1264	47.1277
m_2(meV)	5.07146	5.17047	5.91726	8.36715
m_3(meV)	31.9161	31.3496	35.758	50.2339
$\delta_{\rm CP}$(deg)	−89.7312	−89.8325	−89.8118	−89.7527
$\sigma_{\rm CP}$(deg)	−141.767	−141.319	−141.308	−141.305

Case C, $M_{\rm SUSY}$= 10 TeV, tanβ=5, $\bar{\eta}_b$=0.6

	$\Lambda_{\rm GUT}$	$M_{\rm atm}$	$M_{\rm sol}$	$\Lambda_{\rm EW}$
θ_{13}(deg)	8.23555	8.4017	8.40701	8.40928
θ_{12}(deg)	34.4111	34.3761	34.3762	34.3795
θ_{23}(deg)	45.3658	46.0225	46.0428	46.0513
m_2(meV)	5.34767	5.44726	6.25125	8.62702
m_3(meV)	32.3656	31.756	36.4037	50.2358
$\delta_{\rm CP}$(deg)	−88.327	−88.4582	−88.4621	−88.4615
$\sigma_{\rm CP}$(deg)	−142.808	−142.312	−142.298	−142.298

Case C, $M_{\rm SUSY}$= 10 TeV, tanβ=30, $\bar{\eta}_b$=0.6

	$\Lambda_{\rm GUT}$	$M_{\rm atm}$	$M_{\rm sol}$	$\Lambda_{\rm EW}$
θ_{13}(deg)	8.13366	8.29703	8.32527	8.40815
θ_{12}(deg)	34.4324	34.4138	34.4489	34.5726
θ_{23}(deg)	45.2753	45.925	46.0322	46.3454
m_2(meV)	5.13788	5.25095	6.03882	8.54172
m_3(meV)	31.432	30.9989	35.5925	50.2346
$\delta_{\rm CP}$(deg)	−88.7229	−88.8395	−88.8359	−88.8133
$\sigma_{\rm CP}$(deg)	−142.513	−142.055	−142.043	−142.044

Case C, $M_{\rm SUSY}$= 10 TeV, tanβ=50, $\bar{\eta}_b$=0.6

	$\Lambda_{\rm GUT}$	$M_{\rm atm}$	$M_{\rm sol}$	$\Lambda_{\rm EW}$
θ_{13}(deg)	7.88012	8.06735	8.15485	8.40513
θ_{12}(deg)	34.4844	34.5045	34.6321	35.0267
θ_{23}(deg)	45.0598	45.8155	46.1522	47.1108
m_2(meV)	5.15188	5.24881	6.00551	8.37443
m_3(meV)	32.4048	31.7906	36.2496	50.2347
$\delta_{\rm CP}$(deg)	−89.7125	−89.8153	−89.7942	−89.7377
$\sigma_{\rm CP}$(deg)	−141.781	−141.326	−141.315	−141.312

Table F.3: Case C – MSSM with $M_{\rm atm} = 10^{15}$ GeV and $M_{\rm sol} = 10^{12}$ GeV.

Case D, $M_{\rm SUSY}$= 1 TeV, tanβ=30, $\bar{\eta}_b$=0.6

	$\Lambda_{\rm GUT}$	$M_{\rm atm}$	$M_{\rm sol}$	$\Lambda_{\rm EW}$
θ_{13}(deg)	8.37301	8.52654	8.52945	8.52476
θ_{12}(deg)	34.3818	34.3629	34.3999	34.5505
θ_{23}(deg)	44.5086	44.9649	45.0581	45.3806
m_2(meV)	5.10896	5.22783	6.01409	8.75328
m_3(meV)	30.4863	30.1422	34.6178	50.2354
$\delta_{\rm CP}$(deg)	−92.2053	−93.0177	−93.0456	−93.0698
$\sigma_{\rm CP}$(deg)	−36.7958	−36.3219	−36.3106	−36.3164

Case D, $M_{\rm SUSY}$= 1 TeV, tanβ=50, $\bar{\eta}_b$=0.6

	$\Lambda_{\rm GUT}$	$M_{\rm atm}$	$M_{\rm sol}$	$\Lambda_{\rm EW}$
θ_{13}(deg)	8.40216	8.55965	8.55951	8.53983
θ_{12}(deg)	34.3755	34.3961	34.5341	35.0223
θ_{23}(deg)	44.4814	45.0363	45.3462	46.3668
m_2(meV)	5.29142	5.39783	6.18029	8.86037
m_3(meV)	31.482	30.9748	35.3344	50.2349
$\delta_{\rm CP}$(deg)	−92.3179	−93.1632	−93.2083	−93.2652
$\sigma_{\rm CP}$(deg)	−36.7117	−36.2242	−36.2164	−36.2447

Case D, $M_{\rm SUSY}$= 3 TeV, tanβ=5, $\bar{\eta}_b$=0.6

	$\Lambda_{\rm GUT}$	$M_{\rm atm}$	$M_{\rm sol}$	$\Lambda_{\rm EW}$
θ_{13}(deg)	8.34831	8.51398	8.51855	8.51844
θ_{12}(deg)	34.3871	34.3516	34.3519	34.3558
θ_{23}(deg)	44.5315	44.9919	45.0076	45.0162
m_2(meV)	5.32791	5.43025	6.23125	8.72156
m_3(meV)	31.8728	31.3125	35.8936	50.2344
$\delta_{\rm CP}$(deg)	−92.1098	−92.983	−93.0079	−93.0086
$\sigma_{\rm CP}$(deg)	−36.867	−36.3555	−36.3412	−36.3413

Case D, $M_{\rm SUSY}$= 3 TeV, tanβ=30, $\bar{\eta}_b$=0.6

	$\Lambda_{\rm GUT}$	$M_{\rm atm}$	$M_{\rm sol}$	$\Lambda_{\rm EW}$
θ_{13}(deg)	8.37043	8.52603	8.52899	8.52438
θ_{12}(deg)	34.3823	34.3636	34.4024	34.5497
θ_{23}(deg)	44.511	44.9747	45.0719	45.3872
m_2(meV)	5.18358	5.30098	6.09758	8.75506
m_3(meV)	30.9396	30.5572	35.0886	50.2352
$\delta_{\rm CP}$(deg)	−92.1953	−93.019	−93.0478	−93.0713
$\sigma_{\rm CP}$(deg)	−36.8032	−36.3228	−36.3113	−36.317

Case D, $M_{\rm SUSY}$= 3 TeV, tanβ=50, $\bar{\eta}_b$=0.6

	$\Lambda_{\rm GUT}$	$M_{\rm atm}$	$M_{\rm sol}$	$\Lambda_{\rm EW}$
θ_{13}(deg)	8.39972	8.55923	8.55902	8.53995
θ_{12}(deg)	34.376	34.398	34.5402	35.0123
θ_{23}(deg)	44.4837	45.0482	45.3674	46.3542
m_2(meV)	5.36569	5.47006	6.26156	8.86092
m_3(meV)	31.9318	31.3814	35.7866	50.2348
$\delta_{\rm CP}$(deg)	−92.3085	−93.1651	−93.2113	−93.2663
$\sigma_{\rm CP}$(deg)	−36.7187	−36.2249	−36.2169	−36.2444

Case D, $M_{\rm SUSY}$= 10 TeV, tanβ=5, $\bar{\eta}_b$=0.6

	$\Lambda_{\rm GUT}$	$M_{\rm atm}$	$M_{\rm sol}$	$\Lambda_{\rm EW}$
θ_{13}(deg)	8.34594	8.51392	8.51862	8.51851
θ_{12}(deg)	34.3876	34.3517	34.3519	34.3557
θ_{23}(deg)	44.5337	45.0006	45.0168	45.0251
m_2(meV)	5.408	5.5086	6.32165	8.72424
m_3(meV)	32.3597	31.7554	36.4032	50.2345
$\delta_{\rm CP}$(deg)	−92.1006	−92.9861	−93.0118	−93.0124
$\sigma_{\rm CP}$(deg)	−36.8738	−36.3552	−36.3404	−36.3405

Case D, $M_{\rm SUSY}$= 10 TeV, tanβ=30, $\bar{\eta}_b$=0.6

	$\Lambda_{\rm GUT}$	$M_{\rm atm}$	$M_{\rm sol}$	$\Lambda_{\rm EW}$
θ_{13}(deg)	8.36821	8.52609	8.52911	8.52462
θ_{12}(deg)	34.3828	34.3643	34.4049	34.5474
θ_{23}(deg)	44.513	44.9846	45.086	45.3911
m_2(meV)	5.26556	5.38129	6.18925	8.75721
m_3(meV)	31.436	31.0107	35.6032	50.2342
$\delta_{\rm CP}$(deg)	−92.1868	−93.0228	−93.0525	−93.0752
$\sigma_{\rm CP}$(deg)	−36.8096	−36.322	−36.3103	−36.3158

Case D, $M_{\rm SUSY}$= 10 TeV, tanβ=50, $\bar{\eta}_b$=0.6

	$\Lambda_{\rm GUT}$	$M_{\rm atm}$	$M_{\rm sol}$	$\Lambda_{\rm EW}$
θ_{13}(deg)	8.39658	8.55826	8.558	8.53972
θ_{12}(deg)	34.3767	34.3999	34.5463	34.9981
θ_{23}(deg)	44.4866	45.0612	45.3893	46.3339
m_2(meV)	5.44578	5.54788	6.3492	8.86036
m_3(meV)	32.4186	31.8209	36.2761	50.2334
$\delta_{\rm CP}$(deg)	−92.2964	−93.1652	−93.2125	−93.2651
$\sigma_{\rm CP}$(deg)	−36.7278	−36.227	−36.2189	−36.2453

Table F.4: Case D – MSSM with $M_{\rm atm} = 10^{15}$ GeV and $M_{\rm sol} = 10^{12}$ GeV.

Bibliography

[1] T. Geib, S. F. King, A. Merle, J. M. No and L. Panizzi, *Probing the Origin of Neutrino Masses and Mixings via Doubly Charged Scalars: Complementarity of the Intensity and the Energy Frontiers*, *Phys. Rev.* **D93** (2016), no. 7 073007 [1512.04391].

[2] T. Geib and A. Merle, *Conversions of bound muons: Lepton flavor violation from doubly charged scalars*, *Phys. Rev.* **D93** (2016), no. 5 055039 [1512.04225].

[3] T. Geib, A. Merle and K. Zuber, $\mu^- - e^+$ *conversion in upcoming LFV experiments*, *Phys. Lett.* **B764** (2017) 157–162 [1609.09088].

[4] T. Geib and A. Merle, $\boldsymbol{\mu^- - e^+}$ *Conversion from Short-Range Operators*, *Phys. Rev.* **D95** (2017), no. 5 055009 [1612.00452].

[5] T. Geib and S. F. King, *A Comprehensive Renormalisation Group Analysis of the Littlest Seesaw Model*, 1709.07425.

[6] P. Domin, S. Kovalenko, A. Faessler and F. Simkovic, *Nuclear (mu-, e+) conversion mediated by Majorana neutrinos*, *Phys. Rev.* **C70** (2004) 065501 [nucl-th/0409033].

[7] **Super-Kamiokande** Collaboration, Y. Fukuda *et. al.*, *Evidence for oscillation of atmospheric neutrinos*, *Phys. Rev. Lett.* **81** (1998) 1562–1567 [hep-ex/9807003].

[8] **SNO** Collaboration, Q. R. Ahmad *et. al.*, *Direct evidence for neutrino flavor transformation from neutral current interactions in the Sudbury Neutrino Observatory*, *Phys. Rev. Lett.* **89** (2002) 011301 [nucl-ex/0204008].

[9] **Particle Data Group** Collaboration, C. Patrignani *et. al.*, *Review of Particle Physics*, *Chin. Phys.* **C40** (2016), no. 10 100001.

[10] **CHOOZ** Collaboration, M. Apollonio *et. al.*, *Limits on neutrino oscillations from the CHOOZ experiment*, *Phys. Lett.* **B466** (1999) 415–430 [hep-ex/9907037].

[11] **CHOOZ** Collaboration, M. Apollonio *et. al.*, *Search for neutrino oscillations on a long baseline at the CHOOZ nuclear power station*, *Eur. Phys. J.* **C27** (2003) 331–374 [hep-ex/0301017].

[12] **Daya Bay** Collaboration, F. P. An *et. al.*, *Observation of electron-antineutrino disappearance at Daya Bay*, *Phys. Rev. Lett.* **108** (2012) 171803 [1203.1669].

[13] **RENO** Collaboration, J. K. Ahn *et. al.*, *Observation of Reactor Electron Antineutrino Disappearance in the RENO Experiment*, *Phys. Rev. Lett.* **108** (2012) 191802 [1204.0626].

[14] **Double Chooz** Collaboration, Y. Abe *et. al.*, *Indication for the disappearance of reactor electron antineutrinos in the Double Chooz experiment*, *Phys. Rev. Lett.* **108** (2012) 131801 [1112.6353].

[15] **KamLAND** Collaboration, K. Eguchi *et. al.*, *First results from KamLAND: Evidence for reactor anti-neutrino disappearance*, *Phys. Rev. Lett.* **90** (2003) 021802 [hep-ex/0212021].

[16] **K2K** Collaboration, M. H. Ahn *et. al.*, *Measurement of Neutrino Oscillation by the K2K Experiment*, *Phys. Rev.* **D74** (2006) 072003 [hep-ex/0606032].

[17] **MINOS** Collaboration, D. G. Michael *et. al.*, *Observation of muon neutrino disappearance with the MINOS detectors and the NuMI neutrino beam*, *Phys. Rev. Lett.* **97** (2006) 191801 [hep-ex/0607088].

[18] **MINOS** Collaboration, P. Adamson *et. al.*, *Search for active neutrino disappearance using neutral-current interactions in the MINOS long-baseline experiment*, *Phys. Rev. Lett.* **101** (2008) 221804 [0807.2424].

[19] **MINOS** Collaboration, P. Adamson *et. al.*, *Measurement of the Neutrino Mass Splitting and Flavor Mixing by MINOS*, *Phys. Rev. Lett.* **106** (2011) 181801 [1103.0340].

[20] **MINOS** Collaboration, P. Adamson *et. al.*, *Combined analysis of ν_μ disappearance and $\nu_\mu \to \nu_e$ appearance in MINOS using accelerator and atmospheric neutrinos*, *Phys. Rev. Lett.* **112** (2014) 191801 [1403.0867].

[21] **OPERA** Collaboration, N. Agafonova *et. al.*, *Observation of a first ν_τ candidate in the OPERA experiment in the CNGS beam*, *Phys. Lett.* **B691** (2010) 138–145 [1006.1623].

[22] **OPERA** Collaboration, N. Agafonova *et. al.*, *New results on $\nu_\mu \to \nu_\tau$ appearance with the OPERA experiment in the CNGS beam*, *JHEP* **11** (2013) 036 [1308.2553]. [Erratum: JHEP04,014(2014)].

[23] **T2K Collaboration** Collaboration, K. Abe *et. al.*, *Observation of Electron Neutrino Appearance in a Muon Neutrino Beam*, *Phys. Rev. Lett.* **112** (2014) 061802 [1311.4750].

[24] **T2K** Collaboration, K. Abe *et. al.*, *Combined Analysis of Neutrino and Antineutrino Oscillations at T2K*, *Phys. Rev. Lett.* **118** (2017), no. 15 151801 [1701.00432].

[25] **NOvA** Collaboration, R. B. Patterson, *The NOvA Experiment: Status and Outlook*, 1209.0716. [Nucl. Phys. Proc. Suppl.235-236,151(2013)].

[26] **NOvA** Collaboration, P. Adamson *et. al.*, *Measurement of the neutrino mixing angle θ_{23} in NOvA*, *Phys. Rev. Lett.* **118** (2017), no. 15 151802 [1701.05891].

[27] **MINOS** Collaboration, P. Adamson *et. al.*, *Measurement of Neutrino and Antineutrino Oscillations Using Beam and Atmospheric Data in MINOS*, *Phys. Rev. Lett.* **110** (2013), no. 25 251801 [1304.6335].

[28] **Super-Kamiokande** Collaboration, S. Fukuda *et. al.*, *Determination of solar neutrino oscillation parameters using 1496 days of Super-Kamiokande I data*, *Phys. Lett.* **B539** (2002) 179–187 [hep-ex/0205075].

[29] S. F. King, *Large mixing angle MSW and atmospheric neutrinos from single right-handed neutrino dominance and U(1) family symmetry*, *Nucl. Phys.* **B576** (2000) 85–105 [hep-ph/9912492].

[30] S. F. King, *Constructing the large mixing angle MNS matrix in seesaw models with right-handed neutrino dominance*, *JHEP* **09** (2002) 011 [hep-ph/0204360].

[31] S. F. King, *Littlest Seesaw*, *JHEP* **02** (2016) 085 [1512.07531].

[32] P. Minkowski, *$\mu \to e\gamma$ at a Rate of One Out of 10^9 Muon Decays?*, *Phys. Lett.* **67B** (1977) 421–428.

[33] O. T. Yanagida, edited by Sawada and A. Sugamoto, eds., *Proceedings: Workshop on the Unified Theories and the Baryon Number in the Universe*, (Tsukuba, Japan), Natl.Lab.High Energy Phys., Natl.Lab.High Energy Phys., 1979.

[34] P. R. M. Gell-Mann and R. Slansky, *Supergravity*. North-Holland, Amsterdam, Netherlands, 1979, p. 315.

[35] S. L. Glashow, *Quarks and Leptons*. Plenum, New York, USA, 1980, p. 707.

[36] R. N. Mohapatra and G. Senjanovic, *Neutrino Mass and Spontaneous Parity Violation*, *Phys. Rev. Lett.* **44** (1980) 912.

[37] S. F. King, *Predicting neutrino parameters from SO(3) family symmetry and quark-lepton unification*, *JHEP* **08** (2005) 105 [hep-ph/0506297].

[38] S. Antusch, S. F. King, C. Luhn and M. Spinrath, *Trimaximal mixing with predicted θ_{13} from a new type of constrained sequential dominance*, *Nucl. Phys.* **B856** (2012) 328–341 [1108.4278].

[39] S. F. King, *Minimal predictive see-saw model with normal neutrino mass hierarchy*, *JHEP* **07** (2013) 137 [1304.6264].

[40] S. F. King, *Minimal see-saw model predicting best fit lepton mixing angles*, *Phys. Lett.* **B724** (2013) 92–98 [1305.4846].

[41] S. F. King, *A model of quark and lepton mixing*, *JHEP* **01** (2014) 119 [1311.3295].

[42] S. F. King, *A to Z of Flavour with Pati-Salam*, *JHEP* **08** (2014) 130 [1406.7005].

[43] F. Björkeroth and S. F. King, *Testing constrained sequential dominance models of neutrinos*, *J. Phys.* **G42** (2015), no. 12 125002 [1412.6996].

[44] S. L. Glashow, J. Iliopoulos and L. Maiani, *Weak Interactions with Lepton-Hadron Symmetry*, *Phys. Rev.* **D2** (1970) 1285–1292.

[45] R. J. Barlow, *The PRISM/PRIME project*, *Nucl. Phys. Proc. Suppl.* **218** (2011) 44–49.

[46] B. Yeo, Y. Kuno, M. Lee and K. Zuber, *Future experimental improvement for the search of lepton-number-violating processes in the e? sector*, *Phys. Rev.* **D96** (2017), no. 7 075027 [1705.07464].

[47] S. F. King, A. Merle and L. Panizzi, *Effective theory of a doubly charged singlet scalar: complementarity of neutrino physics and the LHC*, *JHEP* **1411** (2014) 124 [1406.4137].

[48] F. Capozzi, E. Di Valentino, E. Lisi, A. Marrone, A. Melchiorri and A. Palazzo, *Global constraints on absolute neutrino masses and their ordering*, *Phys. Rev.* **D95** (2017), no. 9 096014 [1703.04471].

[49] I. Esteban, M. C. Gonzalez-Garcia, M. Maltoni, I. Martinez-Soler and T. Schwetz, *Updated fit to three neutrino mixing: exploring the accelerator-reactor complementarity*, *JHEP* **01** (2017) 087 [1611.01514].

[50] S. T. Petcov, *Discrete Flavour Symmetries, Neutrino Mixing and Leptonic CP Violation*, 1711.10806.

[51] **ISS Physics Working Group** Collaboration, A. Bandyopadhyay *et. al.*, *Physics at a future Neutrino Factory and super-beam facility*, *Rept. Prog. Phys.* **72** (2009) 106201 [0710.4947].

[52] **Particle Data Group** Collaboration, K. Olive *et. al.*, *Review of Particle Physics*, *Chin. Phys.* **C38** (2014) 090001.

[53] S. F. King and C. Luhn, *Neutrino Mass and Mixing with Discrete Symmetry*, *Rept. Prog. Phys.* **76** (2013) 056201 [1301.1340].

[54] S. F. King, A. Merle, S. Morisi, Y. Shimizu and M. Tanimoto, *Neutrino Mass and Mixing: from Theory to Experiment*, *New J. Phys.* **16** (2014) 045018 [1402.4271].

[55] S. F. King, *Models of Neutrino Mass, Mixing and CP Violation*, *J. Phys.* **G42** (2015) 123001 [1510.02091].

[56] B. Kayser, F. Gibrat-Debu and F. Perrier, *The Physics of massive neutrinos*, *World Sci. Lect. Notes Phys.* **25** (1989) 1–117.

[57] C. Giunti and C. W. Kim, *Fundamentals of Neutrino Physics and Astrophysics*. 2007.

[58] J. H. Christenson, J. W. Cronin, V. L. Fitch and R. Turlay, *Evidence for the 2π Decay of the K_2^0 Meson*, *Phys. Rev. Lett.* **13** (1964) 138–140.

[59] **KTeV** Collaboration, A. Alavi-Harati *et. al.*, *Observation of direct CP violation in $K_{S,L} \to \pi\pi$ decays*, *Phys. Rev. Lett.* **83** (1999) 22–27 [hep-ex/9905060].

[60] **NA48** Collaboration, V. Fanti *et. al.*, *A New measurement of direct CP violation in two pion decays of the neutral kaon*, *Phys. Lett.* **B465** (1999) 335–348 [hep-ex/9909022].

[61] C. Giunti and C. W. Kim, *Coherence of neutrino oscillations in the wave packet approach*, *Phys. Rev.* **D58** (1998) 017301 [hep-ph/9711363].

[62] W. a Heisenberg, *Uber den anschaulichen Inhalt der quantentheoretischen Kinematik und Mechanik*, *Z. Phys.* **43** (1927) 172–198.

[63] B. Kayser, *On the Quantum Mechanics of Neutrino Oscillation*, *Phys. Rev.* **D24** (1981) 110.

[64] B. Pontecorvo, *Neutrino Experiments and the Problem of Conservation of Leptonic Charge*, *Sov. Phys. JETP* **26** (1968) 984–988. [Zh. Eksp. Teor. Fiz.53,1717(1967)].

[65] C. Giunti, *Light Sterile Neutrinos: Status and Perspectives*, *Nucl. Phys.* **B908** (2016) 336–353 [1512.04758].

[66] S. Gariazzo, C. Giunti, M. Laveder and Y. F. Li, *Updated Global 3+1 Analysis of Short-BaseLine Neutrino Oscillations*, *JHEP* **06** (2017) 135 [1703.00860].

[67] S. M. Bilenky, J. Hosek and S. T. Petcov, *On Oscillations of Neutrinos with Dirac and Majorana Masses*, *Phys. Lett.* **94B** (1980) 495–498.

[68] P. Langacker, S. T. Petcov, G. Steigman and S. Toshev, *On the Mikheev-Smirnov-Wolfenstein (MSW) Mechanism of Amplification of Neutrino Oscillations in Matter*, *Nucl. Phys.* **B282** (1987) 589–609.

[69] B. Pontecorvo, *Mesonium and anti-mesonium*, *Sov. Phys. JETP* **6** (1957) 429. [Zh. Eksp. Teor. Fiz.33,549(1957)].

[70] B. Pontecorvo, *Inverse beta processes and nonconservation of lepton charge*, *Sov. Phys. JETP* **7** (1958) 172–173. [Zh. Eksp. Teor. Fiz.34,247(1957)].

[71] Z. Maki, M. Nakagawa and S. Sakata, *Remarks on the unified model of elementary particles*, *Prog. Theor. Phys.* **28** (1962) 870–880.

[72] S. M. Bilenky and B. Pontecorvo, *Lepton Mixing and Neutrino Oscillations*, *Phys. Rept.* **41** (1978) 225–261.

[73] L. Borodovsky *et. al.*, *Search for muon-neutrino oscillations muon-neutrino —> electron-neutrino (anti-muon-neutrino —> anti-electron-neutrino in a wide band neutrino beam*, *Phys. Rev. Lett.* **68** (1992) 274–277.

[74] **Borexino** Collaboration, C. Arpesella *et. al.*, *Direct Measurement of the Be-7 Solar Neutrino Flux with 192 Days of Borexino Data*, *Phys. Rev. Lett.* **101** (2008) 091302 [0805.3843].

[75] **GALLEX** Collaboration, W. Hampel *et. al.*, *GALLEX solar neutrino observations: Results for GALLEX IV*, *Phys. Lett.* **B447** (1999) 127–133.

[76] **SNO** Collaboration, Q. R. Ahmad *et. al.*, *Measurement of day and night neutrino energy spectra at SNO and constraints on neutrino mixing parameters*, *Phys. Rev. Lett.* **89** (2002) 011302 [nucl-ex/0204009].

[77] X. Qian and P. Vogel, *Neutrino Mass Hierarchy*, *Prog. Part. Nucl. Phys.* **83** (2015) 1–30 [1505.01891].

[78] **JUNO** Collaboration, F. An *et. al.*, *Neutrino Physics with JUNO*, *J. Phys.* **G43** (2016), no. 3 030401 [1507.05613].

[79] **KM3Net** Collaboration, S. Adrian-Martinez *et. al.*, *Letter of intent for KM3NeT 2.0*, *J. Phys.* **G43** (2016), no. 8 084001 [1601.07459].

[80] **IceCube PINGU** Collaboration, M. G. Aartsen *et. al.*, *Letter of Intent: The Precision IceCube Next Generation Upgrade (PINGU)*, 1401.2046.

[81] **DUNE** Collaboration, R. Acciarri *et. al.*, *Long-Baseline Neutrino Facility (LBNF) and Deep Underground Neutrino Experiment (DUNE)*, 1512.06148.

[82] **DUNE** Collaboration, R. Acciarri *et. al.*, *Long-Baseline Neutrino Facility (LBNF) and Deep Underground Neutrino Experiment (DUNE)*, 1601.05471.

[83] **DUNE** Collaboration, R. Acciarri *et. al.*, *Long-Baseline Neutrino Facility (LBNF) and Deep Underground Neutrino Experiment (DUNE)*, 1601.02984.

[84] **ICAL** Collaboration, S. Ahmed *et. al.*, *Physics Potential of the ICAL detector at the India-based Neutrino Observatory (INO)*, *Pramana* **88** (2017), no. 5 79 [1505.07380].

[85] **LAGUNA-LBNO** Collaboration, S. K. Agarwalla *et. al.*, *The mass-hierarchy and CP-violation discovery reach of the LBNO long-baseline neutrino experiment*, *JHEP* **05** (2014) 094 [1312.6520].

[86] J. Lesgourgues and S. Pastor, *Massive neutrinos and cosmology*, *Phys. Rept.* **429** (2006) 307–379 [astro-ph/0603494].

[87] K. N. Abazajian and M. Kaplinghat, *Neutrino Physics from the Cosmic Microwave Background and Large-Scale Structure*, *Ann. Rev. Nucl. Part. Sci.* **66** (2016), no. 1 401–420.

[88] W. Maneschg, A. Merle and W. Rodejohann, *Statistical Analysis of future Neutrino Mass Experiments including Neutrino-less Double Beta Decay*, *EPL* **85** (2009), no. 5 51002 [0812.0479].

[89] **Planck** Collaboration, P. A. R. Ade *et. al.*, *Planck 2015 results. XIII. Cosmological parameters*, *Astron. Astrophys.* **594** (2016) A13 [1502.01589].

[90] **KamLAND-Zen** Collaboration, A. Gando *et. al.*, *Search for Majorana Neutrinos near the Inverted Mass Hierarchy Region with KamLAND-Zen*, *Phys. Rev. Lett.* **117** (2016), no. 8 082503 [1605.02889]. [Addendum: Phys. Rev. Lett.117,no.10,109903(2016)].

[91] **GERDA** Collaboration, M. Agostini *et. al.*, *First results of GERDA Phase II and consistency with background models*, *J. Phys. Conf. Ser.* **798** (2017), no. 1 012106.

[92] V. M. Lobashev, *The search for the neutrino mass by direct method in the tritium beta-decay and perspectives of study it in the project KATRIN*, *Nucl. Phys.* **A719** (2003) 153–160.

[93] C. Kraus *et. al.*, *Final results from phase II of the Mainz neutrino mass search in tritium beta decay*, *Eur. Phys. J.* **C40** (2005) 447–468 [hep-ex/0412056].

[94] K. Eitel, *Direct neutrino mass experiments*, *Nucl. Phys. Proc. Suppl.* **143** (2005) 197–204. [,587(2005)].

[95] **Troitsk** Collaboration, V. N. Aseev *et. al.*, *An upper limit on electron antineutrino mass from Troitsk experiment*, *Phys. Rev.* **D84** (2011) 112003 [1108.5034].

[96] O. Host, O. Lahav, F. B. Abdalla and K. Eitel, *Forecasting neutrino masses from combining KATRIN and the CMB: Frequentist and Bayesian analyses*, *Phys. Rev.* **D76** (2007) 113005 [0709.1317].

[97] M. Steidl, *Experiments for the absolute neutrino mass measurement*, in *Heavy Quarks and Leptons 2008 (HQ&L08) Melbourne, Australia, June 5-9, 2008*, 2009. 0906.0454.

[98] M. Lindner, A. Merle and W. Rodejohann, *Improved limit on theta(13) and implications for neutrino masses in neutrino-less double beta decay and cosmology*, *Phys. Rev.* **D73** (2006) 053005 [hep-ph/0512143].

[99] A. Caldwell, A. Merle, O. Schulz and M. Totzauer, *Global Bayesian analysis of neutrino mass data*, *Phys. Rev.* **D96** (2017), no. 7 073001 [1705.01945].

[100] S. Pascoli, S. T. Petcov and A. Riotto, *Leptogenesis and Low Energy CP Violation in Neutrino Physics*, *Nucl. Phys.* **B774** (2007) 1–52 [hep-ph/0611338].

[101] S. Pascoli, S. T. Petcov and A. Riotto, *Connecting low energy leptonic CP-violation to leptogenesis*, *Phys. Rev.* **D75** (2007) 083511 [hep-ph/0609125].

[102] C. Hagedorn, R. N. Mohapatra, E. Molinaro, C. C. Nishi and S. T. Petcov, *CP Violation in the Lepton Sector and Implications for Leptogenesis*, 1711.02866.

[103] N. Cabibbo, *Time Reversal Violation in Neutrino Oscillation*, *Phys. Lett.* **72B** (1978) 333–335.

[104] V. D. Barger, K. Whisnant and R. J. N. Phillips, *CP Violation in Three Neutrino Oscillations*, *Phys. Rev. Lett.* **45** (1980) 2084.

[105] P. I. Krastev and S. T. Petcov, *Resonance Amplification and t Violation Effects in Three Neutrino Oscillations in the Earth*, *Phys. Lett.* **B205** (1988) 84–92.

[106] S. M. Bilenky and S. T. Petcov, *Massive Neutrinos and Neutrino Oscillations*, *Rev. Mod. Phys.* **59** (1987) 671. [Erratum: Rev. Mod. Phys.60,575(1988)].

[107] S. T. Petcov, *The Nature of Massive Neutrinos*, *Adv. High Energy Phys.* **2013** (2013) 852987 [1303.5819].

[108] S. M. Bilenky, S. Pascoli and S. T. Petcov, *Majorana neutrinos, neutrino mass spectrum, CP violation and neutrinoless double beta decay. 1. The Three neutrino mixing case*, *Phys. Rev.* **D64** (2001) 053010 [hep-ph/0102265].

[109] J. Bernabeu *et. al.*, *EURONU WP6 2009 yearly report: Update of the physics potential of Nufact, superbeams and betabeams*, 1005.3146.

[110] **Intensity Frontier Neutrino Working Group** Collaboration, A. de Gouvea *et. al.*, *Working Group Report: Neutrinos*, in *Proceedings, 2013 Community Summer Study on the Future of U.S. Particle Physics: Snowmass on the Mississippi (CSS2013): Minneapolis, MN, USA, July 29-August 6, 2013*, 2013. 1310.4340.

[111] **LBNE** Collaboration, C. Adams *et. al.*, *The Long-Baseline Neutrino Experiment: Exploring Fundamental Symmetries of the Universe*, 1307.7335.

[112] **Hyper-Kamiokande Proto-Collaboration** Collaboration, K. Abe *et. al.*, *Physics potential of a long-baseline neutrino oscillation experiment using a J-PARC neutrino beam and Hyper-Kamiokande*, *PTEP* **2015** (2015) 053C02 [1502.05199].

[113] S. Weinberg, *Baryon and Lepton Nonconserving Processes*, *Phys. Rev. Lett.* **43** (1979) 1566–1570.

[114] S. F. King, *Neutrino Mass and Flavour Models*, *AIP Conf. Proc.* **1200** (2010) 103–111 [0909.2969].

[115] G. Altarelli and F. Feruglio, *Discrete Flavor Symmetries and Models of Neutrino Mixing*, *Rev. Mod. Phys.* **82** (2010) 2701–2729 [1002.0211].

[116] H. Ishimori, T. Kobayashi, H. Ohki, Y. Shimizu, H. Okada *et. al.*, *Non-Abelian Discrete Symmetries in Particle Physics*, *Prog. Theor. Phys. Suppl.* **183** (2010) 1–163 [1003.3552].

[117] D. Meloni, *GUT and flavor models for neutrino masses and mixing*, 1709.02662.

[118] A. Merle, *keV Neutrino Model Building*, *Int. J. Mod. Phys.* **D22** (2013) 1330020 [1302.2625].

[119] S. S. C. Law and K. L. McDonald, *The simplest models of radiative neutrino mass*, *Int. J. Mod. Phys.* **A29** (2014) 1450064 [1303.6384].

[120] J. Garayoa and T. Schwetz, *Neutrino mass hierarchy and Majorana CP phases within the Higgs triplet model at the LHC*, *JHEP* **03** (2008) 009 [0712.1453].

[121] M. Magg and C. Wetterich, *Neutrino Mass Problem and Gauge Hierarchy*, *Phys. Lett.* **B94** (1980) 61.

[122] G. Lazarides, Q. Shafi and C. Wetterich, *Proton Lifetime and Fermion Masses in an SO(10) Model*, *Nucl. Phys.* **B181** (1981) 287–300.

[123] R. N. Mohapatra and G. Senjanovic, *Neutrino Masses and Mixings in Gauge Models with Spontaneous Parity Violation*, *Phys. Rev.* **D23** (1981) 165.

[124] J. Schechter and J. W. F. Valle, *Neutrino Masses in SU(2) x U(1) Theories*, *Phys. Rev.* **D22** (1980) 2227.

[125] J. C. Montero, C. A. de S. Pires and V. Pleitez, *Neutrino masses through a type II seesaw mechanism at TeV scale*, *Phys. Lett.* **B502** (2001) 167–170 [hep-ph/0011296].

[126] D. Das and A. Santamaria, *Updated scalar sector constraints in the Higgs triplet model*, *Phys. Rev.* **D94** (2016), no. 1 015015 [1604.08099].

[127] N. Haba, H. Ishida, N. Okada and Y. Yamaguchi, *Vacuum stability and naturalness in type-II seesaw*, *Eur. Phys. J.* **C76** (2016), no. 6 333 [1601.05217].

[128] A. Zee, *A Theory of Lepton Number Violation, Neutrino Majorana Mass, and Oscillation*, *Phys. Lett.* **B93** (1980) 389.

[129] T. P. Cheng and L.-F. Li, *Neutrino Masses, Mixings and Oscillations in SU(2) x U(1) Models of Electroweak Interactions*, *Phys. Rev.* **D22** (1980) 2860.

[130] S. T. Petcov, *Remarks on the Zee Model of Neutrino Mixing (mu —> e gamma, Heavy Neutrino —> Light Neutrino gamma, etc.)*, *Phys. Lett.* **115B** (1982) 401–406.

[131] K. S. Babu, *Model of 'Calculable' Majorana Neutrino Masses*, *Phys. Lett.* **B203** (1988) 132.

[132] N. G. Deshpande, J. F. Gunion, B. Kayser and F. I. Olness, *Left-right symmetric electroweak models with triplet Higgs*, *Phys. Rev.* **D44** (1991) 837–858.

[133] C. Jarlskog, M. Matsuda, S. Skadhauge and M. Tanimoto, *Zee mass matrix and bimaximal neutrino mixing*, *Phys. Lett.* **B449** (1999) 240 [hep-ph/9812282].

[134] Y. Koide and A. Ghosal, *Bimaximal neutrino mixing in a Zee type model with badly broken flavor symmetry*, *Phys. Rev.* **D63** (2001) 037301 [hep-ph/0008129].

[135] K. R. S. Balaji, W. Grimus and T. Schwetz, *The Solar LMA neutrino oscillation solution in the Zee model*, *Phys. Lett.* **B508** (2001) 301–310 [hep-ph/0104035].

[136] T. Kitabayashi and M. Yasue, *Large solar neutrino mixing and radiative neutrino mechanism*, *Phys. Lett.* **B524** (2002) 308–318 [hep-ph/0110303].

[137] T. Kitabayashi and M. Yasue, *Large solar neutrino mixing in an extended Zee model*, *Int. J. Mod. Phys.* **A17** (2002) 2519–2534 [hep-ph/0112287].

[138] E. J. Chun, K. Y. Lee and S. C. Park, *Testing Higgs triplet model and neutrino mass patterns*, *Phys. Lett.* **B566** (2003) 142–151 [hep-ph/0304069].

[139] X.-G. He, *Is the Zee model neutrino mass matrix ruled out?*, *Eur. Phys. J.* **C34** (2004) 371–376 [hep-ph/0307172].

[140] V. Cirigliano, A. Kurylov, M. J. Ramsey-Musolf and P. Vogel, *Lepton flavor violation without supersymmetry*, *Phys. Rev.* **D70** (2004) 075007 [hep-ph/0404233].

[141] A. G. Akeroyd and M. Aoki, *Single and pair production of doubly charged Higgs bosons at hadron colliders*, *Phys. Rev.* **D72** (2005) 035011 [hep-ph/0506176].

[142] R. Bouchand and A. Merle, *Running of Radiative Neutrino Masses: The Scotogenic Model*, *JHEP* **07** (2012) 084 [1205.0008].

[143] A. Merle and M. Platscher, *Running of radiative neutrino masses: the scotogenic model revisited*, *JHEP* **11** (2015) 148 [1507.06314].

[144] A. Pilaftsis, *Radiatively induced neutrino masses and large Higgs neutrino couplings in the standard model with Majorana fields*, *Z. Phys.* **C55** (1992) 275–282 [hep-ph/9901206].

[145] P. S. B. Dev and A. Pilaftsis, *Minimal Radiative Neutrino Mass Mechanism for Inverse Seesaw Models*, *Phys. Rev.* **D86** (2012) 113001 [1209.4051].

[146] E. Ma, A. Natale and A. Rashed, *Scotogenic A_4 Neutrino Model for Nonzero θ_{13} and Large δ_{CP}*, *Int. J. Mod. Phys.* **A27** (2012) 1250134 [1206.1570].

[147] E. Ma, *Verifiable radiative seesaw mechanism of neutrino mass and dark matter*, *Phys. Rev.* **D73** (2006) 077301 [hep-ph/0601225].

[148] A. Zee, *Charged Scalar Field and Quantum Number Violations*, *Phys. Lett.* **161B** (1985) 141–145.

[149] A. Zee, *Quantum Numbers of Majorana Neutrino Masses*, *Nucl. Phys.* **B264** (1986) 99.

[150] M. Gustafsson, J. M. No and M. A. Rivera, *The Cocktail Model: Neutrino Masses and Mixings with Dark Matter*, *Phys. Rev. Lett.* **110** (2013) 211802 [1212.4806].

[151] M. Gustafsson, J. M. No and M. A. Rivera, *Radiative neutrino mass generation linked to neutrino mixing and $0\nu\beta\beta$-decay predictions*, *Phys. Rev.* **D90** (2014) 013012 [1402.0515].

[152] R. Foot, H. Lew, X. G. He and G. C. Joshi, *Seesaw Neutrino Masses Induced by a Triplet of Leptons*, *Z. Phys.* **C44** (1989) 441.

[153] E. Ma and D. P. Roy, *Heavy triplet leptons and new gauge boson*, *Nucl. Phys.* **B644** (2002) 290–302 [hep-ph/0206150].

[154] R. N. Mohapatra and J. W. F. Valle, *Neutrino Mass and Baryon Number Nonconservation in Superstring Models*, *Phys. Rev.* **D34** (1986) 1642.

[155] M. Hirsch, M. Diaz, W. Porod, J. C. Romao and J. W. F. Valle, *Neutrino masses and mixings from supersymmetry with bilinear R parity violation: A Theory for solar and atmospheric neutrino oscillations*, *Phys. Rev.* **D62** (2000) 113008 [hep-ph/0004115].

[156] Y. Grossman and H. E. Haber, *Sneutrino mixing phenomena*, *Phys. Rev. Lett.* **78** (1997) 3438–3441 [hep-ph/9702421].

[157] M. A. Diaz, J. C. Romao and J. W. F. Valle, *Minimal supergravity with R-parity breaking*, *Nucl. Phys.* **B524** (1998) 23–40 [hep-ph/9706315].

[158] H. K. Dreiner, *An Introduction to explicit R-parity violation*, hep-ph/9707435. [Adv. Ser. Direct. High Energy Phys.21,565(2010)].

[159] M. A. Diaz, *R-parity breaking in minimal supergravity*, in *High-energy physics. Proceedings, International Europhysics Conference, Jerusalem, Israel, August 19-25, 1997*, pp. 895–898, 1997. hep-ph/9712213.

[160] M. Drees, S. Pakvasa, X. Tata and T. ter Veldhuis, *A Supersymmetric resolution of solar and atmospheric neutrino puzzles*, *Phys. Rev.* **D57** (1998) 5335–5339 [hep-ph/9712392].

[161] A. Faessler, S. Kovalenko and F. Simkovic, *Bilinear R-parity violation in neutrinoless double beta decay*, *Phys. Rev.* **D58** (1998) 055004 [hep-ph/9712535].

[162] E. J. Chun, *Axino neutrino mixing in gauge mediated supersymmetry breaking models*, *Phys. Lett.* **B454** (1999) 304–308 [hep-ph/9901220].

[163] A. Abada and M. Losada, *Constraints on a general three generation neutrino mass matrix from neutrino data: Application to the MSSM with R-parity violation*, *Nucl. Phys.* **B585** (2000) 45–78 [hep-ph/9908352].

[164] F. De Campos, M. A. Diaz, O. J. P. Eboli, M. B. Magro and P. G. Mercadante, *Anomaly mediated supersymmetry breaking without R parity*, *Nucl. Phys.* **B623** (2002) 47–72 [hep-ph/0110049].

[165] M. A. Diaz, M. Hirsch, W. Porod, J. C. Romao and J. W. F. Valle, *Solar neutrino masses and mixing from bilinear R parity broken supersymmetry: Analytical versus numerical results*, *Phys. Rev.* **D68** (2003) 013009 [hep-ph/0302021]. [Erratum: Phys. Rev.D71,059904(2005)].

[166] M. Hirsch and W. Porod, *Neutrino properties and the decay of the lightest supersymmetric particle*, *Phys. Rev.* **D68** (2003) 115007 [hep-ph/0307364].

[167] R. Barbier *et. al.*, *R-parity violating supersymmetry*, *Phys. Rept.* **420** (2005) 1–202 [hep-ph/0406039].

[168] F. de Campos, M. A. Diaz, O. J. P. Eboli, R. A. Lineros, M. B. Magro and P. G. Mercadante, *Neutrinos in anomaly mediated supersymmetry breaking with R-parity violation*, *Phys. Rev.* **D71** (2005) 055008 [hep-ph/0409043].

[169] D. Aristizabal Sierra, M. Hirsch and W. Porod, *R-parity violating sneutrino decays*, *JHEP* **09** (2005) 033 [hep-ph/0409241].

[170] E. J. Chun and S. C. Park, *Neutrino mass from R-parity violation in split supersymmetry*, *JHEP* **01** (2005) 009 [hep-ph/0410242].

[171] M. A. Diaz, C. Mora and A. R. Zerwekh, *Study of a neutrino mass texture generated in supergravity with bilinear R-parity violation*, *Eur. Phys. J.* **C44** (2005) 277–286 [hep-ph/0410285].

[172] A. Dedes, S. Rimmer and J. Rosiek, *Neutrino masses in the lepton number violating MSSM*, *JHEP* **08** (2006) 005 [hep-ph/0603225].

[173] H. K. Dreiner, C. Luhn, H. Murayama and M. Thormeier, *Baryon triality and neutrino masses from an anomalous flavor U(1)*, *Nucl. Phys.* **B774** (2007) 127–167 [hep-ph/0610026].

[174] B. C. Allanach and C. H. Kom, *Lepton number violating mSUGRA and neutrino masses*, *JHEP* **04** (2008) 081 [0712.0852].

[175] H. K. Dreiner, M. Hanussek and S. Grab, *Bounds on R-parity Violating Couplings at the Grand Unification Scale from Neutrino Masses*, *Phys. Rev.* **D82** (2010) 055027 [1005.3309].

[176] H. K. Dreiner, M. Hanussek, J.-S. Kim and C. H. Kom, *Neutrino masses and mixings in the baryon triality constrained minimal supersymmetric standard model*, *Phys. Rev.* **D84** (2011) 113005 [1106.4338].

[177] B. C. Allanach, C. H. Kom and M. Hanussek, *Computation of Neutrino Masses in R-parity Violating Supersymmetry: SOFTSUSY3.2*, *Comput. Phys. Commun.* **183** (2012) 785–793 [1109.3735].

[178] F. Bazzocchi, S. Morisi, E. Peinado, J. W. F. Valle and A. Vicente, *Bilinear R-parity violation with flavor symmetry*, *JHEP* **01** (2013) 033 [1202.1529].

[179] H. K. Dreiner, M. Hanussek and C. Luhn, *What is the discrete gauge symmetry of the R-parity violating MSSM?*, *Phys. Rev.* **D86** (2012) 055012 [1206.6305].

[180] E. Peinado and A. Vicente, *Neutrino Masses from R-Parity Violation with a Z_3 Symmetry*, *Phys. Rev.* **D86** (2012) 093024 [1207.6641].

[181] N. Arkani-Hamed, S. Dimopoulos and G. R. Dvali, *The Hierarchy problem and new dimensions at a millimeter*, *Phys. Lett.* **B429** (1998) 263–272 [hep-ph/9803315].

[182] K. R. Dienes, E. Dudas and T. Gherghetta, *Neutrino oscillations without neutrino masses or heavy mass scales: A Higher dimensional seesaw mechanism*, *Nucl. Phys.* **B557** (1999) 25 [hep-ph/9811428].

[183] N. Arkani-Hamed, S. Dimopoulos, G. R. Dvali and J. March-Russell, *Neutrino masses from large extra dimensions*, *Phys. Rev.* **D65** (2001) 024032 [hep-ph/9811448].

[184] A. E. Faraggi and M. Pospelov, *Phenomenological issues in TeV scale gravity with light neutrino masses*, *Phys. Lett.* **B458** (1999) 237–244 [hep-ph/9901299].

[185] G. R. Dvali and A. Yu. Smirnov, *Probing large extra dimensions with neutrinos*, *Nucl. Phys.* **B563** (1999) 63–81 [hep-ph/9904211].

[186] R. N. Mohapatra, S. Nandi and A. Perez-Lorenzana, *Neutrino masses and oscillations in models with large extra dimensions*, *Phys. Lett.* **B466** (1999) 115–121 [hep-ph/9907520].

[187] R. Barbieri, P. Creminelli and A. Strumia, *Neutrino oscillations from large extra dimensions*, *Nucl. Phys.* **B585** (2000) 28–44 [hep-ph/0002199].

[188] A. E. Faraggi and E. Halyo, *Neutrino masses in superstring derived standard - like models*, *Phys. Lett.* **B307** (1993) 311–317 [hep-th/9303060].

[189] N. Haba, C. Hattori, M. Matsuda, T. Matsuoka and D. Mochinaga, *A Large Majorana mass from Calabi-Yau superstring models*, *Phys. Lett.* **B337** (1994) 63–68 [hep-ph/9311298].

[190] N. Haba, C. Hattori, M. Matsuda, T. Matsuoka and D. Mochinaga, *How can we obtain a large Majorana mass in Calabi-Yau models?*, *Prog. Theor. Phys.* **92** (1994) 153–174 [hep-ph/9401332].

[191] G. Cleaver, M. Cvetic, J. R. Espinosa, L. L. Everett and P. Langacker, *Intermediate scales, mu parameter, and fermion masses from string models*, *Phys. Rev.* **D57** (1998) 2701–2715 [hep-ph/9705391].

[192] J. R. Ellis, G. K. Leontaris, S. Lola and D. V. Nanopoulos, *Fermion mass textures in an M inspired flipped SU(5) model derived from string*, *Phys. Lett.* **B425** (1998) 86–96 [hep-ph/9711476].

[193] P. Langacker, *A Mechanism for ordinary sterile neutrino mixing*, *Phys. Rev.* **D58** (1998) 093017 [hep-ph/9805281].

[194] J. R. Ellis, G. K. Leontaris, S. Lola and D. V. Nanopoulos, *Neutrino textures in the light of Super-Kamiokande data and a realistic string model*, *Eur. Phys. J.* **C9** (1999) 389–408 [hep-ph/9808251].

[195] L. E. Ibanez, C. Munoz and S. Rigolin, *Aspect of type I string phenomenology*, *Nucl. Phys.* **B553** (1999) 43–80 [hep-ph/9812397].

[196] C. Coriano and A. E. Faraggi, *String inspired neutrino mass textures in light of KamLAND and WMAP*, *Phys. Lett.* **B581** (2004) 99–110 [hep-ph/0306186].

[197] J. E. Kim, *Trinification with sin**2 theta(W) = 3/8 and seesaw neutrino mass*, *Phys. Lett.* **B591** (2004) 119–126 [hep-ph/0403196].

[198] J. Giedt, G. L. Kane, P. Langacker and B. D. Nelson, *Massive neutrinos and (heterotic) string theory*, *Phys. Rev.* **D71** (2005) 115013 [hep-th/0502032].

[199] S. Antusch, O. J. Eyton-Williams and S. F. King, *Dirac neutrinos and hybrid inflation from string theory*, *JHEP* **08** (2005) 103 [hep-ph/0505140].

[200] P. Langacker and B. D. Nelson, *String-inspired triplet see-saw from diagonal embedding of SU(2)(L) in SU(2)(A) x SU(2)(B)*, *Phys. Rev.* **D72** (2005) 053013 [hep-ph/0507063].

[201] S. Antusch, J. Kersten, M. Lindner, M. Ratz and M. A. Schmidt, *Mixing parameter tools 1.1 - Documentation*, 2015. Documentation on the MPT package, available online at https://www.hepforge.org/archive/reapmpt/MPT-Documentation-1.1.pdf.

[202] T. P. Cheng and L. F. Li, *Gauge Theory Of Elementary Particle Physics*. Oxford Science Publications, Oxford, UK, 1984.

[203] **KamLAND** Collaboration, T. Araki *et. al.*, *Measurement of neutrino oscillation with KamLAND: Evidence of spectral distortion*, *Phys. Rev. Lett.* **94** (2005) 081801 [hep-ex/0406035].

[204] **T2K** Collaboration, K. Abe *et. al.*, *Indication of Electron Neutrino Appearance from an Accelerator-produced Off-axis Muon Neutrino Beam*, *Phys. Rev. Lett.* **107** (2011) 041801 [1106.2822].

[205] **MEG** Collaboration, J. Adam *et. al.*, *New constraint on the existence of the $\mu^+ \to e^+\gamma$ decay*, *Phys. Rev. Lett.* **110** (2013) 201801 [1303.0754].

[206] **BNL** Collaboration, D. Ambrose *et. al.*, *New limit on muon and electron lepton number violation from K0(L) —> mu+- e-+ decay*, *Phys. Rev. Lett.* **81** (1998) 5734–5737 [hep-ex/9811038].

[207] M. Raidal *et. al.*, *Flavour physics of leptons and dipole moments*, *Eur. Phys. J.* **C57** (2008) 13–182 [0801.1826].

[208] Y. G. Ciu *et. al.*, *Conceptual Design Report for Experimental Search for Lepton Flavor Violating mu-e Conversion at Sensitivity of* 10^{16} *with a Slow-Extracted Bunched Proton Beam (COMET) J-PARC P21*, 2009. http://comet.phys.sci.osaka-u.ac.jp:8080/comet/internal/publications/comet-cdr-v1.0.pdf/view.

[209] A. de Gouvea and P. Vogel, *Lepton Flavor and Number Conservation, and Physics Beyond the Standard Model*, *Prog. Part. Nucl. Phys.* **71** (2013) 75–92 [1303.4097].

[210] R. H. Bernstein and P. S. Cooper, *Charged Lepton Flavor Violation: An Experimenter's Guide*, *Phys. Rept.* **532** (2013) 27–64 [1307.5787].

[211] Y. Kuno and Y. Okada, *Muon decay and physics beyond the standard model*, *Rev. Mod. Phys.* **73** (2001) 151–202 [hep-ph/9909265].

[212] W. J. Marciano, T. Mori and J. M. Roney, *Charged Lepton Flavor Violation Experiments*, *Ann. Rev. Nucl. Part. Sci.* **58** (2008) 315–341.

[213] A. de Gouvea and N. Saoulidou, *Fermilab's intensity frontier*, *Ann. Rev. Nucl. Part. Sci.* **60** (2010) 513–538.

[214] J. L. Hewett *et. al.*, *Fundamental Physics at the Intensity Frontier*, 1205.2671.

[215] J. Aysto *et. al.*, *Physics with low-energy muons at a neutrino factory complex*, hep-ph/0109217.

[216] S. T. Petcov, *The Processes mu –> e Gamma, mu –> e e anti-e, Neutrino' –> Neutrino gamma in the Weinberg-Salam Model with Neutrino Mixing*, *Sov. J. Nucl. Phys.* **25** (1977) 340. [Erratum: Yad. Fiz.25,1336(1977)].

[217] S. M. Bilenky, S. T. Petcov and B. Pontecorvo, *Lepton Mixing, mu –> e + gamma Decay and Neutrino Oscillations*, *Phys. Lett.* **67B** (1977) 309.

[218] W. J. Marciano and A. I. Sanda, *Exotic Decays of the Muon and Heavy Leptons in Gauge Theories*, *Phys. Lett.* **67B** (1977) 303–305.

[219] B. W. Lee, S. Pakvasa, R. E. Shrock and H. Sugawara, *Muon and Electron Number Nonconservation in a v-a Six Quark Model*, *Phys. Rev. Lett.* **38** (1977) 937. [Erratum: Phys. Rev. Lett.38,1230(1977)].

[220] B. W. Lee and R. E. Shrock, *Natural Suppression of Symmetry Violation in Gauge Theories: Muon - Lepton and Electron Lepton Number Nonconservation*, *Phys. Rev.* **D16** (1977) 1444.

[221] A. Pich, *Lepton universality*, *NATO Sci. Ser. B* **363** (1997) 173–190 [hep-ph/9701263].

[222] A. Blum and A. Merle, *General Conditions for Lepton Flavour Violation at Tree- and 1-Loop Level*, *Phys. Rev.* **D77** (2008) 076005 [0709.3294].

[223] T. Cheng and L. Li, *Gauge Theory of Elementary Particle Physics*. Oxford science publications. Clarendon Press, 1984.

[224] G. 't Hooft, *Symmetry Breaking Through Bell-Jackiw Anomalies*, *Phys. Rev. Lett.* **37** (1976) 8–11.

[225] F. R. Klinkhamer and N. S. Manton, *A Saddle Point Solution in the Weinberg-Salam Theory*, *Phys. Rev.* **D30** (1984) 2212.

[226] M. Doi, T. Kotani and E. Takasugi, *Double beta Decay and Majorana Neutrino*, *Prog. Theor. Phys. Suppl.* **83** (1985) 1.

[227] J. J. Gomez-Cadenas, J. Martin-Albo, M. Mezzetto, F. Monrabal and M. Sorel, *The Search for neutrinoless double beta decay*, *Riv. Nuovo Cim.* **35** (2012) 29–98 [1109.5515].

[228] S. M. Bilenky, *Neutrinoless double beta-decay*, *Phys. Part. Nucl.* **41** (2010) 690–715 [1001.1946].

[229] S. M. Bilenky and C. Giunti, *Neutrinoless double-beta decay: A brief review*, *Mod. Phys. Lett.* **A27** (2012) 1230015 [1203.5250].

[230] M. Agostini *et. al.*, *Search of Neutrinoless Double Beta Decay with the GERDA Experiment*, *Nucl. Part. Phys. Proc.* **273-275** (2016) 1876–1882.

[231] **EXO-200** Collaboration, J. B. Albert *et. al.*, *Search for Majorana neutrinos with the first two years of EXO-200 data*, *Nature* **510** (2014) 229–234 [1402.6956].

[232] **KamLAND-Zen** Collaboration, A. Gando *et. al.*, *Limit on Neutrinoless $\beta\beta$ Decay of ^{136}Xe from the First Phase of KamLAND-Zen and Comparison with the Positive Claim in ^{76}Ge*, *Phys. Rev. Lett.* **110** (2013), no. 6 062502 [1211.3863].

[233] **SINDRUM II** Collaboration, J. Kaulard *et. al.*, *Improved limit on the branching ratio of mu- –> e+ conversion on titanium*, *Phys. Lett.* **B422** (1998) 334–338.

[234] **NA48/2** Collaboration, K. Massri, *Searches for Lepton Number Violation and resonances in the $K^{\pm} \to \pi\mu\mu$ decays at the NA48/2 experiment*, in *51st Rencontres de Moriond on EW Interactions and Unified Theories La Thuile, Italy, March 12-19, 2016*, 2016. 1607.04216.

[235] **BaBar** Collaboration, J. P. Lees *et. al.*, *Searches for Rare or Forbidden Semileptonic Charm Decays*, *Phys. Rev.* **D84** (2011) 072006 [1107.4465].

[236] **T. Iijima for the BELLE** Collaboration, O. Seon *et. al.*, *Search for Lepton-number-violating B+->D-l+l'+ Decays*, *Phys. Rev.* **D84** (2011) 071106 [1107.0642].

[237] **Belle** Collaboration, Y. Miyazaki *et. al.*, *Search for Lepton-Flavor-Violating and Lepton-Number-Violating $\tau \to \ell hh'$ Decay Modes*, *Phys. Lett.* **B719** (2013) 346–353 [1206.5595].

[238] A. Atre, V. Barger and T. Han, *Upper bounds on lepton-number violating processes*, *Phys. Rev.* **D71** (2005) 113014 [hep-ph/0502163].

[239] **Particle Data Group** Collaboration, K. Nakamura *et. al.*, *Review of particle physics*, *J. Phys.* **G37** (2010) 075021.

[240] P. Fileviez Perez and M. B. Wise, *Breaking Local Baryon and Lepton Number at the TeV Scale*, *JHEP* **08** (2011) 068 [1106.0343].

[241] W. Rodejohann, *Neutrino-less Double Beta Decay and Particle Physics*, *Int. J. Mod. Phys.* **E20** (2011) 1833–1930 [1106.1334].

[242] C.-S. Chen, C. Q. Geng and J. N. Ng, *Unconventional Neutrino Mass Generation, Neutrinoless Double Beta Decays, and Collider Phenomenology*, *Phys. Rev.* **D75** (2007) 053004 [hep-ph/0610118].

[243] V. Cirigliano, A. Kurylov, M. J. Ramsey-Musolf and P. Vogel, *Neutrinoless double beta decay and lepton flavor violation*, *Phys. Rev. Lett.* **93** (2004) 231802 [hep-ph/0406199].

[244] K. S. Babu and C. Macesanu, *Two loop neutrino mass generation and its experimental consequences*, *Phys. Rev.* **D67** (2003) 073010 [hep-ph/0212058].

[245] L. M. Krauss, S. Nasri and M. Trodden, *A Model for neutrino masses and dark matter*, *Phys. Rev.* **D67** (2003) 085002 [hep-ph/0210389].

[246] M. Aoki, S. Kanemura and O. Seto, *Neutrino mass, Dark Matter and Baryon Asymmetry via TeV-Scale Physics without Fine-Tuning*, *Phys. Rev. Lett.* **102** (2009) 051805 [0807.0361].

[247] F. del Aguila, A. Aparici, S. Bhattacharya, A. Santamaria and J. Wudka, *A realistic model of neutrino masses with a large neutrinoless double beta decay rate*, *JHEP* **1205** (2012) 133 [1111.6960].

[248] M. C. Gonzalez-Garcia, M. Maltoni and T. Schwetz, *Updated fit to three neutrino mixing: status of leptonic CP violation*, *JHEP* **11** (2014) 052 [1409.5439].

[249] M. C. Gonzalez-Garcia, M. Maltoni and T. Schwetz, *Global Analyses of Neutrino Oscillation Experiments*, *Nucl. Phys.* **B908** (2016) 199–217 [1512.06856].

[250] J. Bergstrom, M. C. Gonzalez-Garcia, M. Maltoni and T. Schwetz, *Bayesian global analysis of neutrino oscillation data*, *JHEP* **09** (2015) 200 [1507.04366].

[251] H. Pas, M. Hirsch, H. V. Klapdor-Kleingrothaus and S. G. Kovalenko, *Towards a superformula for neutrinoless double beta decay*, *Phys. Lett.* **B453** (1999) 194–198.

[252] H. Päs, M. Hirsch, H. V. Klapdor-Kleingrothaus and S. G. Kovalenko, *A Superformula for neutrinoless double beta decay. 2. The Short range part*, *Phys. Lett.* **B498** (2001) 35–39 [hep-ph/0008182].

[253] J. Bergstrom, A. Merle and T. Ohlsson, *Constraining New Physics with a Positive or Negative Signal of Neutrino-less Double Beta Decay*, *JHEP* **1105** (2011) 122 [1103.3015].

[254] F. Simkovic, J. Vergados and A. Faessler, *Few active mechanisms of the neutrinoless double beta-decay and effective mass of Majorana neutrinos*, *Phys. Rev.* **D82** (2010) 113015 [1006.0571].

[255] **GERDA Collaboration** Collaboration, M. Agostini *et. al.*, *Results on neutrinoless double beta decay of 76Ge from GERDA Phase I*, *Phys. Rev. Lett.* **111** (2013) 122503 [1307.4720].

[256] M. Nebot, J. F. Oliver, D. Palao and A. Santamaria, *Prospects for the Zee-Babu Model at the CERN LHC and low energy experiments*, *Phys. Rev.* **D77** (2008) 093013 [0711.0483].

[257] S. F. King, A. Merle and A. J. Stuart, *The Power of Neutrino Mass Sum Rules for Neutrinoless Double Beta Decay Experiments*, *JHEP* **1312** (2013) 005 [1307.2901].

[258] A. Merle and W. Rodejohann, *The Elements of the neutrino mass matrix: Allowed ranges and implications of texture zeros*, *Phys. Rev.* **D73** (2006) 073012 [hep-ph/0603111].

[259] **ATLAS Collaboration** Collaboration, G. Aad *et. al.*, *Search for doubly-charged Higgs bosons in like-sign dilepton final states at $\sqrt{s} = 7$ TeV with the ATLAS detector*, *Eur. Phys. J.* **C72** (2012) 2244 [1210.5070].

[260] **CMS Collaboration** Collaboration, S. Chatrchyan *et. al.*, *A search for a doubly-charged Higgs boson in pp collisions at $\sqrt{s} = 7$ TeV*, *Eur. Phys. J.* **C72** (2012) 2189 [1207.2666].

[261] E. J. Chun and P. Sharma, *Search for a doubly-charged boson in four lepton final states in type II seesaw*, *Phys. Lett.* **B728** (2014) 256–261 [1309.6888].

[262] G. Azuelos, K. Benslama and J. Ferland, *Prospects for the search for a doubly-charged Higgs in the left-right symmetric model with ATLAS*, *J. Phys.* **G32** (2006), no. 2 73–91 [hep-ph/0503096].

[263] C.-S. Chen, C.-Q. Geng, J. N. Ng and J. M. Wu, *Testing radiative neutrino mass generation at the LHC*, *JHEP* **0708** (2007) 022 [0706.1964].

[264] T. Han, B. Mukhopadhyaya, Z. Si and K. Wang, *Pair production of doubly-charged scalars: Neutrino mass constraints and signals at the LHC*, *Phys. Rev.* **D76** (2007) 075013 [0706.0441].

[265] C.-S. Chen, C.-Q. Geng and D. V. Zhuridov, *Same-sign single dilepton productions at the LHC*, *Phys. Lett.* **B666** (2008) 340–343 [0801.2011].

[266] A. G. Akeroyd and S. Moretti, *Production of doubly charged scalars from the decay of a heavy SM-like Higgs boson in the Higgs Triplet Model*, *Phys. Rev.* **D84** (2011) 035028 [1106.3427].

[267] A. G. Akeroyd and H. Sugiyama, *Production of doubly charged scalars from the decay of singly charged scalars in the Higgs Triplet Model*, *Phys. Rev.* **D84** (2011) 035010 [1105.2209].

[268] H. Sugiyama, K. Tsumura and H. Yokoya, *Discrimination of models including doubly charged scalar bosons by using tau lepton decay distributions*, *Phys. Lett.* **B717** (2012) 229–234 [1207.0179].

[269] F. del Aguila, M. Chala, A. Santamaria and J. Wudka, *Distinguishing between lepton number violating scalars at the LHC*, *EPJ Web Conf.* **60** (2013) 17002 [1307.0510].

[270] F. del Aguila, M. Chala, A. Santamaria and J. Wudka, *Discriminating between lepton number violating scalars using events with four and three charged leptons at the LHC*, *Phys. Lett.* **B725** (2013) 310–315 [1305.3904].

[271] K. S. Babu, A. Patra and S. K. Rai, *New Signals for Doubly-Charged Scalars and Fermions at the Large Hadron Collider*, *Phys. Rev.* **D88** (2013) 055006 [1306.2066].

[272] A. Chaudhuri, W. Grimus and B. Mukhopadhyaya, *Doubly charged scalar decays in a type II seesaw scenario with two Higgs triplets*, *JHEP* **1402** (2014) 060 [1305.5761].

[273] A. Alloul, M. Frank, B. Fuks and M. R. de Traubenberg, *Doubly-charged particles at the Large Hadron Collider*, *Phys. Rev.* **D88** (2013) 075004 [1307.1711].

[274] B. Dutta, R. Eusebi, Y. Gao, T. Ghosh and T. Kamon, *Exploring the Doubly Charged Higgs of the Left-Right Symmetric Model using Vector Boson Fusion-like Events at the LHC*, *Phys. Rev.* **D90** (2014) 055015 [1404.0685].

[275] F. del Aguila and M. Chala, *LHC bounds on Lepton Number Violation mediated by doubly and singly-charged scalars*, *JHEP* **1403** (2014) 027 [1311.1510].

[276] S. F. King, *Atmospheric and solar neutrinos with a heavy singlet*, *Phys. Lett.* **B439** (1998) 350–356 [hep-ph/9806440].

[277] S. F. King, *Atmospheric and solar neutrinos from single right-handed neutrino dominance and U(1) family symmetry*, *Nucl. Phys.* **B562** (1999) 57–77 [hep-ph/9904210].

[278] S. Antusch and S. F. King, *Sequential dominance*, *New J. Phys.* **6** (2004) 110 [hep-ph/0405272].

[279] S. F. King, *Leptogenesis MNS link in unified models with natural neutrino mass hierarchy*, *Phys. Rev.* **D67** (2003) 113010 [hep-ph/0211228].

[280] P. F. Harrison, D. H. Perkins and W. G. Scott, *Tri-bimaximal mixing and the neutrino oscillation data*, *Phys. Lett.* **B530** (2002) 167 [hep-ph/0202074].

[281] P. F. Harrison and W. G. Scott, *Symmetries and generalizations of tri - bimaximal neutrino mixing*, *Phys. Lett.* **B535** (2002) 163–169 [hep-ph/0203209].

[282] Z.-z. Xing, *Nearly tri bimaximal neutrino mixing and CP violation*, *Phys. Lett.* **B533** (2002) 85–93 [hep-ph/0204049].

[283] X. G. He and A. Zee, *Some simple mixing and mass matrices for neutrinos*, *Phys. Lett.* **B560** (2003) 87–90 [hep-ph/0301092].

[284] M.-C. Chen and S. F. King, *A4 See-Saw Models and Form Dominance*, *JHEP* **06** (2009) 072 [0903.0125].

[285] S. F. King, *Vacuum misalignment corrections to tri-bimaximal mixing and form dominance*, *JHEP* **01** (2011) 115 [1011.6167].

[286] S. Antusch, L. E. Ibanez and T. Macri, *Neutrino masses and mixings from string theory instantons*, *JHEP* **09** (2007) 087 [0706.2132].

[287] S. F. King and C. Luhn, *Littlest Seesaw model from $S_4\times$ U(1)*, *JHEP* **09** (2016) 023 [1607.05276].

[288] S. F. King, *Invariant see-saw models and sequential dominance*, *Nucl. Phys.* **B786** (2007) 52–83 [hep-ph/0610239].

[289] Z.-z. Xing and S. Zhou, *Tri-bimaximal Neutrino Mixing and Flavor-dependent Resonant Leptogenesis*, *Phys. Lett.* **B653** (2007) 278–287 [hep-ph/0607302].

[290] C. H. Albright and W. Rodejohann, *Comparing Trimaximal Mixing and Its Variants with Deviations from Tri-bimaximal Mixing*, *Eur. Phys. J.* **C62** (2009) 599–608 [0812.0436].

[291] C. H. Albright, A. Dueck and W. Rodejohann, *Possible Alternatives to Tri-bimaximal Mixing*, *Eur. Phys. J.* **C70** (2010) 1099–1110 [1004.2798].

[292] S. F. King and C. Luhn, *On the origin of neutrino flavour symmetry*, *JHEP* **10** (2009) 093 [0908.1897].

[293] S. F. King and C. Luhn, *A New family symmetry for SO(10) GUTs*, *Nucl. Phys.* **B820** (2009) 269–289 [0905.1686].

[294] C. S. Lam, *Symmetry of Lepton Mixing*, *Phys. Lett.* **B656** (2007) 193–198 [0708.3665].

[295] C. S. Lam, *Determining Horizontal Symmetry from Neutrino Mixing*, *Phys. Rev. Lett.* **101** (2008) 121602 [0804.2622].

[296] C. S. Lam, *The Unique Horizontal Symmetry of Leptons*, *Phys. Rev.* **D78** (2008) 073015 [0809.1185].

[297] E. Ma and G. Rajasekaran, *Softly broken A(4) symmetry for nearly degenerate neutrino masses*, *Phys. Rev.* **D64** (2001) 113012 [hep-ph/0106291].

[298] K. S. Babu, E. Ma and J. W. F. Valle, *Underlying A(4) symmetry for the neutrino mass matrix and the quark mixing matrix*, *Phys. Lett.* **B552** (2003) 207–213 [hep-ph/0206292].

[299] E. Ma, *A(4) symmetry and neutrinos with very different masses*, *Phys. Rev.* **D70** (2004) 031901 [hep-ph/0404199].

[300] K. S. Babu and X.-G. He, *Model of geometric neutrino mixing*, hep-ph/0507217.

[301] G. Altarelli and F. Feruglio, *Tri-bimaximal neutrino mixing from discrete symmetry in extra dimensions*, *Nucl. Phys.* **B720** (2005) 64–88 [hep-ph/0504165].

[302] X.-G. He, Y.-Y. Keum and R. R. Volkas, *A(4) flavor symmetry breaking scheme for understanding quark and neutrino mixing angles*, *JHEP* **04** (2006) 039 [hep-ph/0601001].

[303] G. Altarelli and F. Feruglio, *Tri-bimaximal neutrino mixing, A(4) and the modular symmetry*, *Nucl. Phys.* **B741** (2006) 215–235 [hep-ph/0512103].

[304] C. Luhn, *Trimaximal TM_1 neutrino mixing in S_4 with spontaneous CP violation*, *Nucl. Phys.* **B875** (2013) 80–100 [1306.2358].

[305] F. Björkeroth, F. J. de Anda, I. de Medeiros Varzielas and S. F. King, *Towards a complete $A_4\times$ SU(5) SUSY GUT*, *JHEP* **06** (2015) 141 [1503.03306].

[306] F. Björkeroth, F. J. de Anda, I. de Medeiros Varzielas and S. F. King, *Leptogenesis in minimal predictive seesaw models*, *JHEP* **10** (2015) 104 [1505.05504].

[307] G. Altarelli, F. Feruglio and Y. Lin, *Tri-bimaximal neutrino mixing from orbifolding*, *Nucl. Phys.* **B775** (2007) 31–44 [hep-ph/0610165].

[308] S. F. King and M. Malinsky, *Towards a Complete Theory of Fermion Masses and Mixings with SO(3) Family Symmetry and 5-D SO(10) Unification*, *JHEP* **11** (2006) 071 [hep-ph/0608021].

[309] F. Björkeroth, F. J. de Anda, I. de Medeiros Varzielas and S. F. King, *Towards a complete $\Delta(27) \times SO(10)$ SUSY GUT*, *Phys. Rev.* **D94** (2016), no. 1 016006 [1512.00850].

[310] S. F. King, J. Zhang and S. Zhou, *Renormalisation Group Corrections to the Littlest Seesaw Model and Maximal Atmospheric Mixing*, *JHEP* **12** (2016) 023 [1609.09402].

[311] **T2K** Collaboration, K. Abe *et. al.*, *Precise Measurement of the Neutrino Mixing Parameter θ_{23} from Muon Neutrino Disappearance in an Off-Axis Beam*, *Phys. Rev. Lett.* **112** (2014), no. 18 181801 [1403.1532].

[312] **JADE** Collaboration, S. Bethke *et. al.*, *Experimental Investigation of the Energy Dependence of the Strong Coupling Strength*, *Phys. Lett.* **B213** (1988) 235–241.

[313] S. Bethke, *JET PHYSICS IN e+ e- ANNIHILATION: EVIDENCE FOR THE RUNNING OF alpha-s*, in *Current issues in hadron physics. Proceedings, 23rd Rencontres de Moriond, Hadronic Session, Les Arcs, France, March 13-19, 1988*, pp. 379–384, 1988.

[314] S. Bethke, *Experimental tests of asymptotic freedom*, *Nucl. Phys. Proc. Suppl.* **54A** (1997) 314–326 [hep-ex/9609014].

[315] M. Peskin and D. Schroeder, *An Introduction to Quantum Field Theory*. Advanced book classics. Addison-Wesley Publishing Company, 1995.

[316] M. Srednicki, *Quantum Field Theory*. Cambridge University Press, 2007.

[317] S. Pokorski, *Gauge Field Theories*. Cambridge Monographs on Mathematical Physics. Cambridge University Press, 2000.

[318] S. Weinberg, *The Quantum Theory of Fields*. No. 2 in The Quantum Theory of Fields 3 Volume Hardback Set. Cambridge University Press, 1996.

[319] W. Pauli and F. Villars, *On the Invariant regularization in relativistic quantum theory*, *Rev. Mod. Phys.* **21** (1949) 434–444.

[320] G. 't Hooft and M. Veltman, *Regularization and Renormalization of Gauge Fields*, *Nucl. Phys.* **B44** (1972) 189–213.

[321] G. Leibbrandt, *Introduction to the Technique of Dimensional Regularization*, *Rev. Mod. Phys.* **47** (1975) 849.

[322] A. Pak and A. Smirnov, *Geometric approach to asymptotic expansion of Feynman integrals*, *Eur. Phys. J.* **C71** (2011) 1626 [1011.4863].

[323] F. Feng, *A Recursive Method to Calculate UV-divergent Parts at One-Loop Level in Dimensional Regularization*, *Comput. Phys. Commun.* **183** (2012) 1519–1524 [1202.0931].

[324] S. Weinberg, *High-energy behavior in quantum field theory*, *Phys. Rev.* **118** (1960) 838–849.

[325] J. C. Collins, *Renormalization: An Introduction to Renormalization, the Renormalization Group and the Operator-Product Expansion.* Cambridge University Press, 1984.

[326] G. 't Hooft, *Renormalization of Massless Yang-Mills Fields*, *Nucl. Phys.* **B33** (1971) 173–199.

[327] G. 't Hooft, *Renormalizable Lagrangians for Massive Yang-Mills Fields*, *Nucl. Phys.* **B35** (1971) 167–188.

[328] C. G. Callan, Jr., *Broken scale invariance and asymptotic behavior*, *Phys. Rev.* **D5** (1972) 3202–3210.

[329] K. Symanzik, *Small distance behavior in field theory and power counting*, *Commun. Math. Phys.* **18** (1970) 227–246.

[330] K. Symanzik, *Small distance behavior analysis and Wilson expansion*, *Commun. Math. Phys.* **23** (1971) 49–86.

[331] S. Antusch, J. Kersten, M. Lindner, M. Ratz and M. A. Schmidt, *Running neutrino mass parameters in see-saw scenarios*, *JHEP* **03** (2005) 024 [hep-ph/0501272].

[332] M. Neubert, *Effective Field Theory and Heavy Quark Physics*, *TASI Lectures* (2004) [hep-ph/0512222v1].

[333] A. Buras, *Weak Hamiltonian, CP violation and rare decays*, hep-ph/9806471.

[334] H. Georgi, *Effective Field Theory*, *Ann. Rev. Nucl. Part. Sci.* **43** (1993) 209.

[335] T. Appelquist and J. Carazzone, *Infrared Singularities and Massive Fields*, *Phys. Rev.* **D11** (1975) 2856.

[336] J. C. Collins, F. Wilczek and A. Zee, *Low-Energy Manifestations of Heavy Particles: Application to the Neutral Current*, *Phys. Rev.* **D18** (1978) 242.

[337] D. Toussaint, *Renormalization Effects From Superheavy Higgs Particles*, *Phys. Rev.* **D18** (1978) 1626.

[338] Y. Kazama and Y.-P. Yao, *A Systematic Investigation of Effects of Heavy Particles via Factorized Local Operators and Renormalization. Group 1: General Formulation in Quantum Electrodynamics*, *Phys. Rev.* **D21** (1980) 1116.

[339] Y. Kazama and Y.-P. Yao, *A Systematic Investigation of Effects of Heavy Particles via Factorized Local Operators and Renormalization Group. 2. Explicit Calculations in Quantum Electrodynamics*, *Phys. Rev.* **D21** (1980) 1138.

[340] J. Ambjorn, *On the Decoupling of Massive Particles in Field Theory*, *Commun. Math. Phys.* **67** (1979) 109.

[341] T. Hagiwara and N. Nakazawa, *Perturbative Effect of Heavy Particles in Effective Lagrangian Approach*, *Phys. Rev.* **D23** (1981) 959.

[342] E. B. Manoukian, *ON THE DECOUPLING THEOREM IN FIELD THEORY*, *J. Math. Phys.* **22** (1981) 572–573.

[343] E. B. Manoukian, *GENERALIZED DECOUPLING THEOREM IN QUANTUM FIELD THEORY*, *J. Math. Phys.* **22** (1981) 2258–2262.

[344] E. B. Manoukian, *DECOUPLING THEOREM OF QUANTUM FIELD THEORY IN MINKOWSKI SPACE*, *Int. J. Theor. Phys.* **22** (1983) 315–321.

[345] C. W. Bauer, S. Fleming and M. E. Luke, *Summing Sudakov logarithms in B —> X(s gamma) in effective field theory*, *Phys. Rev.* **D63** (2000) 014006 [hep-ph/0005275].

[346] C. W. Bauer, S. Fleming, D. Pirjol and I. W. Stewart, *An Effective field theory for collinear and soft gluons: Heavy to light decays*, *Phys. Rev.* **D63** (2001) 114020 [hep-ph/0011336].

[347] C. W. Bauer and I. W. Stewart, *Invariant operators in collinear effective theory*, *Phys. Lett.* **B516** (2001) 134–142 [hep-ph/0107001].

[348] C. W. Bauer, D. Pirjol and I. W. Stewart, *Soft collinear factorization in effective field theory*, *Phys. Rev.* **D65** (2002) 054022 [hep-ph/0109045].

[349] C. W. Bauer, D. Pirjol and I. W. Stewart, *Power counting in the soft collinear effective theory*, *Phys. Rev.* **D66** (2002) 054005 [hep-ph/0205289].

[350] W. E. Caswell and G. P. Lepage, *Effective Lagrangians for Bound State Problems in QED, QCD, and Other Field Theories*, *Phys. Lett.* **B 167** (1986) 437.

[351] B. A. Thacker and G. P. Lepage, *Heavy quark bound states in lattice QCD*, *Phys. Rev.* **D 43** (1991) 196.

[352] G. P. Lepage, L. Magnea, C. Nakhleh, U. Magnea and K. Hornbostel, *Improved nonrelativistic QCD for heavy quark physics*, *Phys. Rev.* **D 46** (1992) 4052 [hep-lat/9205007].

[353] T. Kinoshita and M. Nio, *Radiative corrections to the muonium hyperfine structure. 1. The alpha**2 (Z-alpha) correction*, *Phys. Rev.* **D53** (1996) 4909–4929 [hep-ph/9512327].

[354] G. Paz, *An Introduction to NRQED*, *Mod. Phys. Lett.* **A30** (2015), no. 26 1550128 [1503.07216].

[355] B. Henning, X. Lu and H. Murayama, *How to use the Standard Model effective field theory*, 1412.1837.

[356] D. Sivia, *Data Analysis: A Bayesian Tutorial*. Oxford science publications. Clarendon Press, 1996.

[357] G. Cowan, *Statistical Data Analysis*. Oxford science publications. Clarendon Press, 1998.

[358] G. Bohm and G. Zech, *Einführung in Statistik und Messwertanalyse für Physiker*. DESY, 2006.

[359] S. Antusch, J. Kersten, M. Lindner, M. Ratz and M. A. Schmidt, *Renormalization group Evolution of Angles and Phases (REAP)*, 2017. Most recent version and documentation on the REAP package, available online at http://reapmpt.hepforge.org and https://www.hepforge.org/downloads/reapmpt.

[360] M. Lindner, M. Platscher and F. S. Queiroz, *A Call for New Physics : The Muon Anomalous Magnetic Moment and Lepton Flavor Violation*, 1610.06587.

[361] F. Jegerlehner and A. Nyffeler, *The Muon g-2*, *Phys. Rept.* **477** (2009) 1–110 [0902.3360].

[362] T. Blum, A. Denig, I. Logashenko, E. de Rafael, B. Lee Roberts, T. Teubner and G. Venanzoni, *The Muon (g-2) Theory Value: Present and Future*, 1311.2198.

[363] *Hadronic contributions to the muon anomalous magnetic moment Workshop.* $(g-2)_\mu$*: Quo vadis? Workshop. Mini proceedings*, 2014.

[364] **SINDRUM** Collaboration, U. Bellgardt *et. al.*, *Search for the Decay mu+ —> e+ e+ e-*, *Nucl. Phys.* **B299** (1988) 1–6.

[365] K. Hayasaka *et. al.*, *Search for Lepton Flavor Violating Tau Decays into Three Leptons with 719 Million Produced Tau+Tau- Pairs*, *Phys. Lett.* **B687** (2010) 139–143 [1001.3221].

[366] R. K. Kutschke, *The Mu2e Experiment at Fermilab*, 1112.0242.

[367] S. Weinberg and G. Feinberg, *Electromagnetic Transitions Between mu Meson and Electron*, *Phys. Rev. Lett.* **3** (1959) 111–114.

[368] W. J. Marciano and A. I. Sanda, *The Reaction mu- Nucleus –> e- Nucleus in Gauge Theories*, *Phys. Rev. Lett.* **38** (1977) 1512.

[369] D. N. Dinh, A. Ibarra, E. Molinaro and S. T. Petcov, *The $\mu - e$ Conversion in Nuclei, $\mu \to e\gamma, \mu \to 3e$ Decays and TeV Scale See-Saw Scenarios of Neutrino Mass Generation*, *JHEP* **08** (2012) 125 [1205.4671]. [Erratum: JHEP09,023(2013)].

[370] J. Bernabeu, E. Nardi and D. Tommasini, *μ - e conversion in nuclei and Z' physics*, *Nucl. Phys.* **B409** (1993) 69–86 [hep-ph/9306251].

[371] A. Crivellin, M. Hoferichter and M. Procura, *Improved predictions for $\mu \to e$ conversion in nuclei and Higgs-induced lepton flavor violation*, *Phys. Rev.* **D89** (2014) 093024 [1404.7134].

[372] M. Frank, *mu - e conversion in nuclei in the left-right supersymmetric model*, *Eur. Phys. J.* **C17** (2000) 501–512.

[373] E. Arganda, M. J. Herrero and A. M. Teixeira, *mu-e conversion in nuclei within the CMSSM seesaw: Universality versus non-universality*, *JHEP* **10** (2007) 104 [0707.2955].

[374] H.-B. Zhang, T.-F. Feng, G.-H. Luo, Z.-F. Ge and S.-M. Zhao, *Muon conversion to electron in nuclei within the $\mu\nu$SSM with a 125 GeV Higgs*, *JHEP* **07** (2013) 069 [1305.4352]. [Erratum: JHEP10,173(2013)].

[375] M. Raidal and A. Santamaria, *Muon electron conversion in nuclei versus mu → e gamma: An Effective field theory point of view*, *Phys. Lett.* **B421** (1998) 250–258 [hep-ph/9710389].

[376] L. S. Kisslinger, *Test of lepton quantum numbers by muon capture*, *Phys. Rev. Lett.* **26** (1971) 998–1000. [Erratum: Phys. Rev. Lett.28,869(1972)].

[377] M. D. Shuster and M. Rho, *Exotic muon capture in nuclei and lepton conservation*, *Phys. Lett.* **B42** (1972) 45–48.

[378] D. A. Bryman, M. Blecher, K. Gotow and R. J. Powers, *Search for the reaction mu- cu —> e+ co*, *Phys. Rev. Lett.* **28** (1972) 1469–1471.

[379] R. Abela, G. Backenstoss, W. Kowald, J. Wuest, H. G. Seiler, M. Seiler and L. M. Simons, *NEW UPPER LIMIT FOR MU- —> E+ CONVERSION*, *Phys. Lett.* **B95** (1980) 318–322.

[380] A. Badertscher *et. al.*, *A Search for Muon - Electron and Muon - Positron Conversion in Sulfur*, *Nucl. Phys.* **A377** (1982) 406–440.

[381] R. A. Burnham *et. al.*, *Search for μe Conversion in Ti*, *Phys. Rev. Lett.* **59** (1987) 970–973.

[382] S. Ahmad *et. al.*, *Search for Muon - Electron and Muon - Positron Conversion*, *Phys. Rev.* **D38** (1988) 2102.

[383] **SINDRUM II** Collaboration, W. H. Bertl *et. al.*, *A Search for muon to electron conversion in muonic gold*, *Eur. Phys. J.* **C47** (2006) 337–346.

[384] A. Badertscher *et. al.*, *Search for $\mu^- \to e^+$ Conversion on Sulfur*, *Phys. Lett.* **79B** (1978) 371. [Erratum: Phys. Lett.80B,434(1979)].

[385] **SINDRUM II** Collaboration, C. Dohmen *et. al.*, *Test of lepton flavor conservation in mu —> e conversion on titanium*, *Phys. Lett.* **B317** (1993) 631–636.

[386] A. Czarnecki, X. Garcia i Tormo and W. J. Marciano, *Muon decay in orbit: spectrum of high-energy electrons*, *Phys. Rev.* **D84** (2011) 013006 [1106.4756].

[387] P. Haenggi, R. D. Viollier, U. Raff and K. Alder, *Muon decay in orbit*, *Phys. Lett.* **51B** (1974) 119–122.

[388] C. E. Porter and H. Primakofe, *The effect of bohr orbit binding on negative μ-meson β-decay*, *Phys. Rev.* **83** (Aug, 1951) 849–850.

[389] R. Watanabe, M. Fukui, H. Ohtsubo and M. Morita, *Angular Distribution of Electrons in Bound Muon Decay*, *Prog. Theor. Phys.* **78** (1987) 114–122.

[390] R. Watanabe, K. Muto, T. Oda, T. Niwa, H. Ohtsubo, R. Morita and M. Morita, *Asymmetry and Energy Spectrum of Electrons in Bound-Muon Decay*, *Atom. Data Nucl. Data Tabl.* **54** (1993) 165–178.

[391] O. U. Shanker, *High-energy Electrons From Bound Muon Decay*, *Phys. Rev.* **D25** (1982) 1847.

[392] O. U. Shanker and R. Roy, *High-energy electrons from bound muon decay*, *Phys. Rev.* **D55** (1997) 7307–7308.

[393] A. Czarnecki, X. Garcia i Tormo and W. J. Marciano, *Muon decay in orbit spectra for $\mu - e$ conversion experiments*, *Hyperfine Interact.* **210** (2012), no. 1-3 19–23 [1111.4237].

[394] R. Kitano, M. Koike and Y. Okada, *Detailed calculation of lepton flavor violating muon electron conversion rate for various nuclei*, *Phys. Rev.* **D66** (2002) 096002 [hep-ph/0203110].

[395] H. De Vries, C. W. De Jager and C. De Vries, *Nuclear charge and magnetization density distribution parameters from elastic electron scattering*, *Atom. Data Nucl. Data Tabl.* **36** (1987) 495–536.

[396] G. Fricke, C. Bernhardt, K. Heilig, L. A. Schaller, L. Schellenberg, E. B. Shera and C. W. de Jager, *Nuclear Ground State Charge Radii from Electromagnetic Interactions*, *Atom. Data Nucl. Data Tabl.* **60** (1995) 177.

[397] A. Brody, D. Day, B. Lewis and S. Washington. *The Nuclear Charge Density Archive*, http://faculty.virginia.edu/ncd/index.html.

[398] M. Gonzalez, T. Gutsche, J. C. Helo, S. Kovalenko, V. E. Lyubovitskij and I. Schmidt, *Limits on lepton flavor violation from $\mu^- - e^-$ conversion*, *Phys. Rev.* **D87** (2013), no. 9 096020 [1303.0596].

[399] A. Faessler, T. Gutsche, S. Kovalenko, V. E. Lyubovitskij and I. Schmidt, *Scalar meson mediated nuclear mu- - e- conversion*, *Phys. Rev.* **D72** (2005) 075006 [hep-ph/0507033].

[400] A. Faessler, T. Gutsche, S. Kovalenko, V. E. Lyubovitskij, I. Schmidt and F. Simkovic, *Effective Lagrangian approach to nuclear mu- e- conversion and the role of vector mesons*, *Phys. Rev.* **D70** (2004) 055008 [hep-ph/0405164].

[401] A. Faessler, T. Gutsche, S. Kovalenko, V. E. Lyubovitskij, I. Schmidt and F. Simkovic, *Vector mesons in nuclear mu- e- conversion*, *Phys. Lett.* **B590** (2004) 57–62 [hep-ph/0403033].

[402] T. S. Kosmas, A. Faessler, F. Simkovic and J. D. Vergados, *State by state calculations for all channels of the exotic (mu-, e-) conversion process*, *Phys. Rev.* **C56** (1997) 526–534 [nucl-th/9704021].

[403] A. Faessler, V. Rodin and F. Simkovic, *Nuclear matrix elements for neutrinoless double-beta decay and double-electron capture*, *J. Phys.* **G39** (2012) 124006 [1206.0464].

[404] J. Barea, J. Kotila and F. Iachello, *$0\nu\beta\beta$ and $2\nu\beta\beta$ nuclear matrix elements in the interacting boson model with isospin restoration*, *Phys. Rev.* **C91** (2015), no. 3 034304 [1506.08530].

[405] J. Hyvärinen and J. Suhonen, *Nuclear matrix elements for $0\nu\beta\beta$ decays with light or heavy Majorana-neutrino exchange*, *Phys. Rev.* **C91** (2015), no. 2 024613.

[406] J. Engel, *Uncertainties in nuclear matrix elements for neutrinoless double-beta decay*, *J. Phys.* **G42** (2015), no. 3 034017.

[407] F. Simkovic, V. Rodin, A. Faessler and P. Vogel, *0nbb and 2nbb nuclear matrix elements, quasiparticle random-phase approximation, and isospin symmetry restoration*, *Phys. Rev.* **C87** (2013), no. 4 045501 [1302.1509].

[408] J. Barea, J. Kotila and F. Iachello, *Nuclear matrix elements for double-β decay*, *Phys. Rev.* **C87** (2013), no. 1 014315 [1301.4203].

[409] J. Suhonen and O. Civitarese, *Review of the properties of the 0 nu beta-beta- nuclear matrix elements*, *J. Phys.* **G39** (2012) 124005.

[410] J. Suhonen and O. Civitarese, *Double-beta-decay nuclear matrix elements in the QRPA framework*, *J. Phys.* **G39** (2012) 085105.

[411] **SINDRUM II** Collaboration, W. Honecker *et. al.*, *Improved limit on the branching ratio of mu —> e conversion on lead*, *Phys. Rev. Lett.* **76** (1996) 200–203.

[412] **DeeMe** Collaboration, M. Aoki, *A new idea for an experimental search for mu-e conversion*, *PoS* **ICHEP2010** (2010) 279.

[413] N. Otuka *et. al.*, *Towards a More Complete and Accurate Experimental Nuclear Reaction Data Library (EXFOR): International Collaboration Between Nuclear Reaction Data Centres (NRDC)*, *Nuclear Data Sheets* **120** (2014) 272–276.

[414] P. C. Divari, J. D. Vergados, T. S. Kosmas and L. D. Skouras, *The Exotic double charge exchange mu- —> e+ conversion in nuclei*, *Nucl. Phys.* **A703** (2002) 409–431 [nucl-th/0203066].

[415] L. Lavoura, *General formulae for f(1) —> f(2) gamma*, *Eur. Phys. J.* **C29** (2003) 191–195 [hep-ph/0302221].

[416] H. H. Patel, *Package-X: A Mathematica package for the analytic calculation of one-loop integrals*, *Comput. Phys. Commun.* **197** (2015) 276–290 [1503.01469].

[417] V. Berestetsky, E. Lifshitz and L. Pitaevsky, *Quantum Electrodynamics*. Pergamon Press, Oxford, UK, 1982.

[418] H. C. Chiang, E. Oset, T. S. Kosmas, A. Faessler and J. D. Vergados, *Coherent and incoherent (mu-, e-) conversion in nuclei*, *Nucl. Phys.* **A559** (1993) 526–542.

[419] O. U. Shanker, *Z Dependence of Coherent μe Conversion Rate in Anomalous Neutrinoless Muon Capture*, *Phys. Rev.* **D20** (1979) 1608.

[420] R. Alonso, M. Dhen, M. B. Gavela and T. Hambye, *Muon conversion to electron in nuclei in type-I seesaw models*, *JHEP* **01** (2013) 118 [1209.2679].

[421] G. Passarino and M. J. G. Veltman, *One Loop Corrections for e+ e- Annihilation Into mu+ mu- in the Weinberg Model*, *Nucl. Phys.* **B160** (1979) 151–207.

[422] G. 't Hooft and M. J. G. Veltman, *Scalar One Loop Integrals*, *Nucl. Phys.* **B153** (1979) 365–401.

[423] D. Yu. Bardin and G. Passarino, *The standard model in the making: Precision study of the electroweak interactions*. 1999.

[424] **COMET** Collaboration, R. Akhmetshin *et. al.*, *COMET International Review Document (TDR-2014)*, 2014. http://comet.kek.jp/Documents_files/IPNS-Review-2014.pdf.

[425] **COMET** Collaboration, Y. G. Cui *et. al.*, *Conceptual design report for experimental search for lepton flavor violating mu- - e- conversion at sensitivity of 10**(-16) with a slow-extracted bunched proton beam (COMET)*, .

[426] K. S. Babu and R. N. Mohapatra, *New vector - scalar contributions to neutrinoless double beta decay and constraints on R-parity violation*, *Phys. Rev. Lett.* **75** (1995) 2276–2279 [hep-ph/9506354].

[427] G. Prezeau, M. Ramsey-Musolf and P. Vogel, *Neutrinoless double beta decay and effective field theory*, *Phys. Rev.* **D68** (2003) 034016 [hep-ph/0303205].

[428] M. GonzĞlez, M. Hirsch and S. G. Kovalenko, *QCD running in neutrinoless double beta decay: Short-range mechanisms*, *Phys. Rev.* **D93** (2016), no. 1 013017 [1511.03945].

[429] J. D. Vergados and M. Ericson, *Study of the (μ^-, e^+) Reaction Mediated by Majorana Neutrinos*, *Nucl. Phys.* **B195** (1982) 262–284.

[430] A. N. Kamal and J. N. Ng, *Majorana Lepton Mediated μ^- to e^+ Conversion in Nuclei*, *Phys. Rev.* **D20** (1979) 2269.

[431] C. E. Picciotto and M. S. Zahir, *Neutrinoless Double Beta Decay in Left-right Symmetric Models*, *Phys. Rev.* **D26** (1982) 2320.

[432] J. D. Vergados, *Lepton violating double beta decay in modern gauge theories*, *Phys. Rev.* **C24** (1981) 640–653.

[433] F. Simkovic, P. Domin, S. V. Kovalenko and A. Faessler, *The (muon-, e+) conversion in nuclei mediated by light Majorana neutrinos*, *Part. Nucl. Lett.* **104** (2001) 40–52 [hep-ph/0103029].

[434] F. Simkovic, G. Pantis, J. D. Vergados and A. Faessler, *Additional nucleon current contributions to neutrinoless double beta decay*, *Phys. Rev.* **C60** (1999) 055502 [hep-ph/9905509].

[435] T. S. Kosmas, G. K. Leontaris and J. D. Vergados, *Lepton flavor nonconservation*, *Prog. Part. Nucl. Phys.* **33** (1994) 397–448 [hep-ph/9312217].

[436] J. D. Bjorken and S. D. Drell, *Relativistic Quantum Mechanics*. Mc Graw-Hill Inc., 1964.

[437] J. Engel and J. MenŐndez, *Status and Future of Nuclear Matrix Elements for Neutrinoless Double-Beta Decay: A Review*, 1610.06548.

[438] T. Yanagida, *HORIZONTAL SYMMETRY AND MASSES OF NEUTRINOS*, *Conf. Proc.* **C7902131** (1979) 95–99.

[439] M. Gell-Mann, P. Ramond and R. Slansky, *Complex Spinors and Unified Theories*, *Conf. Proc.* **C790927** (1979) 315–321 [1306.4669].

[440] S. L. Glashow, *The Future of Elementary Particle Physics*, *NATO Sci. Ser. B* **61** (1980) 687.

[441] P. Pritimita, N. Dash and S. Patra, *Neutrinoless Double Beta Decay in LRSM with Natural Type-II seesaw Dominance*, 1607.07655.

[442] A. Faessler, A. Meroni, S. T. Petcov, F. Simkovic and J. Vergados, *Uncovering Multiple CP-Nonconserving Mechanisms of $(\beta\beta)_{0\nu}$ Decay*, *Phys. Rev.* **D83** (2011) 113003 [1103.2434].

[443] M. Agostini, *First results from GERDA Phase II*, 2016. Talk presented on 08 July 2016 at the Neutrino 2016 Conference, London, UK, http://neutrino2016.iopconfs.org.

[444] M. Agostini, A. Merle and K. Zuber, *Probing flavor models with ^{76} Ge-based experiments on neutrinoless double-β decay*, *Eur. Phys. J.* **C76** (2016), no. 4 176 [1506.06133].

[445] J. MenŐndez, *What do we know about neutrinoless double-beta decay nuclear matrix elements?*, in *NuPhys2015: Prospects in Neutrino Physics (NuPhys) London, UK, December 16-18, 2015*, 2016. 1605.05059.

[446] F. F. Deppisch, *Non-Standard Mechanisms for Neutrinoless Double Beta Decay*, *Phys. Procedia* **61** (2015) 223–226.

[447] T. Ohlsson, *Special issue on neutrino oscillations: Celebrating the nobel prize in physics 2015 in nuclear physics b*, .

[448] Z. Xing and S. Zhou, *Neutrinos in Particle Physics, Astronomy and Cosmology*. Advanced Topics in Science and Technology in China. Springer Berlin Heidelberg, 2011.

[449] S. Antusch, J. Kersten, M. Lindner and M. Ratz, *Running neutrino masses, mixings and CP phases: Analytical results and phenomenological consequences*, *Nucl. Phys.* **B674** (2003) 401–433 [hep-ph/0305273].

[450] A. Denner, H. Eck, O. Hahn and J. Kublbeck, *Feynman rules for fermion number violating interactions*, *Nucl. Phys.* **B387** (1992) 467–484.

[451] H. E. Haber and G. L. Kane, *The Search for Supersymmetry: Probing Physics Beyond the Standard Model*, *Phys. Rept.* **117** (1985) 75–263.

[452] S. K. Jones and C. H. Llewellyn Smith, *Leptoproduction of Supersymmetric Particles*, *Nucl. Phys.* **B217** (1983) 145–171.

[453] C. Cohen-Tannoudji, B. Diu and F. Laloe, *Quantum Mechanics Volume II*. Hermann, and John Wiley & Sons, Paris, 1977.

[454] D. A. Varshalovich, A. N. Moskalev and V. K. Khersonskii, *Quantum Theory of Angular Momentum*. World Scientific Publishing, 1988.

[455] J. Suhonen, *From Nucleons to Nucleus*. Springer Verlag, 2007.

[456] N. L. Manakov, S. I. Marmo and A. V. Meremianin, *A new technique in the theory of angular distributions in atomic processes: the angular distribution of photoelectrons in single and double photoionization*, *Journal of Physics B: Atomic, Molecular and Optical Physics* **29** (1996), no. 13 2711.

[457] S. Antusch and V. Maurer, *Running quark and lepton parameters at various scales*, *JHEP* **11** (2013) 115 [1306.6879].

[458] T. Blazek, S. Raby and S. Pokorski, *Finite supersymmetric threshold corrections to CKM matrix elements in the large tan Beta regime*, *Phys. Rev.* **D52** (1995) 4151–4158 [hep-ph/9504364].

[459] S. Antusch and C. Sluka, *Predicting the Sparticle Spectrum from GUTs via SUSY Threshold Corrections with SusyTC*, *JHEP* **07** (2016) 108 [1512.06727].